University of Stuttgart
Germany

Daniel
Vallicotti

Magneto-Electro-Mechanical Coupling Phenomena Across Multiple Length Scales: Variational Framework and Stability Analysis

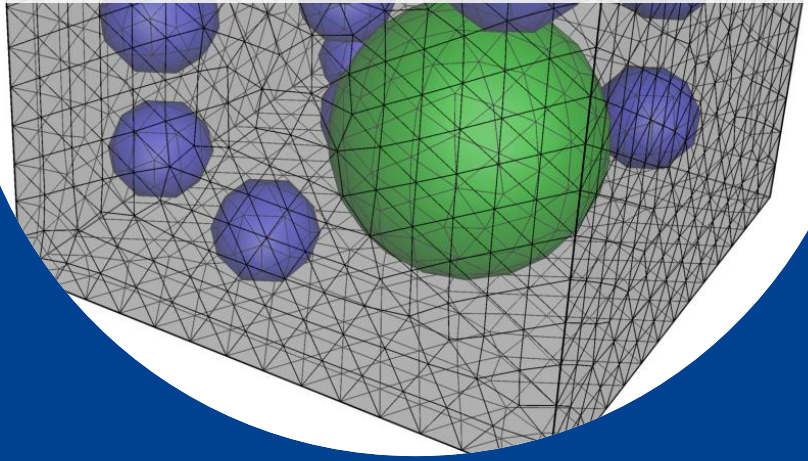

2

Publication series of the
Institute of Applied Mechanics (IAM)

Magneto-Electro-Mechanical Coupling Phenomena Across Multiple Length Scales: Variational Framework and Stability Analysis

Von der Fakultät Bau- und Umweltingenieurwissenschaften der Universität Stuttgart
und dem Stuttgart Center for Simulation Science
zur Erlangung der Würde eines Doktor-Ingenieurs (Dr.-Ing.)
genehmigte Abhandlung

von

Daniel Vallicotti

aus Winnenden

Hauptberichter:	Prof. Dr.-Ing. M.-A. Keip
1. Mitberichter:	Prof. Dr.-Ing. habil. P. Steinmann
2. Mitberichter:	Prof. Dr.-Ing. Dr. h. c. W. Ehlers

Tag der mündlichen Prüfung: 29. Januar 2019

Institut für Mechanik (Bauwesen) der Universität Stuttgart

2019

Publication series of the Institute of Applied Mechanics (IAM), Volume 2
Institute of Applied Mechanics
University of Stuttgart, Germany, 2019

Organisation und Verwaltung:

Institut für Mechanik (Bauwesen)
Lehrstuhl für Materialtheorie
Universität Stuttgart
Pfaffenwaldring 7
70569 Stuttgart
Tel.: +49 (0)711 685-66378
Fax: +49 (0)711 685-66347

Institut für Mechanik (Bauwesen)
Lehrstuhl für Materialtheorie
Universität Stuttgart
Pfaffenwaldring 7
70569 Stuttgart
Tel.: +49 (0)711 685-66377
Fax: +49 (0)711 685-66347

ISBN 978-3-937859-23-1 (D 93 Stuttgart)

Acknowledgements

This work is the result from my time as a research associate at the Institute of Applied Mechanics (Civil Engineering) at the University of Stuttgart. I take this opportunity to sincerely thank all the people that scientifically contributed to this dissertation, enriched my experience in the office and overall supported me during my studies.

I want to express my deepest gratitude to Professor Christian Miehe who inspired me by his unparalleled dedication and enthusiasm for the field. Without his expertise and support this work would not have been possible. Working with such a brilliant mind was a pure pleasure and a profound experience. His guidance will never be forgotten.

I would like to thank Professor Marc-André Keip for taking over the supervision of this work and for his immediate support and careful thoughts even in hard times. A sincere thanks to Professor Paul Steinmann and Professor Wolfgang Ehlers for their interest in the work and the acceptance of becoming co-referees of this dissertation.

Furthermore I would like to thank all my colleagues from both chairs of the Institute of Applied Mechanics for the fruitful discussions, collaborations and the amazing atmosphere. My gratitude goes to Ilona Zimmermann and Dominic Zäh for their supervisions of my bachelor and master theses and for fueling my interest in the field. It was a great pleasure working with you. I couldn't be more happy with my former officemates Lukas Böger and Aref Nateghi. Your support and input are highly appreciated and I will miss the daily discussions. For the productive collaborations with Stephan Teichtmeister and Ashish Sridhar I am most grateful. Your contributions to this work are invaluable. A big thanks goes to Matthias Rambausek, Elten Polukhov, Daniel Kienle, Felix Göküzüm, Omkar Nadgir and Khiem Nguyen for the related discussions. I would also like to gratefully acknowledge the financial support of this work through the German Research Foundation (DFG) within the SimTech Cluster of Excellence (EXC 310).

Most importantly I thank my parents, sister and Daniela for their limitless support, encouragement and confidence during all the years. Without you this would not have been possible.

Stuttgart, January 2019 Daniel Vallicotti

Table of Contents

Abstract **v**

Zusammenfassung **vii**

1. Introduction **1**
1.1. Electro-mechanical coupling phenomena 1
1.2. Magneto-mechanical coupling phenomena 3
1.3. Magneto-electro-mechanical coupling phenomena 4
1.4. State of the art: multiscale magneto-electro-mechanics 6
1.5. Instabilities in magneto-electro-mechanical composites 9
1.6. Objectives and overview 10

I Fundamentals of Magneto-Electro-Mechanics

2. Foundations of Continuum Mechanics and Magneto-Electrostatics **17**
2.1. Fundamentals of continuum mechanics 17
2.1.1. Motion of a material body 18
2.1.2. The deformation gradient 19
2.1.3. Strain measures and commutative diagrams 20
2.1.4. The concept of mechanical stresses: Euler's cut principle 22
2.1.5. Mechanical power expressions 24
2.2. Fundamentals of electrostatics 25
2.2.1. Coulomb's law and the electric field 25
2.2.2. Principle of superposition and Faraday's law 26
2.2.3. Gauss's law of electrostatics 27
2.2.4. The electric field in ponderable media 28
2.2.5. Linear dielectrics, susceptibility, and dielectric constant 29
2.2.6. Electric boundary conditions at interfaces 29
2.2.7. Geometrical transformations and electric power expressions 30
2.3. Fundamentals of magnetostatics 30
2.3.1. First principle of magnetostatics 31
2.3.2. Biot-Savart's law and second principle of magnetostatics 31

2.3.3. Ampère's law of magnetostatics . . . 32
2.3.4. The magnetic field in magnetizable media . . . 32
2.3.5. Magnetic boundary conditions at interfaces . . . 33
2.3.6. Geometrical transformations and magnetic power expressions . . . 33
2.4. Extended balance laws of mechanics . . . 34

3. The Concept of Micro-to-Macro Transition 37
3.1. The concept of representative volume elements . . . 38
3.2. Averaging theorems of magneto-electro-mechanics . . . 39
3.3. The generalized Hill-Mandel macrohomogeneity condition . . . 41

4. Constitutive Inequalities and Convexity 47
4.1. Existence of solutions . . . 47
4.2. Convexity and uniqueness of solutions . . . 48
4.3. Weaker convexity conditions . . . 50
4.3.1. Poly-convexity . . . 50
4.3.2. Quasi-convexity . . . 50
4.3.3. Rank-one convexity and strong ellipticity . . . 51
4.3.4. Summary of weak convexity statements . . . 53

5. Variational Principle of Gradient-Extended Dissipative Solids 55
5.1. Incremental variational framework on the macroscale . . . 55
5.1.1. Generalized multifield state variables . . . 56
5.1.2. Concept of material frame invariance and reduced states . . . 56
5.1.3. Generalized variational principle . . . 56
5.2. Incremental variational framework on the microscale . . . 58
5.2.1. Generalized multifield state variables . . . 58
5.2.2. Concept of material frame invariance . . . 58
5.2.3. Generalized rate-type variational principle . . . 59
5.2.4. Generalized time-discrete variational principle . . . 60
5.2.5. Microscopic variational principle of homogenization . . . 61
5.3. Generalized macroscopic driving routine . . . 62

II Minimization and Mixed-Principles: A Comparison

6. Minimization and Mixed Principles: A Comparison 67
6.1. Variational electro-elasticity . . . 67
6.2. Energetic arrangement of phenomenological electro-elasticity . . . 68
6.3. Extended principle of phenomenological electro-elasticity . . . 69
6.4. Enthalpy principle of phenomenological electro-elasticity . . . 71

6.5. Energetic congruent transformation of energy to enthalpy 72
6.6. Energetic congruent transformation: an example 73
6.7. Challenges of minimization principles 75
6.7.1. The extended canonical potential with Coulomb gauge 76
6.7.2. Extended mixed formulation of Hu-Washizu-type 79
6.7.3. Equivalent reduced integration ansatz 81
6.8. Challenges of minimization principles: numerical examples 82
6.9. Electric vector potential: an application 90

III Multiscale Magneto-Electro-Mechanical Stability Analysis

7. Magneto-Electro-Mechanical Stability Analysis 93
7.1. Microscopic structural instabilities 94
7.1.1. Structural stability in the canonical energy formulation 95
7.1.2. Structural stability in the extended energy formulation 96
7.1.3. Structural stability in the convenient enthalpy formulation 97
7.2. Microscopic material instabilities 97
7.2.1. Material stability in the canonical energy formulation 98
7.2.2. Material stability in the extended energy formulation 99
7.2.3. Material stability in the convenient enthalpy formulation 101
7.3. Macroscopic structural instabilities 102
7.3.1. Structural stability in the canonical energy formulation 102
7.3.2. Structural stability in the extended energy formulation 103
7.3.3. Structural stability in the convenient enthalpy formulation 103
7.4. Macroscopic material instabilities 104
7.4.1. Material stability in the canonical energy formulation 104
7.4.2. Material stability in the extended energy formulation 105
7.4.3. Material stability in the convenient enthalpy formulation 107
7.5. Alternative FE implementation of homogenization 108
7.5.1. Energy formulation based on vector potentials 108
7.5.2. Enthalpy formulation based on Dirichlet conditions 110
7.6. Summary of multiscale instabilities 112
7.7. Explanatory analytical example 112
7.7.1. Definition of the model problem 115
7.7.2. Limit-point analysis for electric loading 116
7.7.3. Limit-point analysis for combined electro-mechanical loading 120
7.8. Numerical examples 121
7.8.1. Problem 1: analysis of an inhomogeneous material element 121
7.8.2. Problem 2: multiscale analysis of magneto-active composites 129
7.8.3. Problem 3: multiscale analysis of magneto-electro-mechanics 135

IV Phase-Field Modeling of Micro-Magneto-Electro-Mechanics

8. Phase-field modeling of finite deformation micro-electro-mechanics 143
8.1. Two-scale finite deformation micro-electro-mechanics 144
8.1.1. Macroscopic variables and primary fields 144
8.1.2. Macroscopic rate-type variational principle 144
8.1.3. Macroscopic incremental variational principle 145
8.1.4. Microscopic variables and primary fields 145
8.1.5. Microscopic rate-type variational principle 146
8.1.6. Microscopic incremental variational principle 147
8.1.7. Microscopic variational principle of homogenization 147
8.2. Finite element implementation of homogenization 148
8.2.1. Generalized arrays and microscopic equilibrium 148
8.2.2. Homogenized macroscopic stresses and moduli 149
8.3. Energy storage and dissipation potential 150
8.4. Numerical examples 151
8.4.1. Problem 1: polycrystalline micro-structure 152
8.4.2. Problem 2: influence of inclusion shape 155
8.4.3. Problem 3: influence of micro-structure orientation 156

9. Phase-field modeling of finite deformation micro-magneto-mechanics 159
9.1. Two-scale finite deformation micro-magneto-mechanics 159
9.1.1. Macroscopic variables and gradient fields 159
9.1.2. Microscopic variables and gradient fields 160
9.1.3. Microscopic rate-type variational principle 160
9.1.4. Microscopic incremental variational principle 162
9.2. Finite element implementation of homogenization 162
9.2.1. Generalized arrays 162
9.2.2. Microscopic staggered solution scheme 163
9.2.3. Algorithmic two-scale solution scheme 165
9.3. Representative numerical model problems 168
9.3.1. Problem 1: evolution and motion of magnetic domain walls 169
9.3.2. Problem 2: influence of different volume fractions 170
9.3.3. Problem 3: influence of micro-structure orientation 171
9.3.4. Problem 4: the magnetic stiffening-effect 173

10.Conclusion 175

Bibliography 177

Abstract

Optimal material design and functionality is an everlasting goal of material sciences. In recent years this trend spreads to every branch of engineering sciences and motivates computational material modeling to improve and support experimental observations. Especially in the field of coupled multiphysics problems, i.e. magneto-electro-mechanics, chemo-mechanics, and thermo-mechanics, numerical methods are necessary to predict the complex interacting phenomena. With the rapid advances in micro-electronics and data-processing, multiscale material models can be incorporated in the development process of innovative functional materials. In this work, the broad field of magneto-electro-mechanically coupled devices is in focus. Here, the interactions of electric, magnetic and mechanical fields give rise to smart materials, that are capable of mimicking the human muscular and nervous system. Advanced industrial applications, such as artificial muscles, flying devices, active damping, or data-storage-systems require rigorous testing for reliable components. This work provides the basis for multiscale investigations of magneto-electro-mechanics both in a phenomenological and micro-mechanically motivated setting.

In the present work, the field of magneto-electro-mechanical systems is divided into two general groups: (i) piezoelectric and piezomagnetic materials (with a focus on the subclasses of ferroelectric and ferromagnetic materials), and (ii) electro-active polymers (EAPs) and magnetorheological elastomers (MREs). They differ substantially in their material properties. Piezoelectrics usually are single phase, brittle, ceramic materials that are used for their short response times, light weight, and low excitation fields. They find use in the industry as sensors and actuators. Likewise, piezomagnetic materials are capable of small mechanical deformations under moderate magnetic fields. Their electric and magnetic properties are due to several homogeneously polarized/magnetized regions on the microscale, which yield linear coupling phenomena. The possibility of spontaneous polarization and magnetization even under no applied fields characterizes the subgroup of ferroelectrics and ferromagnetics. Here, non-linear coupling as well as possible hysteresis under high cyclic loading is evident. In contrast, EAPs and MREs are composite materials, consisting of an elastomeric matrix material with embedded electric or magnetic particles, respectively. Here, the interactions of particles within the specimen yield moderate to large deformations, and can alter the effective mechanical properties of the system. These intriguing materials are a field of current research and respective applications are still of rather academical nature. In a new ambitious approach, two- and three-phase magneto-electro-mechanical composite materials are being developed. Here, the magneto-electric coupling effect, i.e. the alteration of electric polarization by application of a magnetic field or vise versa, is exploited to display brain activities by measuring small magnetic fields. While brittle, small strain, two-phase materials are already realized as magneto-electric sensors, three-phase composites with a surrounding matrix material might cover the range of large deformations.

In any case, experiments have shown, that the magneto-electro-mechanical material responses are subjected to structural and material instabilities on multiple length scales. This ranges from buckling of embedded fibers, to dielectric breakdown and ultimately failure of the material. Naturally, these instability modes need to either be prevented or, for non-destructive instabilities, be actively controlled for improved deformation modes. This task motivates the formulation of multiscale stability criteria that can accompany standard finite element simulations of the multiphysics material.

The present work deals with the difficulties of magneto-electro-mechanical excitation and related multiscale instabilities that prevent the adaptation of these materials in everyday life applications. For that, variational principles based on both, pure minimization and extended mixed energy-enthalpy saddle-point structures are introduced and compared in terms of numerical convenience and accuracy of solutions. Energetic criteria for the formulation of multiscale instability checks are reformulated in terms of the widespread enthalpy ansatz of magneto-electro-mechanics, and advantages of this extended setting are presented. For the material formulation, both, a phenomenological, as well as micro-magneto-electro-mechanical approach related to the domain theories of Brown [30, 32], among many others, are employed.

The work is divided into four parts. First, in Part I, the necessary basis of magneto-electro-mechanical multiscale material modeling is provided. For that, the continuum mechanical description of physical objects is enriched with the main concepts of electro- and magnetostatics. Furthermore, a generalized Hill-Mandel homogeneity condition is formulated, accounting for the scale-bridging and providing suitable boundary conditions for the micro-structure. The concept of uniqueness of solution and the related notion of convexity and weaker convexity conditions serve as a root for the multiscale coupled stability analysis. Part II discusses the differences and difficulties of minimization and mixed principles. Here, the ansatz of an electric and magnetic vector potential requires special treatment for the uniqueness of said potential. For that, a Coulomb gauge method as well as a Hu-Washizu-type finite element formulation is presented. A Legendre-Fenchel transformation on the energy yields the convenient mixed energy-enthalpy formulation, related to electric and magnetic scalar potentials. It is shown that this transformation is only energetically congruent for restricted boundary conditions. The concepts of structural and material instability of the macro- and micro-structure are formulated for the magneto-electro-mechanical case in Part III. A local convexity condition and the notion of quasi- or rank-one convexity serve as the energetic starting points for structural and material instability checks. A reformulation in terms of the convenient enthalpy yields the remarkable result of a decoupled, diagonal stiffness matrix, which decreases the numerical effort of an accompanying stability analysis. Local and global limit-point instabilities related to the evolution of electric breakdown or magneto-electro-mechanical instability are displayed. Finally, large strain micro-magneto-electro-mechanically motivated material modeling is realized in Part IV. The evolution and motion of magnetic and electric domains on the micro-structure are captured by a phase-field approach, where the order parameter is the magnetic director or the polarization, respectively. The difficulty in the large strain theory is the objective treatment of the physical unity constraint of magnetization and the two-scale algorithmic solution scheme of homogenization to connect the dissipative micro-structure to homogenized macroscopic quantities. The characteristic magnetic and electric hysteresis curves, and the typical effective material response, based on particle-particle interactions on the microscale, are shown for different two-scale boundary-value-problems.

Zusammenfassung

Ständige Verbesserungen in Materialdesign und -funktionalität ist das übergeordnete Ziel der Materialwissenschaften. In den letzten Jahren greift dieser Anspruch auf andere Bereiche der Ingenieurwissenschaften über und steigert das Interesse an computerunterstützter Materialmodellierung. Kostenintensive und aufwendige Experimente sollen dadurch reduziert und allgemein verbessert werden. Insbesondere im Gebiet der physikalisch gekoppelten Problemstellungen, wie zum Beispiel der Magneto-Elektro-Mechanik, Chemo-Mechanik und Thermo-Mechanik, sind numerische Verfahren notwendig, um die komplexen Interaktionen vorhersagen zu können. Durch die rasanten Fortschritte in der Halbleitertechnologie und der Datenverarbeitung können immer elaboriertere Mehrskalen-Materialmodelle im Entwicklungsprozess neuartiger Funktionsmaterialien herangezogen werden. In dieser Arbeit wird das breite Spektrum der magneto-elektro-mechanisch gekoppelten Materialien aufgegriffen. Diese intelligenten Materialien, die anhand von elektrischen und magnetischen Feldern mit der Umwelt interagieren, besitzen die Fähigkeit, auf äußere Signale zu reagieren. Das ermöglicht fortschrittliche Anwendungen, wie zum Beispiel künstliche Muskeln, neuartige Flugobjekte, aktive Dämpfungssysteme oder verbesserte Datenspeicherungsmethoden. Solche Anwendungen erfordern jedoch ausgiebige Tests um die Sicherheit und Langlebigkeit der Bauteile zu gewährleisten. Diese Arbeit stellt die Grundlagen der Materialmodellierung magneto-elektro-mechanischer Materialien auf unterschiedlichen Längenskalen bereit. Dazu werden phänomenologische und mikromechanisch motivierte Ansätze vorgestellt.

Das Gebiet der magneto-elektro-mechanischen Systeme ist in dieser Abhandlung in zwei allgemeine Klassen unterteilt: (i) piezoelektrische und piezomagnetische Materialien (mit einem Fokus auf den Unterklassen der ferroelektrischen und ferromagnetischen Materialien) und (ii) elektroaktive Polymere (EAPs) und magnetorheologische Elastomere (MREs). Diese unterscheiden sich essenziell in ihren Materialeigenschaften. Die spröden Piezokeramiken werden vor allem aufgrund ihrer kurzen Reaktionszeiten, ihres niedrigen Gewichtes und relativ niedrigen Erregungsströmen in der Automobil- und Raumfahrtindustrie als Sensoren und Aktuatoren verwendet. Selbiges gilt für piezomagnetische Materialien. Hier können kleine Deformationen schon durch moderate Magnetfelder erzeugt werden. Ihre elektrischen und magnetischen Eigenschaften verdanken diese Materialien ihrer Mikrostruktur. Mehrere homogen polarisierte oder magnetisierte Bereiche, sogenannte Domänen, resultieren in linearen Systemantworten. Die Fähigkeit einer spontanen Polarisation oder Magnetisierung sogar ohne angelegte Felder charakterisiert ferroelektrische und ferromagnetische Materialien. Hierbei können nicht-lineare Systemantworten und Hysteresekurven unter zyklischer Belastung beobachtet werden. Im Gegensatz dazu zeichnen sich EAPs und MREs (oder auch magnetorheologische Fluide) durch ihre möglichen großen Deformationen aus. Diese Kompositmaterialien bestehen aus einem Matrixmaterial, in der Regel ein weiches Elastomer, und eingebetteten elektrischen oder magnetischen Einschlüssen. Die effektive Systemantwort resultiert aus der Interaktion der Partikeln auf der Mikroskala. Mögliche Anwendungen dieser Funktionsmaterialien sind noch von akademischer Natur. Ein neuer, vielversprechender Ansatz sind zwei- und dreiphasige magneto-elektro-mechanische Kompositmaterialien. Hier versucht man den magneto-elektrischen Kopplungseffekt, die Möglichkeit die elektrische Polarisation durch ein angelegtes Magnetfeld zu ändern, auszunutzen, um aus einer Rückrechnung mit dem Kopplungskoeffizienten die Feldstärke des angelegten Magnetfeldes zu messen. Das ermöglicht unter anderem die

Messung von Gehirnströmen. Zweiphasige magneto-elektrische Komposite, basierend auf spröden Keramiken, sind schon in Entwicklung. Diese sind, materialbedingt, jedoch nur für kleine Deformationen zu verwenden. Dreiphasige Materialien, mit einer umschließenden, weichen Elastomermatrix, sind auch im Bereich der großen Deformationen einsetzbar.

Experimente zeigen, dass die magneto-elektro-mechanische Systemantwort Längenskalen übergreifenden Struktur- und Materialinstabilitäten unterliegt. Diese äußern sich in Form von Ausknicken eingebundener Fasern, dielektrischem Zusammenbruch und schlussendlich Materialversagen. Diese Instabilitätsmodi gilt es zu verhindern oder, im Falle von nicht destruktiven Instabilitäten, aktiv zu kontrollieren, um größere Deformationszustände zu ermöglichen. Um derartige Instabilitäten in Berechnungen zu erkennen, gilt es Stabilitätskriterien zu formulieren, die begleitend zu einer Mehrskalensimulation ausgewertet werden können.

Diese Abhandlung befasst sich mit der magneto-elektro-mechanischen Anregung und den damit verbundenen mehrskalen Instabilitäten. Es werden Variationsprinzipe, basierend auf reinen Minimierern aber auch Sattelpunktstrukturen, vorgestellt und im Bezug auf numerische Umsetzung und Genauigkeit der Lösung verglichen. Basierend auf energetischen Stabilitätskriterien werden skalenübergreifende Auswertungen in der weit verbreiteten Enthalpieformulierung hergeleitet und Vorteile dieser Formulierung ausgearbeitet. Dabei werden für die Materialmodellierung sowohl phenomenologische, als auch mikro-magneto-elektro-mechanisch motivierte Ansätze, basierend auf der renommierten Domänentheorie, u. a. von Brown [30, 32] verwendet.

Die Arbeit ist in vier Teile untergliedert. In Abschnitt I werden die Grundlagen der Magneto-Elektro-Mechanik zusammengefasst. Dabei werden die kontinuumsmechanischen Ansätze um Konzepte der Elektro- und Magnetostatik erweitert. Basierend auf einer verallgemeinerten Hill-Mandel Homogenitätsbedingung werden die Skalenübergänge und Randbedingungen der Mikroskala hergeleitet. Grundlagen der Konvexitätstheorie und die damit verbundene Eindeutigkeit der Lösung werden als Basis der darauf folgenden Stabilitätskriterien rekapituliert. Abschnitt II beschäftigt sich mit den Unterschieden und Schwierigkeiten der minimierungs und gemischten Variationsformulierung. Die dabei auftretenden magnetischen und elektrischen Vektorpotentiale verlangen zusätzliche Methoden, um die Eindeutigkeit der Potentiale zu gewährleisten. Dazu wird eine Coulomb Justierung und ein erweiterter Hu-Washizu Finite-Elemente-Ansatz vorgestellt. Des Weiteren wird die energetische Kongruenz der Minimierungs- und Sattelpunktprinzipe für spezifizierte Randbedingungen gezeigt. In Abschnitt III werden, basierend auf einer lokalen Konvexitätsbedingung und dem Konzept der Quasi- und Rang-1-Konvexität, Struktur- und Materialinstabilitätskriterien der gekoppelten Magneto-Elektro-Mechanik hergeleitet. In Verbindung mit der Enthalpieformulierung zeigt sich, dass eine Diagonalstruktur in den Steifigkeitsmatrizen entsteht, welche sich als vorteilhaft für die numerische Umsetzung und Lösungsgeschwindigkeit herausstellt. Lokale und globale Stabilitätsanalysen der Makro- und Mikrostruktur werden anhand von analytischen und numerischen Beispielen validiert. Die mikro-mechanische Materialmodellierung in Abschnitt IV charakterisiert, basierend auf einem Phasenfeld, die effektive Systemantwort durch die Evolution magnetischer und elektrischer Domänen. Dabei liegt die Schwierigkeit in der algorithmischen Lösungsroutine und den Skalenübergängen der dissipativen Mikrostruktur zu homogenisierten makroskopischen Größen. Die effektive Systemantwort sowie die charakteristischen Hysteresekurven zeigen sich in repräsentativen numerischen Beispielen.

Chapter 1

Introduction

The idea to reproduce nature's adaptive, optimal design and functionality to react on outer stimuli is an everlasting goal of modern material science. Smart or multifunctional materials are investigated for a few decades and found to emulate nature's characteristic behavior by mimicking the human muscular and nervous system. In recent years, the rise in computational power, numerical methods and the possibility of advanced multiscale simulations renewed the interest in these multiphysics materials. Complex and highly optimized micro-structures, to enhance the coupling behavior, are now in focus, and computer simulations support the endeavor of experimentalists by providing new insight and partially eliminating trial-and-error approaches. While the class of smart materials is very broad and hard to specify, the most popular systems contain electro-mechanic, magneto-mechanic and magneto-electro-mechanic coupling properties. Here, electric and magnetic stimuli result in a mechanical system response, that is deformation or alteration of the mechanical properties of the specimen. In the following, recent developments in the field of magneto-electro-mechanics are summarized and the underlying principles are explained. Then, the necessity of computational scale-bridging methods is motivated, while recalling the basic principles of multiscale modeling. A summary on the state of the art in material modeling of composite multiphysic materials is given and the goals of this work and its structure are outlined.

1.1. Electro-mechanical coupling phenomena

In this work, the class of electro-active materials is subdivided into piezoelectric and the related ferroelectric materials, as well as electro-active polymers. Piezoelectricity relates to the Greek terms for "pressure electricity" and is characterized by a polarization, generated under mechanical stresses (direct effect), or a mechanical deformation under applied electrical loading (converse effect). Most prominent are *piezoceramic materials* such as barium titanate ($BaTiO_3$) and lead zirconate titanate (PZT). Industrial applications favor these materials due to their light weight, low power requirements, fast electro-mechanical response and high generative forces. They are used as sensors and actuators in everyday life applications, such as in the automotive industry as piezo-inline-injectors for diesel en-

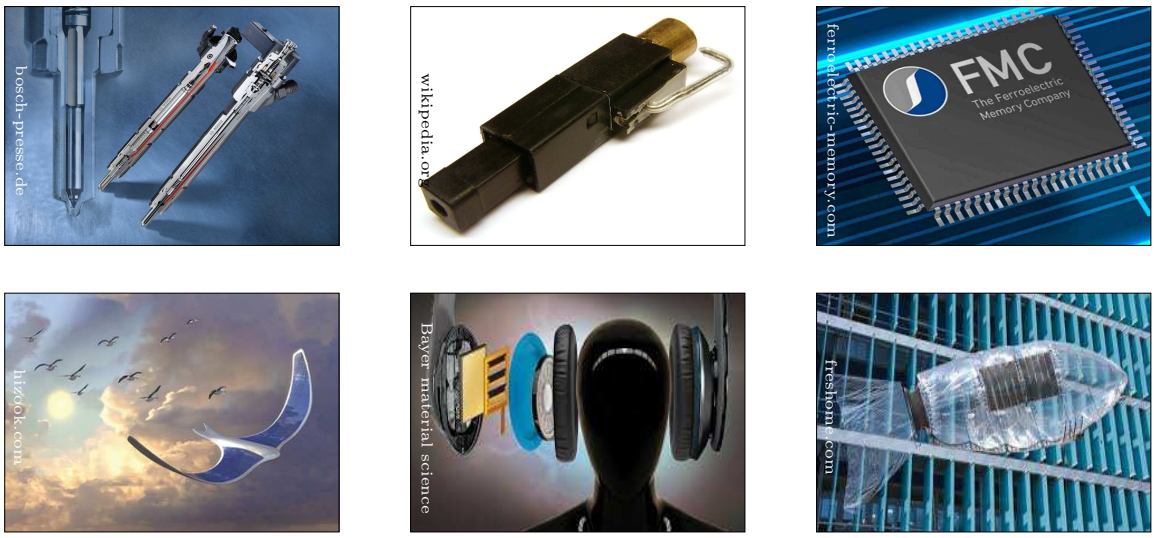

Figure 1.1: *Examples of industrial applications of piezoelectrics and electro-active elastomers.* Piezo-inline-injector for common-rail diesel engines, standard piezo ignition devices and ferroelectric random-access memory. Electro-active polymer applications are mainly still in experimental phase: concept studies for new flying devices and electro-active membranes used in speakers.

gines, air bag sensors and keyless door entry. Further famous representatives are lighters, disk drives and inkjet printers, see Figure 1.1. Piezoelectricity is understood as the linear electro-mechanical coupling in crystalline materials and the effect is governed on the microscale by the evolution and motion of homogeneously polarized regions, called ferroelectric domains. Applied mechanical stresses or sufficiently high electric fields can change the orientation of the domains. Seminal works on piezoceramic materials rooted in material sciences can be found in Jaffe et al. [102], Lines & Glass [137], and Moulson & Herbert [176]. Ferroelectricity, a subclass of piezoelectricity, is characterized by a local electric polarization of the material, so-called spontaneous polarization, that remains even after removing the applied electric field. The remanent polarization and the related remanent strains give rise to the typical non-linear dielectric and butterfly hysteres loops.

While the brittle ceramic materials are restricted to small strains, the class of *electro-active polymers* is capable of enormous electrically induced deformations up to several hundred percents. One distinguishes between electronic and ionic active materials, where the difference lies in their way of actuation. In electro-active polymers a non-conductive polymer layer in-between two electrodes results in charge separation. The related Coulomb-type electrostatic forces between the electrodes give rise to the large deformation in EAPs. The possible high actuation speeds come with the cost of high necessary voltages, which are hard to create in small, portable devices, and also increase the risk of material failure. Experimental investigations on these materials can be found in Kornbluh et al. [120, 121], and Pelrine et al. [192, 193]. Electro-active gels and conducting polymers belong to the class of ionic active materials. Diffusion of mobile ions actuate the material at low voltages, however restricted to low speeds due to the nature of the diffusion process itself. In the present work ionic materials are not considered. Both approaches do not fully satisfy the needs of the industry, resulting in very limited use cases, e.g. design studies for artificial muscles and advanced flying devices, see Figure 1.1. Applications for EAP based devices are presented in Bar-Cohen [10], Bar-Cohen & Zhang [11], and Smith [233]. Nowadays, composite materials based on polymer matrix and embed-

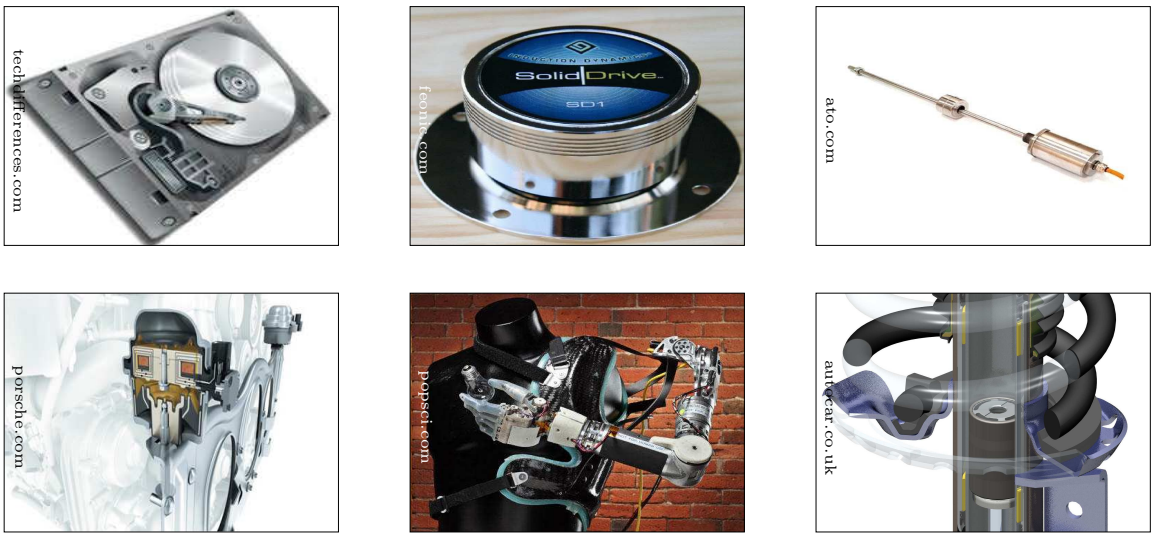

Figure 1.2: *Examples of industrial applications of magnetostrictive and magnetorheological materials.* Magnetic recording devices, transducers and probes are just a small fraction of possible use cases for magnetostrictive devices. Magnetorheological elastomers and fluids are used as engine mounts, artificial muscles and active damping systems.

ded conductive particles are used to enhance the electro-mechanical coupling phenomena, Tian et al. [248] and Ponte Castañeda & Siboni [198]. Here, high electric gradients on the interfaces between the particles and the surrounding matrix material result in high local deformations, even for lower applied electric fields.

1.2. Magneto-mechanical coupling phenomena

In parallel to the electro-active materials, similar phenomena induced by applied magnetic fields are experienced in the fields of *piezomagnetic*, *ferromagnetic* and *magnetorheological* materials. Piezo- and ferromagnetism are the magnetic dual to piezo- and ferroelectricity, where an applied mechanical stress changes the magnetic state of the specimen or, as an inverse effect, magnetic fields result in mechanical deformation. The related phenomenon of magnetostriction, i.e. mechanical deformation during the process of magnetization, is ever so slightly observed in pure metals, e.g. Cobalt (Co) and Iron (Fe) at room temperature, in the order of a few microstrains. Advanced alloys such as Terfenol-D ($Tb_xDy_{1-x}Fe_2$ with $x \approx 0.3$), Galfenol (Ga_xFe_{1-x} with $0.1 < x < 0.4$) or Cobalt Iron Oxide ($CoFe_2O_4$) are capable of "giant" magnetostrictive responses up to a few hundreds to thousands of microstrains, Abbundi & Clark [1], Sandlund et al. [209], Clark et al. [45], as well as Claeyssen et al. [44], and Olabi & Grunwald [186]. These alloys find use in sonar technology, fuel injectors or speaker devices, as well as magnetic recording media and high-performance permanent magnets, see Figure 1.2 and Bertram [21], Greaves [78], Goll & Kronmüller [77], and Schrefl et al. [213]. Their characteristic function is again related to the evolution and motion of magnetic domains within the micro-structure, where the orientation of homogeneously magnetized ferromagnetic domains can be altered by mechanical stress or applied magnetic fields. This time-dependent dissipative response yields the characteristic butterfly hysteresis curves on the macroscale, Hubert & Schäfer [98].

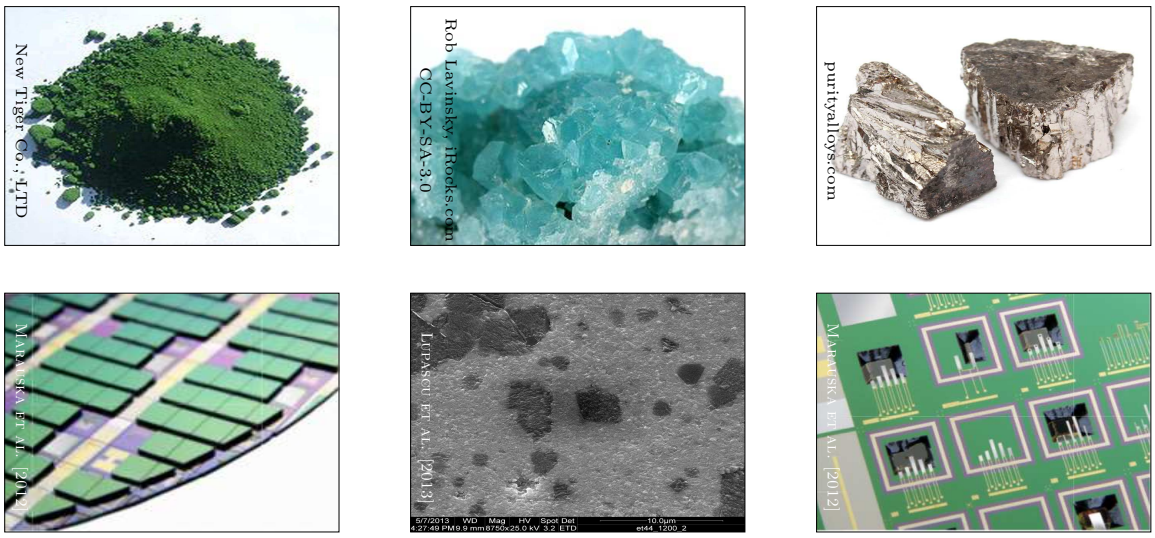

Figure 1.3: *Examples of multiferroic materials.* Organic and inorganic compound materials such as chromium(III)-oxide (Cr_2O_3), boracite ($Mn_3B_7O_{13}$) and bismuth-ferrite ($BiFeO_3$) are known to have a small magneto-electric coupling coefficient. For an improved coupling, two-phase composite materials based on magnetostrictive and piezoelectric materials are manufactured. They are utilized as precise magneto-electric sensors Marauska et al. [140], e.g. for measurements of brain activity.

Magnetorheological elastomers are composite materials consisting of micro- or nano-sized magnetizable particles, embedded or suspended into a solid or fluid matrix material. The magnetorheological effect, i.e. mechanical deformation or alteration of mechanical properties under applied magnetic fields, is only due to the coupling and interaction of the magnetic particles, whereas the matrix material in general is non-magnetizable. While MREs are easy and cheap to manufacture, experiments have shown that the distribution of particles within the matrix plays a crucial role to the overall deformation. One distinguishes between isotropic micro-structures, where particles are uniformly distributed, and anisotropic materials, where the application of a magnetic field in the curing process results in a rearrangement of the particles in chain-like geometries in field direction, see for example Jolly et al. [105]. The emerging possibilities of optimized micro-structures fitting to specific applications is a current field of active research, Galipeau & Ponte Castañeda [71, 72], Metsch et al. [153], and Kalina et al. [106]. However, especially magnetorheological fluids are already employed in the industry. Their ability to modify the mechanical stiffness of the composite under applied magnetic fields favors their use in active damping systems for buildings, as engine mounts or even on a smaller scale for bicycle dampers, see Figure 1.2 and refer to Böse et al. [27] and Dyke et al. [61]. Experimental investigations for both isotropic and anisotropic MREs are reported in Jolly et al. [105], Bednarek [16], Davis [50], Ginder et al. [76], Bellan & Bossis [17], Kallio [107], Varga et al. [258, 259], Danas et al. [49], as well as Boczkowska & Awietjan [26].

1.3. Magneto-electro-mechanical coupling phenomena

The magneto-electric coupling effect is the phenomenon of inducing an electric polarization by an applied magnetic field, or vice versa, the change of magnetization under

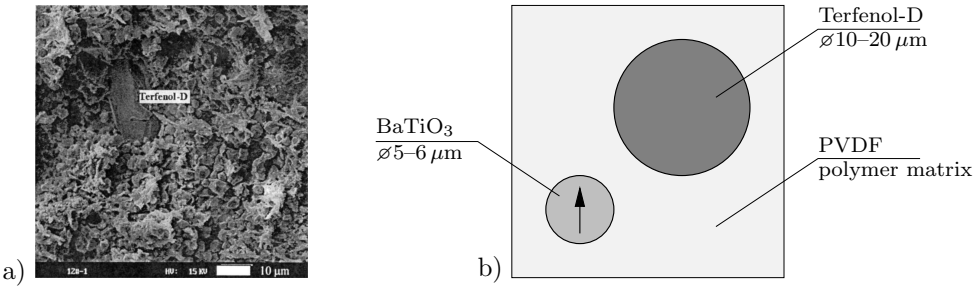

Figure 1.4: *Magneto-electric particulate composites.* a) Micrograph of three-phase Terfenol-D/PZT/PVDF composite. The irregular phase is the polymer binder (PVDF), the small particles (⌀5–6 µm) are piezoelectric (PZT), and the large particle (⌀10–20 µm) is magnetostrictive (Terfenol-D), see Nan et al. [179]. b) Schematic representation of a simplified model with spherical particulates. Poling of piezoelectric particle leads to a transversely isotropic material model.

an external electric field. This effect is helpful for the measurement of small magnetic fields, e.g. for analyzing brain activities using magnetoencephalography, or for magnetic resonance imaging. Single-phase materials that experience this coupling intrinsically, so-called multiferroics, do exist in nature, however their coupling coefficient is rather negligible, Figure 1.3. To improve or find alternatives to existing devices such as SQUIDs (superconductive quantum interference devices), that already indirectly measure neural currents in the brain via their magnetic fields, composite materials are in focus for improved magneto-electric coupling coefficients. Here, the magneto-electric effect at room temperature is created extrinsically by combining magnetostrictive and piezoelectric materials. These multiferroic, two-phase, nano or laminated composite materials, Shvartsman et al. [227], and Etier et al. [67], are already in use as sensor devices, Figure 1.3, however are subjected to difficulties in the assembly process. For a functioning device, the piezoelectric constituent needs to be prepoled, which is not easy to achieve, as the magnetic constituent is a conducting material. Furthermore, these ceramic materials are dense and brittle. To encounter these problems, three-phase composites combining magnetostrictive and piezoelectric particles with an elastic binding matrix are in development. Here, the magneto-electric coupling coefficients are defined via

$$\alpha_H = \frac{\text{magnetic}}{\textit{elastic}} \times \frac{\textit{elastic}}{\text{electric}} \quad \text{and} \quad \alpha_E = \frac{\text{electric}}{\textit{elastic}} \times \frac{\textit{elastic}}{\text{magnetic}} \,,$$

which indicates the indirect coupling link through an elastic interaction. Figure 1.4a shows a micrograph of a three-phase composite, while Figure 1.4b visualizes a simplified composite in a schematic drawing. The magnetic and electric (relatively) inactive polymer-based binder material encloses rare earth alloy magnetostrictive particles, such as Terfenol-D or ferrite materials, e.g. cobalt or nickel ferrite, as well as piezoceramic inclusions based on lead zirconate titanate or barium titanate. Generally speaking, the conjunction of the materials is rather simple and for moderate strains, that are expected in the material, reliable. The functioning of the three-phase composite is a combination of the magnetostrictive and piezoelectric effect. Under an external magnetic field, the magnetostrictive particles exhibit a strain, deforming the polymer matrix. The mechanical deformation then induces a stress on the piezoelectric particle which, as a result, alters its polarization. This change of polarization can then be measured and together with the knowledge of the coupling coefficient, the magnetic field strength can be determined. Naturally, a high coupling coefficient is desirable, yielding an interest in optimization of

the underlying micro-structure. For an overview on the coupling phenomena and the working principle of two- and three-phase materials see Shi et al. [225], Nan et al. [179, 180], Eerenstein et al. [62], and Martins & Lanceros-Méndez [144].

1.4. State of the art: multiscale magneto-electro-mechanics

The description of the aforementioned magneto-, electro- and magneto-electro-mechanic effects by a continuum mechanical model has been a subject of extensive research. They all base on the theoretical foundations on finite strain magneto-electro-mechanical interactions in solids, proposed in the seminal works of Toupin [252, 251], Eringen [63], Tiersten [249, 250], Brown [30, 31, 34], Pao [190], Maugin [145], Eringen & Maugin [64, 65], and Kovetz [123]. Two different approaches to the field need to be distinguished: *phenomenological models* that describe the macroscopic effects while not resolving the evolution and motion of magnetic and electric domains on the microscale, and *micro-magneto-electric models* which incorporate the modeling of micro-structures with their underlying magnetic and electric domains.

Phenomenological modeling of ferroic materials, containing piezoelectric and magnetostrictive materials in a small strain setting, can be found in the works of Bassiouny et al. [14, 15], Bassiouny & Maugin [12, 13], Huber & Fleck [97], Kamlah [109], Landis [131], McMeeking & Landis [151], Schröder & Romanowski [218], Klinkel [119], and Miehe & Rosato [165], in terms of piezoelectricity and in Smith et al. [234], Linnemann et al. [138] as well as Miehe et al. [170] for magnetostrictive materials, respectively. In both cases, the dissipative effects are described by internal macro-variables. The extensions to multiferroic materials are rather thin, see Zohdi [283, 284], and Miehe et al. [171].

For a better understanding of the underlying micro-structure and the evolution and motion of domains within the single- and polycrystals, micro-magnetic and micro-electric models, that resolve the domains directly, were developed based on the theory of magnetization Landau & Lifshitz [129]. The essential difference to the macroscopic models based on internal variables is that the optimal micro-structure is obtained by solving the micro-magnetic/electric equations, Brown [33, 34], instead of optimizing an assumed domain state. The powerful phase-field approach was employed, where the magnetization or polarization is understood as an order parameter or a generalized internal variable. For capturing the motion of domain walls, interpreted as diffuse interfaces, together with the geometric structure of the respective order parameters, the differences between micro-magnetic and micro-electric theory emerge. While for piezoelectric materials a *Ginzburg-Landau* or *Allen-Cahn* equation needs to be solved and the magnitude of the polarization is not underlying physical constraints, the *Landau-Lifshitz-Gilbert* (LLG) equation, Gilbert [75], poses difficulties in the numerical treatment of magnetostrictive media. The magnetization is subjected to a physical *unity constraint*, demanding $\mathbb{m} \in \mathcal{S}^{d-1}$, i.e. while the magnetization direction can change, the magnitude needs to stay constant, lying on the hypersphere in $\mathcal{R}^d$. This specific constraint is called Heisenberg-Weiss relation and imposes complications on the theoretical formulations, especially on their numerical treatment. Several approaches to encounter these difficulties can be found in the literature, ranging from equivalent model formulations, Miehe & Ethiraj [163] and Krishnaprasad & Tan [125], to numerical workarounds, Wang et al. [265],

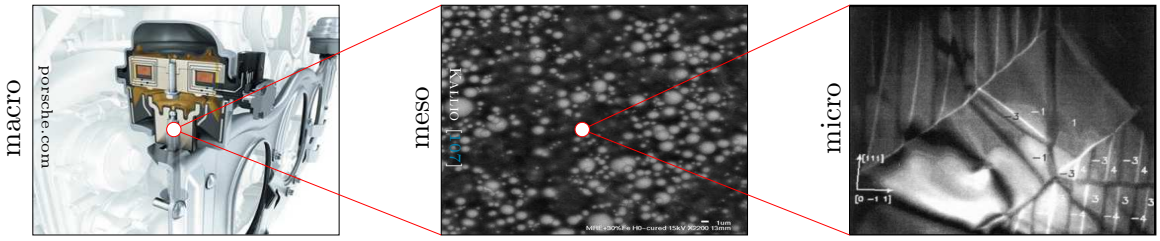

Figure 1.5: *Multiscale modeling on different length-scales.* Precise material models require the incorporation of different physical effects on several length-scales. The macroscopic response of magnetorheological devices is only due to the particle-particle interactions on the mesoscale. The magnetic properties of the magnetostrictive inclusions is due to evolving magnetic domains on the micro-structure. Scale-bridging techniques need to be employed to transition the microscopic and mesoscopic material properties to the macro-structure.

Szambolics et al. [243] or Landis [133]. The most recent approach from Sridhar et al. [235], based on an operator split and renormalization routine, is employed and recalled in this work. The author refers to Zhang & Bhattacharya [277, 278], Su & Landis [239], Schrade et al. [212], and the recent work Miehe et al. [172] for the electric, as well as Shu et al. [226], Zhang & Chen [275, 276], Hu et al. [96], Liang et al. [136], and Sridhar et al. [235] for magnetic problems. While an extension of the phase-field model to coupled micro-magneto-electro-mechanics is possible, the author is not aware of any recent works in this field. Multiscale simulations of two-phase magneto-electric composites based on the Preisach model can be found in Schröder et al. [220], and Schröder & Labusch [217].

In the field of electro-active materials, phenomenological macroscopic models are given in a number of works such as Dorfmann & Ogden [59], McMeeking & Landis [152], Vu & Steinmann [262, 263], Zhao et al. [281], Suo et al. [241], Bustamante et al. [37], Ponte Castañeda & Siboni [198], Thylander et al. [247], Jiménez & McMeeeking [104], and Rosato & Miehe [203]. Furthermore, numerical treatment of finite electro-mechanics based on variational principles are proposed for non-dissipative response by Vu et al. [264], Vu & Steinmann [262], Steinmann & Vu [238], and Miehe et al. [173]. Extensions to dissipative behavior is covered by Rosato [202], Rosato & Miehe [203], and Zäh & Miehe [273]. Related to the modeling of MREs, the author refers to Brigadnov & Dorfmann [29], Dorfmann & Ogden [56, 57, 58], Dorfmann et al. [60], Steigmann [236], as well as Saxena et al. [210, 211], and references cited therein.

As an extension to the macroscopic phenomenological models based on material parameters taken from experimental data, microscopically motivated material models are considered based on homogenization techniques, bridging different length- and time scales. The incorporation of an inhomogeneous micro-structure aims to reduce uncertainties and empirical assumptions, while enabling the possibility of optimizing the micro-structure for improved macroscopic performance. Figure 1.5 displays a typical length-scale bridging problem, where different physical effects on the macro-, meso-, and microscale need to be considered for an appropriate material model of the system. The macroscopic properties of an active damping system are influenced by a MRE that is integrated in the system. Particle-particle and particle-matrix interactions on the mesoscale give rise to the magnetorheological effect and determine the macroscopic deformation, depending on the arrangement of particles within the composite material. The magnetic properties

of the ferromagnetic inclusions are determined by the evolution of magnetic domains on the microscale. For an accurate prediction of the systems overall response, the incorporation of the different scales is essential. It is important to note, that the concept of scale bridging, i.e. the computation of effective material response, is only of mathematical or computational nature. The different physical principles stay within each scale and only give rise to the characteristic constitutive relations. This work is located in the field of two-scale computational homogenization schemes, where effective material properties are computed numerically, based on a general representative volume element as an underlying micro-structure, and an additional macroscopic boundary-value-problem with no explicit constitutive law. The two simulations are connected by an appropriate scale transition. This approach is a generalized extension to arbitrary micro-structures, in contrast to the limited range of applications based on the analytical solutions of Hill [91, 92], Tanaka & Mori [244] and Willis [266]. It is rooted on the famous Hill macro-homogeneity condition, Hill [91], demanding equality of macro- and microscopic work. For purely mechanical problems, the author refers to Smit et al. [232], Miehe et al. [167, 168], Miehe [158], Feyel & Chaboche [69], Terada & Kikuchi [245], Kouznetsova et al. [122], and Geers et al. [73], for both the linear and non-linear range of elastic and dissipative materials, solved by a finite element framework. Extensions to generalized multifield problems, incorporating additional multiphysics effects, such as thermal, magnetic, or electric contributions, can be found in Nemat-Nasser & Hori [183]. The variational framework of homogenization employed in this work is rooted in Miehe [159], where the computational scale-bridging of generalized gradient extended mechanical materials was rigorously exploited. Here, this principal serves as a canonical ingredient for the determination of macroscopic potential densities in terms of their microscopic counterparts.

In the field of phenomenological multiscale electro-mechanics, the non-dissipative small strain theory of Schröder [215] was implemented in a full FE^2 setting in Schröder & Keip [216], and in Zäh & Miehe [272] for dissipative solids. Theories on homogenization of finite electro-mechanics were formulated in deBotton et al. [51], Müller et al. [177], Klassen et al. [118], Ponte Castañeda & Siboni [198], Cao & Zhao [38], Rudykh et al. [207], Keip et al. [115], and more recently in Miehe et al. [174], as well as Lefèvre & Lopez-Pamies [134], and Keip & Schröder [113]. For the magneto-mechanical case, the author refers to Ponte Castañeda & Galipeau [197], Galipeau & Ponte Castañeda [71, 72], Chatzigeorgiou et al. [41], and Keip & Rambausek [111, 112]. Computational homogenization of phenomenological magneto-electro-elasticity at small and finite strain is dealt with in Schröder et al. [219] and Miehe et al. [174], respectively. Incorporation of micro-magneto-electro-mechanics into a computational homogenization framework was proposed by Zäh & Miehe [272], Keip et al. [116], and Sridhar et al. [235]. However, in these works only the micro-structure was solved by a finite element analysis. The macroscopic boundary-value-problem was not discretized and only effective macroscopic quantities were computed based on appropriate volume averaging routines.

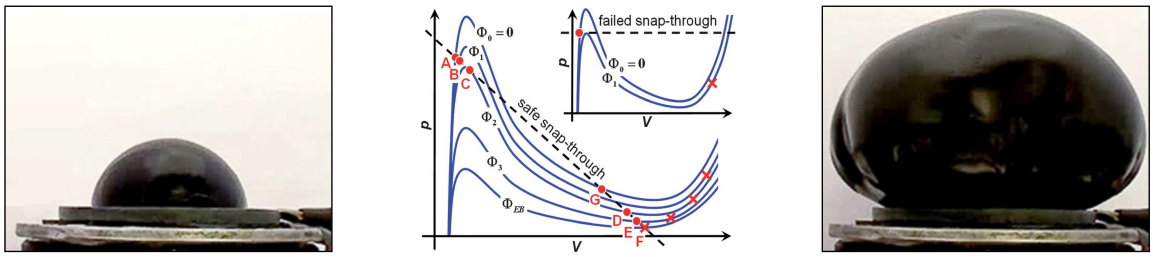

Figure 1.6: *Electro-mechanical snap-through instability.* A dielectric balloon is inflated close to a local limit-point in the pressure-volume graph. An additional electrical excitation pushes the system into a snap-through instability mode, which, when performed successfully, can vastly enhance the deformation state. The pictures are taken from Keplinger et al. [117] and Li et al. [135].

1.5. Instabilities in magneto-electro-mechanical composites

While soft mechanical materials, such as rubbers, are able to deform for several hundred percents, electrically excited dielectric and composite materials tend to fail under considerably lower deformations. This is due to two failure modes: *electrical breakdown* and *electro-mechanical instability*. In the field of stiff ceramic materials, electrical breakdown, i.e. the loss of charge separation due to mobilized charges within the dielectric material is prominent. After a certain applied voltage, the former insulating material acts as a conductor, leading to electrical discharge and ultimately failure of the material. For soft dielectrics the voltage induced deformation is usually limited by electro-mechanical instability. Experiments have shown, that a positive feedback between applied voltage, electric field and the resulting mechanical deformation exists, i.e. a material thins down under applied electrical loading, leading to higher effective electric fields which then further squeeze the material. This so-called *pull-in instability* drastically reduces the thickness of the insulator which often end up in electric breakdown. Electro-mechanical instability is a prominent mode of failure in insulators and power transmission cables and needs to be treated with caution. Plante & Dubowsky [195] have shown that electro-mechanical instability can also lead to a snap-through-type deformation, yielding coexisting states of different deformation. They found wrinkled states of high deformation next to flat states of a thin dielectric membrane under external electric field loading. This motivates the exploitation of instability phenomena to further increase possible mechanical stretch even under moderate applied fields, and gives rise to a new field of research. Related, an electro-mechanical snap-through of an EAP balloon was theoretically and experimentally shown in Rudykh et al. [206], Keplinger et al. [117], and Li et al. [135]. Here, an inflated balloon close to a local limit point was further actuated by an electric field. For a stable snap-through, vastly extended deformation states were achieved, see Figure 1.6. Further micro-structural instability modes, such as buckling of micro-fibers or particles, as well as macroscopic shear bands or structural instabilities can occur. The detection of these local and global micro- and macro-instabilities is essential for the development and especially the safety and longevity of advanced functional materials.

In the field of electro-elasticity, these phenomena have been investigated in Zhao & Suo [279], Zhao et al. [281], Bertoldi & Gei [19] and Siboni et al. [229], see also the review Zhao & Wang [280]. Recently Miehe et al. [173, 174] proposed a framework for computational tracking into the post-critical range. Enthalpy-based ener-

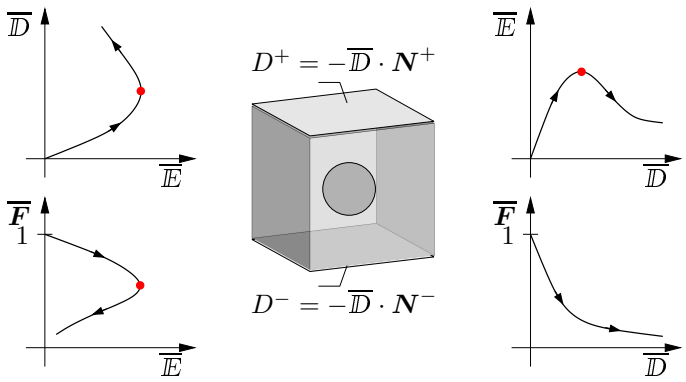

Figure 1.7: *Typical pre- and postcritical limit-point response in magneto-electro-elasticity.* Pull-in instability of a dielectric micro-structure $\mathcal{B}$. Monotoneous increasing loading by the enthalpy-variable $\overline{\mathbb{E}}$ is restricted to the pre-critical range of the field-induction $\overline{\mathbb{D}}$-$\overline{\mathbb{E}}$, and field-stretch $\overline{\boldsymbol{F}}$-$\overline{\mathbb{E}}$ equilibrium curves. In contrast, driving by the energy-variable $\overline{\mathbb{D}}$ allows a straightforward tracking of the equilibrium curves. This is an argument for an energy-based formulation of computational homogenization.

getic instability criteria were formulated and embedded into a finite element framework for an accompanying stability analysis for multiscale magneto-electro-mechanical material modeling. The characteristic electric equilibrium path, see Figure 1.7, poses additional difficulties on the numerical treatment of coupled magneto-electro-mechanics. Clearly, the choice of control variables highly influences the possibility of post-critical equilibrium.

Employing two-scale homogenization techniques give rise to additional classes of instabilities. In the theory of homogenization of mechanical composites, it is well-known that long wavelength microscopic structural instabilities induce macroscopic material instabilities in the form of a local loss of ellipticity, see Triantafyllidis & Maker [253], Müller [178], Geymonat et al. [74], Miehe et al. [169], and Michel et al. [156]. Application of a Bloch-Floquet wave analysis enables the detection of microscopic instabilities for different wave lengths, and buckling modes of the micro-structure, and yields new sizes of periodic representative volume elements, see Bertoldi & Boyce [18], Bertoldi et al. [20], and Michel et al. [157]. These concepts hold and are extended to magneto-electro-mechanics, where Dorfmann & Ogden [55] considered the electro-elastic wave propagation in finite strain electro-elasticity and Destrade & Ogden [54] investigated the wave propagation in magneto-elasticity. Furthermore, Bertoldi & Gei [19] proposed analytic solutions for micro- and macroscopic instabilities in layered dielectrics. Stability analysis in fiber-reinforce materials was discussed in Siboni et al. [229], and Siboni & Ponte Castañeda [228], while Rudykh et al. [208] investigated the effect of coupled electro-mechanical loading scenarios. The recent work of Polukhov et al. [196] shows multiscale stability analysis for periodic, quasi-incompressible polymer composites and displays unstable loading ranges and related microscopic buckling modes.

1.6. Objectives and overview

In this work, variational-based homogenization techniques for coupled magneto-electro-mechanic composite materials are developed. Starting point is a generalized Hill-Mandel

macro-homogeneity condition for gradient extended dissipative materials. This enables a general framework for phenomenological as well as micro-mechanically motivated material modeling of the multiphysics problem. The author proposes both, pure minimization principles based on magnetic and electric vector potentials, as well as mixed saddle-point formulations related to scalar potentials. The advantages and intrinsic difficulties of either approach are discussed and energetic consistency, based on a Legendre-Fenchel transformation with additional Neumann-type loading terms, is shown. The main focus lies on the development of stability criteria for the macro- and the microscopic problem based on weaker convexity conditions, embedded into a finite element framework for accompanying stability analyses. Here, energetic criteria are formulated in terms of a more convenient enthalpy setting, which shows to be superior in terms of speed and numerical treatment. These concepts are employed on multiscale magneto-electro-mechanical boundary-value-problems with periodic micro-structures. In a final step, the phenomenological modeling is extended by a phase-field approach that accounts for the evolution of magnetic and electric domains. This allows further insight in the coupled material response based on particle-particle interactions on the microscale. The subsequent chapters are arranged into four main parts:

Part I deals with fundamentals of magneto-electro-mechanics, homogenization theory and the notion of convexity and uniqueness of solutions is discussed. Furthermore, the generalized variational principle for gradient extended dissipative solids with the related Euler-Lagrange equations is derived. The two-scale variational framework is embedded into a macroscopic driving routine that is described for a general boundary-value-problem. In Chapter 2 the basic finite strain continuum mechanics, electrostatic and magnetostatic field equations are provided. They serve as the backbone for any coupled magneto-electro-mechanical material model. For that, in addition to the classical mechanical quantities, the electric and magnetic field are physically motivated. Starting from Coulomb's law and Biot-Savart's law, the famous Gauss laws of electro- and magnetostatics are derived, together with Faraday's and Ampère's law. These fundamental equations need to be incorporated into the variational concept. As on overview, the mathematical description of purely mechanical balance principles is extended to the magneto-electro-mechanical case, where the interaction of matter with electric and magnetic fields is considered. Chapter 3 presents the concept of scale bridging. A differentiation between macroscopic bodies and underlying heterogeneous micro-structures is employed, where the effective macroscopic quantities are obtained by an appropriate averaging routine of the constitutive microscopic material response. This ansatz provides a better insight on material properties. The bridging of different length scales is related to suitable micro-to-macro transition concepts based on surface and volume averaging of the macro- and microscopic magneto-electro-mechanical counterparts. The famous Hill-Mandel macro-homogeneity conditions serves as a starting point to determine appropriate boundary conditions that fulfill the demand of equal macro- and microscopic stress-power. The notion of convexity and uniqueness of solutions is introduced in Chapter 4. First, the necessity for weaker convexity condition for the framework of finite strain is discussed. Based on a classical convexity conditions, the existence and uniqueness of a solution is derived. This statement will later be exploited for the formulation of micro- and macroscopic structural stability checks. Additionally, the concepts of poly-, quasi- and rank-one convexity are introduced that serve as a starting point for material stability criteria. The hierarchy of convexity notations summarizes the chapter. A general variational principle for

gradient-extended dissipative solids on the microscale and elastic macroscopic response is formulated in Chapter 5. The primary and constitutive field variables are introduced and general Euler-Lagrange equations are obtained by a stationary principle on both, the macro- and microscale. Here, the variational principle of homogenization provides the macroscopic incremental potential density. A backward-Euler time-discretization routine is employed for the time-dependent problem. While a framework for a full FE^2 computation is provided, the macroscopic boundary value problem in this work is reduced to a one Gauss-point problem. The general macroscopic driving routine with a nested iteration allows for energetic or enthalpic loading of the micro-structure. This enables a possible computation into post-critical loading regimes, that is necessary for the subsequent multiscale stability analysis.

In **Part II** the different modeling approaches based on electric vector and scalar potentials are compared for large strain phenomenological electro-elasticity. The energetic equality of pure Dirichlet-type vector potential and pure Neumann-type scalar potential boundary-value-problems is shown. Finally, the intrinsic difficulty of vector potentials, namely its non-uniqueness, is displayed and different solution methods are introduced. Chapter 6 starts from a canonical energy arrangement based on an electric vector potential. The related variational minimization principle is formulated and resulting Euler-Lagrange equations are derived. A Legendre-Fenchel transformation in the electric slots yields an extended energy-enthalpy principle that gets reduced by a reformulation of the electric field in terms of a scalar potential. It is shown, that the three formulations are not energetically equivalent for arbitrary boundary value problems. A restriction to pure Dirichlet-type boundary conditions for the vector potential and pure Neumann-type conditions for the scalar potential however yields energetically congruent formulations, which is shown in a numerical example. While the energetic formulation of electric vector potentials is found to be advantageous in terms of stability analysis it comes with an additional difficulty of non-uniqueness. Possibilities to encounter this drawback by a Coulomb-gauge or a mixed finite element formulation are presented and compared. It is shown that a reduced integration ansatz for the Coulomb-gauge penalty energy is equivalent to an advanced Hu-Washizu-type mixed finite element formulation.

The notion of convexity is employed to formulate energetic criteria for magneto-electro-mechanical multiscale structural and material instability. In **Part III** the checks are provided in all three modeling approaches, i.e. energy, extended energy and convenient enthalpy formulation. An analytical example displays the characteristic problem of limit-point instabilities in electro-elasticity. Numerical two-scale boundary value problems of magneto-electro-mechanics investigate typical instability phenomena on both the macro- and microscale. Chapter 7 starts with the energetic criteria for micro- and macroscopic structural and material instability. They are based on local convexity for structural and rank-one convexity for material instability. A Legendre-Fenchel transformation on the magnetic and electric slots provides an extended energy formulation that ultimately gets reduced to the convenient enthalpy formulation by exploitation of the necessary condition of the Legendre-Fenchel transformation. It is shown that the energetic stability criteria, now reformulated in terms of the energy-enthalpy, get simplified due to a block diagonal structure of the related tangent moduli and stiffness matrices. This remarkable finding is a major advantage of the convenient enthalpy formulation in terms of multiscale magneto-electro-mechanical stability analysis. An explanatory analytical example of a homogeneous material element covers the basic phenomena of electro-mechanic instabil-

ities in both the energy and energy-enthalpy formulation. An extension to numerical examples of coupled composite materials follows for electro-, magneto-, and magneto-electro-mechanics.

In **Part IV**, the phenomenological approaches are enriched by a micro-magneto-electro-mechanical model of the underlying micro-structure of the composite material. The magnetic and electric properties, stemming from the evolution and motion of magnetic and electric domains are resolved by a phase-field model. Chapter 8 provides the rate-type variational principles of micro-electro-mechanics for both, the two-field macro-structure, and the three-field dissipative micro-structure. The use of a macroscopic driving routine allows for a simplification of the FE^2 scenario, such that only the micro-structure needs to be discretized. The related macroscopic quantities are obtained by a generalized scale-bridging method and averaging theorems. The focus is set on the influence of the micro-structure, i.e. the shape, volume fraction, and orientation of inclusions within the matrix on the effective material response. For that, numerical examples are provided, that yield the characteristic butterfly and dielectric hysteresis curves and the overall macroscopic deformation. Likewise, Chapter 9, deals with the evolution of magnetic domains. The difficulty of the physical unity constraint of the magnetization is accounted for by a staggered solution scheme that is embedded into the two-scale computation. The solution algorithm is treated in detail. Numerical examples display the effect of particle-particle and particle-matrix interactions on the microscale on the overall macroscopic deformation.

— Part I —

Fundamentals of Magneto-Electro-Mechanics and Stability Analysis in Computational Homogenization

Chapter 2

Foundations of Continuum Mechanics and Magneto-Electrostatics

This chapter summarizes the basic notions of non-linear continuum mechanics by providing the fundamental geometric objects for the description of bodies under finite deformations. Starting point is an arbitrary base system, however restrictions to Cartesian coordinates are made and referred to throughout this work. To describe the kinematics of a continuum body in both the Lagrangian and Eulerian configuration, fundamental mapping properties are iterated and the concept of stress and strains in different geometrical settings are reviewed. To enhance purely mechanical formulations, the electric and magnetic quantities are motivated and introduced based on electro- and magneto-static field equations. The related Maxwell's equations of electro-magnetism are presented for the static case. This serves as a background for the pending multiphysics modeling of coupled magneto-electro-mechanics.

2.1. Fundamentals of continuum mechanics

Classical continuum mechanics of continuous media provides the basis for the description of deforming bodies in a mathematical framework. For a proper description of physical bodies a reference coordinate system is required. In general, any arbitrary coordinate system is possible, however a convenient choice are standard Cartesian coordinates. This simplifies the use of so-called metric tensors that are needed for tensorial operations within the underlying differential geometry approach. The kinematic description of deforming bodies in large strain continuum mechanics is based on the introduction of the non-linear deformation map, describing the motion from the Lagrangian to the Eulerian manifold. Further mapping objects that connect the tangent and co-tangent spaces of the Lagrangian and Eulerian manifolds are presented. This summary of large strain continuum mechanics follows the lectures notes Miehe [160, 162] on advanced mechanics held at the Institute of Applied Mechanics at the University of Stuttgart and is by no means complete. For further explanations including an introduction to tensor algebra and analysis, the interested reader is referred to the classical textbooks Truesdell & Noll [254], Gurtin [80], Marsden & Hughes [142], Ogden [185], Holzapfel [95], Başar

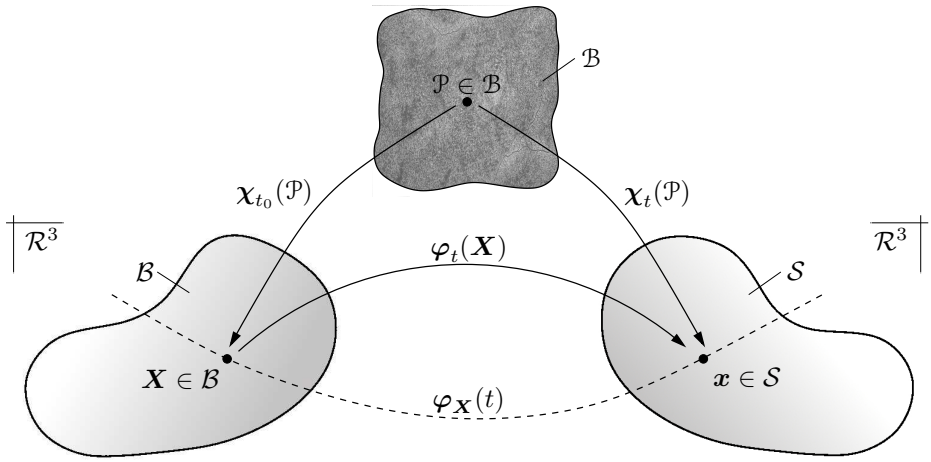

Figure 2.1: *Description, placement and motion of a material body.* Particles of a material body $\mathcal{P} \in \mathcal{B}$ are placed in the mathematical space $\mathcal{R}^3$ by the placement map $\boldsymbol{\chi}(\mathcal{P})$. The motion of an arbitrary reference body $\mathcal{B}$ in the Euclidean space is described by the deformation map $\boldsymbol{\varphi}(\boldsymbol{X}, t)$, mapping points from the reference to the current configuration $\mathcal{B} \to \mathcal{S}$. The path of a particle $\boldsymbol{X}$ over time is identified as $\boldsymbol{\varphi}_{\boldsymbol{X}}(t)$.

& Weichert [5], Haupt [87], Gurtin et al. [81], and Steinmann [237].

2.1.1. Motion of a material body: path, velocity, and acceleration

A material body $\mathcal{B}$ is a physical object containing different characteristics such as texture, micro-structure, etc. that influence the mechanical response of the body under different loading conditions. A proper description of its behavior can only be achieved by providing a mathematical framework that idealizes the body as an open set of material points $\mathcal{P} \in \mathcal{B}$. Each point $\mathcal{P}$ is in a one-to-one relationship to a point in the domain $\mathcal{B} \subset \mathcal{R}^3$ in the Euclidean space, uniquely defined by the configuration or placement map

$$\boldsymbol{\chi}(\mathcal{P}) : \begin{cases} \mathcal{B} \to \mathcal{B} \subset \mathcal{R}^3 \\ \mathcal{P} \mapsto \boldsymbol{X} = \boldsymbol{\chi}(\mathcal{P}), \end{cases} \tag{2.1}$$

where $\boldsymbol{X} \in \mathcal{B}$ denotes the place a particle occupies in the Euclidean space. The motion of the body is given by a parametrization of the placement by time such that $\boldsymbol{\chi}_t$ resembles a family of configurations. A natural approach to describe the state of the body is to invent an arbitrary, undeformed *reference, material or Lagrangian configuration* at time $t = t_0$. This configuration is based on the Lagrangian coordinates $\boldsymbol{X} := \boldsymbol{\chi}_{t_0}(\mathcal{P}) \in \mathcal{B} \subset \mathcal{R}^3$, while any other *current, spatial or Eulerian configuration* is denoted as $\boldsymbol{x} := \boldsymbol{\chi}_t(\mathcal{P}) \in \mathcal{S} \subset \mathcal{R}^3$ at current time t. A relative description of the body's motion in the Euclidean space is given by the non-linear deformation map

$$\boldsymbol{\varphi}(\boldsymbol{X}, t) : \begin{cases} \mathcal{B} \times \mathcal{T} \to \mathcal{S} \subset \mathcal{R}^3 \\ \boldsymbol{X} \mapsto \boldsymbol{x} = \boldsymbol{\varphi}(\boldsymbol{X}, t) := \boldsymbol{\chi}_t(\mathcal{P}) \circ \boldsymbol{\chi}_{t_0}^{-1}(\boldsymbol{X}), \end{cases} \tag{2.2}$$

as a composition of the placement maps. It relates at time $t \in \mathcal{T} \subset \mathcal{R}^+$ the current position $\boldsymbol{x} = \boldsymbol{\varphi}_t(\boldsymbol{X}) \in \mathcal{S}$ to the reference position $\boldsymbol{X} \in \mathcal{B}$. Likewise, the path of a particle in $\mathcal{R}^3$ over time t is defined as $\boldsymbol{x} = \boldsymbol{\varphi}_{\boldsymbol{X}}(t) \in \mathcal{S}$, see Figure 2.1 for a graphical interpretation

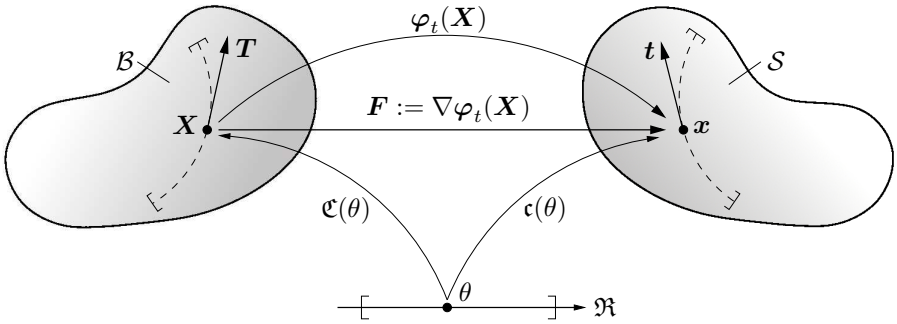

Figure 2.2: *The deformation gradient as a tangent map.* The deformation gradient $\boldsymbol{F}(\boldsymbol{X},t)$ maps material tangent vectors $\boldsymbol{T}$ at $\boldsymbol{X}$ to Lagrangian curves $\mathfrak{C}(\theta)$ onto spatial tangent vectors $\boldsymbol{t}=\boldsymbol{F}\boldsymbol{T}$ at $\boldsymbol{x}$ to deformed material curves $\mathfrak{c}(\theta,t)$.

of the motion. Derivations of the motion with respect to the time yield, depending on the chosen frame, the reference or spatial velocity and acceleration. Parametrized by the Lagrangian coordinates $\boldsymbol{X}\in\mathcal{B}$, the material velocity and acceleration are spatial vector fields and obtained by the path or motion such that

$$\boldsymbol{V}(\boldsymbol{X},t)=\frac{d}{dt}\boldsymbol{\varphi}_{\boldsymbol{X}}(t)=\frac{\partial}{\partial t}\boldsymbol{\varphi}(\boldsymbol{X},t)\quad\text{and}\quad\boldsymbol{A}(\boldsymbol{X},t)=\frac{d^2}{dt^2}\boldsymbol{\varphi}_{\boldsymbol{X}}(t)=\frac{\partial^2}{\partial t^2}\boldsymbol{\varphi}(\boldsymbol{X},t)\,. \tag{2.3}$$

Another representation of the same Eulerian objects parametrized by the current position $\boldsymbol{x}\in\mathcal{S}$ is called spatial velocity and spatial acceleration and can be obtained by a composition of (2.3) with the inverse motion

$$\boldsymbol{v}(\boldsymbol{x},t)=\boldsymbol{V}(\boldsymbol{X},t)\circ\boldsymbol{\varphi}_t^{-1}(\boldsymbol{x})\quad\text{and}\quad\boldsymbol{a}(\boldsymbol{x},t)=\boldsymbol{A}(\boldsymbol{X},t)\circ\boldsymbol{\varphi}_t^{-1}(\boldsymbol{x})\,. \tag{2.4}$$

Note that for general material time derivatives of spatial objects the classical split into local and convective part is also possible and helps to identify the spatial acceleration for a known spatial velocity

$$\boldsymbol{a}(\boldsymbol{x},t)=\frac{d}{dt}\boldsymbol{v}(\boldsymbol{x},t)=\frac{\partial}{\partial t}\boldsymbol{v}(\boldsymbol{x},t)+\nabla_{\boldsymbol{x}}\boldsymbol{v}(\boldsymbol{x},t)\cdot\boldsymbol{v}(\boldsymbol{x},t)\,. \tag{2.5}$$

This proves to be advantageous, e.g in fluid mechanics, where the motion function $\boldsymbol{\varphi}(\boldsymbol{X},t)$ is not known. We identify the spatial velocity gradient $\boldsymbol{l}:=\nabla_{\boldsymbol{x}}\boldsymbol{v}(\boldsymbol{x},t)$ for later use, and in terms of the spatial gradient operator $\nabla_{\boldsymbol{x}}=\operatorname{grad}(\cdot)$.

2.1.2. The deformation gradient: line, area, and volume map

Probably the most fundamental object in the description of finite strain continuum mechanics is the *deformation gradient*. It is obtained by the directional or Frechét derivative of the deformation map with respect to the reference coordinates

$$\boldsymbol{F}(\boldsymbol{X})=\nabla_{\boldsymbol{X}}\boldsymbol{\varphi}(\boldsymbol{X},t)\,. \tag{2.6}$$

Subjected to the one-to-one relationship of the deformation map, the deformation gradient is bound by the constraint of non-penetrable material, i.e. $J=\det[\boldsymbol{F}]>0$. To identify the use of the deformation gradient consider a line element parametrized by a common variable $\theta\in\mathfrak{R}$, projected onto the reference and the current configuration by a linear

map $\mathfrak{C}(\theta)\colon \theta \mapsto \boldsymbol{X}(\theta) \in \mathcal{B}$ and $\mathfrak{c}(\theta)\colon \theta \mapsto \boldsymbol{x}(\theta, t) \in \mathcal{S}$, respectively as displayed in Figure 2.2. The curves are subjected to the deformation map as they are embedded into the continuum, i.e. $\mathfrak{c}(\theta, t) = \boldsymbol{\varphi}(\mathfrak{C}(\theta), t)$. Tangent vectors onto the curves in the reference and the current configuration in their respective tangent space are obtained by the derivatives $\boldsymbol{T} := d\mathfrak{C}(\theta)/d\theta \in T_X\mathcal{B}$ and $\boldsymbol{t} := d\mathfrak{c}(\theta, t)/d\theta \in T_x\mathcal{S}$. Application of the chain rule yields

$$\boldsymbol{t} := \frac{d}{d\theta}\mathfrak{c}(\theta, t) = \nabla_{\boldsymbol{X}}\boldsymbol{\varphi}(\mathfrak{C}(\theta), t)\frac{d}{d\theta}\mathfrak{C}(\theta) = \boldsymbol{F}\boldsymbol{T} \tag{2.7}$$

and thereby identifies the deformation gradient to linearly map tangents from the reference to associated tangent vectors of the spatial configuration

$$\boldsymbol{F} : \begin{cases} T_X\mathcal{B} \to T_x\mathcal{S} \\ \boldsymbol{T} \mapsto \boldsymbol{t} = \boldsymbol{F}\boldsymbol{T}\,. \end{cases} \tag{2.8}$$

Based on the concept of projected line elements with associated tangent vectors two further fundamental mappings can be identified, see Figure 2.3. A linear combination of two Lagrangian tangents $\boldsymbol{T}_1$ and $\boldsymbol{T}_2$ spans a material surface on the referential body. Their cross product defines the area vector $\boldsymbol{A} = \boldsymbol{T}_1 \times \boldsymbol{T}_2 = \boldsymbol{N}A$ expressed in terms of the normal vector $\boldsymbol{N} \in T_X^*\mathcal{B}$, an object of the referential co-tangent space at point $\boldsymbol{X}$. Following the chain rule procedure and employing Nanson's formula results in the transformation rule for area elements $\boldsymbol{a} = \boldsymbol{n}a = \mathrm{cof}[\boldsymbol{F}] \cdot \boldsymbol{N}A$ with $\mathrm{cof}[\boldsymbol{F}] = J\boldsymbol{F}^{-T}$ and reveals the mapping of normal vectors from the referential to the spatial co-tangent space via

$$\boldsymbol{F}^{-T} : \begin{cases} T_X^*\mathcal{B} \to T_x^*\mathcal{S} \\ \boldsymbol{N} \mapsto \boldsymbol{n} = \boldsymbol{F}^{-T}\boldsymbol{N}\,. \end{cases} \tag{2.9}$$

Likewise, the volume $V = (\boldsymbol{T}_1 \times \boldsymbol{T}_2) \cdot \boldsymbol{T}_3$ of a parallelpiped spanned by three linearly independent Lagrangian tangents, transforms to its Eulerian counterpart by the determinant of the deformation gradient, namely the Jacobian $J = \det[\boldsymbol{F}]$, such that

$$J : \begin{cases} \mathcal{R}^3_+ \to \mathcal{R}^3_+ \\ V \mapsto v = JV\,. \end{cases} \tag{2.10}$$

These three basic mappings represent the backbone of object transformations in-between the Lagrangian and Eulerian tangent and co-tangent space and provide the basis for further tensorial operations.

2.1.3. Strain measures: Green's and Almansi's strain

The deformation of a unit vector in the Lagrangian as well as Eulerian setting is under investigation. Consider a Lagrangian director $\boldsymbol{T}(\boldsymbol{X})$ of unit length

$$|\boldsymbol{T}|_{\boldsymbol{G}} = \sqrt{\boldsymbol{T} \cdot \boldsymbol{G}\boldsymbol{T}} = 1\,, \tag{2.11}$$

with respect to the material metric tensor $\boldsymbol{G} = \delta_{AB}\boldsymbol{E}^A \otimes \boldsymbol{E}^B$ in the Euclidean space. The Eulerian counterpart $\boldsymbol{t} = \boldsymbol{F}\boldsymbol{T}$ is likewise defined as

$$|\boldsymbol{t}|_{\boldsymbol{g}} = \sqrt{\boldsymbol{t} \cdot \boldsymbol{g}\boldsymbol{t}} = \sqrt{\boldsymbol{T} \cdot (\boldsymbol{F}^T\boldsymbol{g}\boldsymbol{F})\boldsymbol{T}} = |\boldsymbol{T}|_{\boldsymbol{C}} = \lambda\,, \tag{2.12}$$

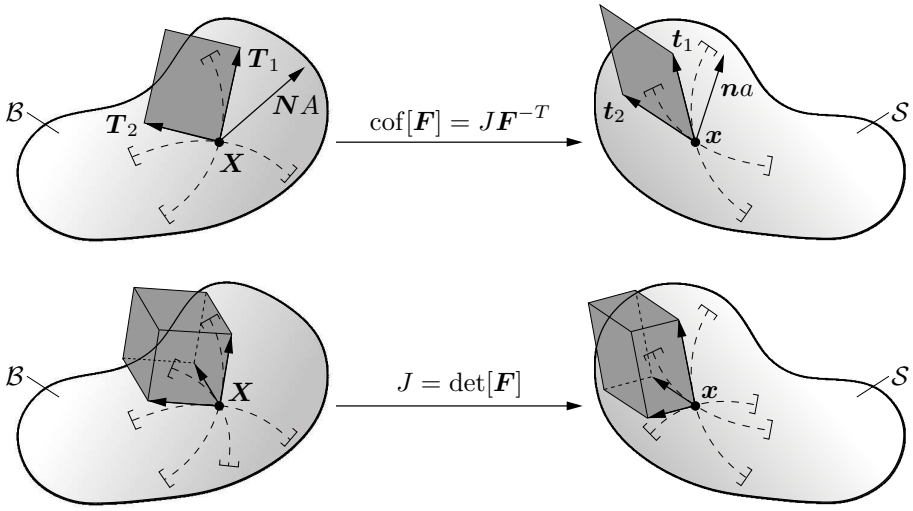

Figure 2.3: *The normal and volume map.* The area map or Nanson's formula transforms areas bound by two tangents to Lagrangian curves to Eulerian areas by $\boldsymbol{n}a = \mathrm{cof}[\boldsymbol{F}] \cdot \boldsymbol{N}A$. A parallelpiped spanned by three linearly independent material tangents transforms to its spatial counterpart by the determinant of the deformation gradient $J = \det[\boldsymbol{F}]$, the so-called volume map $v = JV$.

with the scalar valued stretch λ. Here the right Cauchy-Green tensor $\boldsymbol{C} := \boldsymbol{\varphi}_t^*(\boldsymbol{g}) = \boldsymbol{F}^T\boldsymbol{g}\boldsymbol{F}$ is introduced as the *reference representation of the spatial metric* $\boldsymbol{g} = \delta_{ab}\boldsymbol{e}^a \otimes \boldsymbol{e}^b$. It links, in the sense of geometrical mappings, the material tangent and co-tangent spaces and is obtained by a *pull-back* operation $\boldsymbol{\varphi}_t^*([\,\cdot\,])$ of a current tensor $[\,\cdot\,]$, in this case of the current metric $\boldsymbol{g}$.
In analogy, for an Eulerian director $\boldsymbol{t}(\boldsymbol{x})$ of unit length $|\boldsymbol{t}|_{\boldsymbol{g}} = 1$, with respect to the current metric $\boldsymbol{g}$ in the current configuration, the Lagrangian counterpart reads $\boldsymbol{T} = \boldsymbol{F}^{-1}\boldsymbol{t}$. Evaluating the length of the undeformed Lagrangian tensor to be $|\boldsymbol{T}|_{\boldsymbol{G}} = 1/\lambda$ yields

$$|\boldsymbol{T}|_{\boldsymbol{G}} = \sqrt{\boldsymbol{T} \cdot \boldsymbol{G}\boldsymbol{T}} = \sqrt{\boldsymbol{t} \cdot (\boldsymbol{F}^{-T}\boldsymbol{G}\boldsymbol{F}^{-1})\boldsymbol{t}} = |\boldsymbol{t}|_{\boldsymbol{c}} = \frac{1}{\lambda} \tag{2.13}$$

and reveals the left Cauchy-Green tensor $\boldsymbol{c} := \boldsymbol{\varphi}_{t*}(\boldsymbol{G}) = \boldsymbol{F}^{-T}\boldsymbol{G}\boldsymbol{F}^{-1}$ to be the spatial representation of the reference metric $\boldsymbol{G}$. It is obtained by a *push-forward* operation $\boldsymbol{\varphi}_{t*}(\boldsymbol{G})$ of the referential metric $\boldsymbol{G}$ and links the spatial tangent and co-tangent space. The full graphical interpretation by commutative diagrams is given in Figure 2.4. Here, additional material and spatial tensors for the inverse of the respective metrics are introduced for convenience. The inverse referential metric $\boldsymbol{G}^{-1}$ in the current configuration is represented by the *Finger tensor* $\boldsymbol{b} := \boldsymbol{\varphi}_{t*}(\boldsymbol{G}^{-1}) = \boldsymbol{F}\boldsymbol{G}^{-1}\boldsymbol{F}^T$ while the inverse current metric $\boldsymbol{g}^{-1}$ is represented by the inverse right Cauchy-Green tensor $\boldsymbol{C}^{-1} := \boldsymbol{\varphi}_t^*(\boldsymbol{g}^{-1}) = \boldsymbol{F}^{-1}\boldsymbol{g}^{-1}\boldsymbol{F}^{-T}$ in the Lagrangian setting. Based on a comparison of metric tensors represented in both the Lagrangian and Eulerian setting, the *strain tensors* are defined. In the Lagrangian setting, the Green strain tensor reads

$$\boldsymbol{E} = \tfrac{1}{2}\left(\boldsymbol{\varphi}_t^*(\boldsymbol{g}) - \boldsymbol{G}\right) = \tfrac{1}{2}\left(\boldsymbol{C} - \boldsymbol{G}\right), \tag{2.14}$$

where the current and the reference metric in the Lagrangian setting are compared. Likewise, in the Eulerian setting the Almansi strain tensor is found as

$$\boldsymbol{e} = \tfrac{1}{2}\left(\boldsymbol{g} - \boldsymbol{\varphi}_{t*}(\boldsymbol{G})\right) = \tfrac{1}{2}\left(\boldsymbol{g} - \boldsymbol{c}\right). \tag{2.15}$$

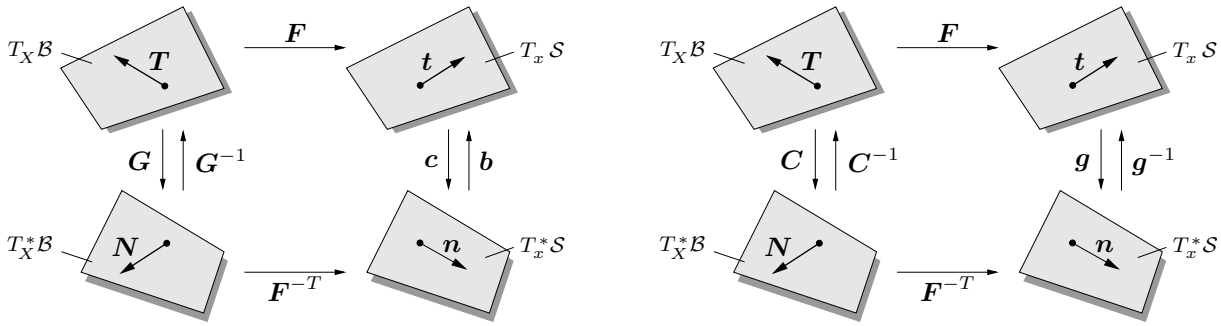

Figure 2.4: *Commutative mappings of metric tensors.* The Lagrangian and Eulerian metric tensors link the respective tangent and co-tangent spaces, i.e. map tangents onto normals in their respective space. The Lagrangian representation of the current metric is the right Cauchy-Green tensor $\boldsymbol{C} = \boldsymbol{\varphi}_t^*(\boldsymbol{g}) = \boldsymbol{F}^T\boldsymbol{g}\boldsymbol{F}$. The Eulerian representation of the reference metric is the left Cauchy-Green tensor $\boldsymbol{c} = \boldsymbol{\varphi}_{t*}(\boldsymbol{G}) = \boldsymbol{F}^{-T}\boldsymbol{G}\boldsymbol{F}^{-1}$. The inverse metric tensors $\boldsymbol{G}^{-1}$ and $\boldsymbol{g}^{-1}$ are represented by the Finger tensor $\boldsymbol{b} = \boldsymbol{\varphi}_{t*}(\boldsymbol{G}^{-1}) = \boldsymbol{F}\boldsymbol{G}^{-1}\boldsymbol{F}^T$ and the inverse right Cauchy-Green tensor $\boldsymbol{C}^{-1} := \boldsymbol{\varphi}_t^*(\boldsymbol{g}^{-1}) = \boldsymbol{F}^{-1}\boldsymbol{g}^{-1}\boldsymbol{F}^{-T}$.

A generalized representation of strain tensors is given by the Seth-Hill family of strain measures

$$\boldsymbol{E}^{(a)} = \begin{cases} \frac{1}{a}(\boldsymbol{C}^{a/2} - \boldsymbol{G}) & \text{if } a \neq 0 \\ \frac{1}{2}\ln(\boldsymbol{C}) & \text{if } a = 0 \end{cases} \quad \text{and} \quad \boldsymbol{e}^{(a)} = \begin{cases} \frac{1}{a}(\boldsymbol{g} - \boldsymbol{c}^{a/2}) & \text{if } a \neq 0 \\ \frac{1}{2}\ln(\boldsymbol{c}) & \text{if } a = 0 \end{cases} \tag{2.16}$$

where the former introduced Green's strain and Almansi's strain are obtained by $a = 2$, see also Seth [224].

2.1.4. The concept of mechanical stresses: Euler's cut principle

Consider an arbitrary subdomain $\mathcal{P}_\mathcal{S} \subset \mathcal{S}$ that is cut out of a material body in its deformed configuration $\mathcal{S}$ enclosed by its boundary $\partial\mathcal{P}_\mathcal{S}$, see Figure 2.5. Following Euler's cut principle, the effects of the rest body on $\mathcal{P}_\mathcal{S}$ are then replaced by the spatial mechanical surface traction $\boldsymbol{t}^m$ and the heat flux h. *Cauchy's theorem* states that the contact force $\boldsymbol{t}^m$, as a function of its spatial position $\boldsymbol{x} \in \partial\mathcal{P}_\mathcal{S}$ at time t, is a linear function of the outward normal $\boldsymbol{n}$

$$\boldsymbol{t}^m(\boldsymbol{x}, t; \boldsymbol{n}) = \boldsymbol{\sigma}^m(\boldsymbol{x}, t)\boldsymbol{n}\,. \tag{2.17}$$

Here, $\boldsymbol{\sigma}^m$ is labeled as the mechanical true or Cauchy stress that relates the actual force to the deformed area and geometrically maps spatial normals $\boldsymbol{n} \in T_x^*\mathcal{S}$ onto spatial traction vectors $\boldsymbol{t}^m \in T_x\mathcal{S}$,

$$\boldsymbol{\sigma}^m : \begin{cases} T_x^*\mathcal{S} \to T_x\mathcal{S}, \\ \boldsymbol{n} \mapsto \boldsymbol{t}^m = \boldsymbol{\sigma}^m\boldsymbol{n}\,. \end{cases} \tag{2.18}$$

The Cauchy stress, while having a basic physical meaning, is not the most convenient stress tensor for modeling purposes. Another Eulerian stress tensor, the Kirchhoff stress $\boldsymbol{\tau}^m = J\boldsymbol{\sigma}^m$ is obtained by multiplication of the Cauchy stress with the Jacobian J. This weighted stress maps spatial normals onto volumetrically scaled Eulerian tangents

$$\boldsymbol{\tau}^m : \begin{cases} T_x^*\mathcal{S} \to T_x\mathcal{S}, \\ \boldsymbol{n} \mapsto J\boldsymbol{t}^m = \boldsymbol{\tau}^m\boldsymbol{n}\,. \end{cases} \tag{2.19}$$

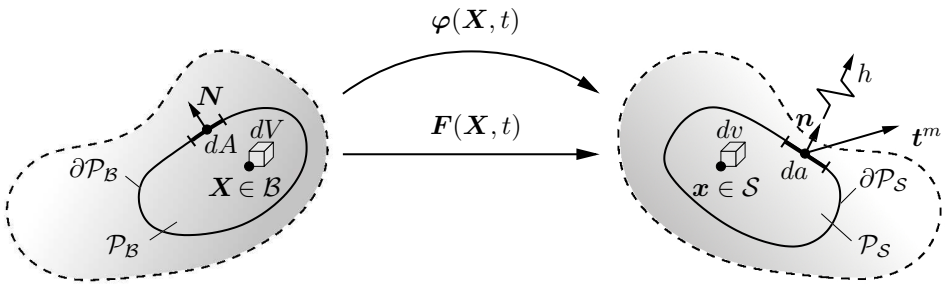

Figure 2.5: *Euler's cut principle.* Lagrangian and Eulerian parts $\mathcal{P}_\mathcal{B}$ and $\mathcal{P}_\mathcal{S}$ cut out of the whole body $\mathcal{B}$ and $\mathcal{S}$. At a point $\boldsymbol{x}\in\partial\mathcal{P}_\mathcal{S}$, the mechanical and thermal actions of the remaining part of $\mathcal{S}$ are replaced by the mechanical traction vector $\boldsymbol{t}^m=\boldsymbol{\sigma}^m\boldsymbol{n}$ and the heat flux $h=\boldsymbol{q}\cdot\boldsymbol{n}$.

With respect to experiments, the most convenient stress tensor is the first Piola-Kirchhoff stress tensor, that relates the actual force to the reference area. It is described by a Cauchy-type relation

$$\boldsymbol{T}^m(\boldsymbol{X},t;\boldsymbol{N})=\tilde{\boldsymbol{P}}^m(\boldsymbol{X},t)\boldsymbol{N}\,. \tag{2.20}$$

Here, $\boldsymbol{T}^m$ is a scaled traction vector of the spatial configuration, obtained by the force equality $\boldsymbol{T}^m dA=\boldsymbol{t}^m da$. The nominal or first Piola-Kirchhoff stress is interpreted as a mapping between the material co-tangent space $T_X^*\mathcal{B}$ and the spatial tangent space $T_x\,\mathcal{S}$

$$\tilde{\boldsymbol{P}}^m:\begin{cases}T_X^*\mathcal{B}\to T_x\,\mathcal{S},\\ \boldsymbol{N}\mapsto\boldsymbol{T}^m=\tilde{\boldsymbol{P}}^m\boldsymbol{N}\,,\end{cases} \tag{2.21}$$

and is called a "two-point" tensor having its bases in both the Lagrangian and Eulerian setting. Another stress tensor is based on a full Lagrangian setting. It relates the Lagrangian traction vector $\boldsymbol{T}^{m*}=\boldsymbol{\varphi}_t^*(\boldsymbol{T}^m)=\boldsymbol{F}^{-1}\boldsymbol{T}^m$, obtained by a pull-back operation, to Lagragian normals $\boldsymbol{N}$ via

$$\boldsymbol{T}^{m*}(\boldsymbol{X},t;\boldsymbol{N})=\boldsymbol{S}^m(\boldsymbol{X},t)\boldsymbol{N}\,. \tag{2.22}$$

Consequently, the second Piola-Kirchhoff stress tensor $\boldsymbol{S}^m$ has the mapping property

$$\boldsymbol{S}^m:\begin{cases}T_X^*\mathcal{B}\to T_X\mathcal{B},\\ \boldsymbol{N}\mapsto\boldsymbol{T}^{m*}=\boldsymbol{S}^m\boldsymbol{N}\,.\end{cases} \tag{2.23}$$

Note that this fully Lagrangian stress tensor is a purely geometric object with no physical meaning. The push-forward and pull-back operators can also be applied onto the stresses, yielding the relation between the Lagrangian, two-point, and Eulerian stress tensors

$$\boldsymbol{S}^m=\begin{cases}\boldsymbol{F}^{-1}\tilde{\boldsymbol{P}}^m,\\ \boldsymbol{F}^{-1}J\boldsymbol{\sigma}^m\boldsymbol{F}^{-T},\\ \boldsymbol{F}^{-1}\boldsymbol{\tau}^m\boldsymbol{F}^{-T},\end{cases}\quad \tilde{\boldsymbol{P}}^m=\begin{cases}\boldsymbol{F}\boldsymbol{S}^m,\\ J\boldsymbol{\sigma}^m\boldsymbol{F}^{-T},\\ \boldsymbol{\tau}^m\boldsymbol{F}^{-T},\end{cases}\quad\text{and}\quad \boldsymbol{\tau}^m=\begin{cases}J\boldsymbol{\sigma}^m,\\ \tilde{\boldsymbol{P}}^m\boldsymbol{F}^T,\\ \boldsymbol{F}\boldsymbol{S}^m\boldsymbol{F}^T,\end{cases} \tag{2.24}$$

see also Figure 2.6a for a commutative stress diagram displaying the introduced stress, traction, and normal tensors in their respective spaces.

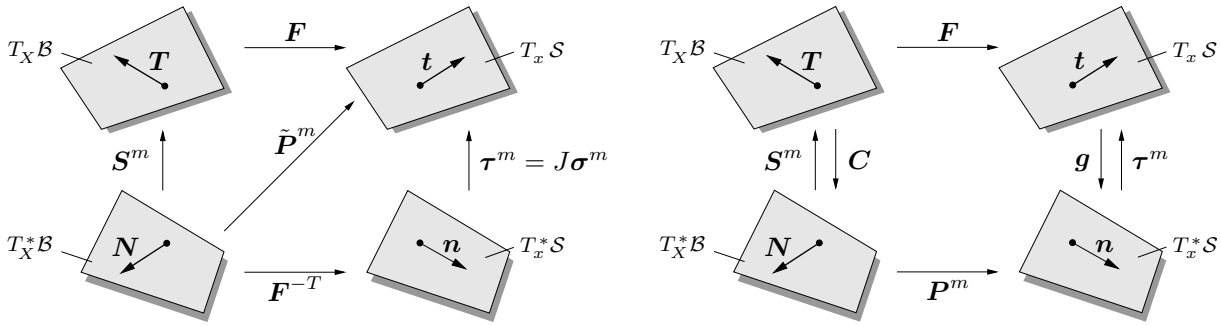

Figure 2.6: *Mapping properties of mechanical stress tensors and stress power.* a) Lagrangian second Piola-Kirchhoff stress $\boldsymbol{S}^m : \boldsymbol{N} \mapsto \tilde{\boldsymbol{T}}^{m*} = \boldsymbol{S}^m\boldsymbol{N}$, two-point first Piola-Kirchhoff stress tensor $\tilde{\boldsymbol{P}}^m : \boldsymbol{N} \mapsto \boldsymbol{T}^m = \tilde{\boldsymbol{P}}^m\boldsymbol{N}$ and Eulerian Kirchhoff stress $\boldsymbol{\tau}^m : \boldsymbol{n} \mapsto J\boldsymbol{t}^m = \boldsymbol{\tau}^m\boldsymbol{n}$ are displayed in the commutative diagram. b) Different representations of the mechanical stress power per unit volume of dual objects $\varrho_0\mathcal{P}^m = \boldsymbol{S}^m : \frac{1}{2}\dot{\boldsymbol{C}} = \boldsymbol{P}^m : \dot{\boldsymbol{F}} = \boldsymbol{\tau}^m : \frac{1}{2}\boldsymbol{\pounds}_{\boldsymbol{v}}\boldsymbol{g}$.

2.1.5. Mechanical power expressions

The concept of mechanical stress power $\mathcal{P}^m$ per unit mass of the reference configuration is employed to define dual objects to the introduced stress tensors of the three different geometric settings. The work needed to deform an (in)elastic continuum from the reference to the current configuration in a time interval $[0, t]$ can be measured by

$$W := \int_{\mathcal{B}} w_0^t \, dV \quad \text{with} \quad w_0^t := \int_0^t \varrho_0\mathcal{P}^m \, d\tau \,. \tag{2.25}$$

Here, w_0^t is the work per unit volume of the reference configuration and obtained by a stress power per unit volume $\varrho_0\mathcal{P}^m$ in a specific time interval. The stress power is defined as stress times strain-rate, resulting in the representation

$$\varrho_0\mathcal{P}^m := \underbrace{\boldsymbol{S}^m : \dot{\boldsymbol{E}}}_{\text{Lagrangian}} = \underbrace{\boldsymbol{P}^m : \dot{\boldsymbol{F}}}_{\text{two-point}} = \underbrace{\boldsymbol{\tau}^m : \boldsymbol{d}}_{\text{Eulerian}} \tag{2.26}$$

for the three different geometric settings. Taking the rate of the Green and Almansi strain reveals $\dot{\boldsymbol{E}} = \frac{1}{2}\dot{\boldsymbol{C}}$ and $\boldsymbol{d} = \frac{1}{2}\boldsymbol{\pounds}_{\boldsymbol{v}}\boldsymbol{g}$. Note that for time derivatives of spatial objects the Lie derivative is introduced

$$\boldsymbol{\pounds}_{\boldsymbol{v}}(\cdot) = \boldsymbol{\varphi}_{t*}\left[\tfrac{d}{dt}\{\boldsymbol{\varphi}_t^*(\cdot)\}\right] . \tag{2.27}$$

It is an objective rate obtained by three consecutive steps. A pull-back of the Eulerian field into the time invariant Lagrangian setting, followed by a material time derivative, i.e. in a fixed reference coordinate system, and ultimately a push-forward of the resulting quantity into the Eulerian configuration. Interpretation of the Lie derivative is the relative change that a deforming observer sees in the Eulerian configuration. With that, (2.26) can be reformulated to

$$\varrho_0\mathcal{P}^m := \underbrace{\boldsymbol{S}^m : \tfrac{1}{2}\dot{\boldsymbol{C}}}_{\text{Lagrangian}} = \underbrace{\boldsymbol{P}^m : \dot{\boldsymbol{F}}}_{\text{two-point}} = \underbrace{\boldsymbol{\tau}^m : \tfrac{1}{2}\boldsymbol{\pounds}_{\boldsymbol{v}}\boldsymbol{g}}_{\text{Eulerian}} . \tag{2.28}$$

For the Lagrangian setting we identify as mechanical work conjugated or dual objects, the second Piola-Kirchhoff stress $\boldsymbol{S}^m$ and the right Cauchy-Green tensor $\boldsymbol{C}$. The geometric two-point setting yields the modified first Piola-Kirchhoff stress $\boldsymbol{P}^m = \boldsymbol{g}\tilde{\boldsymbol{P}}^m$ and the

deformation gradient $\boldsymbol{F}$, while in the Eulerian setting the Kirchhoff stress $\boldsymbol{\tau}^m$ and the spatial metric $\boldsymbol{g}$ are work conjugates. Figure 2.6b summarizes the dual variables in their respective setting.

2.2. Fundamentals of electrostatics

In addition to the purely mechanical quantities, the theory of continuum mechanics is extended by considering electrostatics. A physically motivated approach adds the electric field as a further independent variable to the system of equations. A short overview on the elementary electro-mechanical laws and quantities is given. The author refers to the classical textbooks Toupin [252], Landau & Lifshitz [130], Eringen [63], Penfield & Haus [194], Irodov [100], Maugin [145], Jackson [101], and Griffiths [79] and summarizes briefly the ideas presented therein. While referring to the electrostatic case, the electric point-charges involved within the derivations are assumed to be stationary with respect to each other and any interactions with magnetic quantities are excluded. In a first step, the electric field in vacuum is under consideration. These concepts are then extended to the electric field in matter.

2.2.1. Coulomb's law and the electric field

While a mathematical description of electrostatics is imminent, historically, the fundamental laws of electro-magnetic field theory are obtained by observations and experiments. The existence of positive and negative charges was postulated to explain simple electrostatic experiments. It was shown that charges of opposite sign attract each other, while charges of the same sign are repelling. Furthermore, an equal amount of opposite charges within a body result in an electrically neutral state. The measure of force between two point charges was introduced around 1785 by Charles Augustin de Coulomb and experimentally verified. *Coulomb's law* yields the force $\boldsymbol{f}^e$ between two point charges q_1 and q_2

$$\boldsymbol{f}^e = k q_1 q_2 \frac{\boldsymbol{x}_1 - \boldsymbol{x}_2}{|\boldsymbol{x}_1 - \boldsymbol{x}_2|^3} \,. \tag{2.29}$$

Here, $\boldsymbol{x}_1$ and $\boldsymbol{x}_2$ are the position vectors of q_1 and q_2, respectively, while Coulomb's constant k is given in SI-units by $k = 1/(4\pi\epsilon_0)$ in terms of the permittivity of free space $\epsilon_0 = 8.854 \cdot 10^{-12}$ [F/m]. Note that in case of opposite signs of the point charges the force is attractive whereas charges of same sign yield a repulsive force. While attraction and repulsion of charges was experimentally observed, a physical variable to measure the intensity of such an interaction was postulated. For that, the *electric field* was introduced. Each electric charge gives rise to such a field, and is able to alter an existing field. For an arbitrary system of charges, we observe that a test charge q, placed in the resulting electric field, experiences a force $\boldsymbol{f}^e$ that depends on the location in the field $\boldsymbol{x}$ and the sign of the charge, see Figure 2.7a for a graphical interpretation. An approximation of that force can be expressed by the polynomial form

$$\boldsymbol{f}^e(\boldsymbol{x}, q) = q\,\mathscr{e}(\boldsymbol{x}) + q^2 g(\boldsymbol{x}) + \mathcal{O}(q) \tag{2.30}$$

with $\mathscr{e}$ and g being vectorial coefficients and $\mathcal{O}(q)$ represents higher order terms in q. A restriction to small test charges $q \to 0$, such that the field configuration is not altered,

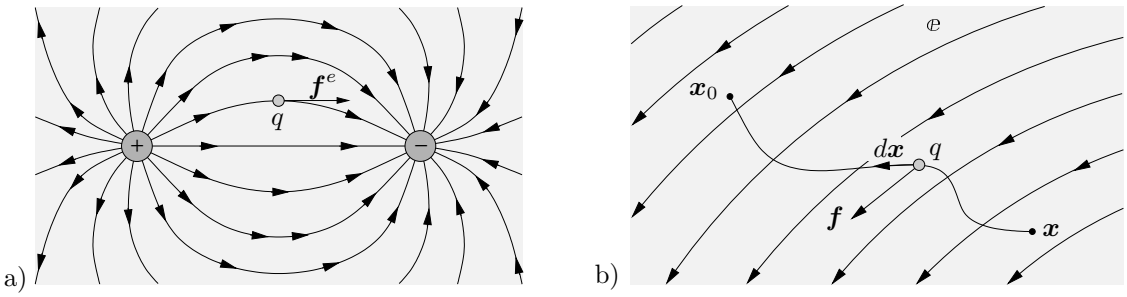

Figure 2.7: *The electric field and electric potential.* a) A test charge q is positioned in an electric field induced by two other charges. The force $\boldsymbol{f}^e = q\mathcal{e}$ acting on the point charge depends on its position in the electric field and is pointing in a direction tangential to the electric field lines. b) A point charge moves between two positions $\boldsymbol{x}$ and $\boldsymbol{x}_0$ within an electric field $\mathcal{e}$. For conservative fields with curl $\mathcal{e} = \boldsymbol{0}$, the line integral $\oint_C \mathcal{e} \cdot d\boldsymbol{x} = 0$ is path independent.

allows to reduce (2.30), introducing the *spatial electric field vector*

$$\mathcal{e}(\boldsymbol{x}) = \lim_{q\to 0} \frac{\boldsymbol{f}^e(\boldsymbol{x}, q)}{q} \quad \text{with} \quad \boldsymbol{f}^e(\boldsymbol{x}, q) = q\mathcal{e}(\boldsymbol{x}) \tag{2.31}$$

given in units Newton per Coulomb [N/C] or Volt per meter [V/m]. For simplicity assume that the position of the test charge q is not altered in the field and also note that $\lim_{q\to 0}$ is physically unreasonable, as the smallest possible charge is the charge of an electron which is of discrete value. A combination of (2.29) and $(2.31)_1$, yields the electric field at position $\boldsymbol{x}$ due to a single point charge q_1 at position $\boldsymbol{x}_1$

$$\mathcal{e}(\boldsymbol{x}) = \frac{q_1}{4\pi\epsilon_0} \frac{\boldsymbol{x} - \boldsymbol{x}_1}{|\boldsymbol{x} - \boldsymbol{x}_1|^3} \,. \tag{2.32}$$

2.2.2. Principle of superposition and Faraday's law of electrostatics

A direct extension of the electric field to multiple sources is achieved by the *principle of superposition*. It states that the resultant force on a test particle q due to multiple source point charges q_i at position $\boldsymbol{x}_i$ for $i = 1, \dots, n$ is the sum of the forces due to the charges individually

$$\mathcal{e}(\boldsymbol{x}) = \frac{1}{4\pi\epsilon_0} \sum_{i=1}^{n} q_i \frac{\boldsymbol{x} - \boldsymbol{x}_i}{|\boldsymbol{x} - \boldsymbol{x}_i|^3} = \frac{1}{4\pi\epsilon_0} \int \rho^e(\boldsymbol{x}') \frac{\boldsymbol{x} - \boldsymbol{x}'}{|\boldsymbol{x} - \boldsymbol{x}'|^3} \, dv' \,. \tag{2.33}$$

For the assumption of many small source point charges, a reformulation in terms of the charge density $\rho^e(\boldsymbol{x}')$ is possible.

The vectorial form of the electric field poses difficulties on its determination. Without additional information it can only be computed up to a gradient of a scalar function satisfying the Laplace equation, see Jackson [101]. To circumvent this difficulty, a reformulation of (2.33) in terms of a gradient of a scalar field is convenient. Vector calculus provides the essential relation $\frac{\boldsymbol{x}-\boldsymbol{x}'}{|\boldsymbol{x}-\boldsymbol{x}'|^3} = -\nabla_{\boldsymbol{x}}(\frac{1}{|\boldsymbol{x}-\boldsymbol{x}'|})$ allowing a significant simplification of the generalized Coulomb's law $(2.33)_2$. As the gradient operator is with respect to $\boldsymbol{x}$, i.e. not related to the integration variable $\boldsymbol{x}'$, it can be taken outside the integral sign

$$\mathcal{e}(\boldsymbol{x}) = -\nabla_{\boldsymbol{x}} \Big(\frac{1}{4\pi\epsilon_0} \int \frac{\rho^e(\boldsymbol{x}')}{|\boldsymbol{x} - \boldsymbol{x}'|} dv' \Big) \,. \tag{2.34}$$

Here, the electric field is directly related to the gradient of a scalar function, namely the *electric potential* such that

$$\mathbb{e} = -\nabla\phi^e(\boldsymbol{x}) \quad \text{with} \quad \phi^e(\boldsymbol{x}) := \frac{1}{4\pi\epsilon_0}\int \frac{\rho^e(\boldsymbol{x}')}{|\boldsymbol{x}-\boldsymbol{x}'|}dv' \,. \tag{2.35}$$

As a result, Faraday's law of electrostatics or the electric compatibility condition

$$\operatorname{curl}\mathbb{e} = \boldsymbol{0} \tag{2.36}$$

is a priori satisfied due to the crucial property $\operatorname{curl}[\nabla s] \equiv 0$ for any scalar quantity s. The electric potential itself has a physical interpretation related to the electromotive force. The interested reader is referred to Jackson [101] and Griffiths [79] for a rigorous treatment.

2.2.3. Gauss's law of electrostatics

Gauss's law or *Gauss's flux theorem* states that "the net electric flux through any hypothetical closed surface is proportional to the net electric charge within that closed surface". For the field lines, originating from positive charges, either have to cross the surface or terminate at negative charges within the bounded surface. On the other hand, field lines originating from charges outside the surface enter and exit the surface, resulting in no net contribution to the flux. Consider a point charge q at the origin of a spherical surface $\mathcal{S}$ of radius $|\boldsymbol{x}-\boldsymbol{x}'|$. Related to the source point charge q the electric field lines are pointing in radial direction of the sphere such that (2.32) reads

$$\mathbb{e} = \frac{q}{4\pi\epsilon_0}\frac{1}{|\boldsymbol{x}-\boldsymbol{x}'|^2}\boldsymbol{n} \,, \tag{2.37}$$

with the outward normal $\boldsymbol{n} := (\boldsymbol{x}-\boldsymbol{x}')/|\boldsymbol{x}-\boldsymbol{x}'|$. Further, a finite area element on the surface of the sphere is defined as $da = |\boldsymbol{x}-\boldsymbol{x}'|^2 \sin\theta d\theta$ in spherical coordinates. The electric flux through the surface $\mathcal{S}$ is defined as the electric field $\mathbb{e}$ multiplied by the area of the surface projected in a plane perpendicular to the field. Integration yields the total flux through the entire surface

$$\oint_{\partial\mathcal{S}} \mathbb{e}\cdot d\boldsymbol{a} = \frac{q}{4\pi\epsilon_0}\int_0^{\pi}\sin\theta d\theta\int_0^{2\pi} d\phi = \frac{1}{\epsilon_0}q \,, \tag{2.38}$$

for a single source point charge. Now suppose multiple source charges q_i within the domain. According to the principle of superposition the resulting electric field is obtained by the sum over all individual fields $\mathbb{e}_i$ for $i = 1,\dots,n$ resulting in

$$\oint_{\partial\mathcal{S}} \mathbb{e}\cdot d\boldsymbol{a} = \sum_{i=1}^{n}\Big(\oint_{\partial\mathcal{S}} \mathbb{e}_i\cdot d\boldsymbol{a}\Big) = \frac{1}{\epsilon_0}\sum_{i=1}^{n} q_i = \frac{1}{\epsilon_0}q_{enc} \,. \tag{2.39}$$

and revealing Gauss's law in its integral formulation. Here, $q_{enc} = \int_{\mathcal{S}}\rho^e\, dv$ is the total amount of charge enclosed by the surface under consideration. Applying the divergence theorem for any volume $\mathcal{V}$ reveals the differential form of Gauss's law as

$$\epsilon_0 \operatorname{div}\mathbb{e} = \rho^e \tag{2.40}$$

connecting the electric field to the electric charge density.

2.2.4. The electric field in ponderable media

The concepts of an electric field in vacuum introduced above are now extended to the more general case of matter within an electric field. This induces several new ideas, where first of all the concept of electrically neutral atoms is revisited. Without an external electric field, we assume that the (positive) nucleus is positioned within the atoms such that it coincides with the average center of the surrounding (negative) electrons. That leads to a non-polar system. An atom within an external electric field however is subjected to Coulomb's law, i.e. electric forces break the symmetry of the atom, separating the center of positive and negative charge and ultimately lead to a dipole within the atom. This separation is countered by the inverse effect, attraction of the different charges within the atom, until an equilibrium between the outer and inner electrical forces is achieved. The electric dipole moment vector is introduced as a measure of said separation of charge containing the information of charge and distance between the average centers of the dipole. A macroscopic effective quantity, averaging the electric dipoles within a material consisting of many atoms, is introduced as the *electric polarization* vector. It is given at any point $\boldsymbol{x}$ of the medium as

$$\mathbb{p}(\boldsymbol{x}) = \sum_i \langle \tilde{\mathbb{p}}_i \rangle \,, \tag{2.41}$$

where $\langle \tilde{\mathbb{p}}_i \rangle$ is the dipole moment of molecule i in the medium per unit volume. Note that, due to the absence of atoms, in vacuum $\mathbb{p} = \boldsymbol{0}$. To quantify the electric field produced by a poled material, the concept of an electric potential is extended for the dielectric case (media with $\mathbb{p} \neq \boldsymbol{0}$). For a polarized body $\mathcal{S}$ the potential is defined by

$$\phi^e(\boldsymbol{x}) = \frac{1}{4\pi\epsilon_0} \int_{\mathcal{S}} \frac{\mathbb{p}(\boldsymbol{x}') \cdot (\boldsymbol{x} - \boldsymbol{x}')}{|\boldsymbol{x} - \boldsymbol{x}'|^3} dv' \,. \tag{2.42}$$

Recalling the gradient definition introduced above together with the divergence theorem allows a simplification to a more convenient form

$$\phi^e(\boldsymbol{x}) = \frac{1}{4\pi\epsilon_0} \int_{\mathcal{S}} \frac{\rho_b^e}{|\boldsymbol{x} - \boldsymbol{x}'|} dv' + \frac{1}{4\pi\epsilon_0} \int_{\partial\mathcal{S}} \frac{\sigma_b^e}{|\boldsymbol{x} - \boldsymbol{x}'|} da' \,, \tag{2.43}$$

where $\rho_b^e := -\operatorname{div} \mathbb{p}$ is the volume density of bound charges and $\sigma_b^e := \mathbb{p} \cdot \boldsymbol{n}$ the surface density of bound charges. Here, the relation of the electric field produced by the polarization of the material to the concept of bound charges is directly evident. For a description of the total electric field consisting of the externally applied field and the field due to polarization of the material, the total charge density is defined. It consists of the volume charge density and *any other charges* not related to the polarization, called free charges ρ_f^e, such that

$$\rho^e = \rho_f^e + \rho_b^e \,. \tag{2.44}$$

Gauss's law for the dielectric body in terms of the *total electric field* can then be rewritten to

$$\epsilon_0 \operatorname{div} \mathbb{e} = \rho^e = \rho_f^e + \rho_b^e = \rho_f^e - \nabla \cdot \mathbb{p} \,. \tag{2.45}$$

Employing the reformulation $\operatorname{div}(\epsilon_0 \mathbb{e} + \mathbb{p}) = \rho_f^e$ and introduction of the electric displacements $\mathbb{d} = \epsilon_0 \mathbb{e} + \mathbb{p}$, the Gauss law of electrostatics in dielectrics takes the simple differential form

$$\operatorname{div} \mathbb{d} = \rho_f^e \tag{2.46}$$

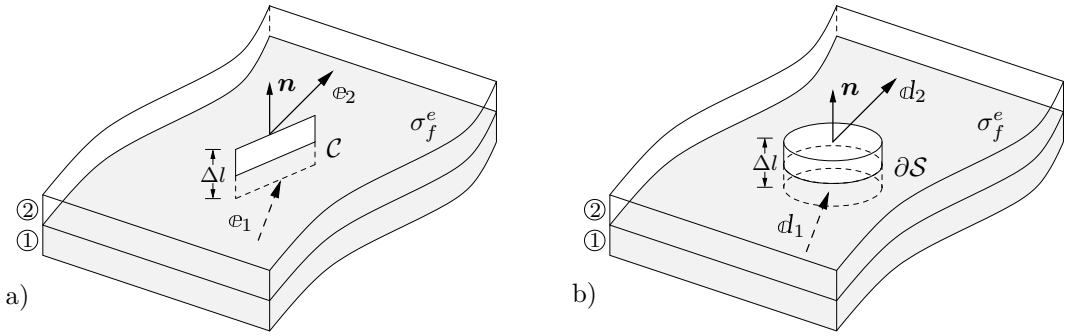

Figure 2.8: *Boundary conditions at a material interface.* For a height $\Delta l \to 0$ of a a) thin rectangular loop $\mathcal{C}$ or b) Gaussian pillbox $\partial\mathcal{S}$ with surface charge density of free charges σ_f^e, the jump conditions for the electric field and electric displacement can be formulated.

For completeness, the integral form in terms of the total enclosed free charges $q_{f,enc}$ in $\mathcal{S}$ reads

$$\oint_{\partial\mathcal{S}} \mathbb{d} \cdot d\boldsymbol{a} = q_{f,enc}\,. \tag{2.47}$$

2.2.5. Linear dielectrics, susceptibility, and dielectric constant

While the effects of the polarization on the electric field were described, the relation of polarization to the external electric field, and the connections between electric field, electric displacement and polarization need some clarification. For moderate external electric fields, the polarization is proportional to the field, following the relation $\mathbb{p} = \epsilon_0 \chi^e \mathbb{e}$ of linear isotropic dielectrics. A new, dimensionless parameter χ^e, the *electric susceptibility*, is introduced, depending on the medium in focus but generally also on external conditions such as temperature. This approach defines directly the third variable, the electric displacements

$$\mathbb{d} = \epsilon_0 \mathbb{e} + \mathbb{p} = \epsilon_0 \mathbb{e} + \epsilon_0 \chi^e \mathbb{e} = \epsilon_0 (1 + \chi^e) \mathbb{e} = \epsilon \mathbb{e}\,, \tag{2.48}$$

in terms of the relative permittivity $\epsilon_r = (1 + \chi^e)$. For any ponderable material, $\epsilon_r > 1$ while in vacuum $\epsilon_r = 1$, such that the dielectric constant of vacuum is exactly the permittivity of free space.

2.2.6. Jump conditions at interfaces between materials

Dealing with dielectric or multiphase materials in general, the interface between neighboring media needs to be treated with caution. To derive the respective conditions for the electric field and electric displacements consider two materials containing $\{\mathbb{e}_1, \mathbb{d}_1\}$ and $\{\mathbb{e}_2, \mathbb{d}_2\}$, respectively. Referring to a closed rectangular loop $\mathcal{C}$ as displayed in Figure 2.8a and recasting the local form of Faraday's law $\operatorname{curl} \mathbb{e} = \boldsymbol{0}$ one obtains for a height $\Delta l \to 0$ the continuity of the tangential component of the electric field over the surface of a discontinuity

$$[\![\mathbb{e}]\!] \times \boldsymbol{n} = \boldsymbol{0}\,, \tag{2.49}$$

with the jump $[\![a]\!] = a_2 - a_1$ of a quantity a across an interface. Starting from Gauss's law of electrostatics, applied to a "pill-box" cut out of both material 1 and 2, see Figure 2.8b,

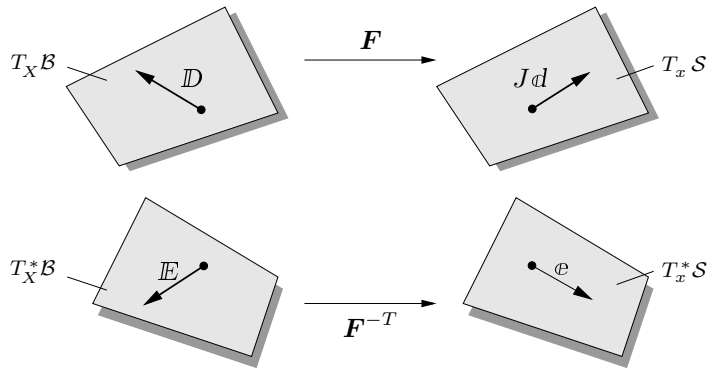

Figure 2.9: *Geometric mapping properties of electric quantities.* The contravariant Kirchhoff-type electric displacement $J\mathbb{d} = \boldsymbol{F}\mathbb{D}$ is mapped via the deformation gradient. The covariant electric field $\mathbb{e} = \boldsymbol{F}^{-T}\mathbb{E}$ is mapped by the normal map.

the boundary condition for the normal component of the electric displacements can be derived. For the height $\Delta l \to 0$ the flux through the sides of the box can be neglected. Free surface charges d on the interface give rise to a jump of the normal component of the electric displacements

$$[\![\mathbb{d}]\!] \cdot \boldsymbol{n} = d\,. \tag{2.50}$$

For a rigorous treatment of the interface boundary conditions between materials and free space the author refers to the work of Rosato [202].

2.2.7. Geometrical transformations and electric power expression

Using the geometric nature of the introduced Eulerian electric field $\mathbb{e}$ and electric displacement $\mathbb{d}$ gives us, by a pull-back operation, the respective Lagrangian fields. The electric field transforms by

$$\mathbb{E} = \boldsymbol{F}^T\mathbb{e} \quad \to \quad \mathbb{e} = \boldsymbol{F}^{-T}\mathbb{E}\,, \tag{2.51}$$

while the electric displacement shifts by a typical Piola-transformation

$$\mathbb{D} = J\boldsymbol{F}^{-1}\mathbb{d} \quad \to \quad J\mathbb{d} = \boldsymbol{F}\mathbb{D}\,, \tag{2.52}$$

see Figure 2.9 for a graphical representation. In analogy to the definition of mechanical stress power, the electric power per unit volume $\varrho_0\mathcal{P}^e$ is defined as negative electric displacement times rate of the electric field

$$\varrho_0\mathcal{P}^e := \underbrace{-\mathbb{D}\cdot\dot{\mathbb{E}}}_{\text{Lagrangian}} = \underbrace{-J\mathbb{d}\cdot\boldsymbol{\pounds}_{\boldsymbol{v}}\mathbb{e}}_{\text{Eulerian}}\,. \tag{2.53}$$

Here, the rate of the Eulerian electric field is obtained by a Lie-derivative, such that $\boldsymbol{\pounds}_{\boldsymbol{v}}\mathbb{e} = \boldsymbol{F}^{-T}\frac{d}{dt}(\boldsymbol{F}^T\mathbb{e})$.

2.3. Fundamentals of magnetostatics

For a coupled magneto-electro-mechanical system, the fundamental relations and equations of magnetostatics are introduced in a concise manner. Based on the seminal works of

Truesdell & Toupin [255], Kovetz [123] and more recently Griffiths [79], the magnetic field quantities are introduced. Here, we restrict ourselves to steady currents and no external electric fields are considered. Steady currents are assumed to produce magnetic fields that are constant in time, the electrostatic equivalent are stationary charges that produce electric fields that are constant in time, as considered above. While both states are rather artificial, they represent a suitable approximation.

2.3.1. Conservation of electric charge

The first principle of magnetostatics states the conservation of charge, i.e. no electric charge can be created or destroyed. For a mathematical treatment of this statement consider a region of time and space dependent electric charge density ρ^e. In a subdomain $\mathcal{S}$ with boundary $\partial\mathcal{S}$ the rate of change of charge within $\mathcal{S}$ is equal to the net flux over $\partial\mathcal{S}$. With the help of the current density vector $\boldsymbol{j}$ at the surface $\partial\mathcal{S}$ and by employing the divergence theorem, one obtains the continuity conditions of electric charge in its local form

$$\frac{d}{dt}\int_{\mathcal{S}} \rho^e \, dv + \int_{\partial\mathcal{S}} \boldsymbol{j}\cdot\boldsymbol{n}\, da = 0 \quad \longrightarrow \quad \dot{\rho}^e + \operatorname{div}\boldsymbol{j} = 0\,, \tag{2.54}$$

with the normal $\boldsymbol{n}$ to the surface $\partial\mathcal{S}$. Restriction to steady currents allows for a simplification of (2.54) to the first principle of magnetostatics stating the current density to have no sources or sinks

$$\operatorname{div}\boldsymbol{j} = 0\,. \tag{2.55}$$

A simple ansatz that a priori fulfills (2.55) is the assumption of a current potential $\boldsymbol{h}$ that defines the current density as $\boldsymbol{j} = \operatorname{curl}\boldsymbol{h}$. This vector potential approach and its physical meaning is further specified in the following.

2.3.2. Biot-Savart's law and conservation of magnetic induction

Analogously to electrostatics, Biot-Savart's law can be seen as "Coulomb's law" of magnetostatics and is used to compute the magnetic induction of steady currents. While the terminology of magnetic fields and magnetic induction is questionable in literature, see Griffiths [79], the author labels the magnetic induction by $\mathbb{b}$ given in Tesla [T]. Then, Biot-Savart's law for the general case of a volume current density reads

$$\mathbb{b}(\boldsymbol{x}) = \frac{\mu_0}{4\pi}\int \boldsymbol{j}(\boldsymbol{x}')\times\frac{\boldsymbol{x}-\boldsymbol{x}'}{|\boldsymbol{x}-\boldsymbol{x}'|^3}\,dv'\,, \tag{2.56}$$

in terms of the permeability of free space $\mu_0 = 4\pi\cdot 10^{-7}$ [N/A^2]. Recalling the vector calculus as employed in (2.31), $\frac{\boldsymbol{x}-\boldsymbol{x}'}{|\boldsymbol{x}-\boldsymbol{x}'|^3} = -\nabla_{\boldsymbol{x}}(\frac{1}{|\boldsymbol{x}-\boldsymbol{x}'|})$ a reformulation to a more convenient form is possible

$$\mathbb{b}(\boldsymbol{x}) = \frac{\mu_0}{4\pi}\nabla\times\int\frac{\boldsymbol{j}(\boldsymbol{x}')}{|\boldsymbol{x}-\boldsymbol{x}'|}\,dv'\,, \tag{2.57}$$

where the vanishing divergence of the magnetic induction is evident. The localized equation is referred to as the *first Gauss law of magnetostatics* and reads

$$\operatorname{div}\mathbb{b} = 0\,. \tag{2.58}$$

This equation displays the absence of magnetic monopoles and is a priori fulfilled by the introduction of a magnetic vector potential $\boldsymbol{a}^m$, as $\operatorname{div}[\operatorname{curl}\boldsymbol{a}^e] = 0$.

2.3.3. Ampère's law of magnetostatics

In analogy to electrostatics, a second equation, namely Ampère's law is formulated based on the curl of the magnetic induction

$$\nabla \times \mathbb{b}(\boldsymbol{x}) = \frac{\mu_0}{4\pi} \nabla \times \nabla \times \int \frac{\boldsymbol{j}(\boldsymbol{x}')}{|\boldsymbol{x} - \boldsymbol{x}'|} \, dv' \,. \tag{2.59}$$

With the mathematical identity $\nabla \times (\nabla \times \boldsymbol{A}) = \nabla(\nabla \cdot \boldsymbol{A})$ for arbitrary vector fields, and after a lengthy reformulation of (2.59) one ends up with

$$\nabla \times \mathbb{b}(\boldsymbol{x}) = \mu_0 \boldsymbol{j}(\boldsymbol{x}) + \frac{\mu_0}{4\pi} \nabla \int \frac{\nabla' \cdot \boldsymbol{j}(\boldsymbol{x}')}{|\boldsymbol{x} - \boldsymbol{x}'|} \, dv' \,, \tag{2.60}$$

which reduces with (2.55) for steady currents to the second equation of magnetostatics

$$\operatorname{curl} \mathbb{b} = \mu_0 \boldsymbol{j} \tag{2.61}$$

named *Ampère's law* in its differential form. For a rigorous mathematical description, the interested reader is referred to Jackson [101].

2.3.4. The magnetic field in magnetizable media

The equations introduced above are valid for magnetic fields in vacuum. In a next step, related to the electric field in ponderable media, magnetizable materials are in focus, where external magnetic fields lead to a current in the material and therefore to so-called *magnetic self-fields*. To identify and quantify such an interaction the concept of electric dipoles is extended to the magnetic case. The author refers to Jackson [101] and Griffiths [79] and without further explanations assumes the existence of magnetic dipoles within a material. In analogy to the electric polarization, the volume average of magnetic dipoles within a unit volume defines the magnetization $\mathbb{m}$ in Ampère per meter [A/m]. The related magnetic vector potential of the magnetized body can be computed based on the principle of superposition, reading

$$\boldsymbol{a}^m(\boldsymbol{x}) = \frac{\mu_0}{4\pi} \int \frac{\mathbb{m}(\boldsymbol{x}') \times (\boldsymbol{x} - \boldsymbol{x}')}{|\boldsymbol{x} - \boldsymbol{x}'|^3} \, dv' \,. \tag{2.62}$$

Integration by parts allows for a reformulation to

$$\boldsymbol{a}^m(\boldsymbol{x}) = \frac{\mu_0}{4\pi} \int \frac{\nabla' \times \mathbb{m}(\boldsymbol{x}')}{|\boldsymbol{x} - \boldsymbol{x}'|} \, dv' \,, \tag{2.63}$$

where the also arising surface integral vanishes for a well behaved and localized magnetization, Jackson [101]. Here we identify the *induced current* $\tilde{\boldsymbol{j}} = \nabla \times m$, related to the magnetization. This vector potential gives rise to the magnetic induction due to magnetization $\tilde{\mathbb{b}} = \operatorname{curl} \boldsymbol{a}^m$. To compute the total magnetic flux consisting of externally applied magnetic fields and the flux due to magnetization of the body, the total current $\boldsymbol{j} + \tilde{\boldsymbol{j}}$ is considered. From (2.55) and (2.63) we directly see that $\operatorname{div} \tilde{\boldsymbol{j}} = 0$ to fulfill the continuity equation. An extension of Ampère's law to the full current reads, together with (2.61), in its differential form

$$\nabla \times \mathbb{b} = \mu_0(\boldsymbol{j} + \tilde{\boldsymbol{j}}) = \mu_0(\boldsymbol{j} + \nabla \times \mathbb{m}) \,. \tag{2.64}$$

Introducing a new magnetic quantity, the magnetic field $\mathbb{h} = 1/\mu_0 \mathbb{b} - \mathbb{m}$ [A/m], which is an auxiliary field dual to the electric displacements, gives a common form of Ampère's law

$$\operatorname{curl} \mathbb{h} = \boldsymbol{j} \tag{2.65}$$

For our purpose of differentiating between magnetic fields due to external current and due to magnetization alone, the magnetic self-field of the body $\mathcal{S}$ is defined by

$$\operatorname{curl}(\frac{\tilde{\mathbb{b}}}{\mu_0} - \mathbb{m}) = \boldsymbol{0} \quad \longrightarrow \quad \tilde{\mathbb{h}} = \frac{\tilde{\mathbb{b}}}{\mu_0} - \mathbb{m}\,, \tag{2.66}$$

where the ansatz of a magnetic scalar potential $\tilde{\phi}^m$ of the self-field a priori fulfills Ampère's law, i.e. $\operatorname{curl}(-\nabla\tilde{\phi}^m) = \operatorname{curl}\tilde{\mathbb{h}} = \boldsymbol{0}$.

2.3.5. Boundary conditions at interfaces between materials

Following the ideas of a jump in the field variables on the interface of electrostatic materials, the boundary conditions for the magnetic induction and magnetic fields are presented analogously. Consider two materials containing $\{\tilde{\mathbb{h}}_1, \tilde{\mathbb{b}}_1\}$ and $\{\tilde{\mathbb{h}}_2, \tilde{\mathbb{b}}_2\}$, respectively. The jump on the interface of the magnetic self-field is given as

$$[\![\tilde{\mathbb{h}}]\!] \times \boldsymbol{n} = \boldsymbol{0}\,, \tag{2.67}$$

related to Ampère's law of magnetostatics $\operatorname{curl}\tilde{\mathbb{h}} = \boldsymbol{0}$. Likewise, the Gauss law $\operatorname{div}\tilde{\mathbb{b}} = 0$ yields

$$[\![\tilde{\mathbb{b}}]\!] \cdot \boldsymbol{n} = 0\,, \tag{2.68}$$

for the magnetic induction due to magnetization.

2.3.6. Geometrical transformations and magnetic power expression

Using the geometric nature of the introduced Eulerian magnetic field $\mathbb{h}$ and magnetic induction $\mathbb{b}$ gives us, by a pull-back operation, the respective Lagrangian fields. The magnetic self-field transforms by

$$\mathbb{H} = \boldsymbol{F}^T \mathbb{h} \quad \rightarrow \quad \mathbb{h} = \boldsymbol{F}^{-T} \mathbb{H}\,, \tag{2.69}$$

while the magnetic induction shifts by a typical Piola-transformation

$$\mathbb{B} = J\boldsymbol{F}^{-1}\mathbb{b} \quad \rightarrow \quad J\mathbb{b} = \boldsymbol{F}\mathbb{B}\,, \tag{2.70}$$

see Figure 2.10 for a graphical representation. In analogy to the definition of mechanical stress power, the magnetic power per unit volume $\varrho_0\mathcal{P}^{mag}$ is defined as negative magnetic induction times rate of the magnetic field

$$\varrho_0\mathcal{P}^{mag} := \underbrace{-\mathbb{B}\cdot\dot{\mathbb{H}}}_{\text{Lagrangian}} = \underbrace{-J\mathbb{b}\cdot\boldsymbol{\pounds}_{\boldsymbol{v}}\mathbb{h}}_{\text{Eulerian}}\,. \tag{2.71}$$

Here, the rate of the Eulerian magnetic field is obtained by a Lie-derivative, such that $\boldsymbol{\pounds}_{\boldsymbol{v}}\mathbb{h} = \boldsymbol{F}^{-T}\frac{d}{dt}(\boldsymbol{F}^T\mathbb{h})$.

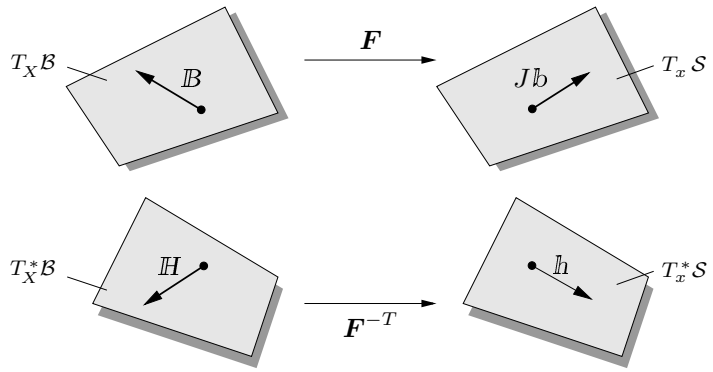

Figure 2.10: *Geometric mapping properties of magnetic quantities.* The contravariant Kirchhoff-type magnetic induction $J\mathbb{b} = \boldsymbol{F}\mathbb{B}$ is mapped via the deformation gradient. The covariant magnetic field $\mathbb{h} = \boldsymbol{F}^{-T}\mathbb{H}$ is mapped by the normal map.

2.4. Extended balance laws of mechanics

The classical balance laws of continuum mechanics are extended to incorporate magneto- and electrostatic effects, i.e. interactions of magnetic and electric fields with a solid. The author leans towards the *dipole-dipole* model in the Chu formulation, Penfield & Haus [194] and Pao & Hutter [191]. In the following assume a subdomain $\mathcal{P}_\mathcal{S}$ cut out of the body $\mathcal{S}$. The action of the rest body $\mathcal{S} \setminus \mathcal{P}_\mathcal{S}$ is expressed in terms of phenomenological quantities, referring to Euler's cut principle. For a general material mechanical tractions and heat flux need to be considered. The global balance laws in the spatial configuration are listed in the following, containing mechanical, electric, and magnetic quantities

$$
\begin{aligned}
&\text{1. mass} && \frac{d}{dt}\int_{\mathcal{P}_\mathcal{S}} \varrho \, dv = 0 \,, \\
&\text{2. linear momentum} && \frac{d}{dt}\int_{\mathcal{P}_\mathcal{S}} \varrho \boldsymbol{v} \, dv = \int_{\mathcal{P}_\mathcal{S}} \varrho \boldsymbol{\gamma} \, dv + \int_{\partial\mathcal{P}_\mathcal{S}} \boldsymbol{t}^m \, da \,, \\
&\text{3. angular momentum} && \frac{d}{dt}\int_{\mathcal{P}_\mathcal{S}} \boldsymbol{x} \times \varrho \boldsymbol{v} \, dv = \int_{\mathcal{P}_\mathcal{S}} \boldsymbol{x} \times \varrho \boldsymbol{\gamma} + \varrho \boldsymbol{\omega} \, dv + \int_{\partial\mathcal{P}_\mathcal{S}} \boldsymbol{x} \times \boldsymbol{t}^m \, da \,, \\
&\text{4. energy} && \frac{d}{dt}\int_{\mathcal{P}_\mathcal{S}} \tfrac{1}{2}\, \varrho \boldsymbol{v}\cdot\boldsymbol{v} + \varrho e \, dv = \int_{\mathcal{P}_\mathcal{S}} \varrho \boldsymbol{\gamma}\cdot\boldsymbol{v} + \varrho r \, dv + \int_{\partial\mathcal{P}_\mathcal{S}} \boldsymbol{t}^m\cdot\boldsymbol{v} - \boldsymbol{q}\cdot\boldsymbol{n} \, da \,.
\end{aligned}
\tag{2.72}
$$

Here, the *mass density* in the current configuration ϱ, the *total body force* per unit mass $\boldsymbol{\gamma} := \boldsymbol{\gamma}^m + \boldsymbol{\gamma}^{ele} + \boldsymbol{\gamma}^{mag}$ containing mechanical, electric, and magnetic contributions as well as the mechanical tractions $\boldsymbol{t}^m = \boldsymbol{\sigma}^m\boldsymbol{n}$ are employed. The general *body couple* $\boldsymbol{\omega} = \boldsymbol{\omega}^{ele} + \boldsymbol{\omega}^{mag}$, the internal energy density per unit mass e, the heat flux vector $\boldsymbol{q}$, and the *total energy supply* per unit mass $r := r^m + r^{ele} + r^{mag}$ are required. These global laws can be transformed to *local statements* for sufficiently smooth fields. For that, the Gauss and localization theorem are employed such that the following equations have to hold at every point $\boldsymbol{x} \in \mathcal{S}$,

$$
\begin{aligned}
&\text{1. mass} && \dot{\varrho} + \varrho \operatorname{div}[\boldsymbol{v}] = 0 \,, \\
&\text{2. linear momentum} && \varrho\dot{\boldsymbol{v}} = \operatorname{div}[\boldsymbol{\sigma}^m] + \varrho\boldsymbol{\gamma}^m + \varrho\boldsymbol{\gamma}^{ele} + \varrho\boldsymbol{\gamma}^{mag} \,, \\
&\text{3. angular momentum} && \operatorname{skew}[\boldsymbol{\sigma}^m] = \varrho\hat{\boldsymbol{\omega}}^{ele} + \varrho\hat{\boldsymbol{\omega}}^{mag} \,, \\
&\text{4. energy} && \varrho\dot{e} = \boldsymbol{\sigma}^m : \boldsymbol{gl} + \varrho r^m + \varrho r^{ele} + \varrho r^{mag} - \operatorname{div}[\boldsymbol{q}],
\end{aligned}
\tag{2.73}
$$

with the skew-symmetric second order tensors $\hat{\boldsymbol{\omega}}^{ele}$ and $\hat{\boldsymbol{\omega}}^{mag}$, as well as the spatial velocity gradient $\boldsymbol{l} = \dot{\boldsymbol{F}}\boldsymbol{F}^{-1}$. Note the non-symmetry of the mechanical Cauchy stress $\boldsymbol{\sigma}^{m}$. For a detailed explanation of the electric and magnetic body forces, body couple and energy supply the author refers to the rigorous treatment in Rosato [202], Zäh [274], Ethiraj [66], and the references cited therein.

Chapter 3

The Concept of Micro-to-Macro Transition

This chapter summarizes the idea of scale-separation and homogenization to determine effective macroscopic parameters based on a heterogeneous micro-structure. The fundamental works of Voigt [261], Reuss [201], Hill [91, 94], Hashin & Shtrikman [86], Willis [267], Suquet [242], Ponte Castañeda & Suquet [200], and the textbooks by Nemat-Nasser & Hori [183], Zohdi & Wriggers [282], and Buryachenko [35] provide a starting point and summarize analytical as well as numerical homogenization techniques. Analytical estimates however, are often restricted to certain assumptions, especially with respect to the geometry of the associated micro-structure. A numerical approach based on a full solution of the microscopic boundary-value-problem enables a general method for the computation of effective overall properties of the material body. Increasing interest in composite materials, with highly optimized micro-structures, further drives the necessity of advances in the field of computational homogenization. While averaging procedures in classical linear and non-linear mechanics are well established,

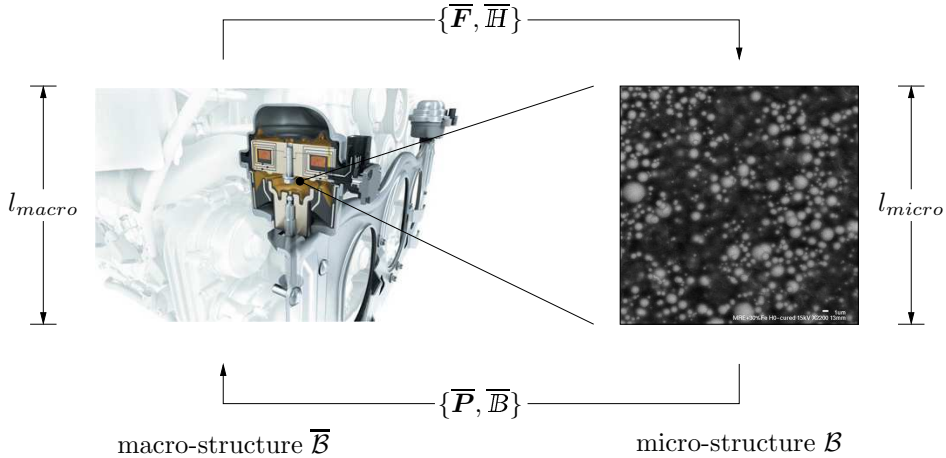

Figure 3.1: *Micro-to-macro scale-bridging concept.* Stiffness of damping devices, here an engine mount, is tunable by an applied magnetic field due to interactions of ferromagnetic particles on the microscale. The macroscopic deformation gradient and magnetic field $\{\overline{\boldsymbol{F}}, \overline{\mathbb{H}}\}$ load the micro-structure $\mathcal{B}$. As a result of the underlying material model the homogenized nominal stress and magnetic induction $\{\overline{\boldsymbol{P}}, \overline{\mathbb{B}}\}$ at a material point of the macro-structure $\overline{\mathcal{B}}$ are obtained.

fundamental progress in the field of multiphysics, e.g. magneto-electro-mechanics, was achieved only recently. The interested reader is referred to Schröder [215], Schröder & Keip [216], Zäh & Miehe [272] for coupled magneto-electro-mechanics at small, and to Chatzigeorgiou et al. [41], Ponte Castañeda & Galipeau [197], Ponte Castañeda & Siboni [198], Miehe et al. [174], and Keip & Rambausek [111] at large strains. In this field, the mostly homogeneous macro-structure is highly influenced by heterogeneities or physical effects on the micro- or even nano-scale. A prominent example are piezoelectric materials, where the electro-mechanical response is driven by the evolution and motion of electric domains on the microscale. Likewise, the effective response of magnetorheological elastomers, consisting of a soft matrix material with embedded micro- or nano-sized ferromagnetic particles, relies on the micro-magneto-mechanical interactions, see Figure 3.1.

Within this chapter the fundamental concept of representative volume elements is introduced which enables the computation of effective properties based on statistically appropriate periodic unit cells. Assumptions and limitations are summarized. Furthermore, the classical averaging theorem of Hill [94] is extended to coupled magneto-electro-mechanics. The realization of appropriate boundary conditions for the micro-structure is attributed to the *Hill-Mandel macro-homogeneity condition* Hill [91], and Mandel [139] which is extended for dissipative micro-magneto-electro-mechanics.

3.1. The concept of representative volume elements

In the theory of continuum mechanics the principle of local action is employed, which assumes a homogeneous stress and strain distribution within the infinitesimal neighborhood of a material particle. While this concept might hold on a macroscopic body, heterogeneities on the microscopic scale, e.g. inclusions with different material properties, fibers, voids, micro-cracks etc., violate this assumption. To provide additional insight on the material behavior of an infinitesimal macroscopic neighborhood of a particle $\overline{\boldsymbol{X}} \in \overline{\mathcal{B}}$ the concepts of *scale separation and homogenization* of micro-mechanics is motivated. The macroscopic behavior is thereby determined by considering an underlying representative volume element, as introduced in the seminal works of Hill [91], Hashin [85] and Nemat-Nasser & Hori [183]. A fundamental definition of a representative volume element was given by Rodney Hill, as a heterogeneous material volume that is statistically representative for the mixture on average. It has to contain a sufficient amount of micro-inhomogeneities such that any other chosen volume of same size results in equal macroscopic parameters. This leads to the conclusion, that the representative volume element is not unique and numerically advantageous structures can be chosen depending on the related boundary-value-problem, see for instance Michel et al. [155]. A graphical interpretation based on an introduced linearly independent coordinate system $(\boldsymbol{a}_1, \boldsymbol{a}_2)$ for the micro-structure and different possible representative volume elements was given in Schröder [214] and is revisited in Figure 3.2. The reference system has to be chosen such that the structural response is invariant for translations of the form $n_1\boldsymbol{a}_1 + n_2\boldsymbol{a}_2$ with $\{ n_1, n_2 \} \in \mathcal{N}$. This again leads to non-uniqueness of the respective coordinate systems which is covered in Anthoine [3]. Naturally, simple two-phase materials with circular inclusions rarely reflect the true heterogeneous micro-structures, but can be a sufficient assumption to cover characteristic microscopic effects. Utilizing the concept

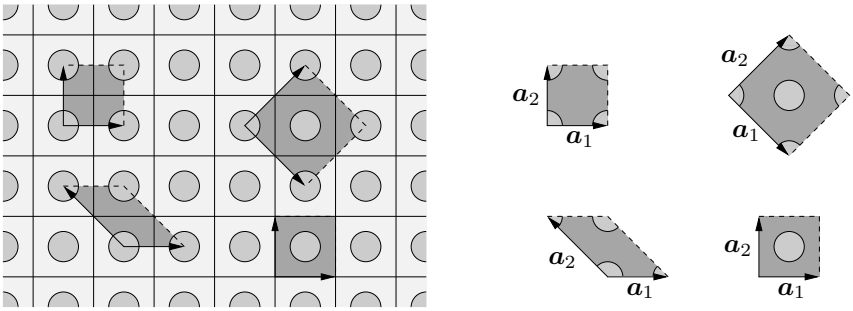

Figure 3.2: *Non-uniqueness of representative volume elements.* Within a heterogeneous, periodic micro-structure, several possible representative volume elements can be chosen, as indicated by the dashed lines. The two linearly independent vectors $\boldsymbol{a}_1$ and $\boldsymbol{a}_2$ build up a local coordinate system to describe the periodicity of the unit cells, see Schröder [214].

of periodic micro-structures it can be advantageous to keep the representative volume element as simple as possible, as the effective response can be computed based on one single periodic cell in a variational setting, see Marcellini [141]. Incorporating studies on microscopic material instabilities in large deformation mechanics, see Müller [178], Schröder [214] and Miehe et al. [169] or more recently in coupled electro-magneto-mechanics Bertoldi & Boyce [18], Bertoldi et al. [20], Michel et al. [157], and Polukhov et al. [196] based on a Bloch-Floquet wave analysis, might lead to enlarged $\mathcal{RVE}$ with respect to a critical wavelength. While the Bloch-Floquet wave analysis is also performed on a single unit cell, enlarged $\mathcal{RVE}$ are necessary to capture the respective instability modes.

Application of the concept of representative volume elements is only valid if a distinction between the macroscopic and microscopic length scale is possible. This requires the microscopic length scale, identifying the size of a representative volume element and determined by the smallest micro-inhomogeneity, to be vastly smaller than the macroscopic length scale which defines the infinitesimal neighborhood

$$l_{micro} \ll l_{macro}\,. \tag{3.1}$$

It is important to note though, that the relative difference of the length scales is of relevance and not their absolute size. The separation of length scales results in two major consequences. First, the macroscopic gradients $\{\,\overline{\boldsymbol{F}}, \overline{\mathbb{E}}, \overline{\mathbb{H}}\,\}$ and dual stress-like fields $\{\,\overline{\boldsymbol{P}}, \overline{\mathbb{D}}, \overline{\mathbb{B}}\,\}$ are constant over the microscopic length scale l_{micro}. Additionally the volume and inertia terms can be eliminated, leading to homogeneous balance equations

$$\mathrm{Div}[\boldsymbol{P}] = \boldsymbol{0}\,, \quad \mathrm{Div}[\mathbb{D}] = 0 \quad \text{and} \quad \mathrm{Div}[\mathbb{B}] = 0 \quad \text{in } \mathcal{B}\,, \tag{3.2}$$

namely balance of linear momentum as well as electric and magnetic Gauss's law without source terms on the microscale.

3.2. Averaging theorems of magneto-electro-mechanics

Following conceptually Hill [93] as well as the works of Nemat-Nasser & Hori [183], and Miehe et al. [168] macroscopic fields can be obtained by surface integrals on the micro-structure, such that $\bar{(\cdot)} := \langle(\cdot)\rangle_{\partial\mathcal{B}} = \frac{1}{|\mathcal{B}|}\int_{\partial\mathcal{B}}(\cdot)\,dA$, where $\bar{(\cdot)}$ corresponds to the

macroscopic counterpart of a microscopic quantity $(\cdot)$, and $\partial\mathcal{B}$ is the boundary of the microscopic body $\mathcal{B}$. Referring to the works of Miehe et al. [174] on coupled magneto-electro-mechanics, the overall deformation gradient and its dual, the Piola-Kirchhoff stress, read

$$\overline{\boldsymbol{F}} := \frac{1}{|\mathcal{B}|}\int_{\partial\mathcal{B}} \boldsymbol{\varphi}\otimes\boldsymbol{N}\,dA \quad \text{and} \quad \overline{\boldsymbol{P}} := \frac{1}{|\mathcal{B}|}\int_{\partial\mathcal{B}} \boldsymbol{T}\otimes\boldsymbol{X}\,dA\,, \tag{3.3}$$

in terms of the boundary displacement $\boldsymbol{\varphi}$ and mechanical boundary traction $\boldsymbol{T}$ on the surface $\partial\mathcal{B}$. In here, $\boldsymbol{N}$ is the referential outward surface normal and $\otimes$ denotes a dyadic product. Similarly, the magnetic contributions, namely the macroscopic magnetic field $\overline{\mathbb{H}}$ and the magnetic induction $\overline{\mathbb{B}}$ are introduced

$$\overline{\mathbb{H}} := -\frac{1}{|\mathcal{B}|}\int_{\partial\mathcal{B}} \phi^m\boldsymbol{N}\,dA \quad \text{and} \quad \overline{\mathbb{B}} := \frac{1}{|\mathcal{B}|}\int_{\partial\mathcal{B}} (\mathbb{B}\cdot\boldsymbol{N})\boldsymbol{X}\,dA\,, \tag{3.4}$$

based on the magnetic scalar potential ϕ^m and the magnetic normal flux $B := -\mathbb{B}\cdot\boldsymbol{N}$. Staying in the mixed energy-enthalpy setting the respective macroscopic electric quantities can be obtained by a straight expansion of the small strain approach of Schröder [215] and Zäh & Miehe [272] such that the macroscopic electric field $\overline{\mathbb{E}}$ and the electric displacements $\overline{\mathbb{D}}$ are defined as

$$\overline{\mathbb{E}} := -\frac{1}{|\mathcal{B}|}\int_{\partial\mathcal{B}} \phi^e\boldsymbol{N}\,dA \quad \text{and} \quad \overline{\mathbb{D}} := \frac{1}{|\mathcal{B}|}\int_{\partial\mathcal{B}} (\mathbb{D}\cdot\boldsymbol{N})\boldsymbol{X}\,dA\,. \tag{3.5}$$

Here, the scalar electric potential ϕ^e and the electric normal flux $D := -\mathbb{D}\cdot\boldsymbol{N}$ are employed. For simple micro-structures without discontinuities it is possible to reformulate (3.3)-(3.5) to a more convenient volume integral representation. The averaged macroscopic magneto-electro-mechanical fields of the mixed energy-enthalpy formulation, obtained by volume integrals, then read

$$\begin{aligned}
\overline{\boldsymbol{F}} &:= \frac{1}{|\mathcal{B}|}\int_{\mathcal{B}} \boldsymbol{F}\,dV\,, & \overline{\boldsymbol{P}} &:= \frac{1}{|\mathcal{B}|}\int_{\mathcal{B}} \boldsymbol{P}\,dV\,,\\
\overline{\mathbb{H}} &:= \frac{1}{|\mathcal{B}|}\int_{\mathcal{B}} \mathbb{H}\,dV\,, \quad \text{and} & \overline{\mathbb{B}} &:= \frac{1}{|\mathcal{B}|}\int_{\mathcal{B}} \mathbb{B}\,dV\,,\\
\overline{\mathbb{E}} &:= \frac{1}{|\mathcal{B}|}\int_{\mathcal{B}} \mathbb{E}\,dV\,, & \overline{\mathbb{D}} &:= \frac{1}{|\mathcal{B}|}\int_{\mathcal{B}} \mathbb{D}\,dV\,.
\end{aligned} \tag{3.6}$$

For completeness the volume averaging for the energy-based variables are also given. Here, next to the macroscopic mechanical deformation gradient $\overline{\boldsymbol{F}}$, the magnetic induction $\overline{\mathbb{B}}$ and electric displacements $\overline{\mathbb{D}}$, obtained by the respective magnetic and electric vector potentials $\boldsymbol{a}^m$ and $\boldsymbol{a}^e$, are the primary driving fields. Consequently, the dual variables are the Piola-Kirchhoff stress tensor, as well as the magnetic and electric field vector. The concept of surface and volume integrals for continuous media is employed, yielding first

$$\begin{aligned}
\overline{\boldsymbol{F}} &:= \frac{1}{|\mathcal{B}|}\int_{\partial\mathcal{B}} \boldsymbol{\varphi}\otimes\boldsymbol{N}\,dA\,, & \overline{\boldsymbol{P}} &:= \frac{1}{|\mathcal{B}|}\int_{\partial\mathcal{B}} \boldsymbol{T}\otimes\boldsymbol{X}\,dA\,,\\
\overline{\mathbb{B}} &:= \frac{1}{|\mathcal{B}|}\int_{\partial\mathcal{B}} \boldsymbol{N}\times\boldsymbol{a}^m\,dA\,, \quad \text{and} & \overline{\mathbb{H}} &:= \frac{1}{2|\mathcal{B}|}\int_{\partial\mathcal{B}} \boldsymbol{X}\times\mathbb{H}_t\,dA\,,\\
\overline{\mathbb{D}} &:= \frac{1}{|\mathcal{B}|}\int_{\partial\mathcal{B}} \boldsymbol{N}\times\boldsymbol{a}^e\,dA\,, & \overline{\mathbb{E}} &:= \frac{1}{2|\mathcal{B}|}\int_{\partial\mathcal{B}} \boldsymbol{X}\times\mathbb{E}_t\,dA\,.
\end{aligned} \tag{3.7}$$

Here, $\times$ is the cross-product and $\{ \mathbb{H}_t \, , \mathbb{E}_t \}$ are the magnetic and electric fields tangential to the boundary of the surface $\partial\mathcal{B}$, respectively. For micro-structures without discontinuities, simplification of (3.7) to volume integrals reveals

$$\begin{aligned} \overline{\boldsymbol{F}} &:= \frac{1}{|\mathcal{B}|} \int_{\mathcal{B}} \boldsymbol{F} \, dV \, , & \overline{\boldsymbol{P}} &:= \frac{1}{|\mathcal{B}|} \int_{\mathcal{B}} \boldsymbol{P} \, dV \, , \\ \overline{\mathbb{B}} &:= \frac{1}{|\mathcal{B}|} \int_{\mathcal{B}} \mathbb{B} \, dV \, , \quad \text{and} & \overline{\mathbb{H}} &:= \frac{1}{|\mathcal{B}|} \int_{\mathcal{B}} \mathbb{H} \, dV \, , \\ \overline{\mathbb{D}} &:= \frac{1}{|\mathcal{B}|} \int_{\mathcal{B}} \mathbb{D} \, dV \, , & \overline{\mathbb{E}} &:= \frac{1}{|\mathcal{B}|} \int_{\mathcal{B}} \mathbb{E} \, dV \, . \end{aligned} \tag{3.8}$$

It is important to note, that these average theorems for the constitutive variables only apply, if the hypotheses of separation of length-scales (3.1), and the resulting homogeneous balance equations, hold. Also, averaging for more complex micro-structures with discontinuities, such as voids or cracks, needs to incorporate additional contributions due to internal boundaries. The reader is referred to Schröder [214] for a detailed analysis.

3.3. The generalized Hill-Mandel macrohomogeneity condition

A Hill-Mandel continuity condition as introduced by Hill [91] and Mandel [139] is extended to the general case of coupled dissipative micro-magneto-electro-mechanics. It states that the macroscopic stress-power has to be equal to the averaged microscopic stress power. This condition allows the formulation of appropriate boundary conditions for the micro-structure and is one of the fundamental principles of computational homogenization. The reader is referred to the works of Schröder [215], Schröder & Keip [216], Zäh & Miehe [272], Keip et al. [115], and Sridhar et al. [235] for a starting point of the macrohomogeneity condition in dissipative electro- and magneto-mechanics. These concepts are now extended to the general case for both the mixed energy-enthalpy and the energetic modeling approach.

The dissipative nature of micro-magnetics and micro-electrics requires a rate-type approach. In a time continuous setting a generalized Hill-Mandel condition is formulated. The phase field order parameters, namely the magnetization $\boldsymbol{\mathcal{M}}$ and the electric polarization $\boldsymbol{\mathcal{P}}$ are treated as internal variables and therefore a separation of macro- and microscopic variables is necessary. While in the mixed energy-enthalpy setting the rate of the primary fields $\{ \dot{\boldsymbol{F}}, \dot{H}, \dot{\mathbb{E}} \}$ as well as the dissipative magnetization and electric polarization with their respective gradient fields $\{ \dot{\boldsymbol{\mathcal{M}}}, \nabla\dot{\boldsymbol{\mathcal{M}}}, \dot{\boldsymbol{\mathcal{P}}}, \nabla\dot{\boldsymbol{\mathcal{P}}} \}$ are prominent on the microscale, only the former mentioned variables have a macroscopic counterpart. The macro- and microscopic state variables can be summarized to be

$$\overline{\mathfrak{c}} := \{ \dot{\overline{\boldsymbol{F}}}, \dot{\overline{H}}, \dot{\overline{\mathbb{E}}} \} \quad \text{and} \quad \mathfrak{c} := \{ \dot{\boldsymbol{F}}, \dot{H}, \dot{\boldsymbol{\mathcal{M}}}, \nabla\dot{\boldsymbol{\mathcal{M}}}, \dot{\mathbb{E}}, \dot{\boldsymbol{\mathcal{P}}}, \nabla\dot{\boldsymbol{\mathcal{P}}} \} \, , \tag{3.9}$$

respectively. Their dual stresses and stress-like fields read

$$\overline{\mathfrak{s}} := \{ \overline{\boldsymbol{P}}, \overline{\mathbb{B}}, \overline{\mathbb{D}} \} \quad \text{and} \quad \mathfrak{s} := \{ \boldsymbol{P}, \mathbb{B}, M, \boldsymbol{\mathfrak{M}}, \mathbb{D}, \mathbb{P}, \boldsymbol{\mathfrak{P}} \} \, . \tag{3.10}$$

These constitutive dual variables are obtained by the derivation of a general energy and dissipation function and are specified in later stages of the work. The Hill-Mandel macro-

homogeneity condition can thus be formulated in a general form

$$\overline{\mathfrak{s}} \cdot \overline{\mathfrak{c}} = \frac{1}{|\mathcal{B}|} \int_{\mathcal{B}} \mathfrak{s} \cdot \mathfrak{c} \, dV \,. \tag{3.11}$$

Here, "$\cdot$" is a general scalar product also valid for tensors of higher order. The Hill-Mandel condition is used to transfer the given macroscopic loading variables to the micro-structure via appropriate boundary conditions, see Hill [94] for the purely mechanical case. In a first step, the right hand side of (3.11) gives

$$\frac{1}{|\mathcal{B}|} \int_{\mathcal{B}} \mathfrak{s} \cdot \mathfrak{c} \, dV = \frac{1}{|\mathcal{B}|} \int_{\partial\mathcal{B}} \boldsymbol{T} \cdot \dot{\boldsymbol{\varphi}} - B\dot{\phi}^m + \boldsymbol{M}^m \cdot \dot{\mathfrak{M}} - D\dot{\phi}^e + \boldsymbol{M}^e \cdot \dot{\mathfrak{P}} \, dA \,, \tag{3.12}$$

with the traction vector $\boldsymbol{T} = \boldsymbol{P} \cdot \boldsymbol{N}$, the magnetic and electric surface flux $B = -\mathbb{B} \cdot \boldsymbol{N}$ and $D = -\mathbb{D} \cdot \boldsymbol{N}$, the magnetic and electric micro-tractions $\boldsymbol{M}^m = \mathfrak{M} \cdot \boldsymbol{N}$ and $\boldsymbol{M}^e = \mathfrak{P} \cdot \boldsymbol{N}$ and the outward unit normal $\boldsymbol{N} \in \partial\mathcal{B}$. Here Gauss' integral theorem is used as well as the Euler-Lagrange equations of the coupled microscopic problem. While most of the parts are obtained in a straight forward manner, the dissipative magnetic part based on the rate of the magnetization and its gradient is explained in detail. Application of Gauss' integral theorem yields

$$\frac{1}{|\mathcal{B}|} \int_{\mathcal{B}} \mathbb{M} \cdot \dot{\mathfrak{M}} + \mathfrak{M} : \nabla\dot{\mathfrak{M}} \, dV = \frac{1}{|\mathcal{B}|} \int_{\mathcal{B}} \mathbb{M} \cdot \dot{\mathfrak{M}} - \mathrm{Div}[\mathfrak{M}] \cdot \dot{\mathfrak{M}} \, dV + \frac{1}{|\mathcal{B}|} \int_{\partial\mathcal{B}} (\mathfrak{M} \cdot \boldsymbol{N}) \dot{\mathfrak{M}} \, dA \,. \tag{3.13}$$

The rate of magnetization can be written as $\dot{\mathfrak{M}} = \dot{\boldsymbol{\Theta}} \times \mathfrak{M}$ with the spin of the magnetization $\dot{\boldsymbol{\Theta}} \in \mathcal{R}^d$, see Keip & Sridhar [114]. Furthermore, the effective magnetic field $\mathbb{H}_{eff} = \mathrm{Div}[\mathfrak{M}] - \mathbb{M}$ is introduced. Insertion into (3.13) yields

$$\frac{1}{|\mathcal{B}|} \int_{\mathcal{B}} \mathbb{M} \cdot \dot{\mathfrak{M}} + \mathfrak{M} : \nabla\dot{\mathfrak{M}} \, dV = -\frac{1}{|\mathcal{B}|} \int_{\mathcal{B}} \mathbb{H}_{eff} \cdot (\dot{\boldsymbol{\Theta}} \times \mathfrak{M}) \, dV + \frac{1}{|\mathcal{B}|} \int_{\partial\mathcal{B}} (\mathfrak{M} \cdot \boldsymbol{N}) \cdot \dot{\mathfrak{M}} \, dA \,. \tag{3.14}$$

We identify the magnetic equilibrium equation given by Brown [33], i.e. $\mathfrak{M} \times \mathbb{H}_{eff} = \boldsymbol{0}$ and obtain the final form

$$\frac{1}{|\mathcal{B}|} \int_{\mathcal{B}} \mathbb{M} \cdot \dot{\mathfrak{M}} + \mathfrak{M} : \nabla\dot{\mathfrak{M}} \, dV = \frac{1}{|\mathcal{B}|} \int_{\partial\mathcal{B}} \boldsymbol{M}^m \cdot \dot{\mathfrak{M}} \, dA \,. \tag{3.15}$$

Starting from (3.11), together with the right hand side of (3.12), boundary conditions that link the macroscopic driving fields to the micro-structure are formulated. In the following, three classes of boundary constraints are in focus:

- (D) Dirichlet: uniform displacement-type with constant magnetization/polarization.
- (N) Neumann: uniform traction-type with zero micro-tractions.
- (P) Periodic: non-trivial periodic primary fields with anti-periodic tractions.

For large scale differences one can split the microscopic deformation and magnetic as well as electric potential into homogeneous macroscopic contributions and superimposed microscale fluctuation fields, such that

$$\dot{\boldsymbol{\varphi}} = \dot{\overline{\boldsymbol{F}}} \cdot \boldsymbol{X} + \dot{\widetilde{\boldsymbol{\varphi}}}, \quad -\dot{\phi}^m = \dot{\overline{\mathbb{H}}} \cdot \boldsymbol{X} - \dot{\widetilde{\phi}}^m \quad \text{and} \quad -\dot{\phi}^e = \dot{\overline{\mathbb{E}}} \cdot \boldsymbol{X} - \dot{\widetilde{\phi}}^e \,. \tag{3.16}$$

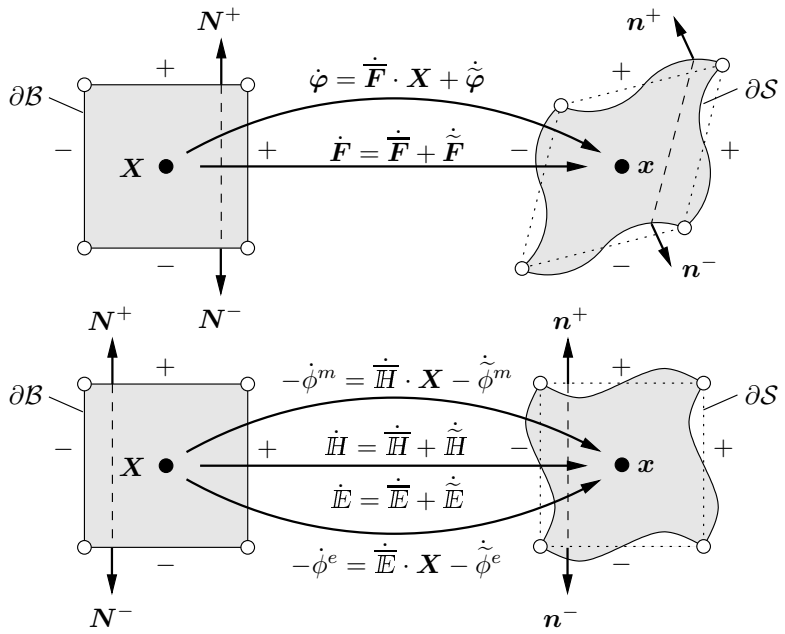

Figure 3.3: *Non-trivial periodic boundary conditions for the micro-structure.* The microscopic rates of deformation, scalar magnetic and scalar electric potential are decomposed into linear macroscopic parts and superimposed fine-scale fluctuations according to $\dot{\boldsymbol{\varphi}} = \overline{\dot{\boldsymbol{F}}} \cdot \boldsymbol{X} + \tilde{\dot{\boldsymbol{\varphi}}}$, $-\dot{\phi}^m = \overline{\dot{\mathbb{H}}} \cdot \boldsymbol{X} - \tilde{\dot{\phi}}^m$ and $-\dot{\phi}^e = \overline{\dot{\mathbb{E}}} \cdot \boldsymbol{X} - \tilde{\dot{\phi}}^e$. Periodic boundary conditions are applied for the superimposed fluctuation fields. Normal vectors on opposite faces '+' and '−' are related by $\boldsymbol{N}^+ = -\boldsymbol{N}^-$ at associated points $\boldsymbol{X}^+ \in \partial\mathcal{B}^+$ and $\boldsymbol{X}^- \in \partial\mathcal{B}^-$.

Note that the magnetization and polarization have no macroscopic counterpart due to the ansatz of internal variables. With this separation and the surface averaging (3.3)-(3.5)$_2$ at hand a reformulation of (3.11) together with (3.12) gives

$$0 = \frac{1}{|\mathcal{B}|} \int_{\partial\mathcal{B}} \boldsymbol{T} \cdot \tilde{\dot{\boldsymbol{\varphi}}} - B\tilde{\dot{\phi}}^m + \boldsymbol{M}^m \cdot \dot{\mathfrak{M}} - D\tilde{\dot{\phi}}^e + \boldsymbol{M}^e \cdot \dot{\mathfrak{P}} \, dA \,. \tag{3.17}$$

Here, all homogeneous macroscopic parts canceled out with the left side of (3.11), i.e. the macroscopic stress power. Replacing the traction-type variables $\boldsymbol{T}, B, D$ with the respective stresses obtained by Cauchy-type theorems, (3.17) can be rewritten together with (3.16) as

$$\begin{aligned} 0 = \; & \frac{1}{|\mathcal{B}|} \int_{\partial\mathcal{B}} (\boldsymbol{P} - \overline{\boldsymbol{P}}) \cdot \boldsymbol{N} \cdot (\dot{\boldsymbol{\varphi}} - \overline{\dot{\boldsymbol{F}}} \cdot \boldsymbol{X}) \, dA \\ & + \frac{1}{|\mathcal{B}|} \int_{\partial\mathcal{B}} (\mathbb{B} - \overline{\mathbb{B}}) \cdot \boldsymbol{N} (\dot{\phi}^m - \overline{\dot{\mathbb{H}}} \cdot \boldsymbol{X}) \, dA + \frac{1}{|\mathcal{B}|} \int_{\partial\mathcal{B}} \boldsymbol{M}^m \cdot \dot{\mathfrak{M}} \, dA \\ & + \frac{1}{|\mathcal{B}|} \int_{\partial\mathcal{B}} (\mathbb{D} - \overline{\mathbb{D}}) \cdot \boldsymbol{N} (\dot{\phi}^e - \overline{\dot{\mathbb{E}}} \cdot \boldsymbol{X}) \, dA + \frac{1}{|\mathcal{B}|} \int_{\partial\mathcal{B}} \boldsymbol{M}^e \cdot \dot{\mathfrak{P}} \, dA \,. \end{aligned} \tag{3.18}$$

The modifications performed above result in two obvious boundary conditions, that are the uniform displacement-type (Dirichlet) and uniform traction-type (Neumann) boundary conditions, together with constant magnetization/polarization and zero micro-tractions

on the surface of the micro-structure

$$(D): \begin{cases} \dot{\boldsymbol{\varphi}} = \dot{\overline{\boldsymbol{F}}} \cdot \boldsymbol{X}, \\ -\dot{\phi}^m = \dot{\overline{\mathbb{H}}} \cdot \boldsymbol{X}, \\ -\dot{\phi}^e = \dot{\overline{\mathbb{E}}} \cdot \boldsymbol{X}, \\ \dot{\mathfrak{M}} = \boldsymbol{0}, \\ \dot{\mathcal{P}} = \boldsymbol{0}, \end{cases} \quad \text{and} \quad (N): \begin{cases} \boldsymbol{T} = \overline{\boldsymbol{P}} \cdot \boldsymbol{N}, \\ -B = \overline{\mathbb{B}} \cdot \boldsymbol{N}, \\ -D = \overline{\mathbb{D}} \cdot \boldsymbol{N}, \\ \boldsymbol{M}^m = \boldsymbol{0}, \\ \boldsymbol{M}^e = \boldsymbol{0}. \end{cases} \tag{3.19}$$

The non-trivial periodic boundary conditions are obtained by an additive decomposition of the full boundary $\partial\mathcal{B}$ into points $\boldsymbol{X}^+ \in \partial\mathcal{B}^+$ and $\boldsymbol{X}^- \in \partial\mathcal{B}^-$. Here, $\boldsymbol{X}^+$ and $\boldsymbol{X}^-$ are corresponding points on opposite boundaries, defined by the outward normals $\boldsymbol{N}^+ = -\boldsymbol{N}^-$, see Figure 3.3. The macro-homogeneity condition can then be reformulated and the non-trivial periodic boundary conditions with anti-periodic traction-type fields read

$$(P): \begin{cases} \dot{\tilde{\boldsymbol{\varphi}}}^+ = \dot{\tilde{\boldsymbol{\varphi}}}^-, \\ \dot{\tilde{\phi}}^{m+} = \dot{\tilde{\phi}}^{m-}, \\ \dot{\tilde{\phi}}^{e+} = \dot{\tilde{\phi}}^{e-}, \\ \dot{\mathfrak{M}}^+ = \dot{\mathfrak{M}}^-, \\ \dot{\mathcal{P}}^+ = \dot{\mathcal{P}}^-, \end{cases} \quad \text{with} \quad \begin{cases} \boldsymbol{T}^+ = -\boldsymbol{T}^-, \\ B^+ = -B^-, \\ D^+ = -D^-, \\ \boldsymbol{M}^{m+} = -\boldsymbol{M}^{m-}, \\ \boldsymbol{M}^{e+} = -\boldsymbol{M}^{e-}. \end{cases} \tag{3.20}$$

Note that zero fluctuation fields on the boundary $\partial\mathcal{B}$ and in the full domain $\mathcal{B}$ also satisfy the Hill-Mandel condition. This is usually referred to as Taylor assumption. Also, periodic boundary conditions are proven to be the most reasonable choice for computational homogenization analysis, even for micro-structures that are not periodic, see Terada et al. [246] and Segurado & Llorca [221].

For a *pure energetic* approach based on magnetic and electric vector potentials for the magnetic induction and electric displacements, a similar structure needs to be followed. No further detail is given here and the appropriate Dirichlet and Neumann boundary conditions of the micro-structure, that satisfy the generalized Hill-Mandel condition, are summarized

$$(D): \begin{cases} \dot{\boldsymbol{\varphi}} = \dot{\overline{\boldsymbol{F}}} \cdot \boldsymbol{X}, \\ \dot{\boldsymbol{a}}^m = \frac{1}{2}\dot{\overline{\mathbb{B}}} \cdot \boldsymbol{X}, \\ \dot{\boldsymbol{a}}^e = \frac{1}{2}\dot{\overline{\mathbb{D}}} \cdot \boldsymbol{X}, \\ \dot{\mathfrak{M}} = \boldsymbol{0}, \\ \dot{\mathcal{P}} = \boldsymbol{0}, \end{cases} \quad \text{and} \quad (N): \begin{cases} \boldsymbol{T} = \overline{\boldsymbol{P}} \cdot \boldsymbol{N}, \\ \mathbb{H}_t = \overline{\mathbb{H}} \times \boldsymbol{N}, \\ \mathbb{E}_t = \overline{\mathbb{E}} \times \boldsymbol{N}, \\ \boldsymbol{M}^m = \boldsymbol{0}, \\ \boldsymbol{M}^e = \boldsymbol{0}. \end{cases} \tag{3.21}$$

Here, the surface integrals (3.7) are used. In analogy to (3.20) the non-trivial periodic boundary conditions with anti-periodic traction-type fields are introduced

$$(P): \begin{cases} \dot{\tilde{\boldsymbol{\varphi}}}^+ = \dot{\tilde{\boldsymbol{\varphi}}}^-, \\ \dot{\tilde{\boldsymbol{a}}}^{m+} = \dot{\tilde{\boldsymbol{a}}}^{m-}, \\ \dot{\tilde{\boldsymbol{a}}}^{e+} = \dot{\tilde{\boldsymbol{a}}}^{e-}, \\ \dot{\mathfrak{M}}^+ = \dot{\mathfrak{M}}^-, \\ \dot{\mathcal{P}}^+ = \dot{\mathcal{P}}^-, \end{cases} \quad \text{with} \quad \begin{cases} \boldsymbol{T}^+ = -\boldsymbol{T}^-, \\ \mathbb{H}^+ = -\mathbb{H}^-, \\ \mathbb{E}^+ = -\mathbb{E}^-, \\ \boldsymbol{M}^{m+} = -\boldsymbol{M}^{m-}, \\ \boldsymbol{M}^{e+} = -\boldsymbol{M}^{e-}. \end{cases} \tag{3.22}$$

Further insight on the formulation of boundary conditions for the mixed energy-enthalpy and pure energy approach for non-dissipative magneto-electro-elasticity can be found in Miehe et al. [174]. In there, a rigorous treatment of a general Hill-Mandel condition for coupled multifield problems is presented.

Chapter 4

Constitutive Inequalities and Convexity

Free energy functions are subjected to several restrictions, leading to *constitutive inequalities*. The reader is referred to Truesdell & Noll [254] for an extensive summary on this topic. In the present context of finite deformations, the requirement of convexity of the free energy function, as applicable in the small strain theories, is not reasonable. This demand is too restrictive due to three main reasons:

1. it indicates uniqueness of solutions and excludes *structural instabilities*, such as buckling or wrinkling of structures, which needs to be describable by large strain theories, Hill [89].

2. it is incompatible with the *principle of material frame-indifference* $\psi(\boldsymbol{F}) = \psi(\boldsymbol{QF})$ demanding the objectivity of the free energy, whatever external frame of reference is used to describe it, Coleman & Noll [46].

3. the determinant of the deformation gradient is constrained by $J := \det[\boldsymbol{F}] > 0$, guaranteeing a positive spatial volume element $dv = JdV$, i.e. no material penetration. The *growth conditions* indicated by the limit $\psi(\boldsymbol{F}) \to \infty$ for a Jacobian $J \to 0$ are violated by a convex free energy, Ball [8].

In Marsden & Hughes [142] a summary of the above mentioned limitations of convexity and the related development and introduction of *weaker convexity conditions* is given. The following sub-chapters provide an overview of physically-based inequalities, as well as strong and weak convexity conditions for the free energy function.

4.1. Existence of solutions

There are mainly two approaches to prove the existence of solutions of variational problems; the *classical* and the *direct* one. In the classical approach, the root of the first variation of the considered functional, also known as Euler-Lagrange equation is checked, and the existence of a root, related to the positiveness of the second variation, is validated, see also Meyberg & Vachenauer [154] and Lanczos [128], among others. The

direct approach for the existence of a minimization principle as given in Dacorogna [47], Nguyen [184] and Silhavý [230, p.377], demands the functional

$$\Pi(\boldsymbol{\varphi}) = \int_{\mathcal{B}} \psi(\boldsymbol{F})\, dV \quad \text{with} \quad \boldsymbol{\varphi} \in \mathcal{W}_{\boldsymbol{\varphi}} \tag{4.1}$$

to be *coercive* and to satisfy the *sequentially weakly lower semicontinuity* condition. A coercive incremental work functional tends to infinity $\Pi(\boldsymbol{\varphi}) \to \infty$, for infinite stretches or compression, i.e. for deformation gradients $\|\boldsymbol{F}\| \to \infty$ or Jacobian $J \to 0$, see Ciarlet [43] or Antman [4] for details. The inequality

$$\lim_{k\to\infty} \inf_{\boldsymbol{\varphi}_k} \Pi(\boldsymbol{\varphi}_k) \geq \Pi(\boldsymbol{\varphi}) \quad \text{for } \boldsymbol{\varphi}_k \rightharpoonup \boldsymbol{\varphi} \tag{4.2}$$

states that the minimum of the energy functional $\Pi(\boldsymbol{\varphi}_k)$ is in the limit always greater than the value of the functional at the solution point $\boldsymbol{\varphi}$ and defines the criterion for sequentially weakly lower semicontinuity. Therefore, existence of solutions of variational principles is related to the convexity of the free energy function. A mathematical definition of convexity and weaker convexity conditions is investigated in the proceeding, and the related restrictions on the free energy function are derived.

4.2. Convexity and uniqueness of solutions

The notion of convexity plays a central role in the theory of finite deformations and provides inequalities for the construction of constitutive material models. It is a sufficient but not necessary criterion of sequential weak lower semicontinuity of the free energy function, Dacorogna [47]. In a first instance consider the convexity of a scalar-valued tensor function, such as the free energy function of a hyperelastic material. Assume now a deformation state defined by the deformation map $\boldsymbol{\varphi} \in \mathcal{W}_{\boldsymbol{\varphi}}$ as the solution of the variational principle

$$\boldsymbol{\varphi} = \arg\left\{ \inf_{\boldsymbol{\varphi}\in\mathcal{W}_{\boldsymbol{\varphi}}} \Pi(\boldsymbol{\varphi}) \right\} . \tag{4.3}$$

In other words, $\boldsymbol{\varphi}$ is assumed to be the equilibrium state of the energy functional (4.1). This solution is called *unique* and *globally stable* if, for any kinematically admissible perturbation $\Delta\boldsymbol{\varphi}$, the energy increases such that

$$\Pi(\boldsymbol{\varphi} + \Delta\boldsymbol{\varphi}) \geq \Pi(\boldsymbol{\varphi}) . \tag{4.4}$$

The deformation state $\boldsymbol{\varphi}$ is then called a global minimizer of the functional. From the latter constraint, we conclude $\int_{\mathcal{B}}(\psi(\boldsymbol{F} + \Delta\boldsymbol{F}) - \psi(\boldsymbol{F}))\, dV \geq 0$, which can be traced back to the local *convexity statement*

$$\psi(\boldsymbol{F} + \lambda\Delta\boldsymbol{F}) \leq \lambda\psi(\boldsymbol{F} + \Delta\boldsymbol{F}) + (1-\lambda)\psi(\boldsymbol{F}) \quad \forall\ 0 \leq \lambda \leq 1 \tag{4.5}$$

Graphically speaking, this inequality demands that each line connecting the two points $(\boldsymbol{F}, \psi(\boldsymbol{F}))$ and $(\boldsymbol{F} + \Delta\boldsymbol{F}, \psi(\boldsymbol{F} + \Delta\boldsymbol{F}))$ needs to be above the curve ψ, see Figure 4.1a. It is said to be *strictly convex* if $\leq$ is replaced by $<$. A reformulation of equation (4.5) yields

$$\psi(\boldsymbol{F} + \lambda\Delta\boldsymbol{F}) - \psi(\boldsymbol{F}) \leq \lambda[\psi(\boldsymbol{F} + \Delta\boldsymbol{F}) - \psi(\boldsymbol{F})] . \tag{4.6}$$

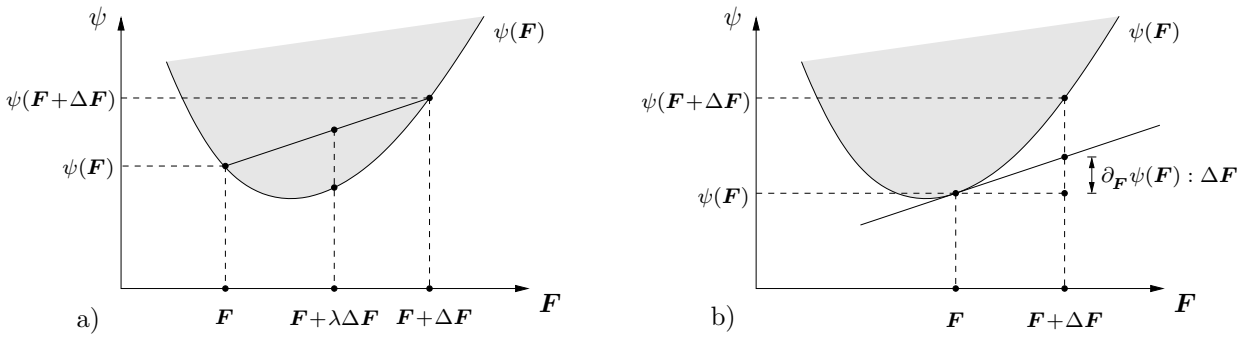

Figure 4.1: *Convexity of the free energy function.* a) Each line connecting the two points $(\boldsymbol{F}, \psi(\boldsymbol{F}))$ and $(\boldsymbol{F}+\Delta\boldsymbol{F}, \psi(\boldsymbol{F}+\Delta\boldsymbol{F}))$ needs to be above the curve ψ, see (4.5). b) The value of the free energy $\psi(\boldsymbol{F}+\Delta\boldsymbol{F})$ evaluated at the deformation state $\boldsymbol{F}+\Delta\boldsymbol{F}$ needs to be higher or at least equal to the tangent $\partial_{\boldsymbol{F}}\psi(\boldsymbol{F})$ for the convexity condition (4.8).

Here, we can identify for the limit case $\lambda \to 0$, by a Gâteaux derivative of the free energy function ψ with respect to its argument $\boldsymbol{F}$ the following expression

$$\lim_{\lambda\to 0} \frac{1}{\lambda}\big[\psi(\boldsymbol{F}+\lambda\Delta\boldsymbol{F}) - \psi(\boldsymbol{F})\big] =: \frac{d}{d\lambda}\psi(\boldsymbol{F}+\lambda\Delta\boldsymbol{F})\Big|_{\lambda=0} = \partial_{\boldsymbol{F}}\psi(\boldsymbol{F}) : \Delta\boldsymbol{F} \,. \tag{4.7}$$

This yields together with (4.6) an alternative representation of convexity

$$\psi(\boldsymbol{F}) + \partial_{\boldsymbol{F}}\psi(\boldsymbol{F}) : \Delta\boldsymbol{F} \leq \psi(\boldsymbol{F}+\Delta\boldsymbol{F}) \,. \tag{4.8}$$

A graphical interpretation of this criterion can be found in Figure 4.1b. The value of the free energy evaluated at the perturbed deformation state $\boldsymbol{F}+\Delta\boldsymbol{F}$ needs to be higher than the tangent $\partial_{\boldsymbol{F}}\psi(\boldsymbol{F})$ to $\psi(\boldsymbol{F})$ evaluated at $\boldsymbol{F}+\Delta\boldsymbol{F}$. Note that $\boldsymbol{P}(\boldsymbol{F}) := \partial_{\boldsymbol{F}}\psi(\boldsymbol{F})$ is the first Piola stress tensor. In a final reformulation in terms of the two arguments $\boldsymbol{F}_1$ and $\boldsymbol{F}_2$, (4.8) yields the two statements

$$\psi(\boldsymbol{F}_1) + \partial_{\boldsymbol{F}}\psi(\boldsymbol{F}_1) : (\boldsymbol{F}_2 - \boldsymbol{F}_1) \leq \psi(\boldsymbol{F}_2) \quad \text{and} \quad \psi(\boldsymbol{F}_2) + \partial_{\boldsymbol{F}}\psi(\boldsymbol{F}_2) : (\boldsymbol{F}_1 - \boldsymbol{F}_2) \leq \psi(\boldsymbol{F}_1) \,. \tag{4.9}$$

Addition of both inequalities yields an equivalent convexity condition

$$[\partial_{\boldsymbol{F}}\psi(\boldsymbol{F}_1) - \partial_{\boldsymbol{F}}\psi(\boldsymbol{F}_2)] : (\boldsymbol{F}_1 - \boldsymbol{F}_2) \geq 0 \,. \tag{4.10}$$

Rewriting this inequality as $[\partial_{\boldsymbol{F}}\psi(\boldsymbol{F}+\lambda\Delta\boldsymbol{F}) - \partial_{\boldsymbol{F}}\psi(\boldsymbol{F})] : \Delta\boldsymbol{F} \geq 0$, and performing the same procedure as in (4.7), gives for twice differentiable free energy functions ψ a third equivalent *infinitesimal convexity condition*

$$\Delta\boldsymbol{F} : \partial^2_{\boldsymbol{F}\boldsymbol{F}}\psi(\boldsymbol{F}) : \Delta\boldsymbol{F} \geq 0 \tag{4.11}$$

demanding the *positive semidefiniteness* of the tangent operator $\mathbb{C} := \partial^2_{\boldsymbol{F}\boldsymbol{F}}\psi(\boldsymbol{F})$. This criterion tends to be the most useful representation of convexity with respect to numerical treatment. Note though that the three convexity conditions of scalar-valued tensor functions (4.5), (4.8) and (4.11) are all equivalent. As outlined in the beginning of this chapter, convexity of the free energy function is too restrictive in the context of finite deformations, such that weaker criteria were developed and summarized in the following.

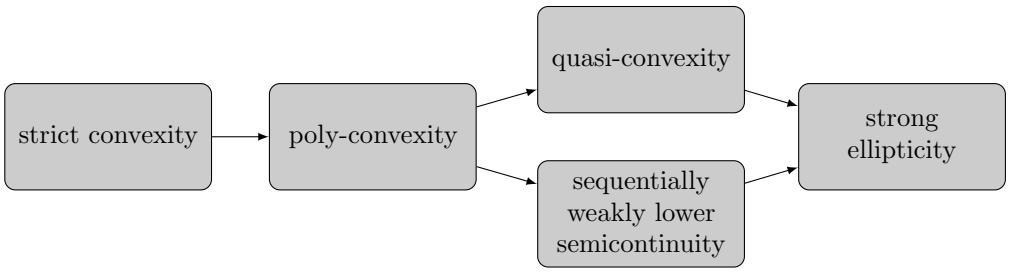

Figure 4.2: *Legendre-Hadamard strong ellipticity condition.* The chain of implication identifies quasi-convexity and sequentially weakly lower semicontinuity as necessary and sufficient conditions for strong ellipticity.

4.3. Weaker convexity: Poly-, quasi- and rank-one convexity

Due to the strong restrictions convexity of the free energy function places on the description of physical material behavior, *weaker convexity statements*, circumventing this drawback, are summarized in the following. Conditions for *poly-convexity*, *quasi-convexity* and *rank-one convexity*, as well as sufficient and necessary conditions for sequentially weakly lower semicontinuity of the energy functional are outlined.

4.3.1. Poly-convexity

The notion of poly-convexity was introduced by Ball [9], and is a less restrictive and sufficient condition for sequentially weakly lower semicontinuity. It is a pointwise check of the free energy function in comparison to the tedious integral statement of quasi-convexity, which will be discussed in the next sub-chapter. Related to (4.8), a poly-convex function is convex with respect to an *extended list of arguments* $\boldsymbol{\xi} := \{\boldsymbol{F}, \operatorname{cof}[\boldsymbol{F}], \det[\boldsymbol{F}]\}$ if

$$\psi(\boldsymbol{\xi}) + \partial_{\boldsymbol{F}}\psi(\boldsymbol{\xi}) : \Delta\boldsymbol{F} + \partial_{\operatorname{cof}[\boldsymbol{F}]}\psi(\boldsymbol{\xi}) : \Delta \operatorname{cof}[\boldsymbol{F}] + \partial_J\psi(\boldsymbol{\xi})\Delta J \leq \psi(\boldsymbol{\xi} + \Delta\boldsymbol{\xi})\,. \tag{4.12}$$

Therefore, poly-convexity is a *local demand* on the free energy function at every material point $\boldsymbol{X} \in \mathcal{B}$. In contrast to convexity, the poly-convexity condition (4.12) does not violate physical principles. Various poly-convex material models exist, such as neo-Hookean, Mooney-Rivlin, or Ogden materials, among others, see Ciarlet [43] for a summary. Note further that poly-convexity is a sufficient condition for quasi-convexity and thus also for sequentially weakly lower semicontinuity, see Figure 4.2.

4.3.2. Quasi-convexity

Quasi-convexity is the fundamental weak convexity condition to proof the existence of solutions for variational problems and was introduced by Morrey [175]. The quasi-convexity condition, for an arbitrary part of the body $\mathcal{D} \subset \mathcal{B}$ of a solid, reads

$$\frac{1}{|\mathcal{D}|}\int_{\mathcal{D}} \psi(\boldsymbol{F} + \nabla\widehat{\boldsymbol{\varphi}})\, dV \geq \psi(\boldsymbol{F})\,, \tag{4.13}$$

with a homogeneous deformation gradient $\boldsymbol{F}$ as well as fluctuations $\widehat{\boldsymbol{\varphi}}$ with compact support $\widehat{\boldsymbol{\varphi}} = \boldsymbol{0}$ on $\partial\mathcal{D}$. It demands that among all possible deformations, with compact support on $\partial\mathcal{D}$, the homogeneous deformation $\boldsymbol{F}$ provides an absolute minimizer of the

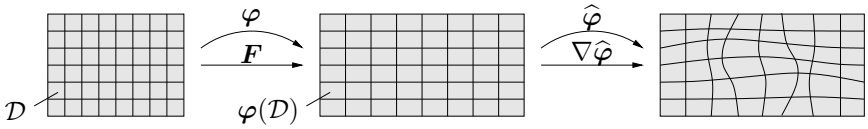

Figure 4.3: *Quasi-convexity condition.* Among all possible deformations with compact support on $\partial\mathcal{D}$, the homogeneous deformation $\boldsymbol{F}$ provides an absolute minimizer of the functional ψ. The homogeneous deformation gradient is denoted by $\boldsymbol{F} = \nabla\boldsymbol{\varphi}$ and $\widehat{\boldsymbol{\varphi}}$ are the fluctuations with $\widehat{\boldsymbol{\varphi}} = \boldsymbol{0}$ on $\partial\mathcal{D}$.

functional ψ, see Figure 4.3 for a graphical interpretation of the condition. Morrey [175] showed that under suitable growth conditions quasi-convexity is a necessary and sufficient condition for a functional to be weakly lower semicontinuous implicating to have at least one global minimizer, Dacorogna [47]. An infinitesimal quasi-convexity criterion for twice differentiable free energy functions ψ was proposed by Krawietz [124]. It is possible to expand the left hand side of (4.13) by a Taylor series truncated after the quadratic term

$$\int_{\mathcal{D}} \psi(\boldsymbol{F} + \nabla\widehat{\boldsymbol{\varphi}})\, dV \approx \int_{\mathcal{D}} \{\psi(\boldsymbol{F}) + \partial_{\boldsymbol{F}}\psi(\boldsymbol{F}) : \nabla\widehat{\boldsymbol{\varphi}} + \tfrac{1}{2}\nabla\widehat{\boldsymbol{\varphi}} : \partial^2_{\boldsymbol{F}\boldsymbol{F}}\psi(\boldsymbol{F}) : \nabla\widehat{\boldsymbol{\varphi}}\}\, dV \ . \quad (4.14)$$

The weak form of the fluctuation boundary condition $\widehat{\boldsymbol{\varphi}} = \boldsymbol{0}$ at the surface $\partial\mathcal{D}$ yields, by application of the Gauss theorem, $\int_{\mathcal{D}} \nabla\widehat{\boldsymbol{\varphi}}\, dV = \boldsymbol{0}$. With the latter two results at hand and the homogeneous deformation gradient, it follows by insertion of (4.14) into (4.13) the *infinitesimal quasi-convexity condition*

$$\int_{\mathcal{D}} \nabla\widehat{\boldsymbol{\varphi}} : \partial^2_{\boldsymbol{F}\boldsymbol{F}}\psi(\boldsymbol{F}) : \nabla\widehat{\boldsymbol{\varphi}}\, dV \geq 0 \ . \quad (4.15)$$

The drawback of both quasi-convexity conditions is their integral form. Note that for a fixed region $\mathcal{D}$, the quasi-convexity condition (4.13) represents the principle of minimum potential energy for the free energy function ψ under homogeneous Dirichlet boundary conditions. Violation would lead to an inhomogeneous state reducing the energy of the system under consideration, also called *interior buckling* (Truesdell & Noll [254, pp.129f]).

4.3.3. Rank-one convexity and strong ellipticity

To circumvent the drawback of quasi-convexity rank-one convexity is introduced as a direct consequence. It is the weakest of all convexity statements and describes local material stability against rank-one perturbations $\Delta\widehat{\boldsymbol{F}} := \boldsymbol{a} \otimes \boldsymbol{N}$, i.e.

$$\psi(\boldsymbol{F} + \lambda\boldsymbol{a} \otimes \boldsymbol{N}) \leq \lambda\psi(\boldsymbol{F} + \boldsymbol{a} \otimes \boldsymbol{N}) + (1 - \lambda)\psi(\boldsymbol{F}) \quad \forall\ 0 \leq \lambda \leq 1 \ , \quad (4.16)$$

where $\boldsymbol{a}$ and $\boldsymbol{N}$ are arbitrary intensities and directions, see Ball [9] and Figure 4.4 for a graphical representation. If the free energy function ψ is continuously differentiable, we obtain in analogy to (4.8) a second statement

$$\psi(\boldsymbol{F}) + \partial_{\boldsymbol{F}}\psi(\boldsymbol{F}) : (\boldsymbol{a} \otimes \boldsymbol{N}) \leq \psi(\boldsymbol{F} + \boldsymbol{a} \otimes \boldsymbol{N}) \ . \quad (4.17)$$

For twice differentiable functions, a result, achieved after suitable mathematical transformations, is the *infinitesimal rank-one convexity condition*

$$(\boldsymbol{a} \otimes \boldsymbol{N}) : \partial^2_{\boldsymbol{F}\boldsymbol{F}}\psi(\boldsymbol{F}) : (\boldsymbol{a} \otimes \boldsymbol{N}) \geq 0 \quad (4.18)$$

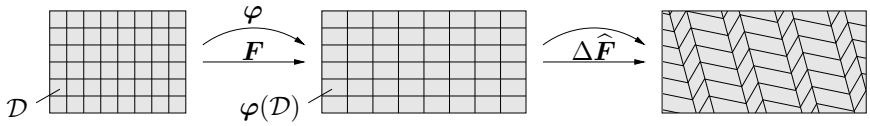

Figure 4.4: *Rank-one convexity condition.* It describes local material stability regarding the formation of first order laminates due to the rank-one perturbations $\Delta\widehat{\boldsymbol{F}} = \boldsymbol{a} \otimes \boldsymbol{N}$. The infinitesimal statement $(\boldsymbol{a} \otimes \boldsymbol{N}) : \partial^2_{\boldsymbol{F}\boldsymbol{F}}\psi(\boldsymbol{F}) : (\boldsymbol{a} \otimes \boldsymbol{N}) \geq 0$ is identical to the Legendre-Hadamard strong ellipticity condition.

which is exactly the *Legendre-Hadamard strong ellipticity condition*, Hadamard [82]. Following Marsden & Hughes [142, p.19] strong ellipticity is the fundamental condition needed to frame a theory of existence and uniqueness of solutions for elastostatics and elastodynamics. If the free energy function is twice differentiable, the subsequent statements can be summarized:

1. rank-one convexity of ψ is equivalent to the Legendre-Hadamard condition,
2. quasi-convexity guarantees rank-one convexity subjected to additional growth conditions, see Morrey [175],
3. strong ellipticity induces rank-one convexity.

The Legendre-Hadamard strong ellipticity condition (4.18) can furthermore be written as

$$\boldsymbol{a} \cdot \boldsymbol{Q}(\boldsymbol{N}) \cdot \boldsymbol{a} \geq 0 \quad \text{with} \quad \boldsymbol{Q} := \partial^2_{\boldsymbol{F}\boldsymbol{F}}\psi(\boldsymbol{F}) \overset{2}{\cdot} \boldsymbol{N} \overset{4}{\cdot} \boldsymbol{N}\,, \tag{4.19}$$

demanding *positive semidefiniteness* of the *acoustic tensor* $\boldsymbol{Q}$. Strong ellipticity guarantees that the time-dependent Euler-Lagrange equation $\mathrm{Div}[\partial_{\boldsymbol{F}}\psi(\boldsymbol{F})] = \varrho_0\ddot{\boldsymbol{\varphi}}$ of the variational minimization (4.3) are strongly elliptic, i.e. a wave propagation with real wave speed is ensured, see Truesdell & Noll [254] and Ogden [185]. Investigating the linearization of the local balance of linear momentum at an equilibrium state with solution $\boldsymbol{\varphi} = \boldsymbol{\varphi}^0$ and constant deformation gradient $\boldsymbol{F}^0 = \nabla\boldsymbol{\varphi}^0$ gives

$$\mathrm{Div}[\partial_{\boldsymbol{F}}\psi(\boldsymbol{F}^0) + \partial^2_{\boldsymbol{F}\boldsymbol{F}}\psi(\boldsymbol{F}^0) : \Delta\boldsymbol{F}] = \varrho_0(\ddot{\boldsymbol{\varphi}}^0 + \Delta\ddot{\boldsymbol{\varphi}})\,. \tag{4.20}$$

Due to the initial assumption that $\boldsymbol{\varphi}^0$ is an equilibrium state, (4.20) reduces to

$$\mathrm{Div}[\partial^2_{\boldsymbol{F}\boldsymbol{F}}\psi(\boldsymbol{F}^0) : \Delta\boldsymbol{F}] = \varrho_0\Delta\ddot{\boldsymbol{\varphi}} \tag{4.21}$$

with the elasticity tensor $\mathbb{C} = \partial^2_{\boldsymbol{F}\boldsymbol{F}}\psi(\boldsymbol{F})$, see Marsden & Hughes [142, p.19]. Performing an ansatz for traveling waves $\boldsymbol{\varphi}(\boldsymbol{X}, t) = \boldsymbol{a}f(\boldsymbol{X} \cdot \boldsymbol{N} - ct)$ with amplitude $\boldsymbol{a}$, direction $\boldsymbol{N}$ as well as wave speed c and inserting the material and time derivative of this approach into (4.21), results in

$$[\boldsymbol{Q} - \varrho_0 c^2\,\boldsymbol{1}] \cdot \boldsymbol{a} = \boldsymbol{0} \quad \text{with} \quad \boldsymbol{Q} := \partial^2_{\boldsymbol{F}\boldsymbol{F}}\psi(\boldsymbol{F}) \overset{2}{\cdot} \boldsymbol{N} \overset{4}{\cdot} \boldsymbol{N} \tag{4.22}$$

assuming arbitrary wave functions f. Truesdell & Noll [254, p.268] call this equation the propagation condition. Furthermore, $\boldsymbol{a}$ is identified as the eigenvector of the acoustic tensor $\boldsymbol{Q}$ with $\varrho_0 c^2$ being its eigenvalue. Note that $(\overset{2}{\cdot})$ refers to a summation over the

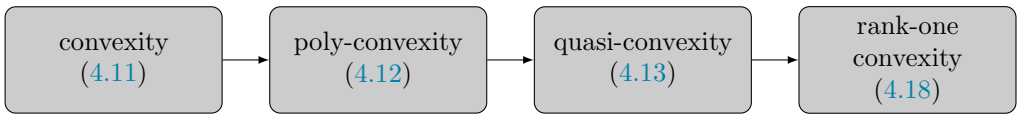

Figure 4.5: *Hierarchy of convexity conditions.* The indicated convexity conditions for a continuous function ψ may be interpreted as evaluated at a specific point of the body (convexity, poly-convexity, rank-1-convexity) or as global conditions on the whole body (quasi-convexity).

second index in Einstein's summation convention. A non-trivial solution is obtained by the conditional equation for the eigenvalues

$$\det[\boldsymbol{Q} - \varrho_0 c^2 \boldsymbol{1}] = 0 \ . \tag{4.23}$$

Multiplication of (4.22) with $\boldsymbol{a}$ gives $\boldsymbol{a} \cdot \boldsymbol{Q}(\boldsymbol{N}) \cdot \boldsymbol{a} = \varrho_0 c^2 \boldsymbol{a} \cdot \boldsymbol{a}$. Only *positive eigenvalues* $\varrho_0 c^2$ of the acoustic tensor $\boldsymbol{Q}$ for all directions $\boldsymbol{N}$ induce *strong ellipticity* of (4.21) and serve as a check for rank-one convexity

$$\varrho_0 c^2 \begin{cases} > 0 & \text{strict rank-one convex} \\ \leq 0 & \text{not strict rank-one convex} \end{cases} \tag{4.24}$$

It is equivalent to Hadamard's fundamental theorem of waves, i.e. that real wave speeds guarantee the infinitesimal stability of the material. An algorithmic criterion for rank-one convexity bases on (4.23) and finds the critical material direction $\boldsymbol{N}$ in which microstructures are formed. For two-dimensional problems, the orientation space can be discretized by an angle θ such that $\boldsymbol{N}(\theta) = [\cos\theta \ \ \sin\theta]^T$. This yields the nonlinear optimization problem

$$\inf_{\theta} \left\{ \det[\boldsymbol{Q}(\theta)] \right\} \begin{cases} > 0 & \text{strict rank-one convex} \\ \leq 0 & \text{not strict rank-one convex} \end{cases} \tag{4.25}$$

for the angle θ minimizing the determinant of the acoustic tensor. Further details are given in Miehe & Schröder [166], Miehe et al. [169], Miehe & Lambrecht [164], or Ortiz et al. [188]. The occurrence of material instabilities in the sense of (4.25), i.e. $\det[\boldsymbol{Q}] < 0$, induces a failure of ellipticity and consequently the development of jump discontinuities of the deformation gradient along a singular surface with normal direction $\boldsymbol{N}$. This concept of material instability is the basis of further investigations in coupled magneto-electro-mechanics in Chapter 7.

4.3.4. Summary of weak convexity statements

The four previously discussed convexity statements of the free energy function ψ are related as shown in Figure 4.5. The arrows can be interpreted such that the stronger convexity condition always induces the weaker ones. In contrast, the inverse relationships are not valid in general. The requirement for convexity implies stability regarding arbitrary perturbations $\Delta\widehat{\boldsymbol{F}}$ and guarantees the existence of solutions for the price of non-physical uniqueness. The weaker statement of poly-convexity asks for stability undergoing combined perturbations of line, area and volume elements. Quasi-convexity on the other hand is an integral statement demanding stability with respect to internal fluctuations $\widehat{\boldsymbol{\varphi}}$ with compact support $\widehat{\boldsymbol{\varphi}} = \boldsymbol{0}$ on the surface $\partial\mathcal{D}$ of an arbitrary part of the body. The difficulty

is its integral character, leading to the definition of rank-one convexity, that requires stability regarding the formation of first-order laminates due to the rank-one perturbation $\Delta\widehat{\boldsymbol{F}} = \boldsymbol{a} \otimes \boldsymbol{N}$.

Quasi-convexity of the free energy function turns out to be a sufficient and necessary condition of sequentially weakly lower semicontinuity of an energy functional. Thus it is considered as the key condition in the analysis of local material stability. Failing the criterion of rank-one convexity implies a loss of quasi-convexity and, thus, the existence of sufficiently regular minimizers.

Chapter 5

Variational Principle of Gradient-Extended Dissipative Solids

Homogenization techniques are used to accurately incorporate microscopic effects on the effective material response. Modeling of multiphysics material such as piezoelectrics, magnetorheological elastomers or fully coupled magneto-electro-elastic composites can be based on variational principles, that give in a canonical form the governing equations of the homogenization principle. The work on rate-type incremental variational principles for dissipative magneto-electro-mechanics at large strains is an extension of the theories suggested by Miehe [158], Lahellec & Suquet [127], and Brassart et al. [28] for purely mechanical problems and the respective literature on micro-magneto and micro-electro-mechanics Zäh & Miehe [272], Miehe & Ethiraj [163], Ethiraj [66], and Sridhar et al. [235]. This chapter provides a general variational principle for *elastic macroscopic* and *dissipative microscopic* response based on a material theory of grade one. For the macro-structure the mechanical deformation and a generalized scalar potential is introduced, and the obtained governing equations serve as a template for the formulation of partially or fully coupled multiphase magneto-electro-elastic composites. Likewise, on the micro-structure the deformation, a scalar potential and a generalized phase field order parameter with their respective gradients are introduced. To satisfy the principle of material frame invariance a set of objective constitutive state variables is deduced and the time-continuous as well as the time-discrete generalized variational principle is derived. Note that in the same manner, variational principles for vector potential approaches can be formulated. However, the more convenient method bases on a mixed energy-enthalpy formulation, i.e. scalar potential is presented here.

5.1. Incremental variational framework on the macroscale

The macroscopic problem is described by a mixed energy-enthalpy function where the related saddle-point variational principle provides the necessary equations for the solution of a boundary value problem on the macroscale. In a general way the variational principle is introduced which can then be used for a standard finite element solution of a full FE^2 approach based on a nested iteration scheme.

5.1.1. Generalized multifield state variables

A simple two-field formulation for the macro-structure is assumed, where no time dependent effects are apparent. The state variables are the macroscopic deformation $\overline{\boldsymbol{\varphi}}$ and a macroscopic scalar potential $\overline{\phi}$. A material theory of grade one is employed incorporating the respective gradient fields, such that the macroscopic state reads

$$\overline{\mathfrak{c}}_0 := \{\, \overline{\boldsymbol{\varphi}},\, \overline{\nabla}\overline{\boldsymbol{\varphi}},\, \overline{\phi},\, \overline{\nabla\phi}\,\}\,. \tag{5.1}$$

Here, $\overline{\nabla} = \overline{\nabla}_{\boldsymbol{X}}$ is the Lagrangian gradient. An energy functional is introduced related to the energy stored in the body and surrounding space for elastic deformations

$$\overline{\mathfrak{E}}(\overline{\boldsymbol{\varphi}}, \overline{\phi}) := \int_{\overline{\mathcal{V}}} \overline{\psi}(\overline{\mathfrak{c}}_0)\, dV\,. \tag{5.2}$$

For heterogeneous solids, the energy storage function also depends on the position $\overline{\boldsymbol{X}} \in \overline{\mathcal{V}}$, which is dropped for compactness.

5.1.2. Concept of material frame invariance and reduced states

Material models need to be invariant with regard to changes of the observer, mathematically described by superimposed rigid body motions onto the state variables of the energy function $\overline{\psi}$ such that

$$\overline{\mathfrak{c}}_0^{+} := \{\, \boldsymbol{Q}(t)\overline{\boldsymbol{\varphi}} + \boldsymbol{c}(t),\, \boldsymbol{Q}(t)\overline{\nabla}\overline{\boldsymbol{\varphi}},\, \overline{\phi} + c(t),\, \overline{\nabla\phi}\,\}\,, \tag{5.3}$$

with the superimposed time-dependent proper orthogonal rotation tensor $\boldsymbol{Q}(t) \in SO(d)$, a time-dependent translation vector $\boldsymbol{c}(t)$ and a scalar shift $c(t)$. Thus, the stored energy is constrained to satisfy the objectivity condition

$$\overline{\psi}^{+}(\overline{\mathfrak{c}}_0^{+}) = \overline{\psi}(\overline{\mathfrak{c}}_0) \quad \forall\, \boldsymbol{Q} \in SO(d)\,. \tag{5.4}$$

This results in a reduced set of objective state variables

$$\overline{\mathfrak{c}} := \{\, \overline{\boldsymbol{C}},\, \overline{\nabla\phi}\,\} \tag{5.5}$$

The energy storage function therefore needs to be formulated in terms of the objective state variables $\overline{\psi}(\overline{\mathfrak{c}})$.

5.1.3. Generalized variational principle

The macroscopic potential is formulated in terms of the elastic energy storage functional and the external mechanical loading contribution

$$\overline{\Pi}(\overline{\boldsymbol{\varphi}}, \overline{\phi}) := \overline{\mathfrak{E}}(\overline{\boldsymbol{\varphi}}, \overline{\phi}) - \overline{\Pi}_{ext}(\overline{\boldsymbol{\varphi}}) \quad \text{with} \quad \overline{\Pi}_{ext}(\overline{\boldsymbol{\varphi}}) = \int_{\overline{\mathcal{V}}} \overline{\boldsymbol{\gamma}}^{m} \cdot \overline{\boldsymbol{\varphi}}\, dV + \int_{\partial\overline{\mathcal{B}}_{\overline{\boldsymbol{T}}}} \overline{\boldsymbol{T}} \cdot \overline{\boldsymbol{\varphi}}\, dA\,. \tag{5.6}$$

Note that full Dirichlet conditions for the scalar field $\overline{\phi}$ are assumed, so no external work contribution is necessary. The macroscopic potential can be reformulated in terms of the macroscopic internal potential per unit undeformed volume, such that

$$\overline{\Pi}(\overline{\boldsymbol{\varphi}}, \overline{\phi}) := \int_{\overline{\mathcal{V}}} \overline{\pi}(\overline{\mathfrak{c}})\, dV - \overline{\Pi}_{ext}(\overline{\boldsymbol{\varphi}}) \quad \text{with} \quad \overline{\pi}(\overline{\mathfrak{c}}) := \overline{\psi}(\overline{\mathfrak{c}})\,. \tag{5.7}$$

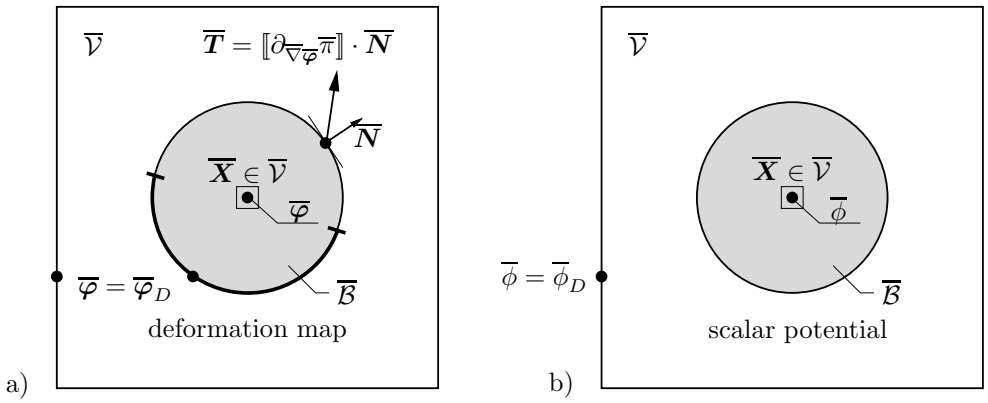

Figure 5.1: *Macroscopic fields and boundary conditions.* a) The deformation map $\overline{\boldsymbol{\varphi}}$ is defined in the macroscopic space $\overline{\mathcal{V}}$. The boundary of the body $\overline{\mathcal{B}} \subset \overline{\mathcal{V}}$ is separated $\partial\overline{\mathcal{B}} = \partial\overline{\mathcal{B}}_{\overline{\boldsymbol{\varphi}}} \cup \partial\overline{\mathcal{B}}_{\overline{\boldsymbol{T}}}$ into prescribed Dirichlet conditions and a Neumann-type jump. b) The generalized scalar potential $\overline{\phi}$ is defined in the full space $\overline{\mathcal{V}} \subset \mathcal{R}^3$. The boundary conditions are of full Dirichlet type.

The independent objective variables on the macroscale can then be obtained by a two-field saddle-point variational principle

$$\{\,\overline{\boldsymbol{\varphi}}, \overline{\phi}\,\} = \arg\Big\{ \inf_{\overline{\boldsymbol{\varphi}} \in \overline{\mathcal{W}}_{\overline{\boldsymbol{\varphi}}}} \sup_{\overline{\phi} \in \overline{\mathcal{W}}_{\overline{\phi}}} \overline{\Pi}(\overline{\boldsymbol{\varphi}}, \overline{\phi}) \Big\} \tag{5.8}$$

based on the macroscopic potential $\overline{\pi}$ per unit undeformed volume, the admissible spaces defined by the Dirichlet conditions

$$\overline{\mathcal{W}}_{\overline{\boldsymbol{\varphi}}} := \{\overline{\boldsymbol{\varphi}} \mid \overline{\boldsymbol{\varphi}} = \overline{\boldsymbol{\varphi}}_D \text{ on } \partial\overline{\mathcal{B}}_{\overline{\boldsymbol{\varphi}}} \text{ and } \partial\overline{\mathcal{V}}\} \quad \text{and} \quad \overline{\mathcal{W}}_{\overline{\phi}} := \{\overline{\phi} \mid \overline{\phi} = \overline{\phi}_D \text{ on } \partial\overline{\mathcal{V}}\}\,. \tag{5.9}$$

and the mechanical external loading contribution. For a graphical interpretation of the macroscopic primary field and their respective Dirichlet and Neumann conditions see Figure 5.1. For the generalized scalar potential we assume pure Dirichlet boundary conditions on the boundary $\partial\overline{\mathcal{V}}$. Further detail on this specific choice is given in later chapters. Setting the variation of the potential (5.7) to zero

$$\begin{aligned} \delta\overline{\Pi}(\overline{\boldsymbol{\varphi}}, \overline{\phi}) := \; & -\int_{\overline{\mathcal{V}}} \big(\overline{\mathrm{Div}}[\partial_{\overline{\nabla\boldsymbol{\varphi}}}\overline{\pi}] + \overline{\boldsymbol{\gamma}}^m\big) \cdot \delta\overline{\boldsymbol{\varphi}}\, dV - \int_{\overline{\mathcal{V}}} \overline{\mathrm{Div}}[\partial_{\overline{\nabla\phi}}\overline{\pi}]\, \delta\overline{\phi}\, dV \\ & + \int_{\partial\overline{\mathcal{B}}_{\overline{\boldsymbol{T}}}} \big([\![\partial_{\overline{\nabla\boldsymbol{\varphi}}}\overline{\pi}]\!] \cdot \overline{\boldsymbol{N}} - \overline{\boldsymbol{T}}\big) \cdot \delta\overline{\boldsymbol{\varphi}}\, dA = 0\,, \end{aligned} \tag{5.10}$$

yields for admissible virtual deformations $\delta\overline{\boldsymbol{\varphi}}$ and virtual potential $\delta\overline{\phi}$ the macroscopic generalized Euler-Lagrange and the mechanical jump conditions

1.	*Balance of linear momentum*	$\overline{\mathrm{Div}}[\partial_{\overline{\nabla\boldsymbol{\varphi}}}\overline{\pi}] + \overline{\boldsymbol{\gamma}}^m = \boldsymbol{0}$	in	$\overline{\mathcal{V}}$,
2.	*General Gauss law*	$\overline{\mathrm{Div}}[-\partial_{\overline{\nabla\phi}}\overline{\pi}] = 0$	in	$\overline{\mathcal{V}}$,
3.	*Mechanical jump*	$[\![\partial_{\overline{\nabla\boldsymbol{\varphi}}}\overline{\pi}]\!] \cdot \overline{\boldsymbol{N}} - \overline{\boldsymbol{T}} = \boldsymbol{0}$	on	$\partial\overline{\mathcal{B}}_{\overline{\boldsymbol{T}}}$.

(5.11)

The mechanical stress equilibrium in the macroscopic body based on a mechanical loading functional is evident. Furthermore, a generalized Gauss law is given here that needs to be fulfilled in the whole domain $\overline{\mathcal{V}}$.

5.2. Incremental variational framework on the microscale

Advanced interactions on different scales need to be incorporated into material models to improve the prediction of effective material response. Related to the multiscale modeling of coupled finite deformation, micro-magneto-electro-elastic solids are able to cover the evolution and motion of magnetic and electric domain walls on the microscale by a phase field order parameter. Non-standard modeling approaches of solids accounting for length scales can be traced back to the work of Capriz et al. [40] for continua with affine microstructures. These concepts were extended by Capriz [39] or more recently by Maugin [146] and Maugin & Muschik [149, 150] for general gradient-type dissipative solids. A full thermodynamic approach was proposed by Frémond [70], while field equations based on rate-type incremental variational formulations were developed first in the field of plasticity by e.g. Hill [88], Martin [143], Simó & Honein [231], Ortiz & Stainier [187], Miehe [158], and many others. These local theories were extended by Miehe [159, 161] to generalized gradient-enhanced standard dissipative media which serve as a starting point for the variational treatment of dissipative micro-magneto-electro-elasticity at finite strains.

5.2.1. Generalized multifield state variables

Following the work of Miehe [159, 161] a generalized rate potential based on the deformation $\boldsymbol{\varphi}$, a generalized scalar variable ϕ and a generalized vector field $\mathbf{q}$ is assumed. Associated with ϕ are the magnetic and electric scalar potentials, while $\mathbf{q}$ covers phase field order parameters, i.e. the magnetization and polarization. A material of grade one is employed here, incorporating the first material gradients of either fields, yielding a generalized state of independent variables for the micro-structure

$$\mathfrak{c}_0 := \{\, \boldsymbol{\varphi},\, \nabla\boldsymbol{\varphi},\, \phi,\, \nabla\phi,\, \mathbf{q},\, \nabla\mathbf{q} \,\}\,. \tag{5.12}$$

Following the idea of standard dissipative materials as outlined in Halphen & Nguyen [83], two functionals related to the energy storage and dissipative mechanisms are introduced, however in an extended manner for coupled multifield problems. The stored energy functional and dissipation potential functional are defined as

$$\mathfrak{E}(\mathfrak{c}_0) := \int_{\mathcal{B}} \psi(\mathfrak{c}_0)\, dV \quad \text{and} \quad \mathfrak{D}(\dot{\mathfrak{c}}_0) := \int_{\mathcal{B}} \Phi(\dot{\mathfrak{c}}_0; \mathfrak{c}_0)\, dV\,. \tag{5.13}$$

Note that the dissipation potential $\Phi(\dot{\mathfrak{c}}_0; \mathfrak{c}_0)$ not only depends on the rate of the state $\dot{\mathfrak{c}}_0$ but also on the current state $\mathfrak{c}_0$ itself.

5.2.2. Concept of material frame invariance and reduced states

Material models need to be invariant with regard to changes of the observer, mathematically described by superimposed rigid body motions onto the state variables of the functionals (5.13). For a Lagrangian set of variables this gives

$$\mathfrak{c}_0^+ := \{\, \boldsymbol{Q}(t)\boldsymbol{\varphi} + \boldsymbol{c}(t),\, \boldsymbol{Q}(t)\nabla\boldsymbol{\varphi},\, \phi + c(t),\, \nabla\phi,\, \boldsymbol{\mathfrak{Q}},\, \nabla\boldsymbol{\mathfrak{Q}} \,\}\,, \tag{5.14}$$

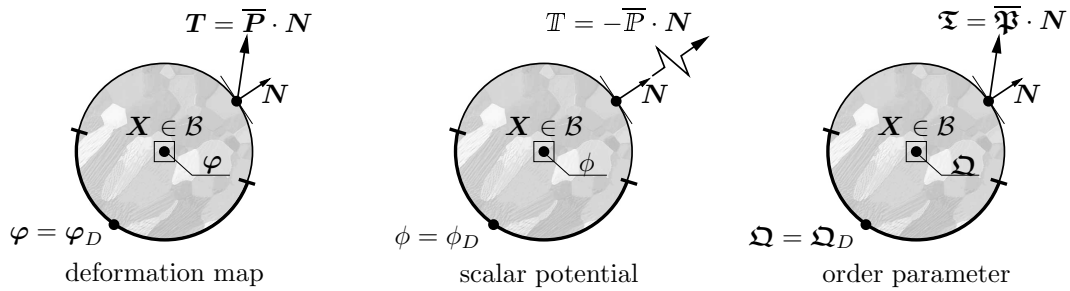

Figure 5.2: *Microscopic fields and boundary conditions.* The deformation map $\boldsymbol{\varphi}$, scalar potential ϕ and generalized Lagrangian order parameter $\mathfrak{Q}$ are introduced at $\boldsymbol{X} \in \mathcal{B}$. The boundary is separated into prescribed Dirichlet and Neumann conditions for the generalized fields. In here, $\{\, \boldsymbol{T}, \mathbb{T}, \mathfrak{T} \,\}$ are the generalized traction vectors for the respective fields, based on Cauchy-type theorems. Note that the loading of either boundary conditions is given by the macroscopic counterparts.

in terms of the Lagrangian gradients $\nabla = \nabla_{\boldsymbol{X}}$. Thus, the stored energy and the dissipation function are constrained to satisfy the objectivity condition

$$\psi^+(\mathfrak{c}_0^+) = \psi(\mathfrak{c}_0) \quad \text{and} \quad \Phi(\dot{\mathfrak{c}}_0^+; \mathfrak{c}_0^+) = \Phi(\dot{\mathfrak{c}}_0; \mathfrak{c}_0) \quad \forall\, \boldsymbol{Q} \in SO(d)\,. \tag{5.15}$$

With that, the state variables reduce to the set of objective state variables

$$\mathfrak{c} := \{\, \boldsymbol{C},\, \nabla\phi,\, \mathfrak{Q},\, \nabla\mathfrak{Q} \,\} \quad \text{and} \quad \dot{\mathfrak{c}} := \{\, \dot{\boldsymbol{C}},\, \nabla\dot{\phi},\, \dot{\mathfrak{Q}},\, \nabla\dot{\mathfrak{Q}} \,\}\,. \tag{5.16}$$

The energy storage and dissipation function need therefore be formulated in terms of the objective state variables $\psi(\mathfrak{c})$ and $\Phi(\dot{\mathfrak{c}}; \mathfrak{c})$.

5.2.3. Generalized rate-type variational principle

The loading of the micro-structure is realized by appropriate boundary conditions satisfying the generalized Hill-Mandel homogeneity condition as introduced in Section 3.3. Therefore, the rate-type potential consists only of the rate of energy and the dissipation functionals

$$\Pi(\dot{\boldsymbol{\varphi}}, \dot{\phi}, \dot{\mathfrak{Q}}) := \frac{d}{dt}\mathfrak{E}(\boldsymbol{\varphi}, \phi, \mathfrak{Q}) + \mathfrak{D}(\dot{\boldsymbol{\varphi}}, \dot{\phi}, \dot{\mathfrak{Q}}; \boldsymbol{\varphi}, \phi, \mathfrak{Q})\,, \tag{5.17}$$

and no external work functional is introduced. A reformulation of (5.17) in terms of the internal rate potential per unit volume at a given state $\mathfrak{c}$ at time t reads

$$\Pi(\dot{\boldsymbol{\varphi}}, \dot{\phi}, \dot{\mathfrak{Q}}) := \int_{\mathcal{B}} \pi(\dot{\mathfrak{c}}; \mathfrak{c})\, dV \quad \text{with} \quad \pi(\dot{\mathfrak{c}}; \mathfrak{c}) := \frac{d}{dt}\psi(\mathfrak{c}) + \Phi(\dot{\mathfrak{c}}; \mathfrak{c})\,. \tag{5.18}$$

At a given state $\{\, \boldsymbol{\varphi}, \phi, \mathfrak{Q} \,\}$, the evolution of the variables are determined by a three-field rate-type saddle-point variational principle

$$\{\, \dot{\boldsymbol{\varphi}},\, \dot{\phi},\, \dot{\mathfrak{Q}} \,\} = \arg\Big\{ \inf_{\dot{\boldsymbol{\varphi}} \in \mathcal{W}_{\dot{\boldsymbol{\varphi}}}} \sup_{\dot{\phi} \in \mathcal{W}_{\dot{\phi}}} \inf_{\dot{\mathfrak{Q}} \in \mathcal{W}_{\dot{\mathfrak{Q}}}} \Pi(\dot{\boldsymbol{\varphi}}, \dot{\phi}, \dot{\mathfrak{Q}}; t) \Big\} \tag{5.19}$$

in terms of the admissible states of the independent generalized variables

$$\begin{aligned} \mathcal{W}_{\dot{\boldsymbol{\varphi}}} &:= \{ \dot{\boldsymbol{\varphi}} \mid [\![\dot{\boldsymbol{\varphi}}]\!] = \dot{\overline{\boldsymbol{F}}} \cdot [\![\boldsymbol{X}]\!] \text{ on } \partial\mathcal{B} \}\,, \\ \mathcal{W}_{\dot{\phi}} &:= \{ \dot{\phi} \mid [\![\dot{\phi}]\!] = -\dot{\overline{\nabla\phi}} \cdot [\![\boldsymbol{X}]\!] \text{ on } \partial\mathcal{B} \}\,, \\ \mathcal{W}_{\dot{\mathfrak{Q}}} &:= \{ \dot{\mathfrak{Q}} \mid [\![\dot{\mathfrak{Q}}]\!] = \boldsymbol{0} \text{ on } \partial\mathcal{B} \}\,. \end{aligned} \tag{5.20}$$

Note carefully that the admissible spaces for the generalized order parameter highly depend on the problem under consideration. For micro-magnetics the variational principle needs to account for the geometric structure of the magnetization director to satisfy the physical constraint of unit length. A rigorous treatment for the specific cases follows in later stages of this work. For a representation of the microscopic field variables and their Dirichlet and Neumann boundary conditions see Figure 5.2. Here, the generalized traction-type variables $\{\boldsymbol{T}, \mathbb{T}, \mathfrak{T}\}$ and the macroscopic stress-type variables $\{\overline{\boldsymbol{P}}, \overline{\mathbb{P}}, \overline{\mathfrak{P}}\}$ are introduced on the Neumann boundary $\partial_N \mathcal{B}$. These variables are problem dependent and will further be specified in the respective modeling approaches. The possible boundary conditions for the multifield microscopic problem are presented in Section 3.3 and are not covered here.
Setting the first variation of the potential (5.18) to zero and employing Gauss-type integral theorems gives

$$\delta\Pi(\dot{\mathfrak{c}}) := \int_{\mathcal{B}} \delta_{\dot{\boldsymbol{\varphi}}}\pi \cdot \delta\dot{\boldsymbol{\varphi}} + \delta_{\dot{\phi}}\pi\, \delta\dot{\phi} + \delta_{\dot{\mathfrak{Q}}}\pi : \delta\dot{\mathfrak{Q}}\, dV + B.C. = 0 \quad . \tag{5.21}$$

Here, the variational derivatives

$$\begin{aligned} \delta_{\dot{\boldsymbol{\varphi}}}\pi &:= -\operatorname{Div}[\partial_{\nabla\boldsymbol{\varphi}}\psi + \partial_{\nabla\dot{\boldsymbol{\varphi}}}\Phi]\,, \\ \delta_{\dot{\phi}}\pi &:= -\operatorname{Div}[\partial_{\nabla\phi}\psi + \partial_{\nabla\dot{\phi}}\Phi]\,, \\ \delta_{\dot{\mathfrak{Q}}}\pi &:= -\operatorname{Div}[\partial_{\nabla\mathfrak{Q}}\psi + \partial_{\nabla\dot{\mathfrak{Q}}}\Phi] + [\partial_{\mathfrak{Q}}\psi + \partial_{\dot{\mathfrak{Q}}}\Phi]\,, \end{aligned} \tag{5.22}$$

of the rate potential per unit undeformed volume are introduced and for all admissible rates of virtual deformation $\delta\dot{\boldsymbol{\varphi}}$, virtual scalar potential $\delta\dot{\phi}$ and virtual order parameter $\delta\dot{\mathfrak{Q}}$ satisfying the possible boundary conditions, one can identify the generalized Euler-Lagrange equations of the rate-type setting as

1. *Balance of linear momentum*	$-\operatorname{Div}[\partial_{\nabla\boldsymbol{\varphi}}\psi + \partial_{\nabla\dot{\boldsymbol{\varphi}}}\Phi] = \boldsymbol{0}$ in $\mathcal{B}$,
2. *General Gauss law*	$-\operatorname{Div}[\partial_{\nabla\phi}\psi + \partial_{\nabla\dot{\phi}}\Phi] = 0$ in $\mathcal{B}$,
3. *Evolution equation*	$[\partial_{\mathfrak{Q}}\psi + \partial_{\dot{\mathfrak{Q}}}\Phi] - \operatorname{Div}[\partial_{\nabla\mathfrak{Q}}\psi + \partial_{\nabla\dot{\mathfrak{Q}}}\Phi] = \boldsymbol{0}$ in $\mathcal{B}$.

(5.23)

This representation of the generalized Euler-Lagrange equations for coupled multifield problems follows the approach of Maugin [146], Maugin & Muschik [149] or more recently Miehe [161] for gradient extended plasticity. Note that more specific assumptions for the energy and dissipation functional will be made for respective modeling of (dissipative) magneto-electro-elasticity.

5.2.4. Generalized time-discrete variational principle

The rate-type variational principle (5.19) gives rise to a time-discrete incremental setting of gradient-type dissipative solids. For a finite time step size of $\tau := t_{n+1} - t_n > 0$ the current fields at t_{n+1} are determined, for known field variables at t_n. From now on we drop the subscript for the current fields, such that objects without subscripts are evaluated at

time t_{n+1}. With that in mind the rate-type potential (5.17) is rewritten to an incremental potential in terms of the incremental energy and dissipation functionals

$$\Pi^\tau(\boldsymbol{\varphi}, \phi, \mathfrak{Q}) := \mathfrak{E}^\tau(\boldsymbol{\varphi}, \phi, \mathfrak{Q}) + \mathfrak{D}^\tau(\boldsymbol{\varphi}, \phi, \mathfrak{Q}) = \int_{\mathcal{B}} \pi^\tau(\mathfrak{c}; \mathfrak{c}_n)\, dV \tag{5.24}$$

or the internal incremental potential per unit volume π^τ. The internal incremental potential density is related to the internal rate potential density by an algorithm

$$\pi^\tau(\mathfrak{c}; \mathfrak{c}_n) := Algo\Big\{ \int_{t_n}^{t_{n+1}} \pi(\dot{\mathfrak{c}}; \mathfrak{c})\, dt \Big\} \tag{5.25}$$

in such a way, that the variation of the incremental potential (5.24) yield geometrically consistent algorithmic counterparts of the continuous generalized Euler-Lagrange equations in (5.23) at discrete time t_{n+1}, i.e.

$$\begin{array}{lll}
1.\ \textit{Balance of linear momentum} & -\operatorname{Div}[\partial_{\nabla\boldsymbol{\varphi}}\psi + \partial_{\nabla\dot{\boldsymbol{\varphi}}^\tau}\Phi] = \boldsymbol{0} & \text{in } \mathcal{B}\,, \\
2.\ \textit{General Gauss law} & -\operatorname{Div}[\partial_{\nabla\phi}\psi + \partial_{\nabla\dot{\phi}^\tau}\Phi] = 0 & \text{in } \mathcal{B}\,, \\
3.\ \textit{Evolution equation} & [\partial_{\mathfrak{Q}}\psi + \partial_{\dot{\mathfrak{Q}}^\tau}\Phi] - \operatorname{Div}[\partial_{\nabla\mathfrak{Q}}\psi + \partial_{\nabla\dot{\mathfrak{Q}}^\tau}\Phi] = \boldsymbol{0} & \text{in } \mathcal{B}\,.
\end{array} \tag{5.26}$$

A possible time discretization based on an implicit backward Euler scheme, gives the incremental potential (5.25) as

$$\pi^\tau(\mathfrak{c}; \mathfrak{c}_n) = \psi(\mathfrak{c}) - \psi_n(\mathfrak{c}_n) + \tau\Phi([\mathfrak{c} - \mathfrak{c}_n]/\tau)\,, \tag{5.27}$$

where ψ_n is the energy function evaluated at time t_n and the rate of the constitutive variables are approximated by $\dot{\mathfrak{c}}^\tau := [\mathfrak{c} - \mathfrak{c}_n]/\tau$.

5.2.5. Microscopic variational principle of homogenization

We now postulate that the macroscopic potential $\overline{\Pi}$ is governed by the displacement, and a scalar potential for a steady state of the order parameter. Then the saddle-point *variational principle of homogenization* is given by

$$\overline{\Pi}(\overline{\boldsymbol{\varphi}}, \overline{\phi}) = \inf_{\boldsymbol{\varphi}\in\mathcal{W}_{\boldsymbol{\varphi}}} \sup_{\phi\in\mathcal{W}_\phi} \frac{1}{|\mathcal{B}|} \int_{\mathcal{B}} \pi^\tau(\mathfrak{c}^*)\, dV - \overline{\mathcal{P}}_{\overline{\boldsymbol{\varphi}}}(\overline{\boldsymbol{\varphi}})\,, \tag{5.28}$$

in terms of the quasi-static set of constitutive fields $\mathfrak{c}^* = \{\boldsymbol{F}, \nabla\phi, \mathfrak{Q}^*, \nabla\mathfrak{Q}^*\}$. The respective admissible spaces for the deformation and the scalar potential are $\mathcal{W}_{\boldsymbol{\varphi}} := \{\boldsymbol{\varphi} \mid [\![\boldsymbol{\varphi}]\!] = \overline{\boldsymbol{F}} \cdot [\![\boldsymbol{X}]\!] \text{ on } \partial\mathcal{B}\}$ and $\mathcal{W}_\phi := \{\phi \mid [\![\phi]\!] = -\overline{\nabla\phi} \cdot [\![\boldsymbol{X}]\!] \text{ on } \partial\mathcal{B}\}$. Note that the microscopic quasi-static state is given as $\pi^*(\boldsymbol{F}, \nabla\phi) = \pi^\tau(\boldsymbol{F}, \nabla\phi, \mathfrak{Q}^*, \nabla\mathfrak{Q}^*)$ and $\mathfrak{Q}^*$ is defined such that $\|\mathfrak{Q}^* - \mathfrak{Q}_n\| \leq \epsilon$, where $\epsilon \ll 1$ is a positive small real number. The two-scale solution algorithm is discussed in further detail in the following.

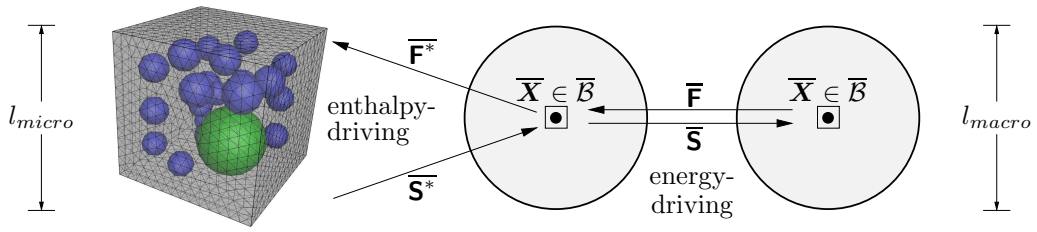

Figure 5.3: *Enthalpy-based computational homogenization coupled with additional local macro-iteration.* A core part of the procedure contains the easy-to-implement Dirichlet driving by $\overline{\mathbf{F}}^* := \{\overline{\boldsymbol{F}}, \overline{\mathbb{G}}\}^T$ within the enthalpy-based setting based on a scalar potential ϕ. An additional nested iteration at the local macroscopic point realizes the driving by $\overline{\mathbf{F}} := \{\overline{\boldsymbol{F}}, \overline{\mathbb{P}}\}^T$ that allows the tracking of post-critical paths, associated with typical pull-in instabilities.

5.3. Generalized macroscopic driving routine

The solution of the coupled two-scale problem can be based on an FE^2 driver that solves two nested boundary-value-problems for the micro- and the macroscale. We reduce this approach such that the inhomogeneous micro-structure is solved by a full finite element computation, while the (usually homogeneous) macro-structure is idealized by a one Gauss-point problem and updated by a standard Newton-Raphson scheme. The macroscopic state is assumed to be mechanically stress free $\overline{\boldsymbol{P}} = \boldsymbol{0}$, i.e. free to deform, unless a deformation is prescribed. Likewise, on electric or magnetic side we assume a homogeneous field without any geometry effects. Both assumptions are a direct extension of the work Zäh [274], and Miehe et al. [174] to dissipative materials on the micro-structure. More advanced macroscopic boundary conditions with included magneto-electro-mechanical tractions were recently published in the works of Danas [48] and Keip & Rambausek [111] however based on a phenomenological model.

The algorithm is based on the definition of a vector of unknowns $\overline{\mathbf{u}}$ filled with either primary or dual variables, depending on the chosen macroscopic boundary conditions. A typical load case scenario would be a mechanical stress free state $\overline{\boldsymbol{P}} = \boldsymbol{0}$ and a linear loading in the coupled variable, e.g. solely in $\overline{\mathbb{G}}_2$ direction, with $\overline{\mathbb{G}} = -\overline{\nabla}\,\overline{\phi}$. In two dimensions the vector of unknowns is then given as

$$\overline{\mathbf{u}} := [\,\overline{F}_{11}, \overline{F}_{22}, \overline{F}_{12}, \overline{F}_{21}, -\overline{\mathbb{P}}_1, -\overline{\mathbb{P}}_2\,]^T \in \mathcal{R}^6\,. \tag{5.29}$$

Here, the advantage of a two-scale problem based on an FE^2 or a driver method in comparison to homogenization approaches without macroscopic iteration is evident. Next to the homogenized stresses also the macroscopic deformations are computable. A generalized equilibrium stress vector is then defined by

$$\overline{\mathbf{S}^*}_{eq}(\overline{\mathbf{u}}) := [\,\overline{P}_{11}, \overline{P}_{22}, \overline{P}_{12}, \overline{P}_{21}, -\overline{\mathbb{P}}_1, -\overline{\mathbb{P}}_2\,]^T \in \mathcal{R}^6\,, \tag{5.30}$$

combining both the unknown $(-\overline{\mathbb{P}}_1, -\overline{\mathbb{P}}_2)$ and prescribed $(\overline{P}_{11} = \overline{P}_{22} = \overline{P}_{12} = \overline{P}_{21} = 0)$ stresses. A macroscopic residuum is then formulated

$$\overline{\mathfrak{R}^*}(\overline{\mathbf{u}}) := \overline{\mathbf{S}^*}(\overline{\mathbf{F}^*}(\overline{\mathbf{u}})) - \overline{\mathbf{S}^*}_{eq}(\overline{\mathbf{u}}) \tag{5.31}$$

based on the homogenized generalized stresses $\overline{\mathbf{S}^*}(\overline{\mathbf{F}^*}(\overline{\mathbf{u}}))$ obtained as volume averages of the microscopic finite element solution on the representative volume element. The entries

of $\overline{\boldsymbol{\mathcal{U}}}$ are then computed based on a standard Newton-Raphson update scheme, where the modified tangent matrix is obtained by the linearization of the residuum

$$\operatorname{Lin} \overline{\mathfrak{R}^*} = \overline{\mathfrak{R}^*}_n + \left. \frac{d\overline{\mathfrak{R}^*}}{d\overline{\boldsymbol{\mathcal{U}}}} \right|_n \Delta\overline{\boldsymbol{\mathcal{U}}}_{n+1} = \boldsymbol{0} \,. \tag{5.32}$$

This modified tangent holds for both, primary and dual field driven problems and reads

$$\overline{\mathfrak{K}^*} := \frac{d\overline{\mathfrak{R}^*}}{d\overline{\boldsymbol{\mathcal{U}}}} = \frac{d}{d\overline{\boldsymbol{\mathcal{U}}}} [\overline{\mathbf{S}^*}(\overline{\mathbf{F}^*}(\overline{\boldsymbol{\mathcal{U}}})) - \overline{\mathbf{S}^*}_{eq}(\overline{\boldsymbol{\mathcal{U}}})] = \partial_{\overline{\mathbf{F}^*}} \overline{\mathbf{S}^*} \cdot \partial_{\overline{\boldsymbol{\mathcal{U}}}} \overline{\mathbf{F}^*} - \partial_{\overline{\boldsymbol{\mathcal{U}}}} \overline{\mathbf{S}^*}_{eq} \,. \tag{5.33}$$

It contains the homogenized stiffness $\overline{\mathbf{C}^*} = \partial_{\overline{\mathbf{F}^*}} \overline{\mathbf{S}^*}$ as introduced in (7.98) as well as two additional auxiliary matrices $\partial_{\overline{\mathbf{F}^*}} \overline{\mathbf{S}^*}$ and $\partial_{\overline{\boldsymbol{\mathcal{U}}}} \overline{\mathbf{S}^*}_{eq}$. These diagonal matrices help to reduce the system of updated variables by eliminating terms for unknown stresses. They have the form

$$\partial_{\overline{\mathbf{F}^*}} \overline{\mathbf{S}^*} = \operatorname{diag}[\, \alpha_1, \alpha_2, ..., \alpha_n, \,] \quad \text{and} \quad \partial_{\overline{\boldsymbol{\mathcal{U}}}} \overline{\mathbf{S}^*}_{eq} = \operatorname{diag}[\, \beta_1, \beta_2, ..., \beta_n \,] \tag{5.34}$$

and contain either 1 for unknown deformations or coupled fields and 0 for unknown mechanical stresses or coupled duals for all $\{\alpha_i\}_{i=1,n}$ and the other way round for $\{\beta_i\}_{i=1,n}$. In the given example of a stress free mechanical state and generalized loading in $\overline{G}_2$ direction the modified tangent has the following entries

$$\overline{\mathfrak{K}^*} = \begin{bmatrix} \overline{\mathsf{C}^*}_{11} & \overline{\mathsf{C}^*}_{12} & \overline{\mathsf{C}^*}_{13} & \overline{\mathsf{C}^*}_{14} & 0 & 0 \\ \overline{\mathsf{C}^*}_{21} & \overline{\mathsf{C}^*}_{22} & \overline{\mathsf{C}^*}_{23} & \overline{\mathsf{C}^*}_{24} & 0 & 0 \\ \overline{\mathsf{C}^*}_{31} & \overline{\mathsf{C}^*}_{32} & \overline{\mathsf{C}^*}_{33} & \overline{\mathsf{C}^*}_{34} & 0 & 0 \\ \overline{\mathsf{C}^*}_{41} & \overline{\mathsf{C}^*}_{42} & \overline{\mathsf{C}^*}_{43} & \overline{\mathsf{C}^*}_{44} & 0 & 0 \\ \overline{\mathsf{C}^*}_{51} & \overline{\mathsf{C}^*}_{52} & \overline{\mathsf{C}^*}_{53} & \overline{\mathsf{C}^*}_{54} & -1 & 0 \\ \overline{\mathsf{C}^*}_{61} & \overline{\mathsf{C}^*}_{62} & \overline{\mathsf{C}^*}_{63} & \overline{\mathsf{C}^*}_{64} & 0 & -1 \end{bmatrix} . \tag{5.35}$$

The update for the entries of the unknown vector $\overline{\boldsymbol{\mathcal{U}}}$ is then given by

$$\overline{\boldsymbol{\mathcal{U}}}_{n+1} = \overline{\boldsymbol{\mathcal{U}}}_n + \Delta\overline{\boldsymbol{\mathcal{U}}}_{n+1} \quad \text{with} \quad \Delta\overline{\boldsymbol{\mathcal{U}}}_{n+1} = -\overline{\mathfrak{K}^*}_n^{-1} \overline{\mathbf{R}^*}_n \,. \tag{5.36}$$

This update algorithm performs till macroscopic convergence is achieved, i.e. $|\overline{\mathfrak{R}^*}| < \text{tol}_{macro}$. Then, the macroscopic loading increment λ is increased and the new homogeneous primary fields are prescribed onto the micro-structure. Note that this driver is capable of either prescribing the mixed energy-enthalpy variables $\{\, \overline{\boldsymbol{F}}, \overline{G} \,\}$ as well as the pure energetic variables $\{\, \overline{\boldsymbol{F}}, \overline{\mathbb{P}} \,\}$ which proves to be advantageous when analyzing limit-point instabilities, see Miehe et al. [174] and Polukhov et al. [196]. This driving routine is the basis of all two-scale computations performed in the following chapters. Modifications of the solution algorithm will be specified if necessary.

— Part II —

Minimization and Mixed-Principles: A Comparison

Chapter 6

Minimization and Mixed Principles: A Comparison

This chapter deals with different possible formulations of magneto-electro-mechanics. It provides insight in the transformation of canonical energy formulations into extended and reduced mixed formulations governed by an energy-enthalpy function. To obtain a descriptive formulation, only phenomenological electro-elasticity is considered here, however the concepts are applicable to a variety of coupled multiphysics problems.

The theoretical foundations for the continuum modeling of electro-mechanical interactions in solids undergoing finite strains were developed by Toupin [252], Tiersten [249], Brown [34], Pao [190], Maugin [145], Hutter et al. [99] and Kovetz [123]. These works form the background for more advanced models presented more recently. One distinguished between two conceptually different approaches, namely the convenient enthalpy ansatz based on a scalar potential as widely used in literature such as in Dorfmann & Ogden [59], McMeeking & Landis [152], Vu et al. [264], Suo et al. [241], Bustamante et al. [37] and Zäh & Miehe [273] as well as a canonical energetic approach based on vector potentials as presented in the works of Biro & Preis [23], Biro et al. [24], Landis [132], Fernandes & Perugia [68] and Vogel et al. [260]. Transformations of the two approaches based on a Legendre-Fenchel transformation of the electric slot are possible and commonly used. While the scalar potential approach is straight forward to implement numerically and therefore more convenient, the use of a vector potential is advantageous due to the underlying minimization principle, especially in terms of a possible use in stability investigations. However it is also known to be challenging in terms of boundary conditions and non-uniqueness of the vector potential in three dimensions. This difficulty is extensively treated in the following chapter and restriction to an unconditioned vector potential are made for a consistent transformation into the convenient enthalpy formulation.

6.1. Variational electro-elasticity

The governing equations of finite electro-elasticity follow from a variational principle. The subsequent definitions of variational principles are conceptually related to previous

works by Toupin [252], Pak & Herrmann [189], Maugin & Epstein [147], Yang & Batra [270], Yang [269], Bustamante et al. [37] and Ponte Castañeda & Siboni [198] in *electro-elasticity*, by Tiersten [249], Brown [34], Maugin & Eringen [148], DeSimone & James [53], Kankanala & Triantafyllidis [110], Bustamante et al. [36] and Ponte Castañeda & Galipeau [197] in *magneto-elasticity* and Miehe et al. [171] in *electro-magneto-mechanics*.

6.2. Energetic arrangement of phenomenological electro-elasticity

Starting point is the canonical energy formulation based on an electric vector potential. In here, no multiscale analysis is considered, the concepts however can easily be extended.

Primary field variables. The primary fields are introduced in a Lagrangian geometric setting with respect to the undeformed configuration $\mathcal{B} \subset \mathcal{R}^3$. In the energy-based formulation, the deformation map $\boldsymbol{\varphi}$ and the *electric vector potential* $\boldsymbol{a}^e$ are the governing fields

$$\boldsymbol{\varphi}\colon \begin{cases} \mathcal{B} \times \mathcal{T} \to \mathcal{R}^3 \\ (\boldsymbol{X}, t) \mapsto \boldsymbol{\varphi}(\boldsymbol{X}, t) = \boldsymbol{x} \end{cases} \quad \text{and} \quad \boldsymbol{a}^e\colon \begin{cases} \mathcal{B} \times \mathcal{T} \to \mathcal{R}^3 \\ (\boldsymbol{X}, t) \mapsto \boldsymbol{a}^e(\boldsymbol{X}, t) \end{cases} . \tag{6.1}$$

The motion $\boldsymbol{\varphi}$ maps at time $t \in \mathcal{T}$ points $\boldsymbol{X} \in \mathcal{B}$ of the reference configuration $\mathcal{B} \subset \mathcal{R}^3$ onto points $\boldsymbol{x} = \boldsymbol{\varphi}_t(\boldsymbol{X}) \in \boldsymbol{\varphi}_t(\mathcal{B})$ of the current configuration $\mathcal{S} := \boldsymbol{\varphi}_t(\mathcal{B}) \subset \mathcal{R}^3$. The electric vector potential $\boldsymbol{a}^e$ is an abstract quantity without physical meaning. Taking the spatial derivatives of these fields defines the deformation gradient and the Lagrangian electric displacement vector

$$\boldsymbol{F} = \nabla \boldsymbol{\varphi}(\boldsymbol{X}, t) \quad \text{and} \quad \mathbb{D} = \operatorname{Curl} \boldsymbol{a}^e(\boldsymbol{X}, t) , \tag{6.2}$$

respectively. With this ansatz equation $(6.2)_1$ ensures the mechanical compatibility condition $\operatorname{Curl} \boldsymbol{F} = \boldsymbol{0}$, while $(6.2)_2$ satisfies a priori Gauss's law $\operatorname{Div} \mathbb{D} = 0$, i.e. the first Maxwell equation of electrostatics while neglecting volume charges.

The canonical potential. Consider as a potential of electro-elasticity based on the energy storage ψ,

$$\Pi(\boldsymbol{\varphi}, \boldsymbol{a}^e) = \int_{\mathcal{B}} \psi(\nabla \boldsymbol{\varphi}, \operatorname{Curl} \boldsymbol{a}^e)\, dV - \Pi_{ext} , \tag{6.3}$$

depending on the deformation field $\boldsymbol{\varphi}$ and the Lagrangian electric vector-potential $\boldsymbol{a}^e$ introduced in (6.1). The external loading contribution is defined in terms of a prescribed mechanical volume force density $\overline{\boldsymbol{\gamma}}^m$, a traction field $\overline{\boldsymbol{T}}$ on $\partial\mathcal{B}_{\boldsymbol{T}}$ and a tangential electric field $\overline{\mathbb{E}}_t$ on $\partial\mathcal{B}_{\mathbb{E}_t}$ as

$$\Pi_{ext} = \int_{\mathcal{B}} \overline{\boldsymbol{\gamma}}^m \cdot \boldsymbol{\varphi}\, dV + \int_{\partial\mathcal{B}_{\boldsymbol{T}}} \overline{\boldsymbol{T}} \cdot \boldsymbol{\varphi}\, dA + \int_{\partial\mathcal{B}_{\mathbb{E}_t}} \overline{\mathbb{E}}_t \cdot \boldsymbol{a}^e\, dA \tag{6.4}$$

based on a split of the boundary $\partial\mathcal{B} = \partial\mathcal{B}_{\boldsymbol{T}} \cup \partial\mathcal{B}_{\boldsymbol{\varphi}}$ and $\partial\mathcal{B} = \partial\mathcal{B}_{\mathbb{E}_t} \cup \partial\mathcal{B}^e_{\boldsymbol{a}}$ for the mechanical and the electrical boundaries with $\partial\mathcal{B}_{\boldsymbol{T}} \cap \partial\mathcal{B}_{\boldsymbol{\varphi}} = \emptyset$ and $\partial\mathcal{B}_{\mathbb{E}_t} \cap \partial\mathcal{B}_{\boldsymbol{a}^e} = \emptyset$.

Minimization principle. With the potential Π defined in (6.3) at hand, the problem in finite electro-elasticity is governed by the *minimization principle*

$$\{\boldsymbol{\varphi}, \boldsymbol{a}^e\} = \arg\{\inf_{\boldsymbol{\varphi}\in\mathcal{W}_{\boldsymbol{\varphi}}} \inf_{\boldsymbol{a}^e\in\mathcal{W}_{\boldsymbol{a}^e}} \Pi(\boldsymbol{\varphi}, \boldsymbol{a}^e)\} \tag{6.5}$$

that determines the deformation field $\boldsymbol{\varphi}$ and the vector potential $\boldsymbol{a}^e$, accounting for Dirichlet-type boundary conditions given in the admissible function spaces $\mathcal{W}_{\boldsymbol{\varphi}}$ and $\mathcal{W}_{\boldsymbol{a}^e}$. They are defined as

$$\mathcal{W}_{\boldsymbol{\varphi}} := \{\boldsymbol{\varphi} \,|\, \boldsymbol{\varphi} = \overline{\boldsymbol{\varphi}} \text{ on } \partial\mathcal{B}_{\boldsymbol{\varphi}}\} \tag{6.6}$$

on the mechanical side for admissible deformations, and on the electrical side

$$\mathcal{W}_{\boldsymbol{a}^e} := \{\boldsymbol{a}^e \in H(\mathrm{Curl}, \mathcal{B}) \cap H(\mathrm{Div}, \mathcal{B}) |\ \boldsymbol{N} \times \boldsymbol{a}^e = \overline{\boldsymbol{a}^e}_t \text{ on } \partial\mathcal{B}_{\boldsymbol{a}^e} \text{ and } \boldsymbol{N} \cdot \boldsymbol{a}^e = 0 \text{ on } \partial\mathcal{B}_{\mathbb{E}_t}\}\,, \tag{6.7}$$

where $\overline{\boldsymbol{a}^e}_t$ is a prescribed vector potential, tangential to a normal $\boldsymbol{N}$ on $\partial\mathcal{B}_{\boldsymbol{a}^e}$.

Necessary condition and Euler equations. Consider an arbitrary field of virtual deformations, that satisfies $\delta\boldsymbol{\varphi} \in \mathcal{W}_{\boldsymbol{\varphi}} := \{\delta\boldsymbol{\varphi} \,|\, \delta\boldsymbol{\varphi} = \boldsymbol{0} \text{ on } \partial\mathcal{B}_{\boldsymbol{\varphi}}\}$, and a virtual electric vector potential satisfying $\delta\boldsymbol{a}^e \in \mathcal{W}_{\boldsymbol{a}^e} := \{\delta\boldsymbol{a}^e \in H(\mathrm{Curl}, \mathcal{B}) \cap H(\mathrm{Div}, \mathcal{B}) |\ \boldsymbol{N} \times \delta\boldsymbol{a}^e = \boldsymbol{0} \text{ on } \partial\mathcal{B}_{\boldsymbol{a}^e} \text{ and } \boldsymbol{N} \cdot \delta\boldsymbol{a}^e = 0 \text{ on } \partial\mathcal{B}_{\mathbb{E}_t}\}$. The necessary condition of the minimization problem (6.5) reads

$$\begin{aligned} \delta\Pi = & \int_{\mathcal{B}} [\partial_{\boldsymbol{F}}\psi : \nabla\delta\boldsymbol{\varphi} + \partial_{\mathbb{D}}\psi \cdot \mathrm{Curl}\, \delta\boldsymbol{a}^e]\, dV \\ & - \int_{\partial\mathcal{B}_T} \overline{\boldsymbol{T}} \cdot \delta\boldsymbol{\varphi}\, dA - \int_{\partial\mathcal{B}_{\mathbb{E}_t}} \overline{\mathbb{E}}_t \cdot \delta\boldsymbol{a}^e\, dA - \int_{\mathcal{B}} \overline{\boldsymbol{\gamma}}^m \cdot \delta\boldsymbol{\varphi}\, dV = 0 \end{aligned} \tag{6.8}$$

for all $\delta\boldsymbol{\varphi} \in \mathcal{W}_{\boldsymbol{\varphi}}$ and $\delta\boldsymbol{a}^e \in \mathcal{W}_{\boldsymbol{a}^e}$. Taking into account Gauss-type integral theorems, we obtain, after localization, the Euler equations

1.	*Balance of linear momentum*	$\mathrm{Div}[\partial_{\boldsymbol{F}}\psi] + \overline{\boldsymbol{\gamma}}^m$	$= \boldsymbol{0}$	in $\mathcal{B}$
2.	*Faraday's law*	$\mathrm{Curl}[\partial_{\mathbb{D}}\psi]$	$= \boldsymbol{0}$	in $\mathcal{B}$
3.	*Prescribed tractions*	$\partial_{\boldsymbol{F}}\psi \cdot \boldsymbol{N}$	$= \overline{\boldsymbol{T}}$	on $\partial\mathcal{B}_{\boldsymbol{T}}$
4.	*Tangential electric field*	$\partial_{\mathbb{D}}\psi \times \boldsymbol{N}$	$= \overline{\mathbb{E}}_t$	on $\partial\mathcal{B}_{\mathbb{E}_t}$

(6.9)

Here, the derivatives of the energy function ψ identify constitutive relationships for the first Piola stress tensor $\boldsymbol{P} := \partial_{\boldsymbol{F}}\psi$ and the Lagrangian electric field $\mathbb{E} := \partial_{\mathbb{D}}\psi$, as energetic conjugates to the primary fields.

6.3. Extended principle of phenomenological electro-elasticity

For a consistent transformation of the canonical energy to the energy-enthalpy formulation, an intermediate extended energy principle is introduced, based on the partial Legendre-Fenchel transformation of the energy storage function, as suggested in Miehe et al. [173], and Miehe et al. [174]. While this formulation is not used in any treatment of the multiphysic problem, it has descriptive purposes for a rigorous reformulation. It is important to note, that for a canonical energy with additional gauging condition it is *not possible* to obtain an equivalent enthalpy formulation. Therefore, a restriction to the potential introduced in (6.3) needs to be made.

Extended mixed potential. The free energy density ψ is redefined by a local partial Legendre-Fenchel transformation in terms of the so-called *energy-enthalpy density* ψ^*

$$\psi(\nabla\boldsymbol{\varphi}, \operatorname{Curl}\boldsymbol{a}^e) = \sup_{\mathbb{E}}[\ \psi^*(\nabla\boldsymbol{\varphi}, \mathbb{E}) + \operatorname{Curl}\boldsymbol{a}^e \cdot \mathbb{E}\ ]\ . \tag{6.10}$$

Associated with this transformation is an *extended mixed potential* $\widetilde{\Pi}^*$ which follows by insertion of (6.10) into (6.3) and reads

$$\widetilde{\Pi}^*(\boldsymbol{\varphi}, \boldsymbol{a}^e, \mathbb{E}) = \int_{\mathcal{B}} [\ \psi^*(\nabla\boldsymbol{\varphi}, \mathbb{E}) + \operatorname{Curl}\boldsymbol{a}^e \cdot \mathbb{E}\ ]\, dV - \Pi_{ext}\ . \tag{6.11}$$

This three-field functional depends on the deformation field $\boldsymbol{\varphi}$, the Lagrangian electric vector potential $\boldsymbol{a}^e$, and electric field $\mathbb{E}$, as well as the external loading contribution as introduced in (6.4).

Three-field saddle-point variational principle. Based on the potential $\widetilde{\Pi}^*$ defined in (6.11), the coupled boundary-value-problem of finite electro-elasto-statics can be defined by the *mixed three-field principle*

$$\{\boldsymbol{\varphi}, \boldsymbol{a}^e, \mathbb{E}\} = \arg\{\inf_{\boldsymbol{\varphi}\in\mathcal{W}_{\boldsymbol{\varphi}}} \inf_{\boldsymbol{a}^e\in\mathcal{W}_{\boldsymbol{a}^e}} \sup_{\mathbb{E}} \widetilde{\Pi}^*(\boldsymbol{\varphi}, \boldsymbol{a}^e, \mathbb{E})\}\,, \tag{6.12}$$

that determines the deformation field $\boldsymbol{\varphi}$, the electric vector potential $\boldsymbol{a}^e$ and the electric field $\mathbb{E}$. Here, the spaces $\mathcal{W}_{\boldsymbol{\varphi}}$ and $\mathcal{W}_{\boldsymbol{a}^e}$ of admissible functions for the deformation and the vector potential are again (6.6) and (6.7), while the admissible mixed variable $\mathbb{E}$ needs to fulfill Faraday's law $\operatorname{Curl}[\mathbb{E}] = \boldsymbol{0}$ in $\mathcal{B}$.

Necessary condition and Euler equations. Consider virtual deformations $\delta\boldsymbol{\varphi} \in \mathcal{W}_{\boldsymbol{\varphi}}$ and virtual electric vector potentials $\delta\boldsymbol{a}^e \in \mathcal{W}_{\boldsymbol{a}^e}$ as well as unconstrained virtual electric fields $\delta\mathbb{E}$ as test functions. The necessary condition of the mixed variational principle (6.12) reads

$$\begin{aligned}\delta\widetilde{\Pi}^* = \int_{\mathcal{B}} &[\partial_{\boldsymbol{F}}\psi^* : \nabla\delta\boldsymbol{\varphi} + \partial_{\mathbb{E}}\psi^* \cdot \delta\mathbb{E} + \operatorname{Curl}\boldsymbol{a}^e \cdot \delta\mathbb{E} + \operatorname{Curl}\delta\boldsymbol{a}^e \cdot \mathbb{E}\,]dV \\ &- \int_{\partial\mathcal{B}_T} \overline{\boldsymbol{T}} \cdot \delta\boldsymbol{\varphi}\, dA - \int_{\partial\mathcal{B}_{\mathbb{E}_t}} \overline{\mathbb{E}}_t \cdot \delta\boldsymbol{a}^e\, dA - \int_{\mathcal{B}} \overline{\boldsymbol{\gamma}}^m \cdot \delta\boldsymbol{\varphi}\, dV = 0\,.\end{aligned} \tag{6.13}$$

Using Gauss-type integral theorems, we obtain the Euler equations

1.	*Balance of linear momentum*	$\operatorname{Div}[\partial_{\boldsymbol{F}}\psi^*] + \overline{\boldsymbol{\gamma}}^m$	$= \boldsymbol{0}$	in $\mathcal{B}$
2.	*Faraday's law*	$\operatorname{Curl}[\mathbb{E}]$	$= \boldsymbol{0}$	in $\mathcal{B}$
3.	*Prescribed tractions*	$\partial_{\boldsymbol{F}}\psi^* \cdot \boldsymbol{N}$	$= \overline{\boldsymbol{T}}$	on $\partial\mathcal{B}_{\boldsymbol{T}}$
4.	*Tangential electric field*	$\mathbb{E} \times \boldsymbol{N}$	$= \overline{\mathbb{E}}_t$	on $\partial\mathcal{B}_{\mathbb{E}_t}$
5.	*Constitutive relation*	$\operatorname{Curl}\boldsymbol{a}^e + \partial_{\mathbb{E}}\psi^*$	$= \boldsymbol{0}$	in $\mathcal{B}$

(6.14)

The first four equations are identical with (6.9), however, now formulated in terms of the mixed variable $\mathbb{E} = \partial_{\mathbb{D}}\psi$. The last equation is the constitutive relationship that links the

electric displacements to the electric field. It is the necessary equation of the Legendre-Fenchel transformation (6.10). Hence, we identify as the dual objects by the derivatives of the electric enthalpy function

$$\boldsymbol{P} := \partial_{\boldsymbol{F}} \psi^* \quad \text{and} \quad \mathbb{D} := -\partial_{\mathbb{E}} \psi^* \,, \tag{6.15}$$

the Piola stress and the electric displacements, where the latter equation is an Euler equation of the mixed variational principle.

6.4. Enthalpy principle of phenomenological electro-elasticity

In a final step, the extended mixed potential gets reduced by an appropriate ansatz for the electric field, and by reformulation of the additional Legendre-Fenchel transformation term. One can show that the equality in-between the canonical and extended mixed energy approach with the enthalpy formulation only holds for specific boundary conditions, and not in the most general case.

Reduced mixed potential. Consider now the mixed variable in the potential (6.11) to follow the ansatz

$$\mathbb{E} = -\nabla \phi^e(\boldsymbol{X}, t) \,, \tag{6.16}$$

in terms of the gradient of a scalar potential function ϕ^e, constrained by

$$\phi^e \in \mathcal{W}_{\phi^e} := \{ \phi^e \,|\, \phi^e = \overline{\phi^e} \text{ on } \partial\mathcal{B}_{\phi^e} \} \,, \tag{6.17}$$

providing an electric potential on the surface $\partial\mathcal{B}_{\phi^e}$. This ansatz satisfies automatically Faraday's law of electrostatics, i.e. equations $(6.14)_2$ and $(6.14)_4$, as $\operatorname{Curl} \nabla \phi^e = 0$ by definition. Reformulation of the mixed term in (6.11) yields

$$\int_{\mathcal{B}} \operatorname{Curl} \boldsymbol{a}^e \cdot \mathbb{E} \, dV = \int_{\mathcal{B}} \operatorname{Div}[\operatorname{Curl} \boldsymbol{a}^e] \phi^e \, dV - \int_{\partial\mathcal{B}} (\operatorname{Curl} \boldsymbol{a}^e \cdot \boldsymbol{N}) \phi^e \, dA \,, \tag{6.18}$$

by employing the integral theorem. Insertion of the admissible functions $\boldsymbol{a}^e \in \mathcal{W}_{\boldsymbol{a}^e}$ defined in (6.7) gives

$$\int_{\mathcal{B}} \operatorname{Curl} \boldsymbol{a}^e \cdot \mathbb{E} \, dV = - \int_{\partial\mathcal{B}} \overline{D} \phi^e \, dA \,, \tag{6.19}$$

with $\overline{D} := -\overline{\mathbb{D}} \cdot \boldsymbol{N}$. A full elimination of the electric displacements is therefore not possible. However, this motivates the definition of a reduced variational functional

$$\Pi^*(\boldsymbol{\varphi}, \phi^e) = \int_{\mathcal{B}} \psi^*(\nabla \boldsymbol{\varphi}, -\nabla \phi^e) \, dV - \Pi_{ext} - \Pi^D_{ext}(\overline{D}) \,, \tag{6.20}$$

depending only on the deformation field $\boldsymbol{\varphi}$ and the scalar electric potential ϕ^e. It includes the additional electric loading term $\Pi^D_{ext}(\overline{D}) = -\int_{\partial\mathcal{B}} \overline{D} \phi^e \, dA$ on the full boundary. Note carefully that for a general boundary-value-problem the reduced functional Π^* *does not coincide* with a three-field energy-enthalpy potential $\widetilde{\Pi}^*$ by replacing the mixed term in (6.11) via (6.19) but needs the definition $\mathbb{E} = -\nabla \phi^e$. We have *for the images of the potentials* defined in (6.3), (6.11) and (6.20)

$$\Pi^*(\boldsymbol{\varphi}, \phi^e) \neq \widetilde{\Pi}^*(\boldsymbol{\varphi}, \boldsymbol{a}^e, \mathbb{E}) = \Pi(\boldsymbol{\varphi}, \boldsymbol{a}^e) \tag{6.21}$$

at their solution points. Hence, the image of Π^* at the solution point is not identical with the image of the energy functional Π for general boundary-value-problems.

Reduced mixed variational principle. With the reduced potential Π^*, defined in (6.20), at hand, the coupled boundary-value-problem of finite electro-elasto-statics can be defined by the *two-field saddle-point principle*

$$\{\boldsymbol{\varphi}, \phi^e\} = \arg\{ \inf_{\boldsymbol{\varphi}\in\mathcal{W}_{\boldsymbol{\varphi}}} \sup_{\phi^e\in\mathcal{W}_{\phi^e}} \Pi^*(\boldsymbol{\varphi}, \phi^e) \}\,, \tag{6.22}$$

that determines the deformation field $\boldsymbol{\varphi}$ and the electric scalar potential ϕ^e for the admissible function spaces $\mathcal{W}_{\boldsymbol{\varphi}}$ and $\mathcal{W}_{\phi^e}$ as defined in (6.6) and (6.17).

Necessary condition and Euler equations. For the arbitrary field of *virtual deformations* $\delta\boldsymbol{\varphi} \in \mathcal{W}_{\boldsymbol{\varphi}}$, and the field of *virtual electric potentials* $\delta\phi^e \in \mathcal{W}_{\phi^e}$, that satisfy the homogeneous form of (6.17), the necessary condition of the two-field saddle-point principle (6.22) reads

$$\begin{aligned} \delta\Pi^* = & \int_{\mathcal{B}} [\partial_{\boldsymbol{F}}\psi^* : \nabla\delta\boldsymbol{\varphi} + \partial_{\mathbb{E}}\psi^* \cdot \delta\mathbb{E}\,] dV \\ & - \int_{\partial\mathcal{B}_T} \overline{\boldsymbol{T}} \cdot \delta\boldsymbol{\varphi}\, dA - \int_{\mathcal{B}} \overline{\boldsymbol{\gamma}}^m \cdot \delta\boldsymbol{\varphi}\, dV + \int_{\partial\mathcal{B}} \overline{D}\phi^e\, dA = 0\,. \end{aligned} \tag{6.23}$$

Considering Gauss-type integral theorems, the Euler equations are obtained

1.	*Balance of linear momentum*	$\mathrm{Div}[\partial_{\boldsymbol{F}}\psi^*] + \overline{\boldsymbol{\gamma}}^m$	$= \boldsymbol{0}$	in $\mathcal{B}$
2.	*Prescribed tractions*	$\partial_{\boldsymbol{F}}\psi^* \cdot \boldsymbol{N} - \overline{\boldsymbol{T}}$	$= \boldsymbol{0}$	on $\partial\mathcal{B}_T$
3.	*Gauss's law*	$\mathrm{Div}[-\partial_{\mathbb{E}}\psi^*]$	$= 0$	in $\mathcal{B}$
4.	*Electric flux*	$-\partial_{\mathbb{E}}\psi^* \cdot \boldsymbol{N}$	$= -\overline{D}$	on $\partial\mathcal{B}$

(6.24)

Again, derivatives of the electric enthalpy density function ψ^* define the dual variables, namely the Piola stress $\boldsymbol{P} := \partial_{\boldsymbol{F}}\psi^*$ and the electric displacements $\mathbb{D} := -\partial_{\mathbb{E}}\psi^*$. From the aspect of numerical convenience, this is the most simple setting of electro-elasto-statics, however energetically *not* identical to the canonical energy approach.

6.5. Energetic congruent transformation of energy to enthalpy

To obtain an energetically consistent transformation from the canonical energy to the numerically more convenient enthalpy formulation, the starting point is a re-definition of the energy functional (6.3) in terms of the electric displacement field $\mathbb{D}$ for an empty Neumann boundary $\partial\mathcal{B}_{\mathbb{E}_t} = \emptyset$ on the electrical side

$$\widehat{\Pi}(\boldsymbol{\varphi}, \mathbb{D}) = \int_{\mathcal{B}} \widehat{\psi}(\boldsymbol{F}, \mathbb{D})\, dV - \widehat{\Pi}_{ext} \quad \text{with} \quad \widehat{\Pi}_{ext} = \int_{\mathcal{B}} \overline{\boldsymbol{\gamma}}^m \cdot \boldsymbol{\varphi}\, dV + \int_{\partial\mathcal{B}_T} \overline{\boldsymbol{T}} \cdot \boldsymbol{\varphi}\, dA\,. \tag{6.25}$$

The coupled boundary-value-problem of finite electro-elasto-statics is governed by the two-field minimization principle

$$\{\boldsymbol{\varphi}, \mathbb{D}\} = \arg\{ \inf_{\boldsymbol{\varphi}\in\mathcal{W}_{\boldsymbol{\varphi}}} \inf_{\mathbb{D}\in\mathcal{W}_{\mathbb{D}}} \widehat{\Pi}(\boldsymbol{\varphi}, \mathbb{D}) \}\,, \tag{6.26}$$

that determines the deformation field $\boldsymbol{\varphi}$ with respect to the function space $\mathcal{W}_{\boldsymbol{\varphi}}$ accounting for mechanical Dirichlet boundary conditions (6.6), and the electric displacement $\mathbb{D}$ with respect to the function space $\mathcal{W}_{\mathbb{D}}$

$$\mathcal{W}_{\mathbb{D}} := \{\mathbb{D} \mid \operatorname{Div} \mathbb{D} = 0 \text{ in } \mathcal{B}\,,\ -\overline{\mathbb{D}} \cdot \boldsymbol{N} = \overline{D} \text{ on } \partial\mathcal{B}\}\,, \tag{6.27}$$

for electrical Dirichlet-type boundary conditions on the full boundary $\partial\mathcal{B}$. It is important to note that if $\mathbb{D}$ is chosen as the primary field directly, Gauss's law of electrostatics is not a priori fulfilled, and needs to be incorporated into the space of admissible states. Following the steps (6.16)-(6.19) one obtains the related two-field mixed energy-enthalpy potential

$$\widehat{\Pi}^*(\boldsymbol{\varphi}, \phi^e) = \int_{\mathcal{B}} \psi^*(\nabla\boldsymbol{\varphi}, -\nabla\phi^e)\, dV - \int_{\mathcal{B}} \overline{\boldsymbol{\gamma}}^m \cdot \boldsymbol{\varphi}\, dV - \int_{\partial\mathcal{B}_T} \overline{\boldsymbol{T}} \cdot \boldsymbol{\varphi}\, dA + \int_{\partial\mathcal{B}} \overline{D}\phi^e\, dA \tag{6.28}$$

with the two-field saddle-point variational principle

$$\{\boldsymbol{\varphi}, \phi^e\} = \arg\{\inf_{\boldsymbol{\varphi}\in\mathcal{W}_{\boldsymbol{\varphi}}} \sup_{\phi^e\in H^1} \widehat{\Pi}^*(\boldsymbol{\varphi}, \phi^e)\}\,. \tag{6.29}$$

Finally, a connection between the prescribed surface charge density $\overline{D}$ and the prescribed tangential vector potential $\overline{\boldsymbol{a}^e}_t$ of the vector-potential-based definition of the function space (6.7) is needed. By using the relation

$$-\overline{D} = \overline{\mathbb{D}} \cdot \boldsymbol{N} = \operatorname{Curl} \boldsymbol{a}^e \cdot \boldsymbol{N} = -\operatorname{Div}[\boldsymbol{N} \times \boldsymbol{a}^e] \tag{6.30}$$

stemming from vector analysis, one can find the relationship between $\overline{D}$ and $\overline{\boldsymbol{a}^e}_t$, namely

$$\operatorname{Div} \overline{\boldsymbol{a}^e}_t = \overline{D}\,. \tag{6.31}$$

With this, the variational equivalence of a pure Dirichlet-based vector potential approach and a pure Neumann-based scalar potential approach is shown.

6.6. Energetic congruent transformation: an example

Introduction of a reduced mixed variational principle (6.29) shows the equality in the averaged energy of the energetic formulation based on a pure minimization principle and the enthalpy formulation based on a saddle-point problem for pure Dirichlet-type vector potential and pure Neumann-type scalar potential approaches. In the following we demonstrate the energetic equality by comparing both approaches and evaluating the energy storage functions. For both formulations, a neo-Hookean mechanical model for hyperelastic materials is employed

$$\psi'_{mech}(\boldsymbol{C}) = \frac{1}{2}(\operatorname{tr}[\boldsymbol{C}] - 3) + \frac{1}{\beta}(J^{-\beta} - 1)\,, \tag{6.32}$$

in terms of the shear modulus μ and β defined by Poisson's ratio ν, i.e. $\beta = \frac{\lambda}{\mu} = \frac{2\nu}{1-2\nu}$. The electro-mechanical coupling terms are chosen such that they reflect the relation $\mathbb{d} = \epsilon_0 \mathbb{e} + \mathbb{p}$ for the electric displacement in the current configuration. It yields for the canonical energy the simple quadratic form

$$\psi'_{elec}(\boldsymbol{C}, \mathbb{D}') = \frac{1}{2(J + \chi^e)}\, \boldsymbol{C} : (\mathbb{D}' \otimes \mathbb{D}')\,. \tag{6.33}$$

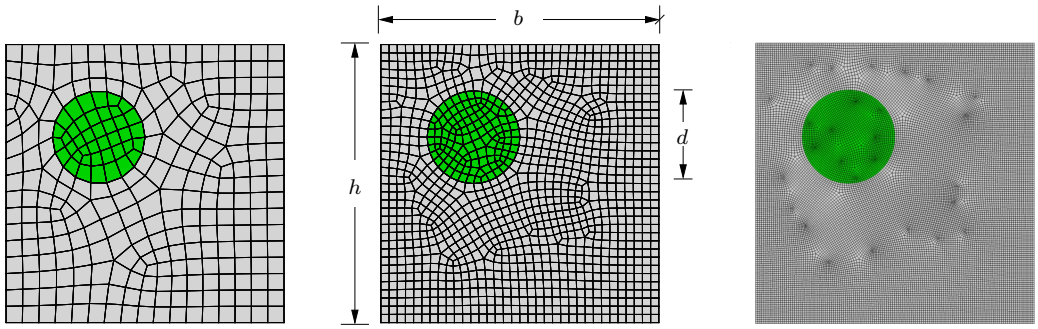

Figure 6.1: *Discretization of the specimen.* The inhomogeneous material of size $b = h = 30\,\mu$m contains a polymeric matrix material (gray) and an eccentric stiff inclusion with high electric permittivity (green) of diameter $d = 10\,\mu$m resulting in a 8.7% volume fraction. Three different spatial discretizations are chosen based on 4-noded bilinear elements, with element sizes $h_1 < h_2 < h_3$.

Note, that the energy is normalized by the shear modulus μ and the electric permittivity of free space ϵ_0 such that $\mathbb{D}' := \mathbb{D}/\sqrt{\mu\epsilon_0}$. Likewise, based on a Legendre-Fenchel transformation, the related energy storage in the mixed formulation reads

$$\psi^{*\prime}_{elec}(\boldsymbol{C}, \mathbb{E}') = -\frac{1}{2}(J + \chi^e)\boldsymbol{C}^{-1} : (\mathbb{E}' \otimes \mathbb{E}')\,, \tag{6.34}$$

with the normalized electric field $\mathbb{E}' := \mathbb{E}/\sqrt{\mu/\epsilon_0}$.
For a numerical example, consider an inhomogeneous material consisting of a polymeric matrix material with an excentric stiff inclusion of high electric permittivity. For convenience, a two-dimensional boundary value problem is considered, with dimensions as shown in Figure 6.1 and the material parameters summarized in Table 6.1. The specimen is loaded by an electric displacement $\overline{\mathbb{D}} = [\,0,\, \overline{\mathbb{D}}_2\,]^T$ in vertical x_2-direction via Dirichlet conditions for the energy formulation, or Neumann loading term for the enthalpy formulation, respectively. In Figure 6.2a the resulting averaged electric field $\overline{\mathbb{E}}_2 = \int_{\mathcal{B}} \mathbb{E}_2\, dV$ is plotted over the applied electric displacement $\overline{\mathbb{D}}_2$ for both the scalar (SP) and vector potential (VP) formulation. For all computations, bilinear shape functions were used. It can be seen, that concerning the averaged $\overline{\mathbb{D}}_2$-$\overline{\mathbb{E}}_2$ curve the approximation of the vector potential approach for the coarsest mesh is less accurate than the scalar potential approach, i.e. close to and after the limit point. The relative difference

$$R_E := \frac{|\overline{\mathbb{E}}_2^{VP} - \overline{\mathbb{E}}_2^{SP}|}{|\overline{\mathbb{E}}_2^{SP}|} \tag{6.35}$$

between both formulations in the $\overline{\mathbb{D}}_2 - \overline{\mathbb{E}}_2$ curve is depicted in Figure 6.2b. It is apparent, that the vector and scalar potential approach converge to one solution of the considered

Table 6.1: Material parameters for polyurethane matrix and $BaTiO_3$ inclusion.

no.	par.	name	PU	$BaTiO_3$	unit
1.	μ	shear modulus	$1.6 \cdot 10^{-6}$	$4.3 \cdot 10^{-2}$	N/μm^2
2.	ν	Poisson ratio	0.35	0.32	–
3.	χ^e	electric susceptibility	4.7	1250	–

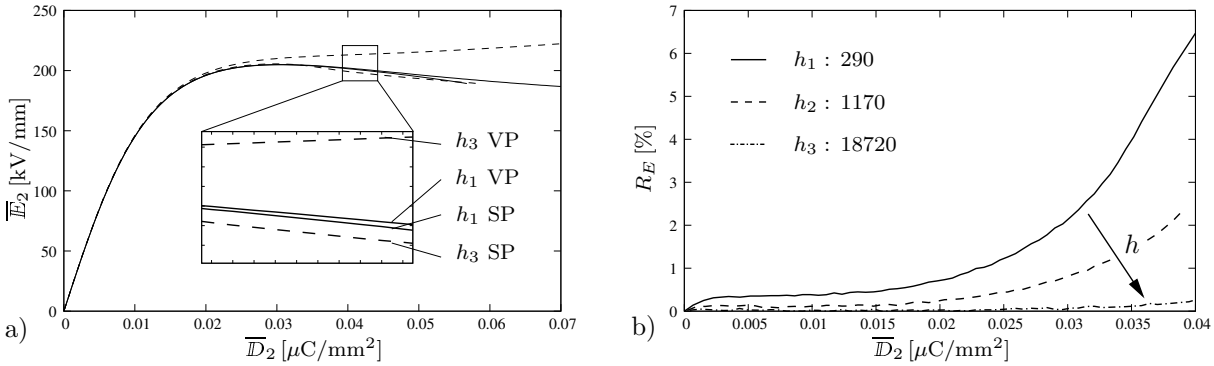

Figure 6.2: *Comparison of energy and enthalpy formulation.* For different element sizes $h_1 < h_2 < h_3$ the averaged $\overline{\mathbb{D}}_2$-$\overline{\mathbb{E}}_2$ diagram is compared for the scalar potential (SP) and vector potential (VP) formulation. The relative difference R_E, defined in (6.35), between the resulting electric field $\overline{\mathbb{E}}_2$ of the scalar and the vector potential approach is plotted over the applied electric displacement $\overline{\mathbb{D}}_2$. For increasing mesh density one can observe convergence to one and the same solution.

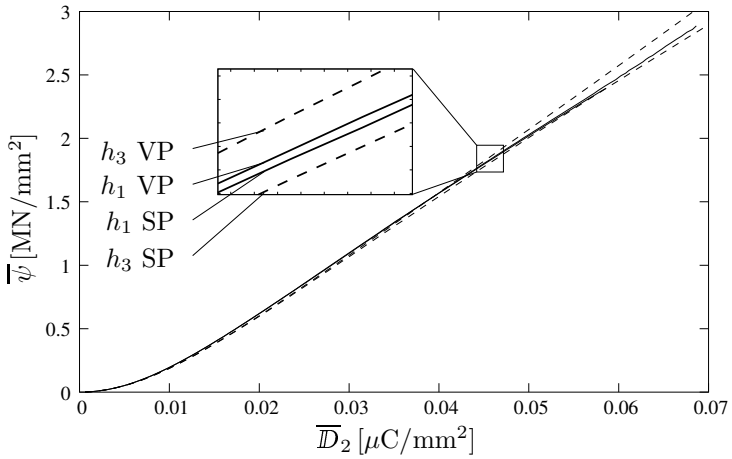

Figure 6.3: *Comparison of energies.* For different element sizes $h_1 < h_2 < h_3$ the averaged energy $\overline{\psi}$ or $\overline{\psi}^*$ is plotted over the applied electric displacement $\overline{\mathbb{D}}_2$ for the vector potential (VP) and scalar potential (SP) formulation, respectively. Both energies are equal beside the apparent approximation error.

boundary value problem. Next, the equality of the vector and scalar potential formulation by comparing the average energies (6.26) and (6.29) is in focus. They are depicted in Figure 6.3 and turn out to be equal up to the approximation error, which becomes significant for the coarse mesh at, and after the limit point. Again, for smaller elements, convergence to one and the same energy is observed. Hence, we notice equality of the energy and enthalpy formulation for sufficient approximation accuracy.

6.7. Challenges of minimization principles

The possibility of adding a gradient vector field to the vector potential without disturbing Gauss's law needs to be taken care of by gauging methods such as the Coulomb gauge, or by use of advanced edge elements with tangent component, such as proposed by Nédélec [181, 182]. In the works of Semenov et al. [222, 223] different gauging methods are analyzed and compared, and additional difficulties in the accuracy of local field solutions

at material interfaces with a large difference in electric susceptibility are shown. In the following a rigorous treatment of the challenges and difficulties of vector potentials in finite magneto-electro-mechanics, and possible solutions are displayed. A *Hu-Washizu-type mixed finite element approach* is developed that improves the computational cost and results, when using the canonical energy ansatz.

Intrinsic difficulty: non-uniqueness of the vector potential. A challenge in application of pure minimizers in electro-mechanics is the treatment of the non-uniqueness of the vector potential. Due to the fact that the curl of a gradient field is zero, $\mathrm{Curl}(\nabla\theta) = \boldsymbol{0}$, the electric displacement $\mathbb{D} = \mathrm{Curl}(\boldsymbol{a}^e) = \mathrm{Curl}(\boldsymbol{a}^e + \nabla\theta)$ is not influenced by addition of an arbitrary gradient field. However, in numerical implementations the condition number of the stiffness matrix is negatively affected by this non-uniqueness. The computational costs of an iterative solver increases, which motivates the use of tools to fix the vector potential, see Landis [132] and Semenov et al. [222]. There are different methods such as the Coulomb gauge, that induce an additional constraint on the vector potential, namely $\mathrm{Div}\,\boldsymbol{a}^e = 0$. Making use of advanced finite elements, such as edge elements, as suggested by Nédélec [181] and Nédélec [182], a priori satisfies the Coulomb gauge condition, however are non-standard and rather inconvenient to implement. While the suggested methods fix the non-uniqueness of the vector potential, additional difficulties arise with the use of gauging approaches. Especially for composite materials, characterized by large differences in electrical susceptibility between two materials, inaccuracies in the local solutions of the electric displacement fields are observed, as discussed in Semenov et al. [222].
It is important to note though, that by restriction to two dimension $d = 2$, the vector potential is unique, as $\mathbb{D}$ reduces to the simple form $\mathbb{D}_1 = \{ -\partial a_z^e/\partial y \}$ and $\mathbb{D}_2 = \{ \partial a_z^e/\partial x \}$, only depending on the entry a_z^e. In the following we stay in three dimensions.

6.7.1. The extended canonical potential with Coulomb gauge

The canonical potential as introduced in (6.3) is extended by a Coulomb gauge condition to ensure the uniqueness of the vector potential, resulting in the extended potential

$$\widetilde{\Pi}(\boldsymbol{\varphi}, \boldsymbol{a}^e) = \int_{\mathcal{B}} \psi(\nabla\boldsymbol{\varphi}, \mathrm{Curl}\,\boldsymbol{a}^e)\, dV + \int_{\mathcal{B}} \psi_{gauge}(\mathrm{Div}\,\boldsymbol{a}^e)\, dV - \Pi_{ext}\,, \tag{6.36}$$

with the penalty-type Coulomb gauge term

$$\psi_{gauge}(\mathrm{Div}\,\boldsymbol{a}^e) = \frac{\epsilon}{2}(\mathrm{Div}\,\boldsymbol{a}^e)^2. \tag{6.37}$$

This term ensures for a penalty parameter $\epsilon \to \infty$ a divergence-free vector potential in the body $\mathcal{B}$.

Variational principle and extended Euler equations. With the extended potential $\widetilde{\Pi}$ at hand, finite electro-elasticity is governed by the pure minimization principle

$$\{\boldsymbol{\varphi}, \boldsymbol{a}^e\} = \arg\{ \inf_{\boldsymbol{\varphi}\in\mathcal{W}_{\boldsymbol{\varphi}}} \inf_{\boldsymbol{a}^e\in\mathcal{W}_{\boldsymbol{a}^e}} \widetilde{\Pi}(\boldsymbol{\varphi}, \boldsymbol{a}^e)\}\,, \tag{6.38}$$

that determines the deformation field $\boldsymbol{\varphi}$ and the vector potential $\boldsymbol{a}^e$, while accounting for Dirichlet-type boundary conditions as given in the admissible function spaces (6.6) and (6.7). For arbitrary fields of virtual deformations, that satisfy $\delta\boldsymbol{\varphi} \in \mathcal{W}_{\boldsymbol{\varphi}} := \{\delta\boldsymbol{\varphi} \,|\, \delta\boldsymbol{\varphi} = \boldsymbol{0} \text{ on } \partial\mathcal{B}_{\boldsymbol{\varphi}}\}$, and fields of virtual electric vector potentials, satisfying $\delta\boldsymbol{a}^e \in \mathcal{W}^e_{\boldsymbol{a}} := \{\delta\boldsymbol{a}^e \in H(\mathrm{Curl}, \mathcal{B}) \cap H(\mathrm{Div}, \mathcal{B}) \,|\, \boldsymbol{N} \times \delta\boldsymbol{a}^e = \boldsymbol{0} \text{ on } \partial\mathcal{B}_{\boldsymbol{a}^e} \text{ and } \boldsymbol{N} \cdot \delta\boldsymbol{a}^e = 0 \text{ on } \partial\mathcal{B}_{\mathbb{E}_t}\}$, the necessary condition of the minimization problem (6.38) reads

$$\begin{aligned} \delta\widetilde{\Pi} = & \int_{\mathcal{B}} [\partial_{\boldsymbol{F}}\psi : \nabla\delta\boldsymbol{\varphi} + \partial_{\mathbb{D}}\psi \cdot \mathrm{Curl}\,\delta\boldsymbol{a}^e + \partial_{\mathrm{Div}\,\boldsymbol{a}^e}\psi_{gauge}\,\mathrm{Div}\,\delta\boldsymbol{a}^e]\,dV \\ & - \int_{\partial\mathcal{B}_T} \overline{\boldsymbol{T}} \cdot \delta\boldsymbol{\varphi}\,dA - \int_{\partial\mathcal{B}_{\mathbb{E}_t}} \overline{\mathbb{E}}_t \cdot \delta\boldsymbol{a}^e\,dA - \int_{\mathcal{B}} \overline{\boldsymbol{\gamma}}^m \cdot \delta\boldsymbol{\varphi}\,dV = 0\,. \end{aligned} \tag{6.39}$$

Taking into account Gauss-type integral theorems, one obtains after localization the extended set of Euler equations

1.	*Balance of linear momentum*	$\mathrm{Div}[\partial_{\boldsymbol{F}}\psi] + \overline{\boldsymbol{\gamma}}^m$	$= \boldsymbol{0}$	in $\mathcal{B}$
2.	*Faraday's law*	$\mathrm{Curl}[\partial_{\mathbb{D}}\psi] + \epsilon\,\mathrm{Grad}[\mathrm{Div}\,\boldsymbol{a}^e]$	$= \boldsymbol{0}$	in $\mathcal{B}$
3.	*Prescribed tractions*	$\partial_{\boldsymbol{F}}\psi \cdot \boldsymbol{N}$	$= \overline{\boldsymbol{T}}$	on $\partial\mathcal{B}_{\boldsymbol{T}}$
4.	*Tangential electric field*	$\partial_{\mathbb{D}}\psi \times \boldsymbol{N}$	$= \overline{\mathbb{E}}_t$	on $\partial\mathcal{B}_{\mathbb{E}_t}$
5.	*Coulomb gauge*	$\epsilon\,\mathrm{Div}\,\boldsymbol{a}^e$	$= 0$	on $\partial\mathcal{B}_{\boldsymbol{a}^e}$

(6.40)

Next to the constitutive relationships for the first Piola stress tensor $\boldsymbol{P} := \partial_{\boldsymbol{F}}\psi$ and the Lagrangian electric field $\mathbb{E} := \partial_{\mathbb{D}}\psi$, one identifies the constraint stemming from the additional Coulomb gauge energy $(6.40)_5$. In the following this ansatz is called the *extended canonical energy* which will be compared to a Hu-Washizu-type mixed formulation.

Finite element implementation. A direct numerical implementation of the energy formulation with additional Coulomb gauge condition in terms of an electric vector potential and prescribed electric Dirichlet conditions on the whole boundary is in focus. The subsequent compact notation of the finite element implementation is based on the generalized array

$$\mathsf{F} := [\,\nabla\boldsymbol{\varphi}, \mathrm{Curl}\,\boldsymbol{a}^e, \mathrm{Div}\,\boldsymbol{a}^e\,]^T\,. \tag{6.41}$$

A finite element discretization is realized in terms of an interpolation matrix $\underline{\mathbf{B}}$ [1] and a global vector of degrees of freedom

$$\underline{\mathbf{d}} = \mathop{\mathbf{A}}_{I=1}^{N^h} [\, \boldsymbol{\varphi},\, \boldsymbol{a}^e \,]_I^T \in \mathcal{R}^{(d+3)N^h} \tag{6.42}$$

at the nodes of the finite element mesh, here with the dimension $d = 3$. The discretized general array reads

$$\mathbf{F}(\boldsymbol{X}, t) \approx \mathbf{F}^h = \underline{\mathbf{B}}(\boldsymbol{X})\underline{\mathbf{d}}(t)\,. \tag{6.43}$$

With this ansatz at hand, the discretized potential (6.36) is given as

$$\widetilde{\Pi}^h(\underline{\mathbf{d}}) = \mathop{\mathbf{A}}_{\#=1}^{E^h} \Big\{ \int_{\mathcal{B}^h_\#} \Psi(\underline{\mathbf{B}}_\# \underline{\mathbf{d}}_\#)\, dV - \int_{\mathcal{B}^h_\#} \underline{\mathbf{N}}_\# \underline{\mathbf{d}}_\# \cdot \overline{\boldsymbol{\gamma}}^m\, dV \int_{\partial\mathcal{B}^h_\#} \underline{\mathbf{N}}_\# \underline{\mathbf{d}}_\# \cdot \overline{\boldsymbol{T}}\, dA \Big\}\,, \tag{6.44}$$

in terms of the total energy $\Psi(\nabla\boldsymbol{\varphi}, \operatorname{Curl} \boldsymbol{a}^e, \operatorname{Div} \boldsymbol{a}^e) := \psi(\nabla\boldsymbol{\varphi}, \operatorname{Curl} \boldsymbol{a}^e) + \psi_{Gauge}(\operatorname{Div} \boldsymbol{a}^e)$. The nodal variables $\underline{\mathbf{d}}$ of the finite element mesh are obtained by the stationary principle of the discrete variational problem

$$\underline{\mathbf{d}} = \arg\{\inf_{\underline{\mathbf{d}}} \widetilde{\Pi}^h(\underline{\mathbf{d}})\}\,. \tag{6.45}$$

First and second derivatives of the potential provide all necessary information for the finite element computation of the equilibrium state. The necessary condition of the discrete variational problem (6.45) reads

$$\underline{\mathbf{R}} := \widetilde{\Pi}^h_{\underline{\mathbf{d}}} = \mathop{\mathbf{A}}_{\#=1}^{E^h} \Big\{ \int_{\mathcal{B}^h_\#} \underline{\mathbf{B}}^T_\# [\partial_{\mathbf{F}} \Psi]\, dV - \int_{\mathcal{B}^h_\#} \underline{\mathbf{N}}^T_\# \cdot \overline{\boldsymbol{\gamma}}^m\, dV \int_{\partial\mathcal{B}^h_\#} \underline{\mathbf{N}}^T_\# \cdot \overline{\boldsymbol{T}}\, dA \Big\} = \boldsymbol{0}\,, \tag{6.46}$$

and provides a non-linear algebraic system of equations for the determination of the nodal variables $\underline{\mathbf{d}}$. A standard Newton-type iteration of the system of equations (6.46) updates the generalized displacements by the algorithm

$$\underline{\mathbf{d}} \Leftarrow \underline{\mathbf{d}} - \underline{\mathbf{K}}^{-1}\underline{\mathbf{R}} \quad \text{until} \quad \|\underline{\mathbf{R}}\| < tol \tag{6.47}$$

in terms of the monolithic tangent matrix of the coupled electro-mechanical problem

$$\underline{\mathbf{K}} := \widetilde{\Pi}^h_{\underline{\mathbf{d}}\underline{\mathbf{d}}} = \mathop{\mathbf{A}}_{\#=1}^{E^h} \Big\{ \int_{\mathcal{B}^h_\#} \underline{\mathbf{B}}^T_\# [\partial^2_{\mathbf{F}\mathbf{F}} \Psi] \underline{\mathbf{B}}_\#\, dV \Big\}\,. \tag{6.48}$$

For $\|\underline{\mathbf{R}}\| < tol$ the equilibrium state is determined.

[1] **Shapes of extended energy FE formulation.** A vector storage of the generalized gradient array (6.41) in the form

$$\mathbf{F} := [\, F_{11}, F_{22}, F_{33}, F_{12}, F_{23}, F_{13}, F_{21}, F_{32}, F_{31}, \mathbb{D}_1, \mathbb{D}_2, \mathbb{D}_3, \operatorname{Div} \boldsymbol{a}^e \,]^T$$

results in the structure of the gradient interpolation matrix related to a finite element # and node I

$$\underline{\mathbf{B}}^I_\# = \begin{bmatrix} N_{,1} & & & N_{,2} & & N_{,3} & & & & & & \\ & N_{,2} & & & N_{,3} & & N_{,1} & & & & & \\ & & N_{,3} & & & & & N_{,2} & N_{,1} & & & \\ & & & & & & & & & N_{,3} & -N_{,2} & N_{,1} \\ & & & & & & & & & -N_{,3} & & N_{,1} \\ & & & & & & & & & N_{,2} & -N_{,1} & \end{bmatrix}^T_I\,,$$

in terms of the shape functions N_I and their material derivatives.

6.7.2. Extended mixed formulation of Hu-Washizu-type

A general Hu-Washizu ansatz is used that defines, next to the deformation $\boldsymbol{\varphi}$ and the vector potential $\boldsymbol{a}^e$, two additional variables. These constitutive variables are equivalent to the divergence of the vector potential v and a Lagrange-parameter-type variable Λ. This ansatz is expected to deal with the difficulties and disadvantages of the penalty formulation presented in later stages of this chapter, namely problem-specific penalty parameters and non-accurate local field solutions. The extended mixed Hu-Washizu (HW) potential is defined as

$$\widetilde{\Pi}_{HW}(\boldsymbol{\varphi}, \boldsymbol{a}^e, v, \Lambda) = \int_{\mathcal{B}} \psi(\nabla\boldsymbol{\varphi}, \operatorname{Curl}\boldsymbol{a}^e)\, dV + \int_{\mathcal{B}} \{\psi_{gauge}(v) + \Lambda[\operatorname{Div}\boldsymbol{a}^e - v]\}\, dV - \Pi_{ext}\,, \tag{6.49}$$

with a redefined energy contribution of the gauge condition $\psi_{gauge} = \frac{\epsilon}{2}v^2$. The split $\partial\mathcal{B} = \partial\mathcal{B}_{\boldsymbol{T}} \cup \partial\mathcal{B}_{\boldsymbol{\varphi}}$ and $\partial\mathcal{B} = \partial\mathcal{B}_{\mathbb{E}_t} \cup \partial\mathcal{B}_{\boldsymbol{a}^e}$ for the mechanical and the electrical boundaries is still valid.

Variational principle and extended Euler equations. The mixed potential $\widetilde{\Pi}_{HW}$ yields a four-field saddle-point principle of finite electro-elasticity

$$\{\boldsymbol{\varphi}, \boldsymbol{a}^e\, v, \Lambda\} = \arg\{\inf_{\boldsymbol{\varphi}\in\mathcal{W}_{\boldsymbol{\varphi}}} \inf_{\boldsymbol{a}^e\in\widetilde{\mathcal{W}}_{\boldsymbol{a}^e}} \sup_{\Lambda\in L^2} \inf_{v\in L^2} \widetilde{\Pi}_{HW}(\boldsymbol{\varphi}, \boldsymbol{a}, v, \Lambda)\} \tag{6.50}$$

that determines, additionally to the deformation field $\boldsymbol{\varphi}$ and the vector potential $\boldsymbol{a}^e$, the gauge variable v and its Lagrange-type dual Λ. Note, that the admissible function space of the vector potential simplifies to

$$\widetilde{\mathcal{W}}_{\boldsymbol{a}^e} := \{\boldsymbol{a}^e \in H(\operatorname{Curl}, \mathcal{B}) \cap H^1(\mathcal{B}) |\ \boldsymbol{N}\times\boldsymbol{a}^e = \overline{\boldsymbol{a}^e}_t \text{ on } \partial\mathcal{B}_{\boldsymbol{a}^e} \text{ and } \boldsymbol{a}^e = \boldsymbol{0} \text{ on } \partial\mathcal{B}_{\mathbb{E}_t}\}\,, \tag{6.51}$$

while $\{\, v, \Lambda \,\} \in L^2$ need to be square integrable. The necessary condition for the stationary principle (6.50) demands a vanishing first variation

$$\begin{aligned}\delta\widetilde{\Pi}_{HW} =& \int_{\mathcal{B}} \{\partial_{\boldsymbol{F}}\psi : \nabla\delta\boldsymbol{\varphi} + \partial_{\mathbb{D}}\psi \cdot \operatorname{Curl}\delta\boldsymbol{a}^e\}\, dV \\ &+ \int_{\mathcal{B}} \{\Lambda \operatorname{Div}\delta\boldsymbol{a}^e + \partial_v\psi_{gauge}\,\delta v - \Lambda\,\delta v + [\operatorname{Div}\boldsymbol{a}^e - v]\,\delta\Lambda\}\, dV \\ &- \int_{\partial\mathcal{B}_{\boldsymbol{T}}} \overline{\boldsymbol{T}} \cdot \delta\boldsymbol{\varphi}\, dA - \int_{\partial\mathcal{B}_{\mathbb{E}_t}} \overline{\mathbb{E}}_t \cdot \delta\boldsymbol{a}^e\, dA - \int_{\mathcal{B}} \overline{\gamma}^m \cdot \delta\boldsymbol{\varphi}\, dV = 0\,,\end{aligned} \tag{6.52}$$

for all $\delta\boldsymbol{\varphi} \in \mathcal{W}_{\boldsymbol{\varphi}}$, $\delta\boldsymbol{a}^e \in \widehat{\mathcal{W}}_{\boldsymbol{a}^e} := \{\delta\boldsymbol{a}^e \in H(\operatorname{Curl}, \mathcal{B}) \cap H^1(\mathcal{B}) |\ \boldsymbol{N}\times\delta\boldsymbol{a}^e = \boldsymbol{0} \text{ on } \partial\mathcal{B}_{\boldsymbol{a}^e} \text{ and } \delta\boldsymbol{a}^e = \boldsymbol{0} \text{ on } \partial\mathcal{B}_{\mathbb{E}_t}\}$ and $\{\, \delta v, \delta\Lambda \,\} \in L^2$. This yields, after applying Gauss-type integration theo-

rems and localization, the extended set of Euler equations

$$
\begin{array}{llrll}
1. & \textit{Balance of linear momentum} & \mathrm{Div}[\partial_{\boldsymbol{F}}\psi] + \overline{\boldsymbol{\gamma}}^{m} &= \boldsymbol{0} & \text{in } \mathcal{B} \\
2. & \textit{Faraday's law} & \mathrm{Curl}[\partial_{\mathbb{D}}\psi] + \nabla\Lambda &= \boldsymbol{0} & \text{in } \mathcal{B} \\
3. & \textit{Prescribed tractions} & \partial_{\boldsymbol{F}}\psi \cdot \boldsymbol{N} &= \overline{\boldsymbol{T}} & \text{on } \partial\mathcal{B}_{\boldsymbol{T}} \\
4. & \textit{Tangential electric field} & \partial_{\mathbb{D}}\psi \times \boldsymbol{N} &= \overline{\mathbb{E}}_t & \text{on } \partial\mathcal{B}_{\mathbb{E}_t} \\
5. & \textit{Gauge variable} & v - \mathrm{Div}\,\boldsymbol{a}^e &= 0 & \text{in } \mathcal{B} \\
6. & \textit{Lagrange-type dual} & \Lambda - \partial_v\psi_{gauge} &= 0 & \text{in } \mathcal{B} \\
7. & \textit{Lagrange-type dual} & \Lambda &= 0 & \text{on } \partial\mathcal{B}_{\boldsymbol{a}^e}
\end{array}
\tag{6.53}
$$

The constitutive equations $\boldsymbol{P} := \partial_{\boldsymbol{F}}\psi$, $\mathbb{E} := \partial_{\mathbb{D}}\psi$ as well as the conditions $v := \mathrm{Div}\,\boldsymbol{a}^e$ and $\Lambda := \partial_v\psi_{gauge}$ are apparent. This ansatz is referred to as *mixed Hu-Washizu principle*.

Finite element implementation. In the sense of a Hu-Washizu principle, two additional variables, namely the gauge variable v and its Lagrange-type dual Λ are introduced, that are computed only in the center of the finite element #. For that, average interpolation matrices are evaluated and additional residual and tangent terms stemming from the mixed variables are employed. The first variation of the mixed Hu-Washizu potential yields the conditions for the gauge variable v and the Lagrange-type parameter Λ as displayed in $(6.53)_{5,6,7}$. We assume that these variables are globally discontinuous but constant within one finite element domain $\mathcal{B}_{\#}$. Focusing on electric Dirichlet problems the discretized mixed variational principle reads

$$
\{\boldsymbol{\varphi}, \boldsymbol{a}^e, v_{\#}, \Lambda_{\#}\} = \arg\{ \inf_{\boldsymbol{\varphi}\in\mathcal{W}_{\boldsymbol{\varphi}}} \inf_{\boldsymbol{a}^e\in\widetilde{\mathcal{W}}_{\boldsymbol{a}^e}} \sup_{\Lambda\in L^2} \inf_{v\in L^2} \widetilde{\Pi}^h_{HW}(\boldsymbol{\varphi}, \boldsymbol{a}^e, v_{\#}, \Lambda_{\#}) \}\,. \tag{6.54}
$$

In a preceding integration, averaged gradient interpolation matrices for the evaluation of the mixed variables are computed on the element level

$$
\underline{\overline{\mathbf{B}}}^{v}_{\#} = \frac{1}{|\mathcal{B}_{\#}|} \int_{\mathcal{B}_{\#}} \underline{\mathbf{B}}^{v}_{\#}\; dV_{\#}\,. \tag{6.55}
$$

Here, the interpolation matrix $\underline{\mathbf{B}}^{v}_{\#}$ is used to compute $\mathrm{Div}\,\boldsymbol{a}^e$ which, related to a node I of element #, has the form

$$
\underline{\mathbf{B}}^{v\,I}_{\#} = \begin{bmatrix} \cdot & \cdot & \cdot & N_{,1} & N_{,2} & N_{,3} \end{bmatrix}^T_I\,. \tag{6.56}
$$

A condensed potential is constructed by optimizing (6.54) on element level with respect to the discrete mixed variables $v_{\#}$ and $\Lambda_{\#}$ such that

$$
\widetilde{\Pi}^h_{HW,cond}(\boldsymbol{\varphi}, \boldsymbol{a}^e) = \inf_{v_{\#}} \sup_{\Lambda_{\#}} \{ \widetilde{\Pi}^h_{HW}(\boldsymbol{\varphi}, \boldsymbol{a}^e, v_{\#}, \Lambda_{\#}) \}\,, \tag{6.57}
$$

where the necessary condition of this variational problem is employed to evaluate the gauge variable by volume averaging, and its Lagrange-type dual as

$$
v^h_{\#} = \frac{1}{|\mathcal{B}_{\#}|}\, \underline{\mathbf{d}} \int_{\mathcal{B}_{\#}} \underline{\overline{\mathbf{B}}}^{v}_{\#}\; dV_{\#} \quad \text{and} \quad \Lambda^h_{\#} = \epsilon v_{\#}\,. \tag{6.58}
$$

With these known variables, the condensed potential in terms of the discrete generalized primary field array $\mathbf{F} := [\,\nabla\boldsymbol{\varphi}, \operatorname{Curl}\boldsymbol{a}^e\,]^T \approx \mathbf{F}^h = \underline{\mathbf{B}}(\boldsymbol{X})\underline{\mathbf{d}}(t)$ with the interpolation matrix $\underline{\mathbf{B}}$ [2] and global vector of degrees of freedom

$$\underline{\mathbf{d}} = \mathop{\mathbf{A}}_{I=1}^{N^h} [\,\boldsymbol{\varphi},\, \boldsymbol{a}^e\,]_I^T \in \mathcal{R}^{(d+3)N^h} \tag{6.59}$$

is given as

$$\widetilde{\Pi}^h_{HW,cond}(\underline{\mathbf{d}}) = \mathop{\mathbf{A}}_{\#=1}^{E^h} \Big\{ \int_{\mathcal{B}^h_\#} \psi(\underline{\mathbf{B}}_\#\underline{\mathbf{d}}_\#)\, dV - \int_{\mathcal{B}^h_\#} \underline{\mathbf{N}}_\#\underline{\mathbf{d}}_\# \cdot \overline{\boldsymbol{\gamma}}^m\, dV \int_{\partial\mathcal{B}^h_\#} \underline{\mathbf{N}}_\#\underline{\mathbf{d}}_\# \cdot \overline{\boldsymbol{T}}\, dA \Big\}. \tag{6.60}$$

The nodal variables $\underline{\mathbf{d}}$ are obtained by the stationary principle, which yields, by a first derivative, the extended residuum with additional constant term

$$\underline{\mathbf{R}} := \mathop{\mathbf{A}}_{\#=1}^{E^h} \Big\{ \Lambda_\# |\mathcal{B}_\#| \underline{\overline{\mathbf{B}}}^v_\# + \int_{\mathcal{B}^h} \underline{\mathbf{B}}^T [\partial_{\mathbf{F}}\psi]\, dV - \int_{\mathcal{B}^h_e} \underline{\mathbf{N}}^T_\# \cdot \overline{\boldsymbol{\gamma}}^m\, dV \int_{\partial\mathcal{B}^h_\#} \underline{\mathbf{N}}^T_e \cdot \overline{\boldsymbol{T}}\, dA, \Big\} \tag{6.61}$$

and by the second derivative the tangent matrix of the coupled system of equations

$$\underline{\mathbf{K}} := \mathop{\mathbf{A}}_{\#=1}^{E^h} \Big\{ \epsilon\, |\mathcal{B}_\#|^2 \underline{\overline{\mathbf{B}}}^{v\,T}_\# \underline{\overline{\mathbf{B}}}^v_\# + \int_{\mathcal{B}^h} \underline{\mathbf{B}}^T [\partial^2_{\mathbf{FF}}\psi] \underline{\mathbf{B}}\, dV \Big\}. \tag{6.62}$$

A Newton-update iterates the equilibrium state such that $\underline{\mathbf{d}} \Leftarrow \underline{\mathbf{d}} - \underline{\mathbf{K}}^{-1}\underline{\mathbf{R}}$ until $\|\underline{\mathbf{R}}\| < tol$.

6.7.3. Equivalent reduced integration ansatz

An equivalent and arguably simpler approach to the Hu-Washizu-type principle, as suggested above, can be found by employing a reduced integration on the extended gauge energy of the canonical potential introduced in (6.36). To show the analogy between the two approaches, we compare the element residuum of the Hu-Washizu approach with the element residuum of the reduced integration scheme. To this end, we split the potential

$$\widetilde{\Pi} = \int_{\mathcal{B}} \psi_{full}(\nabla\boldsymbol{\varphi}, \operatorname{Curl}\boldsymbol{a}^e)\, dV + \int_{\mathcal{B}} \psi_{red}(\operatorname{Div}\boldsymbol{a}^e)\, dV - \Pi_{ext} \tag{6.63}$$

into two parts, where the gauge energy contribution (6.37), now referred to as $\psi_{red}(\operatorname{Div}\boldsymbol{a}^e)$, is assumed to be integrated by a reduced Gauss quadrature in one center point of the

[2] **Shapes of Hu-Washizu-type mixed FE formulation.** A vector storage of the generalized gradient array in the form

$$\mathbf{F} := [\,F_{11}, F_{22}, F_{33}, F_{12}, F_{23}, F_{13}, F_{21}, F_{32}, F_{31}, \mathbb{D}_1, \mathbb{D}_2, \mathbb{D}_3\,]^T$$

results in the structure of the gradient interpolation matrix related to node I of the element $\#$

$$\underline{\mathbf{B}}^I_\# = \begin{bmatrix} N_{,1} & & & N_{,2} & & N_{,3} & & & & & & \\ & N_{,2} & & & N_{,3} & & N_{,1} & & & & & \\ & & N_{,3} & & & & & N_{,2} & N_{,1} & & & \\ & & & & & & & & & N_{,3} & -N_{,2} & \\ & & & & & & & & & -N_{,3} & & N_{,1} \\ & & & & & & & & & N_{,2} & -N_{,1} & \end{bmatrix}^T_I .$$

element, while a standard Gauss quadrature with $2 \times 2 \times 2$ integration points is applied on $\psi_{full}(\nabla\boldsymbol{\varphi}, \operatorname{Curl}\boldsymbol{a}^e)$. The residual expression can be obtained by the first variation with respect to the generalized array $\mathbf{F}$, as defined in (6.41), such that the generalized stresses read

$$\boldsymbol{\mathcal{S}}_{full} = \partial_{\mathbf{F}}\psi_{full} = \begin{bmatrix} \partial_{\boldsymbol{F}}\psi_{full} \\ \partial_{\operatorname{Curl}\boldsymbol{a}^e}\psi_{full} \\ \cdot \end{bmatrix} \quad \text{and} \quad \boldsymbol{\mathcal{S}}_{red} = \partial_{\mathbf{F}}\psi_{red} = \begin{bmatrix} \cdot \\ \cdot \\ \partial_{\operatorname{Div}\boldsymbol{a}^e}\psi_{red} \end{bmatrix}, \tag{6.64}$$

and the related finite element residual is

$$\underline{\mathbf{R}} = \mathop{\mathbf{A}}_{\#=1}^{E^h} \left\{ \sum_{l=1}^{8} \underline{\mathbf{B}}_{\#}^T(\boldsymbol{\xi}_l)\boldsymbol{\mathcal{S}}_{full}^h(\boldsymbol{\xi}_l)\mathfrak{J}(\boldsymbol{\xi}_l) + 8\underline{\mathbf{B}}_{\#}^T(\boldsymbol{\xi}_0)\boldsymbol{\mathcal{S}}_{red}^h(\boldsymbol{\xi}_0)\mathfrak{J}(\boldsymbol{\xi}_0) \right\} = \boldsymbol{0}\,, \tag{6.65}$$

when ignoring the external loading contributions. Here, the coordinates of the quadrature points $\boldsymbol{\xi}_l$ and $\boldsymbol{\xi}_0 = 0$ are used, as well as the determinant of the Jacobian $\mathfrak{J} = \det[\boldsymbol{J}]$ that accounts for the geometrical mapping from parameter to physical space based on $\boldsymbol{J} := \partial\boldsymbol{X}/\partial\boldsymbol{\xi}$. To show the equivalence between this reduced integration and the mixed formulation approach, we compare the residual expression of (6.61) and (6.65). It is obvious that the integral part of (6.61) coincides with the full integration part of (6.65). It remains to show the equivalence of the reduced integration part, based on $\underline{\mathbf{B}}_{\#}(\boldsymbol{\xi}_0)$, with the additional Lagrange-type parameter part, based on the averaged shape functions, or $\overline{\underline{\mathbf{B}}}_{\#}^{v}$, respectively. Using the identity $|\mathcal{B}_{\#}| = 8\mathfrak{J}(\boldsymbol{\xi}_0)$, the definition (6.55) and $\underline{\mathbf{B}}_{\#}^{vI} = \begin{bmatrix} \cdot & \cdot & \cdot & N_{,1} & N_{,2} & N_{,3} \end{bmatrix}_I^T$, and the relation

$$\overline{\nabla}N^I = \nabla N^I(\boldsymbol{\xi}_0) \tag{6.66}$$

between the average shape functions and the shape functions evaluated at $\boldsymbol{\xi}_0$ is evident. For the mixed formulation the term of interest

$$\widetilde{\mathcal{I}} = \Lambda_{\#}|\mathcal{B}_{\#}|\overline{\underline{\mathbf{B}}}_{\#}^{v} = 8\epsilon v_{\#}\overline{\underline{\mathbf{B}}}_{\#}^{v}\mathfrak{J}(\boldsymbol{\xi}_0) = 8\epsilon\overline{\underline{\mathbf{B}}}_{\#}^{v}\underline{\mathbf{d}}_{\#}^{a}\overline{\underline{\mathbf{B}}}_{\#}^{v}\mathfrak{J}(\boldsymbol{\xi}_0) \tag{6.67}$$

should then be equal to the term stemming from the reduced integration

$$\mathcal{I} = 8\underline{\mathbf{B}}_{\#}^T(\boldsymbol{\xi}_0)\partial_{\operatorname{Div}\boldsymbol{a}^e}\psi_{\#,red}(\boldsymbol{\xi}_0)\mathfrak{J}(\boldsymbol{\xi}_0) = 8\underline{\mathbf{B}}_{\#}^T(\boldsymbol{\xi}_0)\epsilon\underline{\mathbf{B}}_{\#}^T(\boldsymbol{\xi}_0)\underline{\mathbf{d}}_{\#}\mathfrak{J}(\boldsymbol{\xi}_0)\,. \tag{6.68}$$

The equation $\mathcal{I} = \tilde{\mathcal{I}}$ indeed holds, when taking the structure of the respective $\underline{\mathbf{B}}$-matrices into account. Therefore, the advantages of the mixed formulation approach can be incorporated in a standard finite element formulation by using a Q1-Q1-red finite element design, as an easy-to-implement alternative.

6.8. Challenges of minimization principles: numerical examples

The above outlined formulations of coupled finite electro-mechanics are now applied to model problems, where we elaborate the difficulties and advantages of both approaches. In the following a simple model structure is presented, governing all relevant effects of electro-mechanics for the canonical energy with Coulomb gauge, as well as the Hu-Washizu-type ansatz, or equally, the reduced integration approach of the extended canonical energy

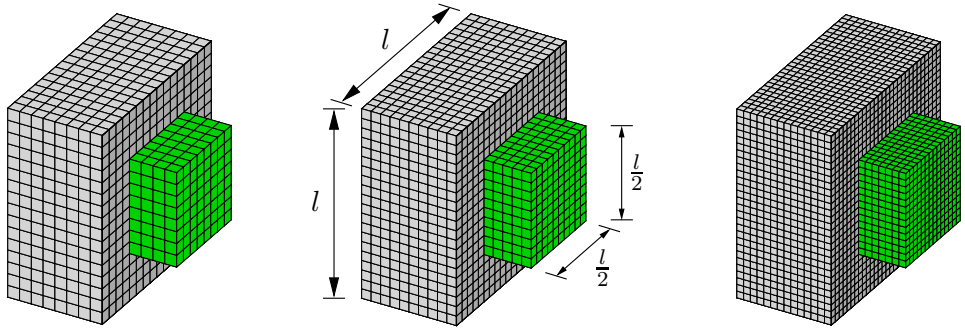

Figure 6.4: *Geometry and discretization of the specimen.* The cubic composite material of dimension $l \times l \times l$ consists of a soft materix material (gray) and a stiff cubic inclusion with high electric susceptibility (green) of dimension $\frac{l}{2} \times \frac{l}{2} \times \frac{l}{2}$. Displayed is only half the surrounding matrix material for better insight. Different mesh densities are considered referred to as h_c, h_m and h_f with $h = \{\, 4096, 8000, 21952 \,\}$ Q1-Q1 brick elements, respectively.

with gauge condition. Note that the presented model problems are related to the findings of Semenov et al. [222], however refined by the suggested mixed ansatz.

The use of an electric vector-potential formulation in terms of numerical speed, accuracy and numerical convenience is in focus. Both, the approach of gauge fixing by a Coulomb penalty method and the mixed formulation are covered and compared to the solution obtained by a standard electric scalar potential computation.

Material modelling and boundary value problem. For the simple case of phenomenological electro-elasticity, the normalized energy storage functions as suggested in (6.32) for the mechanical energy and (6.33) for the coupled part are used. For completeness, the energies are revisited in their normalized form and read

$$\psi'_{mech}(\boldsymbol{C}) = \frac{1}{2}(\mathrm{tr}[\boldsymbol{C}] - 3) + \frac{1}{\beta}(J^{-\beta} - 1) \quad \text{and} \quad \psi'_{elec}(\boldsymbol{C}, \mathbb{D}') = \frac{1}{2(J + \chi^e)}\, \boldsymbol{C} : (\mathbb{D}' \otimes \mathbb{D}') \,. \tag{6.69}$$

Again, they are given in terms of the material parameter $\beta = \frac{\lambda}{\nu} = \frac{2\mu}{1-2\mu}$, $J = \det[\boldsymbol{F}]$, the electric susceptibility χ^e and the normalized electric displacements $\mathbb{D}' := \mathbb{D}/\sqrt{\mu\epsilon_0}$. For the Coulomb gauge the additional penalty energy (6.37) is employed, with the penalty parameter ϵ, while for the Hu-Washizu ansatz $\psi_{HW} := \epsilon v^2 + \Lambda[\mathrm{Div}\, \boldsymbol{a}^e - v]$ is added. The total energies finally add up to

$$\begin{aligned} \Psi'_{CG} &:= \psi'_{mech}(\boldsymbol{C}) + \psi'_{elec}(\boldsymbol{C}, \mathbb{D}') + \psi_{gauge}(\mathrm{Div}\, \boldsymbol{a}^e) \,, \\ \Psi'_{HW} &:= \psi'_{mech}(\boldsymbol{C}) + \psi'_{elec}(\boldsymbol{C}, \mathbb{D}') + \psi_{HW}(v, \Lambda, \mathrm{Div}\, \boldsymbol{a}^e) \,, \end{aligned} \tag{6.70}$$

for the Coulomb gauge (CG) and the Hu-Washizu approach (HW).
For the following boundary-value-problems electro-mechanical composite materials, consisting of a polymeric cube matrix material (gray) with a stiff cube-shaped inclusion (green) of high electric susceptibility, are employed. These kind of specimens are known to induce problems at the so-called reentrant corners, i.e. the corners at the interfaces between the inclusion and the surrounding material, see Demerdash & Wang [52] and Kaltenbacher & Reitzinger [108], especially for gauged energies. Homogeneous materials do not impose difficulties for either formulation. The electric susceptibility of the

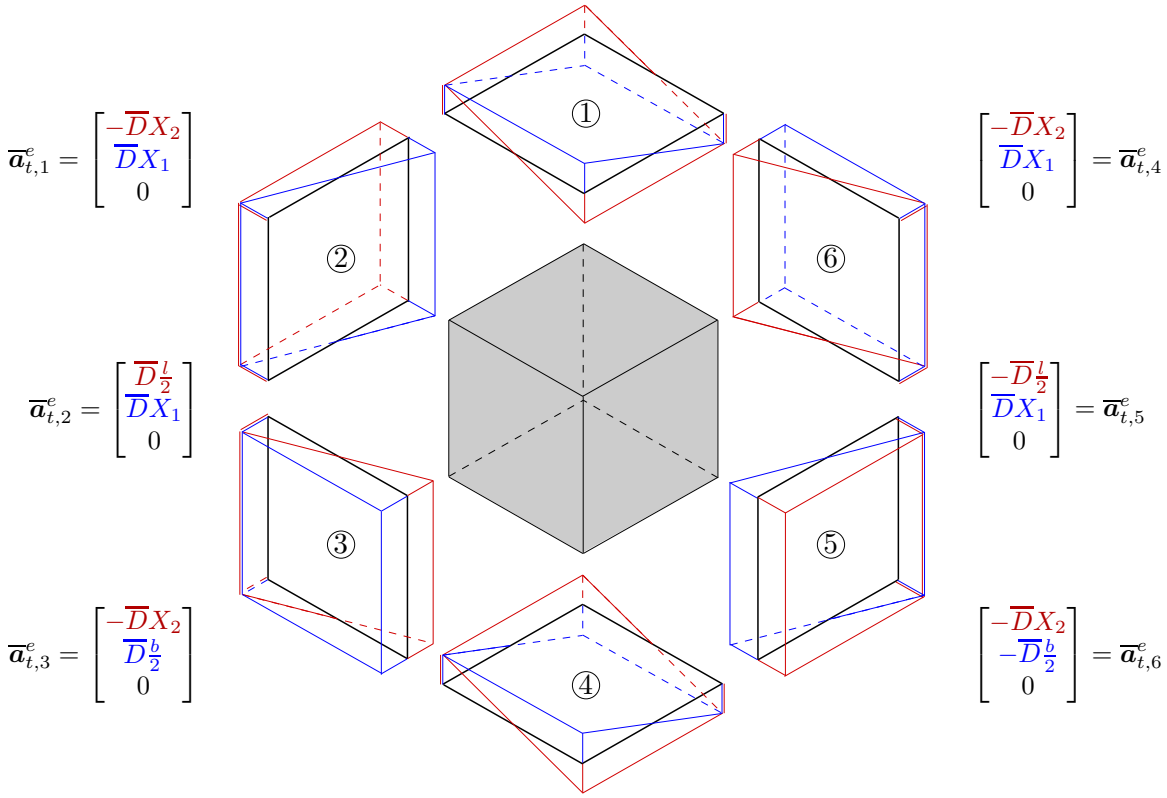

Figure 6.5: *Boundary conditions for vector potential in three dimensions:* Depicted are the boundary conditions for the vector potential $\overline{\boldsymbol{a}}^e_t = \boldsymbol{n} \times \boldsymbol{a}^e$, on each surface of a generalized cube of dimension l, b, h. Note, that the tangential components on all six surfaces need to be prescribed, yielding another difficulties when employing vector potentials in three dimensions.

matrix material is assumed to be $\chi^e_m = 1$, while for the inclusion $\chi^e_i = 1250$. These parameters do not belong to particular materials, however are of physically reasonable range. Geometry and spatial discretization of the specimen, with different mesh densities, are displayed in Figure 6.4. The vector potential is applied as illustrated in Figure 6.5 to induce an electric displacement pointing downwards in negative $\boldsymbol{E}_3$ direction, following the boundary conditions $\overline{\boldsymbol{a}}^e_t = \boldsymbol{N} \times \boldsymbol{a}^e$ on the Dirichlet boundary $\partial\mathcal{B}_{\boldsymbol{a}^e}$. Note, that all surfaces need to be loaded with constant and linear parts, which presents another inconvenience when dealing with vector potential approaches.

Problem 1: accuracy and computational speed of gauged vector potentials. A cut through the specimen is shown in Figure 6.6, with the evolution of the Lagrangian electric displacement along the undeformed $\boldsymbol{E}_1$–axis (dotted line) for $X \in [-0.5, -0.25]$ and $X \in [0.25, 0.5]$ in the matrix material, and in the inclusion for $X \in [-0.25, 0.25]$. The colored lines represent the extended gauged vector potential formulation with varying penalty parameters $\epsilon \in \{0, 1, 10\}$, while the stars display the solution obtained by a standard electric scalar potential formulation, which is used as a reference solution.
Due to the jump in the electric susceptibility inside the inhomogeneous material, it is evident that the resulting normalized electric displacement $\mathbb{D}'_3$ also has a jump at the interface of the two materials. Both, the scalar and vector potential formulations display the jump, however for an increasing penalty factor $\epsilon \to \infty$ the distribution of the electric displacement changes drastically. While for $\epsilon = 0$ both, the scalar and vector potential

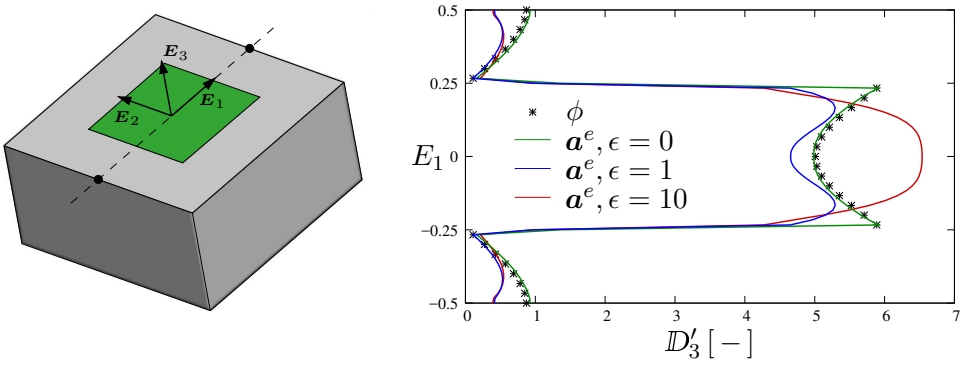

Figure 6.6: *Influence of the penalty parameter on local field solutions.* Gauge fixing induces an inaccurate result in local electric displacement fields. Along the coordinate $\boldsymbol{E}_1$ the jump across the interface of the matrix material (gray) and the inclusion material (green) is displayed for different penalty factors of the Coulomb gauge in comparison to a scalar potential reference solution.

Table 6.2: Computation time of scalar/vector potential for different penalty parameters

	ϕ^e	$\boldsymbol{a}^e, \epsilon = 0$	$\boldsymbol{a}^e, \epsilon = 1$	$\boldsymbol{a}^e, \epsilon = 10$
time in [s]	8801	83975	42609	41032
factor	1	9.5	4.8	4.6

yield the identical result (which is correct, as the energies in either approach coincide as shown above), the additional gauge condition $\operatorname{Div} \boldsymbol{a}^e = 0$, if strongly enforced by a high penalty parameter, changes the local accuracy of the displayed field variable. Note though, that all the presented formulations have problems displaying the correct result, which would be a constant $\mathbb{D}_3'$ in either material, with a jump at the interface. This is due to the chosen 8-noded finite element. Quadratic approximations with 20 nodes are known to produce better results, however induce even more problems with a gauged energy, see Semenov et al. [222].

Comparing the computation times of the boundary value problem, while using an iterative solver for 30 consecutive load steps and $h_f = 21952$ Q1-Q1 brick elements, points out the advantage of a unique vector potential, enforced by the gauge condition. Table 6.2 displays the computation time for the scalar and the vector potential approaches, for varying penalty parameters. While using the vector potential ansatz without Coulomb gauge increases the time relative to the scalar potential by a factor of ≈10, the gauged vector potential can improve the computation time by a factor of 2, in comparison with the ungauged energy due to the improved conditioning of the global stiffness matrix. Naturally, the increased amount of degrees of freedom in the vector potential always results in higher computation times in comparison to the scalar potential. Note, that by further increasing the penalty factor, the computation time is only marginally lowered and the high discrepancies in the local fields do not justify high penalty factors in this specific boundary-value-problem. A compromise when using a vector-potential formulation is a gauged energy with low penalty parameter to ensure computational speed and accuracy within local fields.

Problem 2: influence of mesh densities on standard and mixed approaches. The Hu-Washizu-type mixed formulation is compared to the Coulomb gauge method for

different mesh densities. Again, the representative example of a cubic composite specimen with a stiff and highly susceptible inclusion is studied. A comparison of the accuracy of the numerical solution for local electric displacement fields is shown, while also observing the evolution of $\mathrm{Div}[\boldsymbol{a}^e]$ within the body $\mathcal{B}$, or equally, the violation of the gauge condition. For the three different mesh densities, introduced as h_c, h_m and h_f in Figure 6.4, the local development of the normalized electric displacement field $\mathbb{D}'$ is compared. At first, the penalty parameter $\epsilon = 1$ is chosen, which has proven to be reasonable in the investigation above, and the effect of different meshes is studied. However, to ensure comparability, the penalty parameter is scaled for the different discretization, as it is known to depend quadratically on the mesh densities. The related penalty parameters are summarized in Table 6.3.

In the first row of Figure 6.7 all three entries of the normalized electric displacement vector $\mathbb{D}'$ are shown and plotted over the E_1 coordinate of a cut through the specimen at location $E_2 = 0.125$, $E_3 = 0.125$. Graphical interpretation is provided in the contour plots in the second row of Figure 6.7 as a dashed line for a coordinate system located at the center of the specimen. The coarse mesh with 4096 brick elements is represented by dashed lines, for a Hu-Washizu (HW) ansatz in red and gauge extended canonical scheme (CG) in blue, while the fine mesh of 21952 brick elements is associated with the full lines. As a reference solution the electric displacements based on a scalar potential approach is highlighted by the the black line. The differences of the local electric displacement fields are especially pronounced in $\boldsymbol{E}_2$ and $\boldsymbol{E}_3$ direction, where the jump of $\mathbb{D}'$ is visible due to different susceptibilities of the two materials. Here, it is evident that the HW ansatz is superior to the CG formulation and captures the jump in $\mathbb{D}'$ qualitatively better, especially for finer discretizations.

To investigate and interpret where the differences in the electric displacements with regard to the reference solution of the scalar potential originate from, the divergence of the vector potential is plotted over the coordinate E_1. In the second row of Figure 6.7 the contour plots of $\mathrm{Div}\,\boldsymbol{a}^e$ based on the mesh density h_c are shown. The arrows on the specimen outline the prescribed vector potential, inducing an electric displacement $\mathbb{D} = \mathrm{Curl}\,\boldsymbol{a}^e$. At the interface of the two materials $\mathrm{Div}\,\boldsymbol{a}^e$ has pronounced values unequal to zero which align with the distortion of the local electric displacement fields. This is mainly due to the approximative solution of the finite element method, which produces low, non-zero values for the divergence. These get scaled with the inverse electric susceptibility, the so-called reluctivity Biro et al. [25], which results in higher errors on the side of the highly susceptible inclusion, Semenov et al. [222]. Note again, that a finer mesh reduces $\mathrm{Div}\,\boldsymbol{a}^e$ around the interface, however shifts the peaks into the boundary regions of the specimen.

Problem 3: influence of penalty parameters on CG and HW approaches. In a third study, the penalty parameter ϵ is varied for both the CG and HW scheme and

Table 6.3: Scaling of the penalty parameter for different mesh densities

	elements	$h = h_i/h_c\,, i = \{c, m, f\}$	h^2	$\epsilon_s = \epsilon/h^2$
h_c	4096	1	1	1
h_m	8000	1.95	3.80	0.2630
h_f	21952	5.36	28.73	0.0348

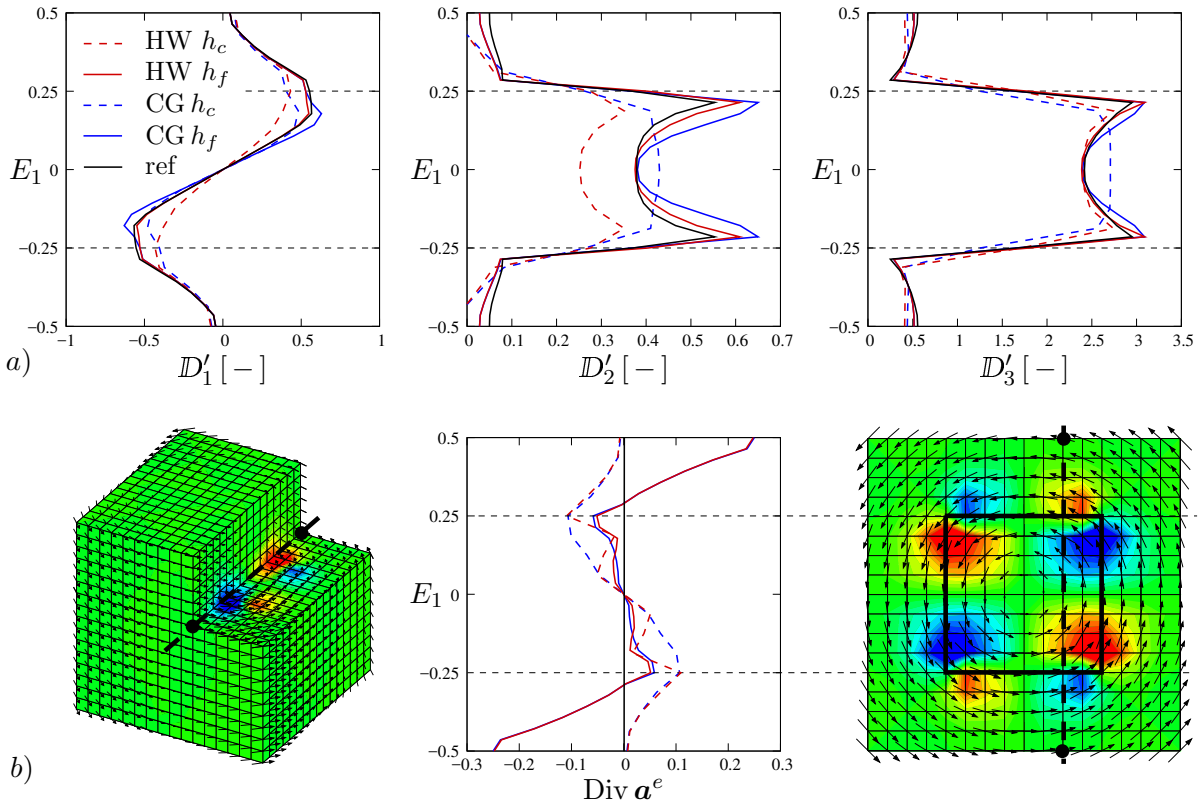

Figure 6.7: *Mesh refinement study for HW and CG approach.* a) The normalized local $\mathbb{D}'$-field is plotted over the coordinate E_1 for CG and HW formulations. Different mesh densities are considered referred to as h_c and h_f, with $\{\,4096,\,21952\,\}$ brick elements, respectively. The reference solution is obtained by a scalar potential approach (black line). b) The second row displays $\operatorname{Div}\boldsymbol{a}^e$ over the coordinate E_1, as well as the vector potential $\boldsymbol{a}^e$ as arrows inducing an electric displacement $\mathbb{D}_3$. Extreme values of $\operatorname{Div}\boldsymbol{a}^e$ arise at the interface between the two materials for the coarse mesh, and at the boundary of the specimen for the fine mesh. This error is qualitatively more pronounced for the CG ansatz.

different discretizations h_c, h_m and h_f are used. Again a comparison in the local electric displacement field is shown in Figure 6.8. In Figure 6.8a the Coulomb gauge is displayed with different penalty parameters $\epsilon = \{\,10,\,1,\,0.1,\,0.01\,\}$, in comparison with the scalar potential reference solution. Note that the used penalty parameters are arbitrarily chosen, however appear to give good results. From left to right, the mesh densities are increased, yielding a better accordance to the reference solution, especially for low penalty parameters. However, it is apparent that the choice of a penalty parameter highly influences the result, especially for coarser meshes. In Figure 6.8b the HW mixed ansatz is shown. Here, the advantage is evident, as the accuracy of the local electric displacement $\mathbb{D}'_3$ is reasonable for all mesh densities and penalty parameters chosen in this study. This yields to a far more convenient application of the vector potential, as, due to coarser meshes, the computation time is reduced while still maintaining an accurate solution without the difficulty of choosing a problem specific penalty parameter. Note, that to ensure comparable results scaled penalty parameters are used following the conversion of Table 6.3.

Summary of observations. Using an electric vector potential yielding a pure minimization principle has its advantages especially in terms of the formulation of stability criteria that need to be based on an energetic approach. However, the use of a vector-potential

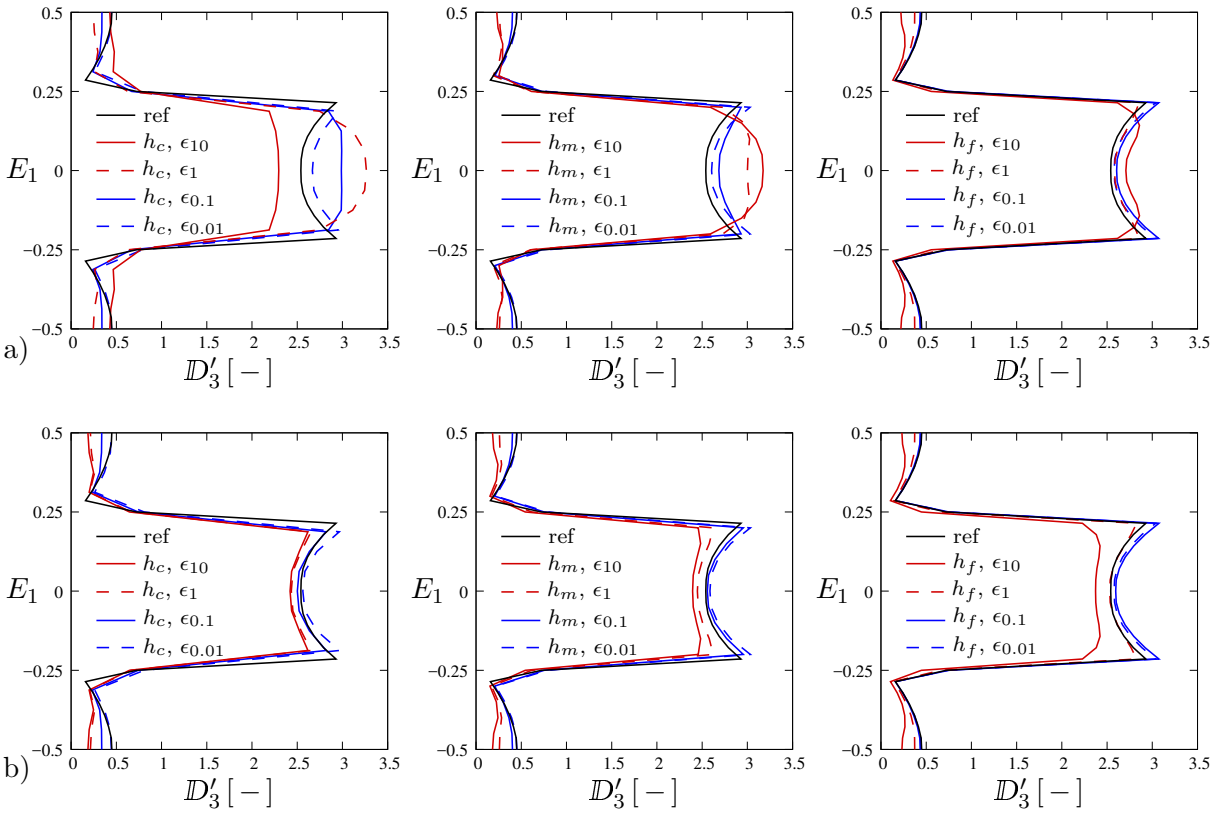

Figure 6.8: *Penalty parameter study for different discretizations.* a) The normalized local $\mathbb{D}_3'$-field is plotted over the coordinate E_1 for a standard finite element ansatz of the Coulomb gauged energy. Different mesh densities and penalty parameters are considered referred to as h_c, h_m and h_f, with $\{\,4096,\ 8000,\ 21952\,\}$ brick elements, respectively. b) Equivalent plots for the HW scheme are displayed. Again, different mesh densities and penalty parameters are considered referred to as h_c, h_m and h_f, with $\{\,4096,\ 8000,\ 21952\,\}$ brick elements, respectively. In both plots, the reference solution (black line) is obtained by a scalar potential approach.

in magneto-electro-statics comes with additional difficulties and draw-backs, namely the non-uniqueness of the vector potential and the overall increased computation time due to additional degrees of freedom in a finite element setting. To handle the non-uniqueness a Coulomb gauge condition implemented by a penalty method is suggested in literature. Computations on a heterogeneous structure with different electric susceptibilities revealed that a gauge condition indeed leads to inaccuracies in local field quantities, especially at the reentrant corners of the material interface. In order to overcome the mentioned difficulties an alternative Hu-Washizu-type finite element formulation can be employed. This formulation coincides with a reduced integration scheme of the extended Coulomb gauge energy. The results of a parameter study depending on different mesh densities and penalty parameters, comparing a scalar potential to the introduced CG and HW vector potential approaches were discussed. Observations can be summarized as follows:

- Vector-potential approaches without Coulomb gauge yield correct results, however tend to be inefficient in terms of computational speed.

- A Coulomb gauge improves the condition number of the stiffness matrix which results in a considerable reduction of the computation time. This is consistent with the findings of Semenov et al. [222].

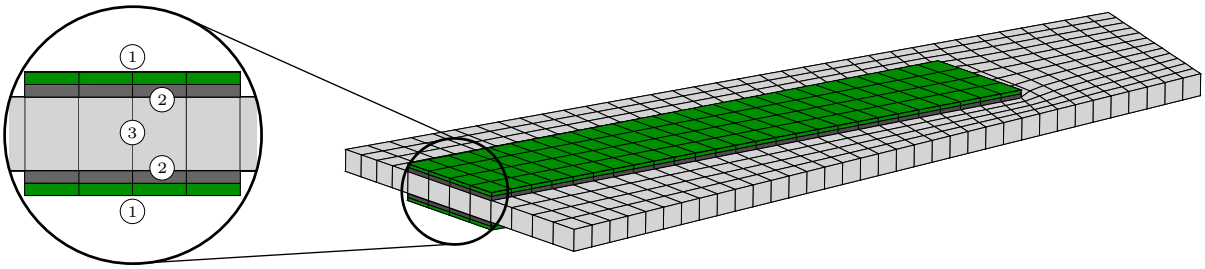

Figure 6.9: *Boundary-value-problem flapping wing.* Two electro-active bi-layers are attached to a wing material (material 3, light gray). The bi-layer consists of a soft electro-active (material 1, green) and a stiff inactive layer (dark gray). A vector potential is applied, such that the resulting electric displacement field points in vertical direction in the active material.

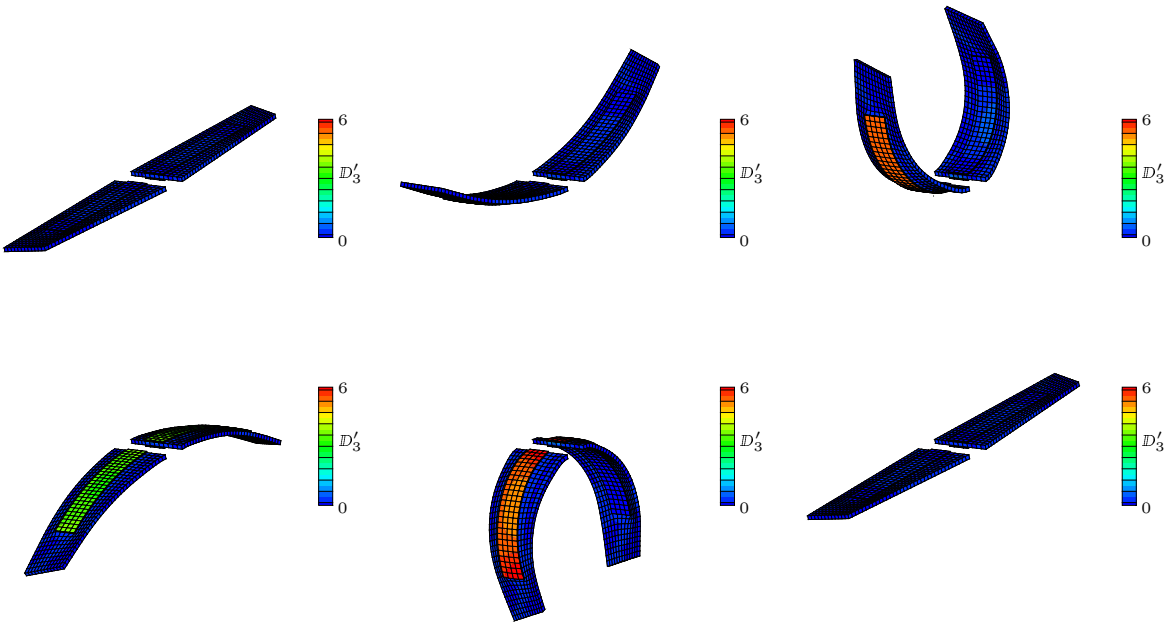

Figure 6.10: *Possible application of EAP.* Electrically induced extension of an EAP in the longitudinal direction causes the wings to curl. Bi-layers on top and bottom of the wing ensure the possibility of bending in positive and negative direction.

- Arising inaccuracies due to the Coulomb gauge can be fixed by higher mesh densities at cost of the computation time, or by a reduced integration of the Coulomb gauge reflecting a mixed HW formulation for the divergence of the vector potential.

- A HW-type formulation is beneficial in terms of computational cost. Coarser meshes can be used while also the inaccuracy of local fields is less pronounced and insensitive to the chosen penalty parameter.

While all these investigations are subjected to phenomenological electro-elasticity, an extension to coupled magneto-elasticity or magneto-electro-elasticity is straightforward.

Table 6.4: Material parameters for flapping wing boundary-value-problem

material	μ	ν	χ
1	$1 \cdot 10^{-2}$	0.35	1250
2	1	0.32	0
3	1	0.32	0

6.9. Electric vector potential: an application

Electro-active polymers (EAP) are prototype materials for a number of technical applications, including soft actuators and artificial muscles Bar-Cohen [10], and Bar-Cohen & Zhang [11]. Electro-active bi-layer materials consist of a soft electro-active strip attached to a stiffer inactive material. By application of an electric field the strip is compressed in thickness direction and stretched in longitudinal direction. Restricted by the stiffness of the attached inactive material the bi-layer material curls. This phenomenon is employed for the development of robot grippers but can also be applied for the movement of wings, in a design study for electro-active flight devices. Such movement of a wing is realized by a multilayered system as proposed in Figure 6.9.

The electro-active bi-layer consists of a soft electro-active material (material 1, green) sandwiched between two electrodes and a stiff inactive material (material 2, dark gray). It is attached to the top and bottom of a wing material (material 3, light gray), arranged such that the electro-active materials are pointing outwards. A vector potential is applied on the electrodes, such that a vertical electric displacement is induced, resulting in a compression of the active material and an elongation in longitudinal direction. The stiff layer prohibits such a deformation, resulting in a curl of the bi-layer and therefore of the whole system. For a movement of the wing over the full range of motion, i.e. upwards and downwards, two electrodes are used in this example. Material parameters of the boundary-value-problem are summarized in Table 6.4. Figure 6.10 displays deformation states for a saw-tooth loading type for the two electrodes. Upward movements are induced by loading the bottom bi-layer, while downward movements are due to loading of the top layer.

— Part III —

Multiscale Magneto-Electro-Mechanical Stability Analysis

Chapter 7

Magneto-Electro-Mechanical Stability Analysis

Soft magneto-electro-mechanical composites show different types of instability phenomena, which may lead to failure of the material or can be exploited for enhancement of their performance. This covers structural instabilities, such as buckling or wrinkling, as well as material instabilities in the form of limit-points in the local constitutive response on both the macro- and the microscale. Experiments of instability phenomena in electro-elasticity can be found in Plante & Dubowsky [195]. The works of Zhao & Suo [279], Zhao et al. [281], Bertoldi & Gei [19], and Siboni et al. [229] provide analytical investigations, see also the review Zhao & Wang [280] on these instability phenomena. In the recent works Miehe et al. [173], and Miehe et al. [174] details on the computational tracking of instabilities in coupled multiphase magneto-electro-active solids are given.
In the case of electro-active materials, especially in dielectric polymers, increasing applied voltages thin down the dielectric considerably. This results in even higher electrical fields for the same voltage which will ultimately further squeeze the material, possibly resulting in an *electrical breakdown*. This failure mode, related to the *pull-in instability*, is one of the key problems with regard to the realization of large electrically induced deformations in electro-active polymers. In both, the modelling of electro-mechanic and magneto-mechanic materials the so-called *limit-point instabilities* are present. This phenomenon is a numerical challenge that can restrict the possible equilibrium path and indicates the onset of further stability issues. In Figure 7.1 the characteristic limit-point behavior of a volume element, related to the pull-in instability, is shown. It is evident, that the full equilibrium path can only be tracked by a suitable choice of the control variables.

In the context of scale-bridging and homogenization, further classes of multiscale instabilities can occur. In the field of coupled magneto-electro-mechanics, instabilities of laminate micro-structures in dielectric composites were analyzed in Rudykh & deBotton [205], Rudykh et al. [208], and in magneto-rheological elastomers by Rudykh & Bertoldi [204]. While the multiscale instabilities are problematic, there is hope for future exploitation of evolving instabilities in magneto-electro-active composites. Enhanced performance of the sensors and actuators might be achieved by willingly incorporating instability effects in the overall response. This motivates the focus on unstable behavior over different scales.

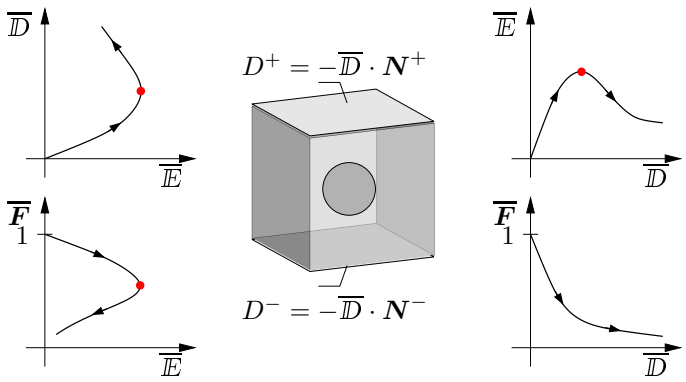

Figure 7.1: *Pre- and post-critical limit-point response in magneto-electro-elasticity.* Displayed is the pull-in instability (indicated by the red dot) of a dielectric micro-structure $\mathcal{B}$. Monotoneously increasing loading by the enthalpy-variable $\overline{\mathbb{E}}$ is restricted to the pre-critical range of the field-displacement $\overline{\mathbb{D}}$-$\overline{\mathbb{E}}$, and field-stretch $\overline{\boldsymbol{F}}$-$\overline{\mathbb{E}}$ equilibrium curves, as displayed on the right. In contrast, loading by the energy-variable $\overline{\mathbb{D}}$ allows a straightforward tracking of the equilibrium curves. This supports the use of energy-based formulations of computational homogenization.

This chapter deals with the development of criteria for an accompanying stability analysis on both the macro- and microscale for phenomenological magneto-electro-elasticity at finite deformations. With regard to the two-scale scenario of computational homogenization the following instability phenomena need to be considered:

- *Microscopic structural instabilities:* This concerns buckling of micro-structural elements (particles, fibers), related to the micro-structural boundary value problem.
- *Microscopic material instabilities:* Snap-through effects such as the pull-in instability, resulting from limit-points in the local micro-structural constitutive response.
- *Macroscopic structural instabilities:* Global phenomena such as buckling and wrinkling of macro-structures, related to the macroscopic boundary value problem.
- *Macroscopic material instabilities:* Snap-through and localization of local macro-structural states due to limit- and bifurcation points of the homogenized response.

In the theory of homogenization of mechanical composites, it is well-known that a connection between long wavelength microscopic structural instabilities and resulting macroscopic material instabilities in the form of a local loss of ellipticity, see Triantafyllidis & Maker [253], Müller [178], Geymonat et al. [74], Miehe et al. [169], Michel et al. [156, 157], Bertoldi & Boyce [18], and Bertoldi et al. [20], is given. To capture this phenomenon, the inherent problem of the cell-size enlargement in nonlinear homogenization of unstable micro-structures can, for periodic composites, be solved by a Bloch wave analysis, see Bertoldi & Boyce [18] for a recent account. Extensions to electro-mechanics have been outlined recently in Bertoldi & Gei [19], Rudykh et al. [208], and Polukhov et al. [196]. This phenomenon however is beyond the scope of this work.

7.1. Structural stability analysis of composite micro-structures

Following conceptually definitions of uniqueness and stability outlined by Hill [89] and Biot [22], the analysis of *structural* stability in the extended setting of magneto-electro-

elastic composites *has to* be based on an *energy functional*, whose second variation needs to be positive semi-definite. While direct energetic approaches based on vector potentials for the modeling of coupled electro-magneto-mechanics do exist, numerically more convenient enthalpy formulations are the standard in literature. An important goal of this work is to express these energy-based statements by enthalpy-based formulations due to a partial Legendre-Fenchel transformation. These mixed formulations can then be exploited in more convenient numerical implementations of the homogenization problem.

7.1.1. Structural stability in the canonical energy formulation

A phenomenological electro-magneto-mechanical micro-state in the canonical energy-based formulation is introduced, characterized by a given deformation and the magnetic and electric vector potentials

$$\mathfrak{s}^0 := \{\, \boldsymbol{\varphi}^0, \boldsymbol{a}^{m\,0}, \boldsymbol{a}^{e\,0} \,\}^T \text{ on } \mathcal{B} \,, \tag{7.1}$$

which are assumed to satisfy an extension to the fully coupled magneto-electro-mechanical minimization principle of (6.5), related to (6.3). Following the notion of convexity and uniqueness of solutions as presented in Chapter 4, the micro-state $\mathfrak{s}^0$ is said to be *globally stable*, if the inequality

$$\overline{\pi}(\mathfrak{s}) - \overline{\pi}(\mathfrak{s}^0) \geq 0 \tag{7.2}$$

holds for *any other admissible state* $\mathfrak{s}$, while satisfying the essential boundary conditions, i.e. $\boldsymbol{\varphi} \in \mathcal{W}_{\varphi}$, $\boldsymbol{a}^e \in \mathcal{W}_{a^e}$, and $\boldsymbol{a}^m \in \mathcal{W}_{a^m}$. Then, the given state $\mathfrak{s}^0$ provides a unique global minimum of the energy functional. Again, as discussed in Chapter 4, this global statement for any arbitrary admissible fields $\mathfrak{s}$ is too restrictive in finite magneto-electro-elasticity. It excludes non-unique solutions related to bifurcation and limit-point instabilities, and induces strong convexity of the energy density function, which is not acceptable. A weaker convexity condition for locally stable micro-states can be developed if $\mathfrak{s}$ is confined to some neighborhood of $\mathfrak{s}^0$. Then, (7.2) is a suitable infinitesimal stability criterion. For the following local structural stability analysis, the deformation $\mathfrak{s}$ is considered to be in the infinitesimal neighborhood of the equilibrium state $\mathfrak{s}^0$, i.e.

$$\mathfrak{s} = \mathfrak{s}^0 + \varepsilon\, \delta\mathfrak{s} \,, \tag{7.3}$$

where $\varepsilon\, \delta\mathfrak{s}$ denotes a perturbation of the equilibrium state $\mathfrak{s}^0$ scaled with an infinitesimally small number ε. A Taylor series expansion of (7.2) up to the second rank gives

$$\overline{\pi}(\mathfrak{s}) - \overline{\pi}(\mathfrak{s}^0) = \frac{d}{d\varepsilon}\Big|_{\varepsilon=0} \overline{\pi}(\mathfrak{s}^0 + \varepsilon\delta\mathfrak{s}) + \frac{1}{2!}\frac{d^2}{d\varepsilon^2}\Big|_{\varepsilon=0} \overline{\pi}(\mathfrak{s}^0 + \varepsilon\delta\mathfrak{s}) \;\geq\; 0 \,, \tag{7.4}$$

where the first and the second directional derivatives are identical to the first and second variations of the functional (6.3) at the equilibrium state $\mathfrak{s}^0$. For an assumed equilibrium state, the first variation vanishes, leaving the condition

$$\overline{\pi}(\mathfrak{s}) - \overline{\pi}(\mathfrak{s}^0) = \frac{1}{2}\frac{d^2}{d\varepsilon^2}\Big|_{\varepsilon=0} \overline{\pi}(\mathfrak{s}^0 + \varepsilon\delta\mathfrak{s}) \;\geq\; 0 \,, \tag{7.5}$$

for a *locally stable deformation state* $\mathfrak{s}^0$. It directly follows, that the infinitesimal stability criterion depends on the sign of the second variation of the macroscopic averaged energy

density at the equilibrium point $\mathfrak{s}^0$. The needed second variation can easily be computed by reformulating (7.5) into

$$\overline{\pi}(\mathfrak{s}) - \overline{\pi}(\mathfrak{s}^0) = \frac{1}{2|\mathcal{B}|} \int_{\mathcal{B}} \delta\mathbf{F} \cdot \mathbf{C}(\mathbf{F}^0) \cdot \delta\mathbf{F} \, dV \;\geq\; 0 \,, \tag{7.6}$$

with the generalized array of primary variables $\mathbf{F} := \{ \boldsymbol{F}, \mathbb{B}, \mathbb{D} \}^T$ and the coupled magneto-electro-mechanical tangent array

$$\mathbf{C} := \partial^2_{\mathbf{F}\mathbf{F}} \psi(\mathbf{F}^0) = \begin{bmatrix} \partial^2_{\boldsymbol{F}\boldsymbol{F}}\psi & \partial^2_{\boldsymbol{F}\mathbb{B}}\psi & \partial^2_{\boldsymbol{F}\mathbb{D}}\psi \\ \partial^2_{\mathbb{B}\boldsymbol{F}}\psi & \partial^2_{\mathbb{B}\mathbb{B}}\psi & \partial^2_{\mathbb{B}\mathbb{D}}\psi \\ \partial^2_{\mathbb{D}\boldsymbol{F}}\psi & \partial^2_{\mathbb{D}\mathbb{B}}\psi & \partial^2_{\mathbb{D}\mathbb{D}}\psi \end{bmatrix} \,. \tag{7.7}$$

7.1.2. Structural stability in the extended energy formulation

Following the idea of an energetic stability criterion based on the more convenient mixed energy-enthalpy function, as an intermediate step, the structural stability criterion of the extended energy formulation is derived. Note that this intermediate configuration is not used in further stages of the work, however is important for the descriptive development of the convenient mixed energy-enthalpy formulation. Characterized by a given deformation field, magnetic and electric vector potentials, *as well as* given magnetic and electric fields

$$\mathfrak{s}^0 := \{ \boldsymbol{\varphi}^0, \boldsymbol{a}^{m\,0}, \boldsymbol{a}^{e\,0}, \mathbb{H}^0, \mathbb{E}^0 \}^T \text{ on } \mathcal{B} \,, \tag{7.8}$$

which satisfy the mixed saddle-point principle related to (6.12) based on the functional $\widetilde{\Pi}$ defined in (6.11), the extended five-field formulation is introduced. As stated in (6.10) it is derived by a Legendre-Fenchel transformation and is of *inf-inf-inf-sup-sup structure*. For a local stability criterion, consider a perturbed admissible state $\mathfrak{s} = \mathfrak{s}^0 + \varepsilon\,\delta\mathfrak{s}$ in the infinitesimal neighborhood of $\mathfrak{s}^0$, satisfying the essential conditions $\boldsymbol{\varphi} \in \mathcal{W}_{\boldsymbol{\varphi}}$, $\boldsymbol{a}^m \in \mathcal{W}_{\boldsymbol{a}^m}$, $\boldsymbol{a}^e \in \mathcal{W}_{\boldsymbol{a}^e}$, $\mathbb{H} \in L^2$ and $\mathbb{E} \in L^2$. Applying the local structural stability condition (7.5), now based on the Taylor series expansion of the extended potential density $\widetilde{\overline{\pi}}$, similarly to (6.11), reveals the criterion

$$\widetilde{\overline{\pi}}(\mathfrak{s}) - \widetilde{\overline{\pi}}(\mathfrak{s}^0) = \frac{1}{2|\mathcal{B}|} \int_{\mathcal{B}} \delta\mathbf{F}_{ext} \cdot \mathbf{C}_{ext}(\mathbf{F}^0_{ext}) \cdot \delta\mathbf{F}_{ext} \, dV \;\geq\; 0 \,, \tag{7.9}$$

with the *extended* array of variables $\mathbf{F}_{ext} := \{\boldsymbol{F}, \mathbb{B}, \mathbb{D}, \mathbb{H}, \mathbb{E}\}^T$ and in terms of the extended magneto-electro-mechanical tangent array

$$\mathbf{C}_{ext} := \partial^2_{\mathbf{F}_{ext}\mathbf{F}_{ext}} \widetilde{\psi}(\mathbf{F}^0_{ext}) = \begin{bmatrix} \partial^2_{\boldsymbol{F}\boldsymbol{F}}\psi^* & \boldsymbol{0} & \boldsymbol{0} & \partial^2_{\boldsymbol{F}\mathbb{H}}\psi^* & \partial^2_{\boldsymbol{F}\mathbb{E}}\psi^* \\ \boldsymbol{0} & \boldsymbol{0} & \boldsymbol{0} & \boldsymbol{1} & \boldsymbol{0} \\ \boldsymbol{0} & \boldsymbol{0} & \boldsymbol{0} & \boldsymbol{0} & \boldsymbol{1} \\ \partial^2_{\mathbb{H}\boldsymbol{F}}\psi^* & \boldsymbol{1} & \boldsymbol{0} & \partial^2_{\mathbb{H}\mathbb{H}}\psi^* & \partial^2_{\mathbb{H}\mathbb{E}}\psi^* \\ \partial^2_{\mathbb{E}\boldsymbol{F}}\psi^* & \boldsymbol{0} & \boldsymbol{1} & \partial^2_{\mathbb{E}\mathbb{H}}\psi^* & \partial^2_{\mathbb{E}\mathbb{E}}\psi^* \end{bmatrix} \,. \tag{7.10}$$

Here, $\widetilde{\psi} := \psi^* + \mathbb{B} \cdot \mathbb{H} + \mathbb{D} \cdot \mathbb{E}$ contains the enthalpy function ψ^* as well as the additional Legendre transformation terms. Note that this short notation accounts for the partial Legendre-Fenchel transformation, where the additional magnetic and electric contributions are obtained by the second and third columns and rows respectively. A reduction of this extended setting, i.e. the elimination of its dependencies on the magnetic induction and electric displacement to obtain the related convenient mixed formulation, is the logical continuation.

7.1.3. Structural stability in the convenient enthalpy formulation

In a final step, the extended mixed energy formulation gets reduced by exploitation of the elimination equations for the magnetic induction and electric displacement, obtained by the partial Legendre-Fenchel transformation. Their respective variations read

$$\delta \mathbb{B} = -\partial^2_{\mathbb{H}\boldsymbol{F}}\psi^* : \delta \boldsymbol{F} - \partial^2_{\mathbb{H}\mathbb{H}}\psi^* \cdot \delta \mathbb{H} - \partial^2_{\mathbb{H}\mathbb{E}}\psi^* \cdot \delta \mathbb{E} \tag{7.11}$$

for the increment of the magnetic induction and

$$\delta \mathbb{D} = -\partial^2_{\mathbb{E}\boldsymbol{F}}\psi^* : \delta \boldsymbol{F} - \partial^2_{\mathbb{E}\mathbb{H}}\psi^* \cdot \delta \mathbb{H} - \partial^2_{\mathbb{E}\mathbb{E}}\psi^* \cdot \delta \mathbb{E} \tag{7.12}$$

for the increment of the electric displacement, based on the derivation of the mixed energy-enthalpy function. Insertion of (7.12) and (7.11) into (7.9) yields the reduced criterion for structural stability of the convenient enthalpy formulation

$$\overline{\pi}^*(\mathfrak{s}) - \overline{\pi}^*(\mathfrak{s}^0) = \frac{1}{2|\mathcal{B}|}\int_{\mathcal{B}} \delta \mathbf{F}^* \cdot \mathbf{C}^*_{stab}(\mathbf{F}^{*\,0}) \cdot \delta \mathbf{F}^*\, dV \;\geq\; 0 \tag{7.13}$$

in terms of the generalized array of the mixed energy-enthalpy formulation $\mathbf{F}^* := \{\, \boldsymbol{F}, \mathbb{H}, \mathbb{E} \,\}^T$ and the reduced tangent array

$$\mathbf{C}^*_{stab} := \begin{bmatrix} \partial^2_{\boldsymbol{F}\boldsymbol{F}}\psi^* & \boldsymbol{0} & \boldsymbol{0} \\ \boldsymbol{0} & -\partial^2_{\mathbb{H}\mathbb{H}}\psi^* & -\partial^2_{\mathbb{H}\mathbb{E}}\psi^* \\ \boldsymbol{0} & -\partial^2_{\mathbb{E}\mathbb{H}}\psi^* & -\partial^2_{\mathbb{E}\mathbb{E}}\psi^* \end{bmatrix} . \tag{7.14}$$

Note the *diagonal structure* of the tangent array, which stands in contrast to the fully populated formulation (7.6) of the energetic approach. This structure can be advantageous for an accompanying finite element stability analysis, as the mechanical and magneto-electrical terms can be analyzed separately. Also, the change of sign of the (coupled) multiphysics fields is important to emphasize here. While the reduced tangent array (7.14) is used for the stability analysis it is not the related tangent for the Newton-type solution scheme of the micro-structure based on the convenient energy-enthalpy and defined by a micro-state

$$\mathfrak{s} := \{\, \boldsymbol{\varphi}, \phi^m, \phi^e \,\}^T \text{ on } \mathcal{B} \,. \tag{7.15}$$

For that, the fully populated tangent is investigated, which is a priori not positive definite for a stable response. This is considered as a specific characteristic of an accompanying stability analysis within the convenient enthalpy formulation.

7.2. Material stability analysis of the micro-structure

In finite elasticity, the necessary condition for *local material instability* is related to a loss of quasi-convexity, a notion introduced by Morrey [175]. Based on this canonical condition weaker conditions are developed, such as the rank-one convexity or ellipticity condition that can be traced back to Hadamard [82], see also Dacorogna [47] for an overview on different notions of weak convexity. The rank-one convexity condition indicates material instability by the loss of positive semi-definiteness of the *acoustic tensor*, which has been widely used in mechanics, see Hill [90], Truesdell & Noll [254],

Ogden [185], Nguyen [184], and model applications as reported for example in Miehe & Schröder [166], Miehe et al. [169], and Miehe & Lambrecht [164]. Extensions to electro-elastic solids can be found in Baesu [6], Baesu et al. [7], Bertoldi & Gei [19], Zhao & Suo [279], Dorfmann & Ogden [55], Suo [240] and the recent works of Rudykh & deBotton [205], Rudykh & Bertoldi [204], Rudykh et al. [208] and Siboni et al. [229] on the stability of dielectric composites. Here, a rigorous derivation of material instability criteria on the micro-structure for all the presented approaches is given, where the focus is set on the development of energetic criteria for the convenient mixed energy-enthalpy formulation.

7.2.1. Material stability in the canonical energy formulation

Quasi-convexity condition. Consider the notion of quasi-convexity, introduced by Morrey [175], as a starting point for a local material stability analysis on the micro-structure. It is extended from pure elasticity as introduced in Chapter 4 to magneto-electro-elasticity by redefining the condition (4.13) for the magneto-electro-static case

$$L(\widehat{\boldsymbol{\varphi}}, \widehat{\boldsymbol{a}}^m, \widehat{\boldsymbol{a}}^e) := \frac{1}{|\mathcal{D}|}\int_{\mathcal{D}} \psi(\boldsymbol{F} + \nabla\widehat{\boldsymbol{\varphi}}, \mathbb{B} + \operatorname{Curl}\widehat{\boldsymbol{a}}^m, \mathbb{D} + \operatorname{Curl}\widehat{\boldsymbol{a}}^e)\, dV \geq \psi(\boldsymbol{F}, \mathbb{B}, \mathbb{D}) \quad (7.16)$$

at a given state $\mathsf{F} := \{\boldsymbol{F}, \mathbb{B}, \mathbb{D}\}^T$ and a local point $\boldsymbol{X} \in \mathcal{B}$ of the micro-structure. The material is said to be stable, if the inequality holds for any arbitrary fluctuation function with zero support $\widehat{\boldsymbol{\varphi}} = \boldsymbol{0}$, $\widehat{\boldsymbol{a}}^m = \boldsymbol{0}$ and $\widehat{\boldsymbol{a}}^e = \boldsymbol{0}$ on the boundary $\partial\mathcal{D}$ of an arbitrary domain of the body $\mathcal{D} \in \mathcal{B}$. Naturally, the above condition requires the functional L to have a local minimum at $\widehat{\mathfrak{s}} := \{\widehat{\boldsymbol{\varphi}}, \widehat{\boldsymbol{a}}^m, \widehat{\boldsymbol{a}}^e\}^T = \boldsymbol{0}$ to hold the inequality. Infinitesimal perturbations of this state imply the estimate

$$L(\boldsymbol{0} + \varepsilon\delta\widehat{\mathfrak{s}}) - L(\boldsymbol{0}) \approx \frac{1}{2}\frac{d^2}{d\varepsilon^2}\Big|_{\varepsilon=0} L(\boldsymbol{0} + \varepsilon\delta\widehat{\mathfrak{s}}) \;\geq\; 0\,, \quad (7.17)$$

yielding in analogy to (4.15) the statement

$$\frac{1}{2|\mathcal{D}|}\int_{\mathcal{D}} \delta\mathsf{F}\cdot\mathsf{C}(\mathsf{F}^0)\cdot\delta\mathsf{F}\, dV \;\geq\; 0\,, \quad (7.18)$$

with $\delta\mathsf{F} := \{\nabla\delta\widehat{\boldsymbol{\varphi}},\ \operatorname{Curl}\delta\widehat{\boldsymbol{a}}^m,\ \operatorname{Curl}\delta\widehat{\boldsymbol{a}}^e\}^T$, and in terms of the coupled magneto-electro-mechanical tangent moduli C. Note that this integral formulation is hard to check in a numerical setting, such that the material instability is usually approached by the rank-one convexity criteria as introduced in the following for the extended magneto-electro-mechanical case.

Rank-one convexity and acoustic tensor. Assume now for the perturbations of the primary fields to be of particular rank-one forms

$$\delta\widehat{\boldsymbol{\varphi}} = \boldsymbol{a} f(\boldsymbol{X}\cdot\boldsymbol{N})\,, \quad \delta\widehat{\boldsymbol{a}}^m = \boldsymbol{c} f(\boldsymbol{X}\cdot\boldsymbol{N})\,, \quad \delta\widehat{\boldsymbol{a}}^e = \boldsymbol{d} f(\boldsymbol{X}\cdot\boldsymbol{N})\,, \quad (7.19)$$

where the scalar function f describes a profile, e.g. a wave in the direction of $\boldsymbol{N}$ with $|\boldsymbol{N}| = 1$. The tensorial objects $\boldsymbol{a}$, $\boldsymbol{c}$ and $\boldsymbol{d}$ are arbitrary intensities. The particular form of perturbations can be derived for a smooth function f as $\delta\widehat{\boldsymbol{F}} = f'\,\boldsymbol{a}\otimes\boldsymbol{N}$, $\delta\widehat{\mathbb{B}} = f'\,\boldsymbol{c}\times\boldsymbol{N}$

and $\delta\widehat{\mathbb{D}} = f'\,\boldsymbol{d}\times\boldsymbol{N}$. This yields the local infinitesimal rank-one convexity criterion for material stability on the microscale as an extension of (4.18) to coupled magneto-electro-mechanics and reads

$$\begin{bmatrix}\boldsymbol{a}\otimes\boldsymbol{N}\\ \boldsymbol{c}\times\boldsymbol{N}\\ \boldsymbol{d}\times\boldsymbol{N}\end{bmatrix}\cdot\mathbf{C}\cdot\begin{bmatrix}\boldsymbol{a}\otimes\boldsymbol{N}\\ \boldsymbol{c}\times\boldsymbol{N}\\ \boldsymbol{d}\times\boldsymbol{N}\end{bmatrix}\;\geq\;0\,, \tag{7.20}$$

with moduli $\mathbf{C}$. This equation can be reformulated into the more convenient form

$$\begin{bmatrix}\boldsymbol{a}\\ \boldsymbol{c}\\ \boldsymbol{d}\end{bmatrix}\cdot\mathbf{Q}(\boldsymbol{N})\cdot\begin{bmatrix}\boldsymbol{a}\\ \boldsymbol{c}\\ \boldsymbol{d}\end{bmatrix}\;\geq\;0 \tag{7.21}$$

in terms of the *generalized acoustic tensor*

$$\mathbf{Q}(\boldsymbol{N}) := \begin{bmatrix} \partial^2_{\boldsymbol{F}\boldsymbol{F}}\psi \overset{2}{\cdot} \boldsymbol{N} \overset{4}{\cdot} \boldsymbol{N} & \partial^2_{\boldsymbol{F}\mathbb{B}}\psi \overset{2}{\cdot} \boldsymbol{N} \overset{3}{\times} \boldsymbol{N} & \partial^2_{\boldsymbol{F}\mathbb{D}}\psi \overset{2}{\cdot} \boldsymbol{N} \overset{3}{\times} \boldsymbol{N} \\ \partial^2_{\mathbb{B}\boldsymbol{F}}\psi \overset{1}{\times} \boldsymbol{N} \overset{3}{\cdot} \boldsymbol{N} & \partial^2_{\mathbb{B}\mathbb{B}}\psi \overset{1}{\times} \boldsymbol{N} \overset{2}{\times} \boldsymbol{N} & \partial^2_{\mathbb{B}\mathbb{D}}\psi \overset{1}{\times} \boldsymbol{N} \overset{2}{\times} \boldsymbol{N} \\ \partial^2_{\mathbb{D}\boldsymbol{F}}\psi \overset{1}{\times} \boldsymbol{N} \overset{3}{\cdot} \boldsymbol{N} & \partial^2_{\mathbb{D}\mathbb{B}}\psi \overset{1}{\times} \boldsymbol{N} \overset{2}{\times} \boldsymbol{N} & \partial^2_{\mathbb{D}\mathbb{D}}\psi \overset{1}{\times} \boldsymbol{N} \overset{2}{\times} \boldsymbol{N} \end{bmatrix}. \tag{7.22}$$

Material stability is characterized by the positive semi-definiteness of the generalized acoustic tensor. This yields the check of rank-one convexity or generalized ellipticity

$$\min_{|\boldsymbol{N}|=1}\left\{\mathbf{q}\cdot\mathbf{Q}(\boldsymbol{N})\cdot\mathbf{q}\right\}\geq 0 \tag{7.23}$$

for all nontrivial $\mathbf{q}\neq\boldsymbol{0}$, where critical directions $\boldsymbol{N}$ are defined such that they minimize the quadratic form of the generalized acoustic tensor.

Local limit-point instability. To identify the limit-point instabilities on the micro-structure, recall the definition of infinitesimal convexity in (7.6). Following Hill [89], a local check at every point $\boldsymbol{X}\in\mathcal{B}$ is sufficient to satisfy the integral condition. As a first energetic criterion for *local* magneto-electro-mechanical stability of the micro-structure, *positive semi-definiteness* of the moduli $\mathbf{C}$ emerges. For the numerical treatment, an accompanying check for the onset of material instability at a local point of the micro-structure is given by

$$\mathbf{p}\cdot\mathbf{C}\cdot\mathbf{p}\geq 0\quad\text{at }\boldsymbol{X}\in\mathcal{B} \tag{7.24}$$

for stable material response. This has to hold for all non-trivial vector arrays $\mathbf{p}\neq\boldsymbol{0}$ and $\mathbf{p}_{mech}\notin SO(3)$, where rotations in the mechanical partition are excluded. The required moduli $\mathbf{C}$ are a priori available in the finite element discretization of the micro-structure.

7.2.2. Material stability in the extended energy formulation

Quasi-convexity condition. The quasi-convexity condition (7.18) is extended to the mixed setting in full analogy to the local structural stability analysis formulated above. The augmented set of variables, or more precisely set of perturbations of the increased collection of primary fields reads $\widehat{\mathfrak{s}} := \{\,\widehat{\boldsymbol{\varphi}},\widehat{\boldsymbol{a}}^m,\widehat{\boldsymbol{a}}^e,\widehat{\mathbb{H}},\widehat{\mathbb{E}}\,\}^T$.

Together with the respective generalized array $\mathbf{F}_{ext} := \{ \boldsymbol{F}, \mathbb{B}, \mathbb{D}, \mathbb{H}, \mathbb{E} \}^T$ and the extended tangent moduli $\mathbf{C}_{ext}$ the quasi-convexity conditions reads

$$\frac{1}{2|\mathcal{D}|} \int_{\mathcal{D}} \delta \mathbf{F}_{ext} \cdot \mathbf{C}_{ext}(\mathbf{F}^0_{ext}) \cdot \delta \mathbf{F}_{ext} \, dV \;\geq\; 0 \,, \tag{7.25}$$

for an arbitrary subdomain $\mathcal{D} \in \mathcal{B}$.

Rank-one convexity and acoustic tensor. Again, assume the particular rank-one forms of the variations of the perturbations with their respective derivative for an assumed smooth function f

$$\left.\begin{array}{r} \delta\widehat{\boldsymbol{\varphi}} = \boldsymbol{a} f(\boldsymbol{X} \cdot \boldsymbol{N}) \\ \delta\widehat{\boldsymbol{a}}^m = \boldsymbol{c} f(\boldsymbol{X} \cdot \boldsymbol{N}) \\ \delta\widehat{\boldsymbol{a}}^e = \boldsymbol{d} f(\boldsymbol{X} \cdot \boldsymbol{N}) \end{array}\right\} \quad \text{and} \quad \left\{\begin{array}{l} \delta\widehat{\boldsymbol{F}} = f' \, \boldsymbol{a} \otimes \boldsymbol{N} \\ \delta\widehat{\mathbb{B}} = f' \, \boldsymbol{c} \times \boldsymbol{N} \\ \delta\widehat{\mathbb{D}} = f' \, \boldsymbol{d} \times \boldsymbol{N} \end{array}\right. \tag{7.26}$$

as well as for the additional mixed variables

$$\delta\widehat{\mathbb{H}} = \boldsymbol{i} f'(\boldsymbol{X} \cdot \boldsymbol{N}) \quad \text{and} \quad \delta\widehat{\mathbb{E}} = \boldsymbol{j} f'(\boldsymbol{X} \cdot \boldsymbol{N}) \,. \tag{7.27}$$

The scalar function f describes a profile such as a wave in the direction of $\boldsymbol{N}$ with $|\boldsymbol{N}| = 1$, and $\boldsymbol{a}$, $\boldsymbol{c}$, $\boldsymbol{d}$, $\boldsymbol{i}$ and $\boldsymbol{j}$ are arbitrary intensities. The infinitesimal rank-one convexity criterion for material stability on the microscale then reads

$$\begin{bmatrix} \boldsymbol{a} \\ \boldsymbol{c} \\ \boldsymbol{d} \\ \boldsymbol{i} \\ \boldsymbol{j} \end{bmatrix} \cdot \mathbf{Q}_{ext}(\boldsymbol{N}) \cdot \begin{bmatrix} \boldsymbol{a} \\ \boldsymbol{c} \\ \boldsymbol{d} \\ \boldsymbol{i} \\ \boldsymbol{j} \end{bmatrix} \;\geq\; 0 \,, \tag{7.28}$$

in terms of the extended acoustic tensor

$$\mathbf{Q}_{ext}(\boldsymbol{N}) := \begin{bmatrix} \partial^2_{\boldsymbol{F}\boldsymbol{F}}\psi^* \overset{2}{\cdot} \boldsymbol{N} \overset{4}{\cdot} \boldsymbol{N} & \boldsymbol{0} & \boldsymbol{0} & \partial^2_{\boldsymbol{F}\mathbb{H}}\psi^* \overset{2}{\cdot} \boldsymbol{N} & \partial^2_{\boldsymbol{F}\mathbb{E}}\psi^* \overset{2}{\cdot} \boldsymbol{N} \\ \boldsymbol{0} & \boldsymbol{0} & \boldsymbol{0} & \boldsymbol{1} \overset{1}{\times} \boldsymbol{N} & \boldsymbol{0} \\ \boldsymbol{0} & \boldsymbol{0} & \boldsymbol{0} & \boldsymbol{0} & \boldsymbol{1} \overset{1}{\times} \boldsymbol{N} \\ \partial^2_{\mathbb{H}\boldsymbol{F}}\psi^* \overset{3}{\cdot} \boldsymbol{N} & \boldsymbol{1} \overset{2}{\times} \boldsymbol{N} & \boldsymbol{0} & \partial^2_{\mathbb{H}\mathbb{H}}\psi^* & \partial^2_{\mathbb{H}\mathbb{E}}\psi^* \\ \partial^2_{\mathbb{E}\boldsymbol{F}}\psi^* \overset{3}{\cdot} \boldsymbol{N} & \boldsymbol{0} & \boldsymbol{1} \overset{2}{\times} \boldsymbol{N} & \partial^2_{\mathbb{E}\mathbb{H}}\psi^* & \partial^2_{\mathbb{E}\mathbb{E}}\psi^* \end{bmatrix} \tag{7.29}$$

that depends on the director $\boldsymbol{N}$. Hence, the positive semi-definiteness of the extended generalized acoustic tensor characterizes microscopic material stability, i.e.

$$\min_{|\boldsymbol{N}|=1} \left\{ \mathbf{q} \cdot \mathbf{Q}_{ext}(\boldsymbol{N}) \cdot \mathbf{q} \right\} \geq 0 \,, \tag{7.30}$$

for all nontrivial $\mathbf{q} \neq \boldsymbol{0}$, where the critical directions $\boldsymbol{N}$ are defined such that they minimize the quadratic form of the generalized acoustic tensor. Note that this intermediate extended formulation is by no means convenient for an accompanying stability analysis, as the respective entries of the tangent moduli might be hard to obtain.

Local limit-point instability. Related to (7.24), a criterion for microscopic material limit-point stability in the extended energy formulation reads

$$\mathbf{p} \cdot \mathbf{C}_{ext} \cdot \mathbf{p} \geq 0 \quad \text{at } \boldsymbol{X} \in \mathcal{B} \tag{7.31}$$

and requires the positive semi-definiteness of the tangent moduli $\mathbf{C}_{ext}$, which is given in (7.10).

7.2.3. Material stability in the convenient enthalpy formulation

Quasi-convexity condition. In a final step, the extended energy formulation will be reduced to the convenient enthalpy formulation by canceling the magnetic induction and electric displacement contributions via the elimination equations obtained from the Legendre-Fenchel transformation. The reduced set of perturbations for the enthalpy setting then reads $\widehat{\mathfrak{s}} := \{\, \widehat{\boldsymbol{\varphi}}, \widehat{\phi}^m, \widehat{\phi}^e \,\}^T$. The quasi-convexity condition can be reformulated into

$$\frac{1}{2|\mathcal{D}|} \int_{\mathcal{D}} \delta\mathbf{F}^* \cdot \mathbf{C}^*_{stab}(\mathbf{F}^{*\,0}) \cdot \delta\mathbf{F}^* \, dV \;\geq\; 0 \tag{7.32}$$

for an arbitrary subdomain $\mathcal{D} \in \mathcal{B}$ with the generalized array $\mathbf{F}^* := \{\, \widehat{\boldsymbol{F}}, \widehat{\mathbb{H}}, \widehat{\mathbb{E}} \,\}^T$ and the tangent moduli $\mathbf{C}^*_{stab}$ in diagonal form, as introduced in (7.14).

Rank-one convexity and acoustic tensor. We choose as the particular form of the variation of the perturbations with their respective derivative for an assumed smooth function f the ansatz

$$\left.\begin{aligned} \delta\widehat{\boldsymbol{\varphi}} &= \boldsymbol{a} f(\boldsymbol{X} \cdot \boldsymbol{N}) \\ -\delta\widehat{\phi}^m &= c f(\boldsymbol{X} \cdot \boldsymbol{N}) \\ -\delta\widehat{\phi}^e &= d f(\boldsymbol{X} \cdot \boldsymbol{N}) \end{aligned}\right\} \quad \text{and} \quad \left\{\begin{aligned} \delta\widehat{\boldsymbol{F}} &= f' \, \boldsymbol{a} \otimes \boldsymbol{N} \\ \delta\widehat{\mathbb{H}} &= f' \, c\boldsymbol{N} \\ \delta\widehat{\mathbb{E}} &= f' \, d\boldsymbol{N} \end{aligned}\right. , \tag{7.33}$$

with the scalar function f and the arbitrary intensities $\boldsymbol{a}$, c and d. Here, f' is the derivative of the scalar function f. Insertion of (7.33) into (7.32) reveals the infinitesimal rank-one convexity criterion for material stability on the microscale of the convenient enthalpy formulation

$$\begin{bmatrix} \boldsymbol{a} \\ c \\ d \end{bmatrix} \cdot \mathbf{Q}^*_{stab}(\boldsymbol{N}) \cdot \begin{bmatrix} \boldsymbol{a} \\ c \\ d \end{bmatrix} \;\geq\; 0 \,. \tag{7.34}$$

The diagonal localization tensor is defined as

$$\mathbf{Q}^*_{stab}(\boldsymbol{N}) := \begin{bmatrix} \partial^2_{\boldsymbol{F}\boldsymbol{F}}\psi^* \overset{2}{\cdot} \boldsymbol{N} \overset{4}{\cdot} \boldsymbol{N} & \boldsymbol{0} & \boldsymbol{0} \\ \boldsymbol{0} & -\partial^2_{\mathbb{H}\mathbb{H}}\psi^* \overset{1}{\cdot} \boldsymbol{N} \overset{2}{\cdot} \boldsymbol{N} & -\partial^2_{\mathbb{H}\mathbb{E}}\psi^* \overset{1}{\cdot} \boldsymbol{N} \overset{2}{\cdot} \boldsymbol{N} \\ \boldsymbol{0} & -\partial^2_{\mathbb{E}\mathbb{H}}\psi^* \overset{1}{\cdot} \boldsymbol{N} \overset{2}{\cdot} \boldsymbol{N} & -\partial^2_{\mathbb{E}\mathbb{E}}\psi^* \overset{1}{\cdot} \boldsymbol{N} \overset{2}{\cdot} \boldsymbol{N} \end{bmatrix} \tag{7.35}$$

and depends on the director $\boldsymbol{N}$. Again, the positive semi-definiteness of the reduced mixed generalized acoustic tensor characterizes microscopic material stability in the enthalpy setting, i.e.

$$\min_{|\boldsymbol{N}|=1} \left\{ \mathbf{q} \cdot \mathbf{Q}^*_{stab}(\boldsymbol{N}) \cdot \mathbf{q} \right\} \geq 0 \,, \tag{7.36}$$

for all nontrivial $\mathbf{q} \neq \boldsymbol{0}$, where the critical directions $\boldsymbol{N}$ are defined such that they minimize the quadratic form of the generalized acoustic tensor.

Local limit-point instability. The condition for microscopic material limit-point stability in the enthalpy setting reads

$$\mathbf{p} \cdot \mathbf{C}^{*}_{stab} \cdot \mathbf{p} \geq 0 \quad \text{at } \boldsymbol{X} \in \mathcal{B} \tag{7.37}$$

and requires the positive semi-definiteness of the tangent moduli $\mathbf{C}^{*}_{stab}$.

7.3. Structural stability analysis of composite macro-structures

Macroscopic instabilities are generally split up in structural and material instabilities. They cover the standard buckling and wrinkling of the macroscopic specimen, as well as limit-point instabilities in the material. The investigation of structural stability of the macro-structure is based on the definition of existence and uniqueness of solution states, Hill [89], based on an energetic formulation. Here, for the different energetic and enthalpic approaches, the respective criteria for structural stability are derived, which are closely related to the above introduced stability checks.

7.3.1. Structural stability in the canonical energy formulation

The macroscopic problem is defined in the canonical variational formulation by a pure minimization problem. It is characterized by a given macroscopic deformation and macroscopic magnetic and electric vector potentials

$$\overline{\mathfrak{s}}^{0} := \{ \overline{\boldsymbol{\varphi}}^{0}, \overline{\boldsymbol{a}^{m}}^{0}, \overline{\boldsymbol{a}^{e}}^{0} \}^{T} \text{ on } \overline{\mathcal{B}}\,. \tag{7.38}$$

Following the same approach as above, the macroscopic state is said to be *globally stable* if for any other admissible macroscopic state $\overline{\mathfrak{s}}$ the inequality

$$\overline{\Pi}(\overline{\mathfrak{s}}) - \overline{\Pi}(\overline{\mathfrak{s}}^{0}) \geq 0 \tag{7.39}$$

holds. Note that $\overline{\mathfrak{s}}$ needs to satisfy the essential conditions $\overline{\boldsymbol{\varphi}} \in \mathcal{W}_{\overline{\boldsymbol{\varphi}}}$, $\overline{\boldsymbol{a}^{e}} \in \mathcal{W}_{\overline{\boldsymbol{a}^{e}}}$, and $\overline{\boldsymbol{a}^{m}} \in \mathcal{W}_{\overline{\boldsymbol{a}^{m}}}$. For a restriction of $\overline{\mathfrak{s}}$ to the neighborhood of the solution state $\overline{\mathfrak{s}}^{0}$, the stability criterion (7.39) can be reformulated by a Taylor series expansion up to the second rank. By employing the equilibrium conditions, i.e. the first variation needs to vanish, the condition

$$\overline{\Pi}(\overline{\mathfrak{s}}) - \overline{\Pi}(\overline{\mathfrak{s}}^{0}) = \frac{1}{2}\frac{d^{2}}{d\varepsilon^{2}}\Big|_{\varepsilon=0} \overline{\Pi}(\overline{\mathfrak{s}}^{0} + \varepsilon\delta\overline{\mathfrak{s}}) \;\geq\; 0 \tag{7.40}$$

for a *locally stable deformation state* $\overline{\mathfrak{s}}^{0}$ appears. This second variation can be computed in a straightforward manner by recasting (7.40) into the form

$$\overline{\Pi}(\overline{\mathfrak{s}}) - \overline{\Pi}(\overline{\mathfrak{s}}^{0}) = \frac{1}{2|\overline{\mathcal{B}}|}\int_{\overline{\mathcal{B}}} \delta\overline{\mathbf{F}} \cdot \overline{\mathbf{C}}(\overline{\mathbf{F}}^{0}) \cdot \delta\overline{\mathbf{F}}\, d\overline{V} \;\geq\; 0\,, \tag{7.41}$$

with the macroscopic generalized array of energetic variables $\overline{\mathbf{F}} := \{ \overline{\boldsymbol{F}}, \overline{\mathbb{B}}, \overline{\mathbb{D}} \}^{T}$, and the coupled magneto-electro-mechanical tangent array

$$\overline{\mathbf{C}} := \partial^{2}_{\overline{\mathbf{F}}\,\overline{\mathbf{F}}}\overline{\psi}(\overline{\mathbf{F}}^{0}) = \begin{bmatrix} \partial^{2}_{\overline{\boldsymbol{F}}\,\overline{\boldsymbol{F}}}\overline{\psi} & \partial^{2}_{\overline{\boldsymbol{F}}\,\overline{\mathbb{B}}}\overline{\psi} & \partial^{2}_{\overline{\boldsymbol{F}}\,\overline{\mathbb{D}}}\overline{\psi} \\ \partial^{2}_{\overline{\mathbb{B}}\,\overline{\boldsymbol{F}}}\overline{\psi} & \partial^{2}_{\overline{\mathbb{B}}\,\overline{\mathbb{B}}}\overline{\psi} & \partial^{2}_{\overline{\mathbb{B}}\,\overline{\mathbb{D}}}\overline{\psi} \\ \partial^{2}_{\overline{\mathbb{D}}\,\overline{\boldsymbol{F}}}\overline{\psi} & \partial^{2}_{\overline{\mathbb{D}}\,\overline{\mathbb{B}}}\overline{\psi} & \partial^{2}_{\overline{\mathbb{D}}\,\overline{\mathbb{D}}}\overline{\psi} \end{bmatrix}\,. \tag{7.42}$$

7.3.2. Structural stability in the extended energy formulation

Likewise, for the extended energy formulation on the macroscale, the two additional macroscopic fields, namely magnetic and electric fields, enhance the energetic formulation such that

$$\overline{\mathfrak{s}}^0 := \{\, \overline{\boldsymbol{\varphi}}^0, \overline{\boldsymbol{a}^m}^0, \overline{\boldsymbol{a}^e}^0, \overline{\mathbb{H}}^0, \overline{\mathbb{E}}^0 \,\}^T \text{ on } \overline{\mathcal{B}} \,, \tag{7.43}$$

defines the macroscopic solution state. It satisfies the mixed saddle-point principle and is obtained by a partial Legendre-Fenchel transformation. Again, for a macroscopic local stability criterion, consider a perturbed admissible state in the infinitesimal neighborhood of $\overline{\mathfrak{s}}^0$, satisfying the essential conditions $\overline{\boldsymbol{\varphi}} \in \mathcal{W}_{\overline{\boldsymbol{\varphi}}}$, $\overline{\boldsymbol{a}^m} \in \mathcal{W}_{\overline{\boldsymbol{a}^m}}$, $\overline{\boldsymbol{a}^e} \in \mathcal{W}_{\overline{\boldsymbol{a}^e}}$, $\overline{\mathbb{H}} \in L^2$ and $\overline{\mathbb{E}} \in L^2$. Applying the local structural stability condition based on the Taylor series expansion reveals the criterion

$$\widetilde{\overline{\Pi}}(\overline{\mathfrak{s}}) - \widetilde{\overline{\Pi}}(\overline{\mathfrak{s}}^0) = \frac{1}{2|\overline{\mathcal{B}}|} \int_{\overline{\mathcal{B}}} \delta\overline{\mathbf{F}}_{ext} \cdot \overline{\mathbf{C}}_{ext}(\overline{\mathbf{F}}^0_{ext}) \cdot \delta\overline{\mathbf{F}}_{ext}\, d\overline{V} \;\geq\; 0 \tag{7.44}$$

with the *extended* array of macroscopic variables $\overline{\mathbf{F}}_{ext} := \{\overline{\boldsymbol{F}}, \overline{\mathbb{B}}, \overline{\mathbb{D}}, \overline{\mathbb{H}}, \overline{\mathbb{E}}\}^T$ in terms of the extended magneto-electro-mechanical tangent array

$$\overline{\mathbf{C}}_{ext} := \partial^2_{\overline{\mathbf{F}}_{ext}\overline{\mathbf{F}}_{ext}} \widetilde{\overline{\psi}}(\overline{\mathbf{F}}^0_{ext}) = \begin{bmatrix} \partial^2_{\overline{\boldsymbol{F}}\,\overline{\boldsymbol{F}}}\overline{\psi^*} & \boldsymbol{0} & \boldsymbol{0} & \partial^2_{\overline{\boldsymbol{F}}\,\overline{\mathbb{H}}}\overline{\psi^*} & \partial^2_{\overline{\boldsymbol{F}}\,\overline{\mathbb{E}}}\overline{\psi^*} \\ \boldsymbol{0} & \boldsymbol{0} & \boldsymbol{0} & \boldsymbol{1} & \boldsymbol{0} \\ \boldsymbol{0} & \boldsymbol{0} & \boldsymbol{0} & \boldsymbol{0} & \boldsymbol{1} \\ \partial^2_{\overline{\mathbb{H}}\,\overline{\boldsymbol{F}}}\overline{\psi^*} & \boldsymbol{1} & \boldsymbol{0} & \partial^2_{\overline{\mathbb{H}}\,\overline{\mathbb{H}}}\overline{\psi^*} & \partial^2_{\overline{\mathbb{H}}\,\overline{\mathbb{E}}}\overline{\psi^*} \\ \partial^2_{\overline{\mathbb{E}}\,\overline{\boldsymbol{F}}}\overline{\psi^*} & \boldsymbol{0} & \boldsymbol{1} & \partial^2_{\overline{\mathbb{E}}\,\overline{\mathbb{H}}}\overline{\psi^*} & \partial^2_{\overline{\mathbb{E}}\,\overline{\mathbb{E}}}\overline{\psi^*} \end{bmatrix} . \tag{7.45}$$

For completeness this formulation is shown, however not used in further treatments of coupled magneto-electro-mechanics.

7.3.3. Structural stability in the convenient enthalpy formulation

In a final step, the macroscopic extended mixed energy formulation gets reduced by exploitation of the elimination equations for the magnetic induction and electric displacements obtained by the partial Legendre-Fenchel transformation. Their respective variations read

$$\delta\overline{\mathbb{B}} = -\partial^2_{\overline{\mathbb{H}}\,\overline{\boldsymbol{F}}}\overline{\psi^*} : \delta\overline{\boldsymbol{F}} - \partial^2_{\overline{\mathbb{H}}\,\overline{\mathbb{H}}}\overline{\psi^*} \cdot \delta\overline{\mathbb{H}} - \partial^2_{\overline{\mathbb{H}}\,\overline{\mathbb{E}}}\overline{\psi^*} \cdot \delta\overline{\mathbb{E}} \tag{7.46}$$

for the increment of the magnetic induction and

$$\delta\overline{\mathbb{D}} = -\partial^2_{\overline{\mathbb{E}}\,\overline{\boldsymbol{F}}}\overline{\psi^*} : \delta\overline{\boldsymbol{F}} - \partial^2_{\overline{\mathbb{E}}\,\overline{\mathbb{H}}}\overline{\psi^*} \cdot \delta\overline{\mathbb{H}} - \partial^2_{\overline{\mathbb{E}}\,\overline{\mathbb{E}}}\overline{\psi^*} \cdot \delta\overline{\mathbb{E}} \tag{7.47}$$

for the increment of the electric displacement, based on the derivation of the mixed energy-enthalpy function. Insertion of the variations into (7.44) yields the reduced criterion for macroscopic structural stability of the convenient enthalpy formulation

$$\overline{\Pi^*}(\overline{\mathfrak{s}}) - \overline{\Pi^*}(\overline{\mathfrak{s}}^0) = \frac{1}{2|\overline{\mathcal{B}}|} \int_{\overline{\mathcal{B}}} \delta\overline{\mathbf{F}^*} \cdot \overline{\mathbf{C}^*}_{stab}(\overline{\mathbf{F}^*}^0) \cdot \delta\overline{\mathbf{F}^*}\, d\overline{V} \;\geq\; 0 \tag{7.48}$$

in terms of the macroscopic generalized array of the mixed energy-enthalpy formulation $\overline{\mathbf{F}^*} := \{\, \overline{\boldsymbol{F}}, \overline{\mathbb{H}}, \overline{\mathbb{E}} \,\}^T$ and the reduced tangent array

$$\overline{\mathbf{C}^*}_{stab} := \begin{bmatrix} \partial^2_{\overline{\boldsymbol{F}}\,\overline{\boldsymbol{F}}}\overline{\psi^*} & \boldsymbol{0} & \boldsymbol{0} \\ \boldsymbol{0} & -\partial^2_{\overline{\mathbb{H}}\,\overline{\mathbb{H}}}\overline{\psi^*} & -\partial^2_{\overline{\mathbb{H}}\,\overline{\mathbb{E}}}\overline{\psi^*} \\ \boldsymbol{0} & -\partial^2_{\overline{\mathbb{E}}\,\overline{\mathbb{H}}}\overline{\psi^*} & -\partial^2_{\overline{\mathbb{E}}\,\overline{\mathbb{E}}}\overline{\psi^*} \end{bmatrix} . \tag{7.49}$$

Consequently, the check of positive semi-definiteness of the macroscopic tangent moduli serves as a stability criterion in the enthalpy setting defined by the state variables

$$\overline{\mathfrak{s}} := \{\, \overline{\boldsymbol{\varphi}}, \overline{\phi^m}, \overline{\phi^e} \,\}^T \text{ on } \overline{\mathcal{B}} \,. \tag{7.50}$$

7.4. Material stability analysis of the macro-structure

Localization type instabilities on the macro-structure are known to be related to long wave-length structural instabilities or bifurcation modes on the microscale, Abeyaratne & Triantafyllidis [2], and Triantafyllidis & Maker [253]. A more general approach to investigate the connection between multiscale instabilities for all nonlinear elastic periodic micro-structures was given in Geymonat et al. [74] and more recently in the works Miehe et al. [169], Michel et al. [156, 157], Bertoldi & Boyce [18], Bertoldi et al. [20], and Polukhov et al. [196]. In the following, criteria for the detection of material instabilities at local points on the macro-structure are derived.

7.4.1. Material stability in the canonical energy formulation

Quasi-convexity condition. In analogy to the material stability analysis of the micro-structure above, the notion of quasi-convexity, introduced by Morrey [175], is used as a foundation for a macroscopic material stability analysis. Starting point is the dual of the functional (7.16)

$$\overline{L}(\widehat{\boldsymbol{\varphi}}, \widehat{\boldsymbol{a}^m}, \widehat{\boldsymbol{a}^e}) := \frac{1}{|\overline{\mathcal{D}}|} \int_{\overline{\mathcal{D}}} \overline{\psi}(\overline{\boldsymbol{F}} + \nabla\widehat{\boldsymbol{\varphi}}, \overline{\mathbb{B}} + \operatorname{Curl}\widehat{\boldsymbol{a}^m}, \overline{\mathbb{D}} + \operatorname{Curl}\widehat{\boldsymbol{a}^e}) d\overline{V} \geq \overline{\psi}(\overline{\boldsymbol{F}}, \overline{\mathbb{B}}, \overline{\mathbb{D}}) \tag{7.51}$$

with respect to a given state $\overline{\mathsf{F}} := \{\overline{\boldsymbol{F}}, \overline{\mathbb{B}}, \overline{\mathbb{D}}\}^T$. Note that the perturbation fields $\widehat{\mathfrak{s}} := \{\widehat{\boldsymbol{\varphi}}, \widehat{\boldsymbol{a}^m}, \widehat{\boldsymbol{a}^e}\}^T$ have zero support on the boundary $\partial\overline{\mathcal{D}}$ of an arbitrary domain $\overline{\mathcal{D}} \subset \overline{\mathcal{B}}$. Analogously to the material stability definition of the micro-structure (7.17), a *stable response* is defined by

$$\overline{L}(\boldsymbol{0} + \varepsilon\delta\widehat{\mathfrak{s}}) - \overline{L}(\boldsymbol{0}) \approx \frac{1}{2}\frac{d^2}{d\varepsilon^2}\Big|_{\varepsilon=0} \overline{L}(\boldsymbol{0} + \varepsilon\delta\widehat{\mathfrak{s}}) \;\geq\; 0 \,, \tag{7.52}$$

revealing similar to (7.18) the macroscopic material stability criterion

$$\frac{1}{2|\overline{\mathcal{D}}|} \int_{\overline{\mathcal{D}}} \delta\overline{\mathsf{F}} \cdot \overline{\mathsf{C}}(\overline{\mathsf{F}}^0) \cdot \delta\overline{\mathsf{F}} \, d\overline{V} \;\geq\; 0 \,, \tag{7.53}$$

in terms of the generalized macroscopic array $\overline{\mathsf{F}} := \{\, \overline{\boldsymbol{F}}, \overline{\mathbb{B}}, \overline{\mathbb{D}} \,\}^T$ and the coupled electro-magneto-mechanical macro-moduli $\overline{\mathsf{C}}$.

Rank-one convexity and acoustic tensor. Consider again a smooth scalar function $\overline{f}(\overline{\boldsymbol{X}} \cdot \overline{\boldsymbol{N}})$ that describes a macroscopic profile of perturbation, e.g. a wave in the direction of $\overline{\boldsymbol{N}}$ with $|\overline{\boldsymbol{N}}| = 1$. Assume now the particular form of perturbations

$$\delta\widehat{\boldsymbol{\varphi}} = \overline{\boldsymbol{a}}\,\overline{f}(\overline{\boldsymbol{X}} \cdot \overline{\boldsymbol{N}}) \,, \quad \delta\widehat{\boldsymbol{a}^m} = \overline{\boldsymbol{c}}\,\overline{f}(\overline{\boldsymbol{X}} \cdot \overline{\boldsymbol{N}}) \,, \quad \delta\widehat{\boldsymbol{a}^e} = \overline{\boldsymbol{d}}\,\overline{f}(\overline{\boldsymbol{X}} \cdot \overline{\boldsymbol{N}}) \,, \tag{7.54}$$

similar to (7.19). Here, $\overline{\boldsymbol{a}}$, $\overline{\boldsymbol{c}}$ and $\overline{\boldsymbol{d}}$ are arbitrary intensities, scaling the smooth, scalar function $\overline{f}$. This ansatz gives the condition

$$\begin{bmatrix} \overline{\boldsymbol{a}} \\ \overline{\boldsymbol{c}} \\ \overline{\boldsymbol{d}} \end{bmatrix} \cdot \overline{\mathbf{Q}}(\overline{\boldsymbol{N}}) \cdot \begin{bmatrix} \overline{\boldsymbol{a}} \\ \overline{\boldsymbol{c}} \\ \overline{\boldsymbol{d}} \end{bmatrix} \geq 0 \tag{7.55}$$

in terms of the generalized macroscopic acoustic tensor

$$\overline{\mathbf{Q}}(\overline{\boldsymbol{N}}) := \begin{bmatrix} \partial^2_{\overline{\boldsymbol{F}}\,\overline{\boldsymbol{F}}}\overline{\psi} \overset{2}{\cdot} \overline{\boldsymbol{N}} \overset{4}{\cdot} \overline{\boldsymbol{N}} & \partial^2_{\overline{\boldsymbol{F}}\,\overline{\mathbb{B}}}\overline{\psi} \overset{2}{\cdot} \overline{\boldsymbol{N}} \times \overline{\boldsymbol{N}} & \partial^2_{\overline{\boldsymbol{F}}\,\overline{\mathbb{D}}}\overline{\psi} \overset{2}{\cdot} \overline{\boldsymbol{N}} \times \overline{\boldsymbol{N}} \\ \partial^2_{\overline{\mathbb{B}}\,\overline{\boldsymbol{F}}}\overline{\psi} \overset{1}{\times} \overline{\boldsymbol{N}} \overset{3}{\cdot} \overline{\boldsymbol{N}} & \partial^2_{\overline{\mathbb{B}}\,\overline{\mathbb{B}}}\overline{\psi} \overset{1}{\times} \overline{\boldsymbol{N}} \overset{2}{\times} \overline{\boldsymbol{N}} & \partial^2_{\overline{\mathbb{B}}\,\overline{\mathbb{D}}}\overline{\psi} \overset{1}{\times} \overline{\boldsymbol{N}} \overset{2}{\times} \overline{\boldsymbol{N}} \\ \partial^2_{\overline{\mathbb{D}}\,\overline{\boldsymbol{F}}}\overline{\psi} \overset{1}{\times} \overline{\boldsymbol{N}} \overset{3}{\cdot} \overline{\boldsymbol{N}} & \partial^2_{\overline{\mathbb{D}}\,\overline{\mathbb{B}}}\overline{\psi} \overset{1}{\times} \overline{\boldsymbol{N}} \overset{2}{\times} \overline{\boldsymbol{N}} & \partial^2_{\overline{\mathbb{D}}\,\overline{\mathbb{D}}}\overline{\psi} \overset{1}{\times} \overline{\boldsymbol{N}} \overset{2}{\times} \overline{\boldsymbol{N}} \end{bmatrix} \tag{7.56}$$

depending on the director $\overline{\boldsymbol{N}}$. Macroscopic material stability is therefore associated with the positive semi-definiteness of this acoustic tensor. This induces the check of macroscopic rank-one convexity

$$\min_{|\overline{\boldsymbol{N}}|=1} \left\{ \overline{\mathbf{q}} \cdot \overline{\mathbf{Q}}(\overline{\boldsymbol{N}}) \cdot \overline{\mathbf{q}} \right\} \geq 0 \,, \tag{7.57}$$

for non-trivial $\overline{\mathbf{q}}$, with critical directions $\overline{\boldsymbol{N}}$ which minimize the quadratic form.

Local limit-point instability. To identify the limit-point instabilities on the macro-structure, recall the definition of infinitesimal convexity in (7.41). Following Hill [89], a local check at every point $\overline{\boldsymbol{X}} \in \overline{\mathcal{B}}$ is sufficient to satisfy the integral condition. As a first energetic criterion for *local* magneto-electro-mechanical stability of the macro-structure, *positive semi-definiteness* of the macro-moduli $\overline{\mathbf{C}}$ emerges. For the numerical treatment, an accompanying check for the onset of material instability at a local point of the macro-structure is given by

$$\overline{\mathbf{p}} \cdot \overline{\mathbf{C}} \cdot \overline{\mathbf{p}} \geq 0 \quad \text{at } \overline{\boldsymbol{X}} \in \overline{\mathcal{B}} \,, \tag{7.58}$$

for stable material response, dual to (7.24). Here, $\overline{\mathbf{p}}$ is a non-trivial vector array with $\overline{\mathbf{p}} \neq \boldsymbol{0}$ and $\overline{\mathbf{p}}_{mech} \notin SO(3)$ (exclusion of macro-rotations in the mechanical partition). Conveniently, the homogenized moduli $\overline{\mathbf{C}}$ are directly available in the computational homogenization procedures.

7.4.2. Material stability in the extended energy formulation

Quasi-convexity condition. The macroscopic energy $\overline{\psi}$ is expressed by the energy-enthalpy $\overline{\psi^*}$ and additional Legendre-Fenchel terms

$$\widetilde{\overline{\psi}} := \overline{\psi^*}(\overline{\boldsymbol{F}}, \overline{H}, \overline{\mathbb{E}}) + \overline{\mathbb{B}} \cdot \overline{H} + \overline{\mathbb{D}} \cdot \overline{\mathbb{E}} \,. \tag{7.59}$$

With that, the macroscopic infinitesimal quasi-convexity condition gets extended by the advanced set of variables

$$\widehat{\overline{\mathfrak{s}}} := \{\widehat{\overline{\boldsymbol{\varphi}}}, \widehat{\overline{\boldsymbol{a}^m}}, \widehat{\overline{\boldsymbol{a}^e}}, \widehat{\overline{H}}, \widehat{\overline{\mathbb{E}}}\}^T \,. \tag{7.60}$$

This yields, as an extended quasi-convexity condition, in analogy to the energetic ansatz (7.53) the following condition

$$\frac{1}{2|\overline{\mathcal{D}}|} \int_{\overline{\mathcal{D}}} \delta\overline{\mathbf{F}}_{ext} \cdot \overline{\mathbf{C}}_{ext}(\overline{\mathbf{F}}^0_{ext}) \cdot \delta\overline{\mathbf{F}}_{ext} \, d\overline{V} \geq 0 \,, \tag{7.61}$$

for a stable macroscopic material response. Here, the extended generalized array of primary fields $\overline{\mathbf{F}}_{ext} := \{\, \overline{\boldsymbol{F}}, \overline{\mathbb{B}}, \overline{\mathbb{D}}, \overline{\mathbb{H}}, \overline{\mathbb{E}} \,\}^T$ and the tangent moduli

$$\overline{\mathbf{C}}_{ext} := \partial^2_{\overline{\mathbf{F}}_{ext}\overline{\mathbf{F}}_{ext}} \widetilde{\overline{\psi}}(\overline{\mathbf{F}}_{ext}) = \begin{bmatrix} \partial^2_{\overline{\boldsymbol{F}}\,\overline{\boldsymbol{F}}}\overline{\psi^*} & \boldsymbol{0} & \boldsymbol{0} & \partial^2_{\overline{\boldsymbol{F}}\,\overline{\mathbb{H}}}\overline{\psi^*} & \partial^2_{\overline{\boldsymbol{F}}\,\overline{\mathbb{E}}}\overline{\psi^*} \\ \boldsymbol{0} & \boldsymbol{0} & \boldsymbol{0} & \boldsymbol{1} & \boldsymbol{0} \\ \boldsymbol{0} & \boldsymbol{0} & \boldsymbol{0} & \boldsymbol{0} & \boldsymbol{1} \\ \partial^2_{\overline{\mathbb{H}}\,\overline{\boldsymbol{F}}}\overline{\psi^*} & \boldsymbol{1} & \boldsymbol{0} & \partial^2_{\overline{\mathbb{H}}\,\overline{\mathbb{H}}}\overline{\psi^*} & \partial^2_{\overline{\mathbb{H}}\,\overline{\mathbb{E}}}\overline{\psi^*} \\ \partial^2_{\overline{\mathbb{E}}\,\overline{\boldsymbol{F}}}\overline{\psi^*} & \boldsymbol{0} & \boldsymbol{1} & \partial^2_{\overline{\mathbb{E}}\,\overline{\mathbb{H}}}\overline{\psi^*} & \partial^2_{\overline{\mathbb{E}}\,\overline{\mathbb{E}}}\overline{\psi^*} \end{bmatrix} \tag{7.62}$$

are employed.

Rank-one convexity and acoustic tensor. For a particular form of the variation of the perturbations as suggested in (7.26) and (7.27), with their respective derivative for an assumed smooth function $\overline{f}$ for the extended approach, assume

$$\left.\begin{aligned} \delta\widehat{\overline{\boldsymbol{\varphi}}} &= \overline{\boldsymbol{a}}\,\overline{f}(\overline{\boldsymbol{X}}\cdot\overline{\boldsymbol{N}}) \\ \delta\widehat{\overline{\boldsymbol{a}^m}} &= \overline{\boldsymbol{c}}\,\overline{f}(\overline{\boldsymbol{X}}\cdot\overline{\boldsymbol{N}}) \\ \delta\widehat{\overline{\boldsymbol{a}^e}} &= \overline{\boldsymbol{d}}\,\overline{f}(\overline{\boldsymbol{X}}\cdot\overline{\boldsymbol{N}}) \end{aligned}\right\} \quad \text{and} \quad \left\{\begin{aligned} \delta\widehat{\overline{\boldsymbol{F}}} &= \overline{f}'\,\overline{\boldsymbol{a}}\otimes\overline{\boldsymbol{N}} \\ \delta\widehat{\overline{\mathbb{B}}} &= \overline{f}'\,\overline{\boldsymbol{c}}\times\overline{\boldsymbol{N}} \\ \delta\widehat{\overline{\mathbb{D}}} &= \overline{f}'\,\overline{\boldsymbol{d}}\times\overline{\boldsymbol{N}} \end{aligned}\right. \tag{7.63}$$

as well as for the additional mixed variables

$$\delta\widehat{\overline{\mathbb{H}}} = \overline{\boldsymbol{i}}\,\overline{f}'(\overline{\boldsymbol{X}}\cdot\overline{\boldsymbol{N}}) \quad \text{and} \quad \delta\widehat{\overline{\mathbb{E}}} = \overline{\boldsymbol{j}}\,\overline{f}'(\overline{\boldsymbol{X}}\cdot\overline{\boldsymbol{N}})\,. \tag{7.64}$$

This ansatz yields the macroscopic infinitesimal rank-one convexity criterion for material stability in the extended energy formulation

$$\begin{bmatrix} \overline{\boldsymbol{a}} \\ \overline{\boldsymbol{c}} \\ \overline{\boldsymbol{d}} \\ \overline{\boldsymbol{i}} \\ \overline{\boldsymbol{j}} \end{bmatrix} \cdot \overline{\mathbf{Q}}_{ext}(\overline{\boldsymbol{N}}) \cdot \begin{bmatrix} \overline{\boldsymbol{a}} \\ \overline{\boldsymbol{c}} \\ \overline{\boldsymbol{d}} \\ \overline{\boldsymbol{i}} \\ \overline{\boldsymbol{j}} \end{bmatrix} \;\geq\; 0\,, \tag{7.65}$$

in terms of the extended acoustic tensor

$$\overline{\mathbf{Q}}_{ext}(\overline{\boldsymbol{N}}) := \begin{bmatrix} \partial^2_{\overline{\boldsymbol{F}}\,\overline{\boldsymbol{F}}}\overline{\psi^*} \overset{2}{\cdot} \overline{\boldsymbol{N}} \overset{4}{\cdot} \overline{\boldsymbol{N}} & \boldsymbol{0} & \boldsymbol{0} & \partial^2_{\overline{\boldsymbol{F}}\,\overline{\mathbb{H}}}\overline{\psi^*} \overset{2}{\cdot} \overline{\boldsymbol{N}} & \partial^2_{\overline{\boldsymbol{F}}\,\overline{\mathbb{E}}}\overline{\psi^*} \overset{2}{\cdot} \overline{\boldsymbol{N}} \\ \boldsymbol{0} & \boldsymbol{0} & \boldsymbol{0} & \boldsymbol{1} \overset{1}{\times} \overline{\boldsymbol{N}} & \boldsymbol{0} \\ \boldsymbol{0} & \boldsymbol{0} & \boldsymbol{0} & \boldsymbol{0} & \boldsymbol{1} \overset{1}{\times} \overline{\boldsymbol{N}} \\ \partial^2_{\overline{\mathbb{H}}\,\overline{\boldsymbol{F}}}\overline{\psi^*} \overset{3}{\cdot} \overline{\boldsymbol{N}} & \boldsymbol{1} \overset{2}{\times} \overline{\boldsymbol{N}} & \boldsymbol{0} & \partial^2_{\overline{\mathbb{H}}\,\overline{\mathbb{H}}}\overline{\psi^*} & \partial^2_{\overline{\mathbb{H}}\,\overline{\mathbb{E}}}\overline{\psi^*} \\ \partial^2_{\overline{\mathbb{E}}\,\overline{\boldsymbol{F}}}\overline{\psi^*} \overset{3}{\cdot} \overline{\boldsymbol{N}} & \boldsymbol{0} & \boldsymbol{1} \overset{2}{\times} \overline{\boldsymbol{N}} & \partial^2_{\overline{\mathbb{E}}\,\overline{\mathbb{H}}}\overline{\psi^*} & \partial^2_{\overline{\mathbb{E}}\,\overline{\mathbb{E}}}\overline{\psi^*} \end{bmatrix} \tag{7.66}$$

depending on the director $\overline{\boldsymbol{N}}$. Hence, the positive semi-definiteness of the extended generalized acoustic tensor characterizes macroscopic material stability, i.e.

$$\min_{|\overline{\boldsymbol{N}}|=1} \left\{ \overline{\mathbf{q}} \cdot \overline{\mathbf{Q}}_{ext}(\overline{\boldsymbol{N}}) \cdot \overline{\mathbf{q}} \right\} \geq 0\,, \tag{7.67}$$

for all non-trivial $\overline{\mathbf{q}} \neq \boldsymbol{0}$.

Local limit-point instability. Similar to (7.58), the local macroscopic limit-point criterion in the extended energy setting demands a *positive semi-definite moduli* $\overline{\mathbf{C}}_{ext}$, inducing the check

$$\overline{\mathbf{p}} \cdot \overline{\mathbf{C}}_{ext} \cdot \overline{\mathbf{p}} \geq 0 \quad \text{at } \overline{\boldsymbol{X}} \in \overline{\mathcal{B}} \tag{7.68}$$

for locally stable magneto-electro-elastic response with non-trivial arrays $\overline{\mathbf{p}}$.

7.4.3. Material stability in the convenient enthalpy formulation

Quasi-convexity condition. Making use of the elimination equations for the magnetic induction and the electric displacement yields, in analogy to (7.46) and (7.47), the reduced criterion for macroscopic material stability in the enthalpy formulation

$$\frac{1}{2|\overline{\mathcal{D}}|} \int_{\overline{\mathcal{D}}} \delta\overline{\mathbf{F}^*} \cdot \overline{\mathbf{C}^*}_{stab}(\overline{\mathbf{F}^{*0}}) \cdot \delta\overline{\mathbf{F}^*}\, d\overline{V} \;\geq\; 0\,, \tag{7.69}$$

with the macroscopic generalized array $\overline{\mathbf{F}^*} := \{\, \overline{\boldsymbol{F}}, \overline{\mathbb{H}}, \overline{\mathbb{E}} \,\}^T$ and in terms of the condensed macroscopic array

$$\overline{\mathbf{C}^*}_{stab} := \begin{bmatrix} \partial^2_{\overline{\boldsymbol{F}}\,\overline{\boldsymbol{F}}}\overline{\psi^*} & \boldsymbol{0} & \boldsymbol{0} \\ \boldsymbol{0} & -\partial^2_{\overline{\mathbb{H}}\,\overline{\mathbb{H}}}\overline{\psi^*} & -\partial^2_{\overline{\mathbb{H}}\,\overline{\mathbb{E}}}\overline{\psi^*} \\ \boldsymbol{0} & -\partial^2_{\overline{\mathbb{E}}\,\overline{\mathbb{H}}}\overline{\psi^*} & -\partial^2_{\overline{\mathbb{E}}\,\overline{\mathbb{E}}}\overline{\psi^*} \end{bmatrix} . \tag{7.70}$$

Note that the diagonal form of $\overline{\mathbf{C}^*}_{stab}$ contains partitions of the macroscopic tangent moduli $\overline{\mathbf{C}^*}$, which is available in formulation of computational homogenization.

Rank-one convexity and acoustic tensor. Again a scalar function $\overline{f}(\overline{\boldsymbol{X}} \cdot \overline{\boldsymbol{N}})$ describing a perturbation profile according to

$$\delta\widehat{\overline{\boldsymbol{\varphi}}} = \overline{\boldsymbol{a}}\,\overline{f}(\overline{\boldsymbol{X}} \cdot \overline{\boldsymbol{N}})\,, \quad \delta\widehat{\overline{\phi^m}} = \overline{c}\,\overline{f}(\overline{\boldsymbol{X}} \cdot \overline{\boldsymbol{N}})\,, \quad \delta\widehat{\overline{\phi^e}} = \overline{d}\,\overline{f}(\overline{\boldsymbol{X}} \cdot \overline{\boldsymbol{N}})\,, \tag{7.71}$$

is assumed. Insertion into (7.69) gives the local result

$$\begin{bmatrix} \overline{\boldsymbol{a}} \\ \overline{c} \\ \overline{d} \end{bmatrix} \cdot \overline{\mathbf{Q}^*}_{stab}(\overline{\boldsymbol{N}}) \cdot \begin{bmatrix} \overline{\boldsymbol{a}} \\ \overline{c} \\ \overline{d} \end{bmatrix} \;\geq\; 0 \tag{7.72}$$

in terms of the macroscopic diagonal acoustic tensor

$$\overline{\mathbf{Q}^*}_{stab}(\overline{\boldsymbol{N}}) := \begin{bmatrix} \partial^2_{\overline{\boldsymbol{F}}\,\overline{\boldsymbol{F}}}\overline{\psi^*} \overset{2}{\cdot} \overline{\boldsymbol{N}} \overset{4}{\cdot} \overline{\boldsymbol{N}} & \boldsymbol{0} & \boldsymbol{0} \\ \boldsymbol{0} & -\partial^2_{\overline{\mathbb{H}}\,\overline{\mathbb{H}}}\overline{\psi^*} \overset{1}{\cdot} \overline{\boldsymbol{N}} \overset{2}{\cdot} \overline{\boldsymbol{N}} & -\partial^2_{\overline{\mathbb{H}}\,\overline{\mathbb{E}}}\overline{\psi^*} \overset{1}{\cdot} \overline{\boldsymbol{N}} \overset{2}{\cdot} \overline{\boldsymbol{N}} \\ \boldsymbol{0} & -\partial^2_{\overline{\mathbb{E}}\,\overline{\mathbb{H}}}\overline{\psi^*} \overset{1}{\cdot} \overline{\boldsymbol{N}} \overset{2}{\cdot} \overline{\boldsymbol{N}} & -\partial^2_{\overline{\mathbb{E}}\,\overline{\mathbb{E}}}\overline{\psi^*} \overset{1}{\cdot} \overline{\boldsymbol{N}} \overset{2}{\cdot} \overline{\boldsymbol{N}} \end{bmatrix} \tag{7.73}$$

depending on macroscopic directors $\overline{\boldsymbol{N}}$. We identify the positive semi-definiteness of the macroscopic acoustic tensor as a requirement for a stable macroscopic material response. This is ensured by the check

$$\min_{|\overline{\boldsymbol{N}}|=1} \left\{ \overline{\mathbf{q}} \cdot \overline{\mathbf{Q}^*}_{stab}(\overline{\boldsymbol{N}}) \cdot \overline{\mathbf{q}} \right\} \geq 0\,, \tag{7.74}$$

for non-trivial $\overline{\mathbf{q}}$, where the critical directions $\overline{\boldsymbol{N}}$ minimize the quadratic form.

Local limit-point instability. The local macroscopic limit-point criterion in the extended energy setting demands a *positive semi-definite moduli* $\overline{\mathbf{C}^*}_{stab}$, inducing the check

$$\overline{\mathbf{p}} \cdot \overline{\mathbf{C}^*}_{stab} \cdot \overline{\mathbf{p}} \geq 0 \quad \text{at } \overline{\boldsymbol{X}} \in \overline{\mathcal{B}} \tag{7.75}$$

for locally stable magneto-electro-elastic response with non-trivial arrays $\overline{\mathbf{p}}$.

7.5. Accompanying multiscale FE stability analysis

The different stability criteria of the macro- and microscale need to be checked in a stability analysis accompanying a finite element computation. For that, the discretization of the related moduli and stiffness matrices are provided in the following. Both, the energetic and mixed energy-enthalpy formulation are covered.

7.5.1. Energy formulation based on vector potentials

Equilibrium state of the micro-structure. A direct numerical implementation of the energy formulation in terms of vector potentials and Dirichlet conditions is in focus. To this end, the energetic primary variables are decomposed by

$$\boldsymbol{\varphi} = \overline{\boldsymbol{F}} \cdot \boldsymbol{X} + \widetilde{\boldsymbol{\varphi}}\,, \quad \boldsymbol{a}^m = \tfrac{1}{2}\,\overline{\mathbb{B}} \times \boldsymbol{X} + \widetilde{\boldsymbol{a}}^m\,, \quad \boldsymbol{a}^e = \tfrac{1}{2}\,\overline{\mathbb{D}} \times \boldsymbol{X} + \widetilde{\boldsymbol{a}}^e \tag{7.76}$$

into linear parts associated with the Dirichlet-type macroscopic driving and the fluctuations. The subsequent compact notation of the FE implementation is based on the arrays

$$\overline{\mathbf{F}} := [\,\overline{\boldsymbol{F}}, \overline{\mathbb{B}}, \overline{\mathbb{D}}\,]^T \quad \text{and} \quad \widetilde{\mathbf{F}} := [\,\nabla\widetilde{\boldsymbol{\varphi}}, \operatorname{Curl}\widetilde{\boldsymbol{a}}^m, \operatorname{Curl}\widetilde{\boldsymbol{a}}^e\,]^T \tag{7.77}$$

assembling the prescribed macro-quantities and primary fluctuation fields. The fluctuations are discretized by a finite element method

$$\widetilde{\mathbf{F}}(\boldsymbol{X}, t) = \underline{\mathbf{B}}(\boldsymbol{X})\underline{\mathbf{d}}(t)\,, \tag{7.78}$$

in terms of the finite element interpolation matrix $\underline{\mathbf{B}}$ and a global vector of discrete fluctuations

$$\underline{\mathbf{d}} = \mathop{\mathbf{A}}_{I=1}^{N^h} \left[\widetilde{\boldsymbol{\varphi}} \quad \widetilde{\boldsymbol{a}}^m \quad \widetilde{\boldsymbol{a}}^e\right]_I^T \in \mathcal{R}^{(d+6)N^h} \tag{7.79}$$

at the nodes of the finite element mesh.[1] With this ansatz at hand, the *discretized energy density functional* reads

$$\overline{\pi}^h(\overline{\mathbf{F}}; \underline{\mathbf{d}}) = \frac{1}{|\mathcal{B}^h|} \int_{\mathcal{B}^h} \psi(\overline{\mathbf{F}} + \underline{\mathbf{B}}\,\underline{\mathbf{d}})\, dV\,. \tag{7.80}$$

[1] **Shapes of energy FE formulation.** A vector storage of the generalized gradient array $(7.77)_2$ in the form

$$\widetilde{\mathbf{F}} := [\,\widetilde{F}_{11}, \widetilde{F}_{22}, \widetilde{F}_{12}, \widetilde{F}_{21}, \widetilde{\mathbb{B}}_1, \widetilde{\mathbb{B}}_2, \widetilde{\mathbb{D}}_1, \widetilde{\mathbb{D}}_2\,]^T$$

results in the structure of the gradient interpolation matrix related to a node I

$$\underline{\mathbf{B}}_I = \begin{bmatrix} N_{,1} & & N_{,2} & & & & & \\ & N_{,2} & & N_{,1} & & & & \\ & & & & N_{,2} & -N_{,1} & & \\ & & & & & & N_{,2} & -N_{,1} \end{bmatrix}_I^T .$$

First and second derivatives of this functional provide all necessary information for the finite element solution of the equilibrium state in the micro-structure and the overall homogenized quantities. We define the arrays

$$\begin{aligned} \underline{\mathbf{R}} &:= \overline{\pi}^h_{,\underline{\mathbf{d}}} &&= \frac{1}{|\mathcal{B}^h|}\int_{\mathcal{B}^h} \underline{\mathbf{B}}^T \partial_{\mathbf{F}}\psi \, dV, \\ \underline{\mathbf{K}} &:= \overline{\pi}^h_{,\underline{\mathbf{d}}\,\underline{\mathbf{d}}} &&= \frac{1}{|\mathcal{B}^h|}\int_{\mathcal{B}^h} \underline{\mathbf{B}}^T \partial^2_{\mathbf{F}\mathbf{F}}\psi \underline{\mathbf{B}} \, dV, \\ \underline{\mathbf{L}} &:= \overline{\pi}^h_{,\underline{\mathbf{d}}\overline{\mathbf{F}}} &&= \frac{1}{|\mathcal{B}^h|}\int_{\mathcal{B}^h} \underline{\mathbf{B}}^T \partial^2_{\mathbf{F}\,\mathbf{F}}\psi \, dV, \end{aligned} \tag{7.81}$$

providing the basis for the computation of the equilibrium state of the micro-structure. This is achieved by typical Newton-Raphson updates

$$\underline{\mathbf{d}} \Leftarrow \underline{\mathbf{d}} - \underline{\mathbf{K}}^{-1}\underline{\mathbf{R}} \quad \text{until} \quad \|\underline{\mathbf{R}}\| < tol_{micro} \tag{7.82}$$

for the nodal fluctuations, based on the finite element tangent matrix $\underline{\mathbf{K}}$, providing an equilibrium state for a vanishing finite element residual $\underline{\mathbf{R}} = \boldsymbol{0}$.

Homogenized overall properties. For an equilibrium state of the micro-structure, the homogenized quantities follow from the functional (7.80) by taking the derivative with respect to the driving array $\overline{\mathbf{F}}$. This gives the homogenized stress array

$$\overline{\mathbf{S}} := [\,\overline{\boldsymbol{P}}, \overline{H}, \overline{\mathbb{E}}\,]^T = \overline{\pi}^h_{,\overline{\mathbf{F}}} = \frac{1}{|\mathcal{B}^h|}\int_{\mathcal{B}^h} \partial_{\mathbf{F}}\psi \, dV, \tag{7.83}$$

obtained as the average of associated micro-quantities, i.e.

$$\overline{\boldsymbol{P}} = \frac{1}{|\mathcal{B}^h|}\int_{\mathcal{B}^h} \boldsymbol{P}\, dV\,, \quad \overline{H} = \frac{1}{|\mathcal{B}^h|}\int_{\mathcal{B}^h} H\, dV\,, \quad \overline{\mathbb{E}} = \frac{1}{|\mathcal{B}^h|}\int_{\mathcal{B}^h} \mathbb{E}\, dV\,, \tag{7.84}$$

see Chapter 3 for more details. The homogenized moduli of the micro-structure are related to the second derivative of the functional (7.80) by the driving array $\overline{\mathbf{F}}$, yielding

$$\overline{\mathbf{C}} := \overline{\pi}^h_{,\overline{\mathbf{F}}\,\overline{\mathbf{F}}} = \langle \mathbf{C} \rangle - \underline{\mathbf{L}}^T \underline{\mathbf{K}}^{-1} \underline{\mathbf{L}} \quad \text{with} \quad \langle \mathbf{C} \rangle := \frac{1}{|\mathcal{B}^h|}\int_{\mathcal{B}^h} \mathbf{C}\, dV\,. \tag{7.85}$$

The second term of the right side in $(7.85)_1$ results from the condensation of the fluctuations, obtained by the implicit function theorem from the equilibrium condition $\underline{\mathbf{R}} = \boldsymbol{0}$. The macro-moduli $\overline{\mathbf{C}}$ provide a *direct input* to the local material stability analysis at local points of the macro-structure.

Finite-Element structural stability analysis. The discretization of the infinitesimal structural stability criterion (7.6) provides the algebraic representation

$$\overline{\pi}^h(\mathfrak{s}) - \overline{\pi}^h(\mathfrak{s}^0) = \frac{1}{2}\underline{\mathbf{d}}^T \underline{\mathbf{K}}\, \underline{\mathbf{d}} \;\geq 0\,, \tag{7.86}$$

directly in terms of the finite element tangent matrix $\underline{\mathbf{K}}$ defined in (7.81). The accompanying check of structural stability of the micro-structure *monitors the eigenvalues* of this matrix, obtained from

$$\left[\, \underline{\mathbf{K}} - \lambda_\alpha \underline{\boldsymbol{1}} \,\right] \underline{\mathbf{v}}_\alpha = 0\,. \tag{7.87}$$

In an incremental analysis, the check of structural stability is controlled by

$$\lambda_\alpha \begin{cases} \geq 0 & \text{stable structural state ,} \\ < 0 & \text{non-stable structural state .} \end{cases} \tag{7.88}$$

For an unstable response, eigenvectors $\underline{\mathbf{v}}$ provide post-critical magneto-electro-elastic modes. The energetic stability criteria are summarized in Box 7.1.
Likewise, for the macroscopic structural stability criterion, the necessary stiffness matrix $\overline{\underline{\mathbf{K}}}$ is obtained in a similar fashion. However, a full finite element analysis of the macro-structure is not performed in this work. The treatment of the macroscopic problem as a macroscopic driving routine doesn't allow for a structural stability analysis and only accounts for limit-point instabilities on the macro-structure, related to the homogenized tangent moduli $\overline{\mathbf{C}}$ and the acoustic tensor $\overline{\mathbf{Q}}$.

7.5.2. Enthalpy formulation based on Dirichlet conditions

Equilibrium state of the micro-structure. The most simple numerical implementation of the magneto-electro-elastic homogenization problem is based on the enthalpy formulation with Dirichlet conditions. To this end, the primary variables are decomposed by

$$\boldsymbol{\varphi} = \overline{\boldsymbol{F}} \cdot \boldsymbol{X} + \widetilde{\boldsymbol{\varphi}} \,, \quad -\phi^m = \overline{\mathbb{H}} \cdot \boldsymbol{X} - \widetilde{\phi}^m \,, \quad -\phi^e = \overline{\mathbb{E}} \cdot \boldsymbol{X} - \widetilde{\phi}^e \tag{7.89}$$

into linear parts associated with the Dirichlet-type macroscopic driving and the fluctuations. The subsequent compact notation of the FE implementation is based on the introduction of the arrays

$$\overline{\mathbf{F}}^* := [\, \overline{\boldsymbol{F}}, \overline{\mathbb{H}}, \overline{\mathbb{E}} \,]^T \quad \text{and} \quad \widetilde{\mathbf{F}}^* := [\, \nabla\widetilde{\boldsymbol{\varphi}}, -\nabla\widetilde{\phi}^m, -\nabla\widetilde{\phi}^e \,]^T \tag{7.90}$$

assembling the prescribed macro-quantities and the gradients of the fluctuation. The fluctuations are discretized by a finite element method

$$\widetilde{\mathbf{F}}^*(\boldsymbol{X}, t) = \underline{\mathbf{B}}(\boldsymbol{X})\underline{\mathbf{d}}(t) \tag{7.91}$$

in terms of the finite element interpolation matrix $\underline{\mathbf{B}}$ and a global vector of discrete fluctuations

$$\underline{\mathbf{d}} = \mathop{\mathbf{A}}_{I=1}^{N^h} \begin{bmatrix} \widetilde{\boldsymbol{\varphi}} & \widetilde{\phi}^m & \widetilde{\phi}^e \end{bmatrix}_I^T \in \mathcal{R}^{(d+2)N^h} \tag{7.92}$$

at the nodes of the finite element mesh.[2] With this ansatz at hand, the *discretized enthalpy density functional* reads

$$\overline{\pi^*}^h(\overline{\mathbf{F}}^*; \underline{\mathbf{d}}) = \frac{1}{|\mathcal{B}^h|} \int_{\mathcal{B}^h} \psi^*(\overline{\mathbf{F}}^* + \underline{\mathbf{B}}\,\underline{\mathbf{d}})\, dV \,. \tag{7.93}$$

[2] **Shapes of enthalpy FE formulation.** For 2D, a vector storage of the generalized gradient array $(7.90)_2$ in the form

$$\widetilde{\mathbf{F}}^* := [\, \widetilde{F}_{11}, \widetilde{F}_{22}, \widetilde{F}_{12}, \widetilde{F}_{21}, \widetilde{\mathbb{H}}_1, \widetilde{\mathbb{H}}_2, \widetilde{\mathbb{E}}_1, \widetilde{\mathbb{E}}_2 \,]^T$$

results in the structure of the gradient interpolation matrix related to a node I

$$\underline{\mathbf{B}}_I = \begin{bmatrix} N_{,1} & & N_{,2} & \\ & N_{,2} & & N_{,1} \\ & & -N_{,1} & -N_{,2} \\ & & & -N_{,1} & -N_{,2} \end{bmatrix}_I^T .$$

The first and second derivatives of this functional provide all necessary information for the finite element solution of the equilibrium state in the micro-structure and the overall homogenized quantities. In particular, the first and second derivatives by the fluctuation field $\underline{\mathbf{d}}$ give the finite element arrays

$$\begin{aligned} \underline{\mathbf{R}}^* &:= \overline{\pi^*}^h_{,\underline{\mathbf{d}}} &&= \frac{1}{|\mathcal{B}^h|}\int_{\mathcal{B}^h} \underline{\mathbf{B}}^T \partial_{\mathbf{F}^*}\psi^*\, dV, \\ \underline{\mathbf{K}}^* &:= \overline{\pi^*}^h_{,\underline{\mathbf{d}}\,\underline{\mathbf{d}}} &&= \frac{1}{|\mathcal{B}^h|}\int_{\mathcal{B}^h} \underline{\mathbf{B}}^T \partial^2_{\mathbf{F}^*\mathbf{F}^*}\psi^*\underline{\mathbf{B}}\, dV, \\ \underline{\mathbf{L}}^* &:= \overline{\pi^*}^h_{,\underline{\mathbf{d}}\overline{\mathbf{F}}^*} &&= \frac{1}{|\mathcal{B}^h|}\int_{\mathcal{B}^h} \underline{\mathbf{B}}^T \partial^2_{\mathbf{F}^*\,\mathbf{F}^*}\psi^*\, dV, \end{aligned} \tag{7.94}$$

providing the basis for the computation of the equilibrium state of the micro-structure. This is achieved by typical Newton-Raphson updates

$$\underline{\mathbf{d}} \Leftarrow \underline{\mathbf{d}} - \underline{\mathbf{K}}^{*-1}\underline{\mathbf{R}}^* \quad \text{until} \quad \|\underline{\mathbf{R}}^*\| < tol_{micro} \tag{7.95}$$

for the nodal fluctuations based on the finite element tangent matrix $\underline{\mathbf{K}}^*$, providing an equilibrium state for a vanishing finite element residual $\underline{\mathbf{R}}^* = \boldsymbol{0}$.

Homogenized overall properties. For an equilibrium state of the micro-structure, the homogenized quantities follow from the functional (7.93) by taking the derivative with respect to the driving array $\overline{\mathbf{F}^*}$. This gives the homogenized stress array

$$\overline{\mathbf{S}^*} := [\,\overline{\boldsymbol{P}}, -\overline{\mathbb{B}}, -\overline{\mathbb{D}}\,]^T = \overline{\pi^*}^h_{,\overline{\mathbf{F}^*}} = \frac{1}{|\mathcal{B}^h|}\int_{\mathcal{B}^h} \partial_{\mathbf{F}^*}\psi^*\, dV, \tag{7.96}$$

obtained as the average of associated micro-quantities, i.e.

$$\overline{\boldsymbol{P}} = \frac{1}{|\mathcal{B}^h|}\int_{\mathcal{B}^h} \boldsymbol{P}\, dV\,, \quad \overline{\mathbb{B}} = \frac{1}{|\mathcal{B}^h|}\int_{\mathcal{B}^h} \mathbb{B}\, dV\,, \quad \overline{\mathbb{D}} = \frac{1}{|\mathcal{B}^h|}\int_{\mathcal{B}^h} \mathbb{D}\, dV\,. \tag{7.97}$$

The homogenized moduli of the micro-structure are related to the second derivative of the functional (7.93) by the driving array $\overline{\mathbf{F}^*}$, yielding

$$\overline{\mathbf{C}^*} := \overline{\pi^*}^h_{,\overline{\mathbf{F}^*}\overline{\mathbf{F}^*}} = \langle \mathbf{C}^* \rangle - \underline{\mathbf{L}}^{*T}\underline{\mathbf{K}}^{*-1}\underline{\mathbf{L}}^* \quad \text{with} \quad \langle \mathbf{C}^* \rangle := \frac{1}{|\mathcal{B}^h|}\int_{\mathcal{B}^h} \mathbf{C}^*\, dV\,. \tag{7.98}$$

The partitions in $\overline{\mathbf{C}^*}_{stab}$, defined in (7.70), provide the basis for the local material stability analysis of the macro-structure. This Dirichlet-type computational homogenization method is in complete formal equivalence to the pure mechanical treatment outlined in Miehe [158], when the deformation gradient $\overline{\boldsymbol{F}}$ of the mechanical theory is replaced for the magneto-electro-mechanical framework by the array $\overline{\mathbf{F}^*}$ in $(7.90)_1$.

Finite Element structural stability analysis. The discretization of the infinitesimal structural stability criterion (7.13) provides the algebraic representation

$$\overline{\pi^*}^h(\mathfrak{s}) - \overline{\pi^*}^h(\mathfrak{s}^0) = \frac{1}{2}\underline{\mathbf{d}}^T\underline{\mathbf{K}}^*_{stab}\,\underline{\mathbf{d}} \;\geq 0 \tag{7.99}$$

in terms of the *extra structural stability matrix*

$$\underline{\mathbf{K}}^{*}_{stab} := \frac{1}{|\mathcal{B}^h|} \int_{\mathcal{B}} \underline{\mathbf{B}}^T \mathbf{C}^{*}_{stab} \underline{\mathbf{B}} \, dV \ , \tag{7.100}$$

with partition of $\underline{\mathbf{K}}^{*}$ defined in (7.94), and related to the *diagonal block partitions* of the tangent $\mathbf{C}^{*}_{stab}$ in (7.14). Hence, as a remarkable result, the structural stability analysis within the enthalpy formulation is related to the positive and negative semi-definiteness of the mechanical, magnetic and electrical block partitions of $\underline{\mathbf{K}}$, see also Miehe et al. [173] for more details. The accompanying check of structural stability on the micro-structure can then be based on *monitoring the eigenvalues* of the structural stability matrix $\underline{\mathbf{K}}_{stab}$, obtained from

$$\left[\, \underline{\mathbf{K}}_{stab} - \lambda_\alpha \underline{\boldsymbol{1}} \, \right] \underline{\mathbf{v}}_\alpha = 0 \ . \tag{7.101}$$

In an incremental analysis, the check of structural stability is controlled by

$$\lambda_\alpha \begin{cases} \geq 0 & \text{stable structural state ,} \\ < 0 & \text{non-stable structural state .} \end{cases} \tag{7.102}$$

For an unstable response, the eigenvectors $\underline{\mathbf{v}}_\alpha$ provide post-critical electro-elastic modes. The energetic structural stability criteria of the convenient enthalpy formulation are summarized in Box 7.2.

7.6. Summary of multiscale instability criteria

The concepts of structural and material instabilities with the related criteria for both the macro- and the micro-structure are summarized in the following. In all cases the check of positive semi-definiteness of either the global FE tangent matrix for structural, or the local (homogenized) tangent moduli for material instabilities can be performed by an eigenvalue analysis of the respective matrix. While this operation is numerically costly, it is simple to perform. In the canonical energy setting, the stability criteria are summarized in Box 7.1 for both, the micro- and macroscopic accompanying procedures. Here, all respective checks are given in terms of an eigenvalue analysis. While a rigorous treatment of the extended energy formulation was presented, the criteria are not further displayed. The focus was set on the development of energetic stability criteria for the numerically convenient enthalpy setting of magneto-electro-mechanics, which has shown, that a diagonal structure of the respective tangents and moduli matrices is obtained due to the Legendre-Fenchel transformation. Box 7.2 summarizes the related criteria with the associated eigenvalue analyses.

7.7. Analytical example: stability of a homogeneous material

The above introduced checks for material or limit-point instability are further demonstrated in a simple model problem of a homogeneous material element. Here, no separation of length scales is considered, likewise no distinction between micro- and macro-structure is necessary. For simplicity only electro-mechanical interactions are covered.

Box 7.1: Accompanying stability checks of canonical energy formulation.

- *Microscopic structural stability.* Let the global FE tangent matrix $\underline{\underline{\mathbf{K}}}$ in (7.81) be given. Check positive semi-definiteness

$$\underline{\underline{\mathbf{K}}}\,\underline{\mathbf{v}}_\alpha = \lambda_\alpha \underline{\mathbf{v}}_\alpha \quad \text{with} \quad \lambda_\alpha \begin{cases} \geq 0 & \text{stable global state,} \\ < 0 & \text{non-stable global state.} \end{cases} \tag{7.103}$$

- *Microscopic material stability.* Let the local tangent moduli $\mathbf{C}$ in (7.7) be given. Check positive semi-definiteness

$$\mathbf{C}\mathbf{p}_\alpha = \mu_\alpha \mathbf{p}_\alpha \quad \text{with} \quad \mu_\alpha \begin{cases} \geq 0 & \text{stable local state,} \\ < 0 & \text{non-stable local state.} \end{cases} \tag{7.104}$$

  Check strong ellipticity with acoustic tensor $\mathbf{Q}(\boldsymbol{N})$ in (7.22)

$$\mathbf{Q}(\boldsymbol{N})\mathbf{q}_\alpha = \nu_\alpha \mathbf{q}_\alpha \quad \text{with} \quad \min_{|\boldsymbol{N}|=1} \nu_\alpha \begin{cases} \geq 0 & \text{stable local state,} \\ < 0 & \text{non-stable local state.} \end{cases} \tag{7.105}$$

- *Macroscopic structural stability.* Let the global FE tangent matrix $\overline{\underline{\underline{\mathbf{K}}}}$ related to (7.81) be given. Check positive semi-definiteness

$$\overline{\underline{\underline{\mathbf{K}}}}\,\overline{\underline{\mathbf{v}}}_\alpha = \overline{\lambda}_\alpha \overline{\underline{\mathbf{v}}}_\alpha \quad \text{with} \quad \overline{\lambda}_\alpha \begin{cases} \geq 0 & \text{stable global state,} \\ < 0 & \text{non-stable global state.} \end{cases} \tag{7.106}$$

- *Macroscopic material stability.* Given are the homogenized tangent moduli $\overline{\mathbf{C}}$ in (7.42). Check positive semi-definiteness

$$\overline{\mathbf{C}}\overline{\mathbf{p}}_\alpha = \overline{\mu}_\alpha \overline{\mathbf{p}}_\alpha \quad \text{with} \quad \overline{\mu}_\alpha \begin{cases} \geq 0 & \text{stable local state,} \\ < 0 & \text{non-stable local state.} \end{cases} \tag{7.107}$$

  Investigate strong ellipticity with acoustic macro-tensor $\overline{\mathbf{Q}}(\overline{\boldsymbol{N}})$ in (7.56)

$$\overline{\mathbf{Q}}(\overline{\boldsymbol{N}})\overline{\mathbf{q}}_\alpha = \overline{\nu}_\alpha \overline{\mathbf{q}}_\alpha \quad \text{with} \quad \min_{|\overline{\boldsymbol{N}}|=1} \overline{\nu}_\alpha \begin{cases} \geq 0 & \text{stable local state,} \\ < 0 & \text{non-stable local state.} \end{cases} \tag{7.108}$$

Box 7.2: Accompanying stability checks of convenient enthalpy formulation.

- *Microscopic structural stability.* Let the diagonal partitions $\underline{\underline{\mathbf{K}}}^*_{stab}$ in (7.100) of global FE tangent matrix $\underline{\underline{\mathbf{K}}}^*$ in (7.94) be given. Check positive semi-definiteness

$$\underline{\underline{\mathbf{K}}}^*_{stab}\underline{\mathbf{v}}_\alpha = \lambda_\alpha \underline{\mathbf{v}}_\alpha \quad \text{with} \quad \lambda_\alpha \begin{cases} \geq 0 & \text{stable global state,} \\ < 0 & \text{non-stable global state.} \end{cases} \tag{7.109}$$

- *Microscopic Material Stability.* Let the diagonal partitions $\mathbf{C}^*_{stab}$ in (7.14) of the local tangent moduli $\mathbf{C}^*$ be given. Check positive semi-definiteness

$$\mathbf{C}^*_{stab}\mathbf{p}_\alpha = \mu_\alpha \mathbf{p}_\alpha \quad \text{with} \quad \mu_\alpha \begin{cases} \geq 0 & \text{stable local state,} \\ < 0 & \text{non-stable local state.} \end{cases} \tag{7.110}$$

  Check strong ellipticity with the diagonalized acoustic tensor $\mathbf{Q}^*_{stab}(\boldsymbol{N})$ in (7.35)

$$\mathbf{Q}^*_{stab}(\boldsymbol{N})\mathbf{q}_\alpha = \nu_\alpha \mathbf{q}_\alpha \quad \text{with} \quad \min_{|\boldsymbol{N}|=1} \nu_\alpha \begin{cases} \geq 0 & \text{stable local state,} \\ < 0 & \text{non-stable local state.} \end{cases} \tag{7.111}$$

- *Macroscopic Structural Stability.* Let the diagonal partitions $\overline{\underline{\underline{\mathbf{K}}}^*}_{stab}$ related to (7.100) be given. Check positive semi-definiteness

$$\overline{\underline{\underline{\mathbf{K}}}^*}_{stab}\overline{\underline{\mathbf{v}}}_\alpha = \overline{\lambda}_\alpha \overline{\underline{\mathbf{v}}}_\alpha \quad \text{with} \quad \overline{\lambda}_\alpha \begin{cases} \geq 0 & \text{stable global state,} \\ < 0 & \text{non-stable global state.} \end{cases} \tag{7.112}$$

- *Macroscopic Material Stability.* Given are the diagonal partitions $\overline{\mathbf{C}^*}_{stab}$ in (7.70) of the homogenized tangent moduli $\overline{\mathbf{C}^*}$. Check positive semi-definiteness

$$\overline{\mathbf{C}^*}_{stab}\overline{\mathbf{p}}_\alpha = \overline{\mu}_\alpha \overline{\mathbf{p}}_\alpha \quad \text{with} \quad \overline{\mu}_\alpha \begin{cases} \geq 0 & \text{stable local state,} \\ < 0 & \text{non-stable local state.} \end{cases} \tag{7.113}$$

  Investigate strong ellipticity with diagonalized macro-tensor $\overline{\mathbf{Q}^*}_{stab}(\overline{\boldsymbol{N}})$ in (7.73)

$$\overline{\mathbf{Q}^*}_{stab}(\overline{\boldsymbol{N}})\overline{\mathbf{q}}_\alpha = \overline{\nu}_\alpha \overline{\mathbf{q}}_\alpha \quad \text{with} \quad \min_{|\overline{\boldsymbol{N}}|=1} \overline{\nu}_\alpha \begin{cases} \geq 0 & \text{stable local state,} \\ < 0 & \text{non-stable local state.} \end{cases} \tag{7.114}$$

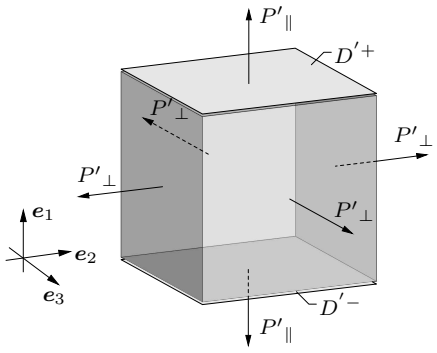

Figure 7.2: *Electro-mechanically loaded homogeneous cube.* A local infinitesimal volume element is electrically loaded by positive and negative electric charges $D^{+/-}$ on the top and bottom surface, respectively. The dimensionless principle stresses $\boldsymbol{P}'$ are applied aligned ($P'_{\parallel}$) or perpendicular ($P'_{\perp}$) to the applied electric loading direction.

7.7.1. Definition of the model problem

To demonstrate the loss of electro-mechanical stability of a homogeneous dielectric elastomer material a simple analytical model problem based on an electro-mechanically loaded cube is considered. As depicted in Figure 7.2 the electrical loading is realized by electrical charges on the top and bottom surface of the cube, while the mechanical loading consists of stresses aligned or perpendicular to the electric loading direction. This most simple example provides an excellent environment for the application of the tools developed above, yielding an intuitive understanding of the underlying phenomena. In the following, *dimensionless quantities*, based on the normalization

$$\psi' = \frac{\psi}{\mu_0} \,, \quad \boldsymbol{P}' = \frac{\boldsymbol{P}}{\mu_0} \,, \quad \mathbb{E}' = \frac{\mathbb{E}}{\sqrt{\mu_0/\epsilon_0}} \,, \quad \mathbb{D}' = \frac{\mathbb{D}}{\sqrt{\mu_0\epsilon_0}} \,, \tag{7.115}$$

are considered, such that the shear modulus μ_0 and the electric permittivity ϵ_0 are eliminated. Here, ψ' represents the normalized energy function, $\boldsymbol{P}'$ the Piola stress, $\mathbb{E}'$ is the electric field, and $\mathbb{D}'$ the electric displacements. For an isochoric deformation of the cube, a framework aligned with the direction of the principal stretch and stress of the isotropic material is considered, i.e.

$$\boldsymbol{F} = \begin{bmatrix} \lambda & & \\ & \lambda^{-1/2} & \\ & & \lambda^{-1/2} \end{bmatrix} \quad \text{and} \quad \boldsymbol{P}' = \begin{bmatrix} P'_{\parallel} & & \\ & P'_{\perp} & \\ & & P'_{\perp} \end{bmatrix} \,, \tag{7.116}$$

where $P'_{\parallel}$ and $P'_{\perp}$ are the principal stresses parallel and perpendicular to the electric loading direction. The placement of electric charges on the top and bottom surface of the cube result in an electric loading in vertical direction (top to bottom), such, that the electric variables read $\mathbb{D}' = [\, D', 0, 0 \,]^T$ and $\mathbb{E}' = [\, E', 0, 0 \,]^T$. The subsequent analysis of the electro-mechanical response of the isochoric cube can be described by the simple relation

$$\{\, \lambda, E' \,\} = f(D', P'_{\parallel}, P'_{\perp}) \,. \tag{7.117}$$

Thus, the cube is considered to be loaded by the surface charge, related to the electric flux $D = -\mathbb{D}' \cdot \boldsymbol{N}$ and the stresses $P'_{\parallel}$ and $P'_{\perp}$, and as response functions the stretch λ and the electric field E' are computed.

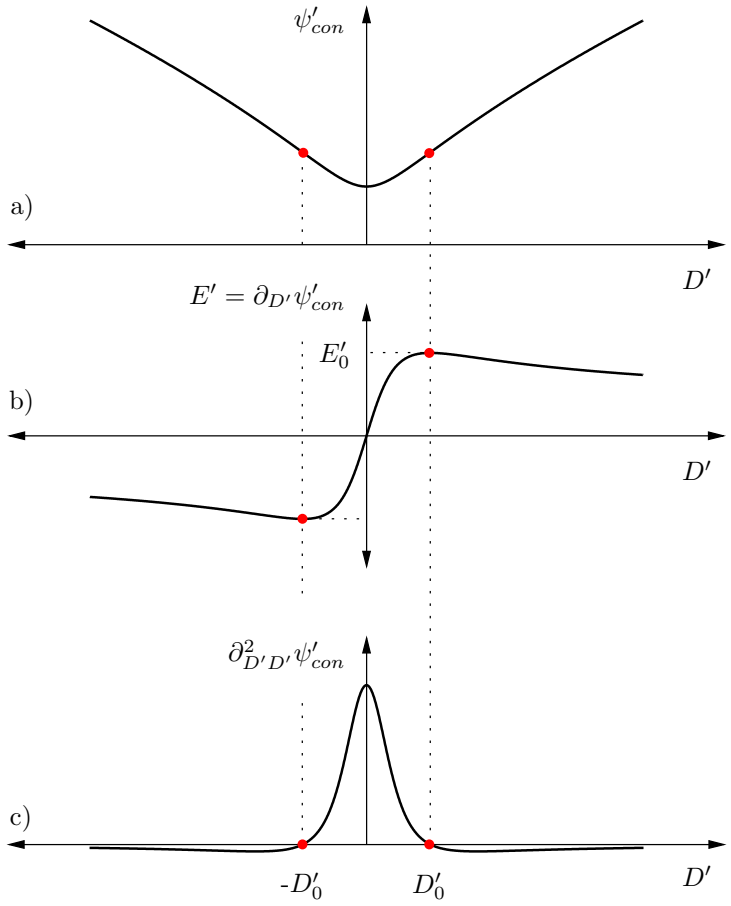

Figure 7.3: *Analytical response function of the condensed energy.* a) Closed-form representation of the condensed energy function ψ'_{con} over the electric displacements D'. The loss of convexity is highlighted in red. b) The first partial derivative with respect to D' reveals a material limit point instability characterized by the critical maximum electric field E'_0. c) Second partial derivative with respect to D' yields the stability point D'_0.

7.7.2. Limit-point analysis for purely electric loading

Canonical energy formulation. First, a mechanically stress free state is considered, with $P'_{\parallel} = 0$ and $P'_{\perp} = 0$, where the cube is only loaded by the electric surface charges. Without further explanation, the normalized energy function for isochoric, isotropic homogeneous dielectric elastomers is introduced

$$\psi'(\lambda, D') = \tfrac{1}{2}\,[\lambda^2 + 2/\lambda] + \tfrac{1}{2}\,D'^2\lambda^2 \ . \tag{7.118}$$

The principal stretch is then obtained by the minimization problem

$$\lambda = \arg\{ \inf_{\lambda} \psi'(\lambda, D') \} \ , \tag{7.119}$$

for zero external stresses. The first variation reveals the balance of mechanical and Maxwell stresses, and yields the closed-form solution for the stretch in terms of the electric displacement

$$\lambda = (1 + D'^2)^{-1/3} \quad \in [1, 0) \ . \tag{7.120}$$

The electric field is obtained by the derivative of the energy (7.118) with respect to the

electric displacements

$$E' = \frac{\partial \psi'}{\partial D'} = D'\lambda^2 = \frac{D'}{(1+D'^2)^{2/3}} \quad \in [0, E'_0] \ , \tag{7.121}$$

where the result (7.120) for the stretch was inserted. The typical limit-point behavior in the $E' - D'$ diagram is characterized by the maximum electric field $E'_0(D'_0)$

$$E'_0 = \frac{\sqrt{3}}{2\sqrt[3]{2}} \approx 0.69 \quad \text{at} \quad D'_0 = \sqrt{3} \approx 1.73 \ . \tag{7.122}$$

This instability phenomenon occurs at a compressive deformation of the dielectric body at

$$\lambda_0 = \frac{1}{\sqrt[3]{4}} \approx 0.63 \ . \tag{7.123}$$

At this point it is obvious, that the electro-mechanical limit-point instability, for specific mechanical boundary conditions, is independent of the stretch itself. This motivates the definition of a *condensed energy function*

$$\psi'_{con}(D') = \inf_{\lambda} \ \psi'(\lambda, D') \ , \tag{7.124}$$

by exploiting the mechanical equilibrium condition. Note though, while the energy function $\psi'(\lambda, D')$ is convex with respect to both variables, the condensed energy is *non-convex*, as shown in Figure 7.3a. Starting from the condensed energy, the electric field is obtained by the differentiation with respect to the electric displacements $E' = \partial \psi'_{con}/\partial D'$, which again results in (7.121) and the related maximum (7.122), see also Figure 7.3b. The tangent modulus is obtained by the second derivative

$$\mathsf{C}_{con}(D') := \frac{\partial^2 \psi'_{con}}{\partial^2 D'} = \frac{3 - D'^2}{3(1+D'^2)^{5/3}} \ , \tag{7.125}$$

that determines the stability point D'_0 in $(7.122)_2$ for $\mathsf{C}_{con} = 0$, see also Figure 7.3c. Note the relation between the change of slope in the condensed energy, the electrical limit-point and the change of sign in the tangent modulus at D'_0 in Figure 7.3a-c, respectively.
Evidently, the use of a condensed energy is only valid for particular mechanical boundary conditions. In a more general way, the convex energy in (7.118) is the appropriate choice, which, following the same procedure, yields the general tangent modulus

$$\mathbf{C}(\lambda, D') = \begin{bmatrix} \partial^2_{\lambda\lambda}\psi' & \partial^2_{\lambda D'}\psi' \\ \partial^2_{D'\lambda}\psi' & \partial^2_{D'D'}\psi' \end{bmatrix} = \begin{bmatrix} 1 + 2\lambda^{-3} + D'^2 & 2D'\lambda \\ 2D'\lambda & \lambda^2 \end{bmatrix} \ . \tag{7.126}$$

Loss of positive semi-definiteness of the tangent modulus, as suggested in Box 7.1, is the necessary criterion for a critical point. A check based on the eigenvalues, or on a zero determinant, reads

$$\det[\mathbf{C}] = (1 + 2\lambda^{-3} - 3D'^2)\lambda^2 = \frac{3 - D'^2}{(1+D'^2)^{2/3}} \geq 0 \, , \tag{7.127}$$

and clearly identifies the stability point as computed in (7.122) and (7.123) for D'_0 and λ_0, respectively.

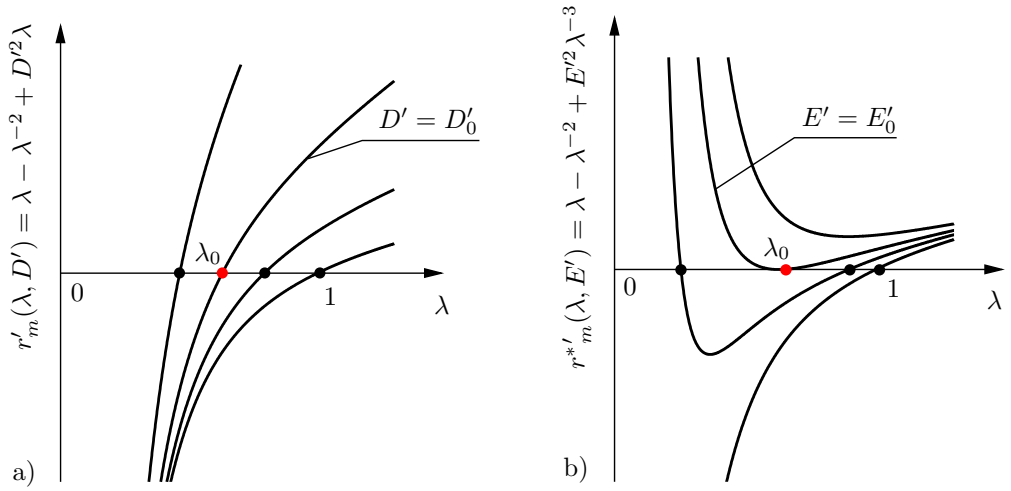

Figure 7.4: *Comparison of the residual functions of the energy and energy-enthalpy formulation.* a) The energy equilibrium condition for fixed values $D' = 3$, $D' = 1$, $D' = D'_0 = \sqrt{3}$, $D' = 0$ (left to right) is shown. Uniqueness of solutions is evident. b) The energy-enthalpy equilibrium condition for fixed values $E' = 0.9$, $E' = E'_0 = \frac{\sqrt{3}}{2\sqrt[3]{2}}$, $E' = 0.5$, $E' = 0$ (top to bottom). Here, starting from the critical electric field level, uniqueness of solution is lost.

Convenient enthalpy formulation. Application of a partial Legendre-Fenchel transformation gives the convenient normalized energy-enthalpy formulation

$$\psi^{*\prime}(\lambda, E') = \inf_{D'}[\, \psi'(\lambda, D') - E'D' \,] \,, \tag{7.128}$$

based on the energy function (7.118). The closed-form of the mixed energy-enthalpy function then reads

$$\psi^{*\prime}(\lambda, E') = \tfrac{1}{2}\,[\lambda^2 + 2/\lambda] - \tfrac{1}{2}\,E'^2\lambda^{-2} \,, \tag{7.129}$$

in terms of the principal stretch and the normalized electric field. Again, for the special case of zero external stresses, the stretch can be obtained by the minimization problem

$$\lambda = \arg\{\, \inf_{\lambda}\ \psi^{*\prime}(\lambda, E') \,\} \quad \text{for} \quad |E'| \leq E'_0 \,. \tag{7.130}$$

Variation yields the necessary condition, i.e. the equilibrium condition with mechanical and electrical Maxwell stress terms

$$\underbrace{\lambda - \lambda^{-2}}_{\text{mechanic } P^m} + \underbrace{E'^2\lambda^{-3}}_{\text{Maxwell } P^e} = 0 \,, \tag{7.131}$$

for zero external stress. While the procedure is identical to the canonical energy formulation, a fundamental difference occurs here due to the admissible electric field range $E' \leq E'_0$. It appears that, while the above equation only has solutions in the range $0 \leq E' \leq E'_0$, these solutions are not unique. At the same level of electric field there are two possible stretch states. One of which is related to the *pre-critical range* $D' := -\partial\psi^{*\prime}/\partial E' = E'\lambda^{-2} < D'_0$, while the other belongs to the *post-critical range* for $D' = E'\lambda^{-2} > D'_0$. Comparison of the residual functions of the energy and energy-enthalpy formulations reveals the differences of the mechanical equilibrium conditions

$$r'_m(\lambda, D') = \lambda - \lambda^{-2} + D'^2\lambda \quad \text{and} \quad r^{*\prime}{}_m(\lambda, E') = \lambda - \lambda^{-2} + E'^2\lambda^{-3} \,, \tag{7.132}$$

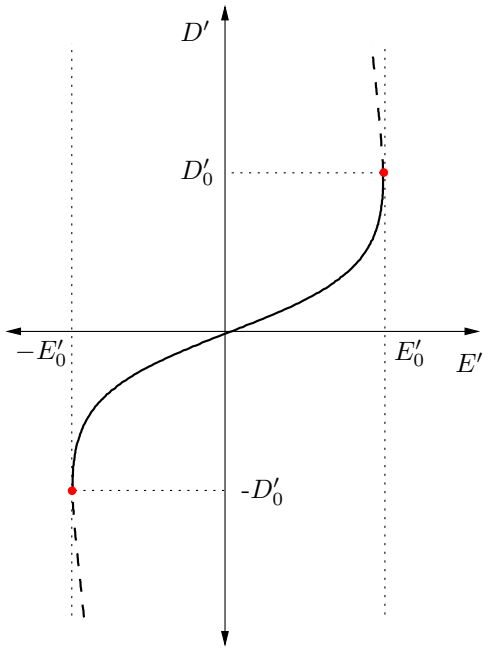

Figure 7.5: *Inverse function $D'(E')$ of the energy-enthalpy formulation.* The tracking of equilibrium states for increasing electric field loading is restricted to the domain defined by $[-E'_0, E'_0]$.

see also Figure 7.4, for different values of D' and E', including the critical values D'_0 and E'_0. While the residual r'_m of the energy function has a one-to-one relationship between λ and D' in the full range of D', see Figure 7.4a, the residual function ${r^*}'_m$ of the energy-enthalpy formulation may have one, two or no solution at all, for $E' < E'_0$, $E' = E'_0$ and $E' > E'_0$, respectively, see Figure 7.4b. Additionally, the horizontal tangent on the residual function ${r^*}'_m$ at the critical point E'_0 indicates the *loss of ellipticity of the mechanical sub-problem* of the energy-enthalpy formulation. With that, a fundamental drawback of the energy-enthalpy formulation in general finite element computational applications is revealed, as the detection of solution states near the critical electric field is difficult to find, even in the admissible range.
The stability criterion for the convenient enthalpy formulation as introduced in Box 7.2 is given in terms of the diagonal tangent modulus

$$\mathbf{C}^*_{stab}(\lambda, E') = \begin{bmatrix} \partial^2_{\lambda\lambda}\psi^{*\prime} & 0 \\ 0 & -\partial^2_{E'E'}\psi^{*\prime} \end{bmatrix} = \begin{bmatrix} 1 + 2\lambda^{-3} - 3{E'}^2\lambda^{-4} & 0 \\ 0 & \lambda^{-2} \end{bmatrix} , \tag{7.133}$$

that is obtained by the full tangent modulus $\mathbf{C}^*$ of the Newton-Raphson solution scheme. Again, the check of the eigenvalues, or in this case the determinant of the diagonal modulus, determines the stability point of (7.122) and (7.123), by

$$\det[\mathbf{C}^*_{stab}] = (1 + 2\lambda^{-3} - 3{E'}^2\lambda^{-4})\lambda^{-2} = 0\,. \tag{7.134}$$

In the convenient energy-enthalpy formulation, the electric part is stable in the range $0 < E' < E'_0$, however the full range of D' is not available as indicated in Figure 7.5. In contrast, the mechanical part loses stability at the critical limit-point E'_0.

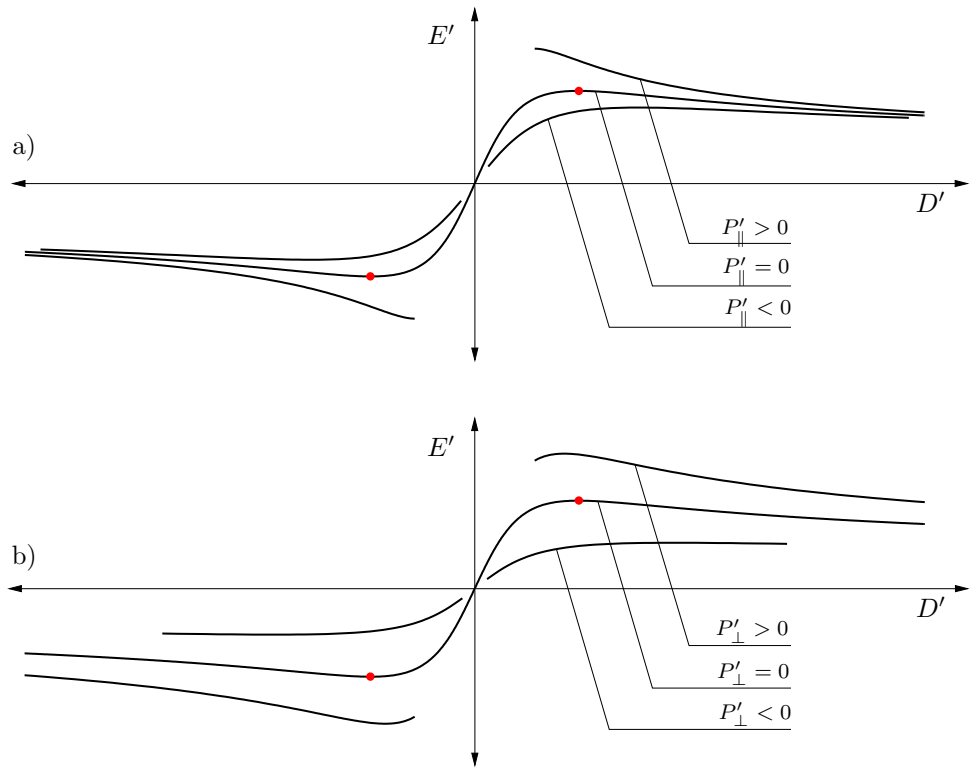

Figure 7.6: *Influence of the stresses $P'_{\parallel}$ and $P'_{\perp}$ on the critical electric field level.* a) Electric equilibrium curve for mechanical loading parallel to the resulting electric field and a fixed value $P'_{\perp} = 0$. b) E'-D' equilibrium path for a fixed value of $P'_{\parallel} = 0$ and mechanical loading perpendicular to the electric field loading. The red dot indicates the critical electric field for the reference solution (without mechanical loading).

7.7.3. Limit-point analysis for combined electro-mechanical loading

The influence of combined electro-mechanical loading onto the onset of limit-point instabilities is now of interest. For that, the mechanical stresses parallel and perpendicular to the electric loading direction are also prescribed, i.e. $P'_{\parallel} \neq 0$ and $P'_{\perp} \neq 0$. We restrict ourselves to the canonical energy formulation. This results in additional external loading components, such that the minimization problem now reads

$$\lambda = \arg\{ \inf_{\lambda} [\, \psi'(\lambda, D') - P'_{\parallel}\lambda - 2P'_{\perp}\lambda^{-1/2} \,] \} \,. \tag{7.135}$$

The necessary condition of the variational principle is the mechanical equilibrium equation that determines, for given stresses and electric displacements, the stretch λ by

$$\lambda - \lambda^{-2} + D'^2\lambda - P'_{\parallel} + P'_{\perp}\lambda^{-3/2} = 0 \,. \tag{7.136}$$

Reformulation for the electric displacements and applying the constitutive relation for the electric field yields the pair of equations

$$D' = \pm[\, \lambda^{-3} - 1 + P'_{\parallel}\lambda^{-1} - P'_{\perp}\lambda^{-5/2} \,]^{1/2} \quad \text{and} \quad E' = D'\lambda^2 \,. \tag{7.137}$$

that determine, for given stresses, implicitly the D'-E' diagram, parametrized by the stretch λ. The influence of mechanical stresses on the dielectric diagram is given in Figure 7.6a for parallel stresses, and in Figure 7.6b for perpendicular stresses. Note that for zero mechanical stresses the respective diagram corresponds to Figure 7.3.

Summary of observations

The above treated homogeneous examples give important insight in the phenomenon of electro-mechanical limit-point instability. In summary, the following observations of an ideal, incompressible dielectric elastomer, with neo-Hookean mechanical response can be made:

1. **Control variables**: The *energy formulation*, controlled by the electric displacements D', allows the analysis of an unstable $E' - D'$ diagram in the full range of loading. In contrast, the *enthalpy formulation* controlled by the electric field E' is *restricted* to the pre-critical range $|E'| \leq E'_0$ of the D'-E' diagram.

2. **Critical points**: In the *energy formulation*, an electro-mechanical instability is characterized by a limit-point in the *electrical* E'-D' diagram, governed by the condensed energy function ${\psi'}_{con}$. In the *energy-enthalpy formulation*, the electro-mechanical instability is characterized by a limit-point in the *mechanical* $P' - \lambda$ diagram.

3. **Material limit-point analysis**: In the *energy formulation*, the stability point is characterized by a singularity in the full tangent modulus $\mathbf{C}$, while in the *enthalpy formulation* a singularity in the diagonal tensor $\mathbf{C}^*_{stab}$ needs to be captured.

4. **Effect of stresses**: Positive/negative axial stresses $\pm P'_{\parallel}$ support/suppress the electro-mechanical instability. Likewise, positive/negative lateral stresses $\pm P'_{\perp}$ support/suppress it.

Further numerical investigation on more complex inhomogeneous materials, on both the macro- and the microscale, are treated in the following chapters. While this simple example was restricted to electro-mechanical problems, fully coupled phenomenological magneto-electro-mechanical models are also investigated.

7.8. Numerical examples: accompanying stability analysis

Macro- and microscopic instabilities of coupled magneto-electro-mechanics prohibit the rise of these smart materials, by restricting the achievable deformations due to electrical breakdown and magneto-electro-mechanical instabilities. To predict these detrimental effects, accompanying stability criteria for a finite element analysis of (composite) materials are necessary. Based on the criteria derived in this chapter, macro- and microscopic structural and material instabilities are predicted and visualized in the following analysis of magneto-electro-elasticity in a phenomenological setting of computational homogenization.

7.8.1. Problem 1: analysis of an inhomogeneous material element

As a direct extension to the explanatory analytical example, a first simple model of phenomenological electro-elasto-statics is in focus. Here, no separation of length scales is

considered and the structural and material electro-mechanical or limit-point instabilities are predicted by a stability checks accompanying the finite element analysis of the inhomogeneous material element.

Convenient enthalpy principle of electro-elasto-statics. The material modeling refers to the convenient enthalpy formulation which provides a two-field saddle-point variational principle as introduced in Chapter 6. The primary field variables for phenomenological finite deformations electro-mechanics are the deformation $\boldsymbol{\varphi}$ and the electric scalar potential ϕ^e in the body, such that

$$\boldsymbol{\varphi}\colon \begin{cases} \mathcal{B}\times\mathcal{T}\to\mathcal{R}^3 \\ (\boldsymbol{X},t)\mapsto\boldsymbol{\varphi}(\boldsymbol{X},t)=\boldsymbol{x} \end{cases} \quad\text{and}\quad \phi^e\colon \begin{cases} \mathcal{B}\times\mathcal{T}\to\mathcal{R} \\ (\boldsymbol{X},t)\mapsto\phi^e(\boldsymbol{X},t)\ . \end{cases} \tag{7.138}$$

The gradients of these two fields are denoted as the deformation gradient and the Lagrangian electric field

$$\boldsymbol{F}=\nabla\boldsymbol{\varphi}(\boldsymbol{X},t) \quad\text{and}\quad \mathbb{E}=-\nabla\phi^e(\boldsymbol{X},t)\ , \tag{7.139}$$

respectively. This ansatz automatically fulfills the mechanical compatibility condition $\operatorname{Curl}\boldsymbol{F}=\boldsymbol{0}$ and Faraday's law $\operatorname{Curl}\mathbb{E}=\boldsymbol{0}$. For the most general case, Chapter 5 provided the variational principle for grade-one dissipative materials, and generalized Euler-Lagrange equations were derived. Here, we reduce the given functions to cover finite electro-elastic response, by eliminating the dependency on a general order parameter. Note that, elastic response allows a time independent treatment. The reduced set of objective state variables then reads $\mathfrak{c}:=\{\boldsymbol{C},\mathbb{E}\}$, related to the two-field saddle-point variational principle

$$\{\boldsymbol{\varphi},\phi^e\}=\arg\Big\{\inf_{\boldsymbol{\varphi}\in\mathcal{W}_{\boldsymbol{\varphi}}}\sup_{\phi^e\in\mathcal{W}_{\phi^e}}\Pi(\boldsymbol{\varphi},\phi^e)\Big\}\,, \tag{7.140}$$

subjected to the admissible spaces $\mathcal{W}_{\boldsymbol{\varphi}}:=\{\boldsymbol{\varphi}\,|\,\boldsymbol{\varphi}=\overline{\boldsymbol{\varphi}}\text{ on }\partial\mathcal{B}_{\boldsymbol{\varphi}}\}$ and $\mathcal{W}_{\phi^e}:=\{\phi^e\,|\,\phi^e=\overline{\phi^e}\text{ on }\partial\mathcal{B}_{\phi^e}\}$. The potential consists of the energy storage, i.e. a mixed energy-enthalpy function and the external loading contribution Π_{ext}

$$\Pi(\boldsymbol{\varphi},\phi^e):=\int_{\mathcal{B}}\psi^*(\mathfrak{c})\,dV-\Pi_{ext}\,, \tag{7.141}$$

as suggested in Chapter 6. The necessary equilibrium condition is obtained by the first variation, yielding the Euler-Lagrange equations, recalled here for completeness,

1.	*Balance of linear momentum*	$\operatorname{Div}[\partial_{\boldsymbol{F}}\psi^*]+\overline{\boldsymbol{\gamma}}^m$	$=\boldsymbol{0}$	in $\mathcal{B}$
2.	*Prescribed tractions*	$\partial_{\boldsymbol{F}}\psi^*\cdot\boldsymbol{N}$	$=\boldsymbol{T}$	on $\partial\mathcal{B}_T$
3.	*Gauss's law*	$\operatorname{Div}[-\partial_{\mathbb{E}}\psi^*]$	$=0$	in $\mathcal{B}$
4.	*Electric surface flux*	$\partial_{\mathbb{E}}\psi^*\cdot\boldsymbol{N}$	$=\overline{D}$	on $\partial\mathcal{B}$

(7.142)

The constitutive dual variables, namely the nominal stress tensors $\boldsymbol{P}:=\partial_{\boldsymbol{F}}\psi^*$ and the electric displacement vector $\mathbb{D}:=-\partial_{\mathbb{E}}\psi^*$ are identified.

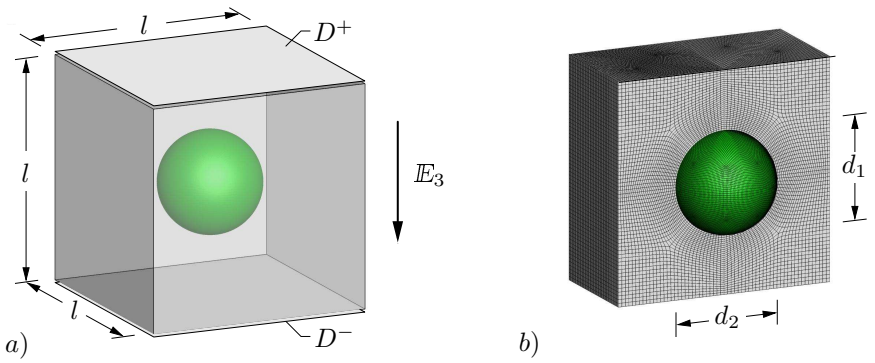

Figure 7.7: *Boundary-value-problem for electric two-phase composite*: EAP cube of dimension $l \times l \times l$ with either a stiff inclusion with high electric permittivity or a void, of aspect ratio $\omega = d_1/d_2$. a) The EAP is loaded by electrical charges D on the top and bottom compliant electrode, inducing an electric field $\mathbb{E}_3$. b) Investigated are spherical ($\omega = 1$), and ellipsoidal inclusions parallel ($\omega > 1$) or perpendicular ($\omega < 1$) to the resulting electric field direction, with varying volume fractions.

Definition of the model problem. Related to the theory of ideal dielectrics, the electro-elastic material response is governed by a simplified function, that adds to a standard neo-Hookean mechanical contribution an additional electrostrictive coupling part quadratic in the electric field

$$\psi^{*\prime}(\mathfrak{c}') = \psi^{*\prime}{}_{mech} + \psi^{*\prime}{}_{elec} \quad \text{with} \quad \begin{cases} \psi^{*\prime}{}_{mech}(\boldsymbol{C}) = \dfrac{1}{2}(\mathrm{tr}[\boldsymbol{C}] - 3) + \dfrac{1}{\beta}(J^{-\beta} - 1) \\ \psi^{*\prime}{}_{elec}(\boldsymbol{C}, \mathbb{E}') = -\dfrac{1}{2}(1 + \dfrac{\chi^e}{J}) J \boldsymbol{C}^{-1} : (\mathbb{E}' \otimes \mathbb{E}') \end{cases} \tag{7.143}$$

For numerical stability, normalized functions are chosen such that $\mathbb{E}' := \mathbb{E}/\sqrt{\mu/\epsilon_0}$. The material parameter $\beta = \frac{\lambda}{\mu} = \frac{2\nu}{1-2\nu}$ accounts for the shear modulus μ and Poisson's ratio ν, while χ^e is the electric susceptibility.

The specimen under consideration is an electro-active-polymer composite, consisting of a soft matrix material and either a stiff inclusion of high electric susceptibility or a void, of spherical or ellipsoidal shape, see Figure 7.7 for an illustration of a representative boundary-value-problem. Here, the matrix material (gray) of dimension $l \times l \times l$ surrounds a (spherical) inclusion (green) of major and minor diameter $d_1 = d_2 = d$. The global and local response of a family of inhomogeneous EAP structures is analyzed. Electrical charges on the top and bottom surface are prescribed, inducing an electrical field $\mathbb{E}_3$, while keeping the mechanical boundary unconstrained and traction free. The finite element discretization is based on standard Q1-Q1 brick-type elements and symmetry boundary-conditions are exploited.

Equilibrium states of the EAP structures are characterized by averaged and normalized electric field and electric displacement vectors, defined by

$$\overline{\mathbb{E}}' := \frac{1}{|\mathcal{B}|} \int_{\mathcal{B}} \mathbb{E}' \, dV \quad \text{and} \quad \overline{\mathbb{D}}' := \frac{1}{|\mathcal{B}|} \int_{\mathcal{B}} \mathbb{D}' \, dV \ , \tag{7.144}$$

where $\mathcal{B}$ is the reference volume of the EAP structure. $\overline{\mathbb{E}}'$-$\overline{\mathbb{D}}'$ diagrams document the *electric global structural response*. The *mechanical structural response* is reported by plotting an averaged deformation

$$\overline{\boldsymbol{F}} := \frac{1}{|\mathcal{B}|} \int_{\mathcal{B}} \boldsymbol{F} \, dV \tag{7.145}$$

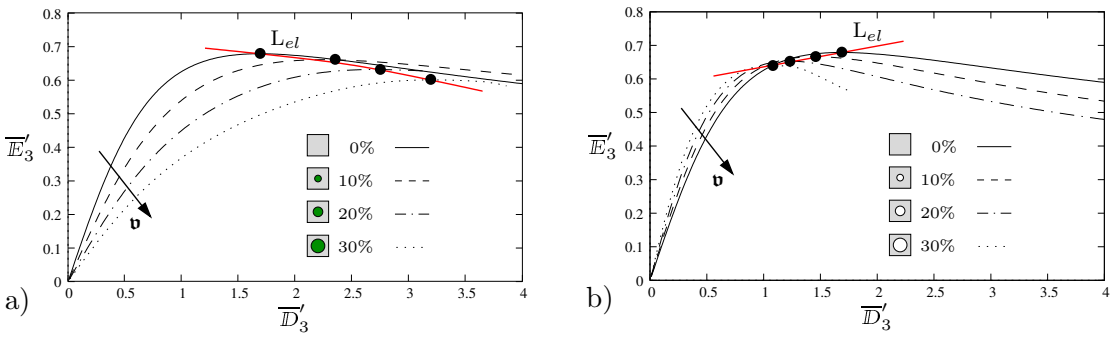

Figure 7.8: *Structural electro-mechanical instabilities of inhomogeneous materials.* Averaged electro-mechanical response of *spherical* a) inclusions and b) voids of different volume fractions is displayed. The onset of structural electro-mechanical instability L_{el} is highlighted. For increasing volume fractions $\mathfrak{v}$ the instability occurs at lower electric field levels.

of the full structure as a function of the averaged electric field $\overline{\mathbb{E}}'$. The local *loss of material stability* at typical Gauss points of the finite element mesh is indicated by highlighting elements in red, which mark unstable zones, i.e.

$$\mathbf{C}^*_{stab}\mathbf{p}_\alpha = \mu_\alpha \mathbf{p}_\alpha \quad \text{with} \quad \mu_\alpha \begin{cases} \geq 0 & \text{stable local state,} \\ < 0 & \text{unstable local state,} \end{cases} \tag{7.146}$$

while the structural instabilities are detected by the global response

$$\underline{\mathbf{K}}^*_{stab}\mathbf{p}_\alpha = \lambda_\alpha \mathbf{p}_\alpha \quad \text{with} \quad \lambda_\alpha \begin{cases} \geq 0 & \text{stable local state,} \\ < 0 & \text{unstable local state.} \end{cases} \tag{7.147}$$

The possibility to find equilibrium states in these unstable regions is one of the major benefits achieved by prescribing full Neumann boundary conditions on the electrical side.

Composites with spherical inclusions or voids. In a first example, spherical inclusions or voids ($\omega = 1$) of different volume fractions are in focus. The inhomogeneity is located in the center of the cube. Volume fractions of $\mathfrak{v} = \{\,0, 10, 20, 30\,\}$ [%] are investigated. Here, the intention is to show the different behavior of structural and material instability, i.e. onset of electro-mechanical instability, while improved actuation behavior is neglected for now. For material parameters physically reasonable values are chosen, with a factor of 1000 in-between the stiffness and the electric susceptibility of the matrix (soft, low susceptibility) and the inclusion (stiff, high susceptibility) material.
Figure 7.8 depicts the overall material response of the specimen. For an increasing volume fraction of the stiff inclusion, Figure 7.8a reflects that the onset of structural electro-mechanical instability occurs for lower electric fields. Note that the critical points, determined by an eigenvalue analysis of the averaged diagonal stiffness matrix $\underline{\mathbf{K}}^*_{stab}$, are highlighted in the plot. Likewise, for increasing spherical voids, the loss of positive semi-definiteness appears earlier, see Figure 7.8b.

The accompanying material stability analysis based on criterion (7.146) is employed for a representative boundary-value-problem with an inclusion or void of 5% volume fraction. Locally, at every Gauss point, an eigenvalue analysis of the diagonal moduli $\mathbf{C}^*_{stab}$ is performed, and the loss of positive semi-definiteness in elements is highlighted in the contour plot in red. Figure 7.9a shows a cut through the specimen and displays the evolution of unstable zones first on the interface between matrix and inclusion material on top and

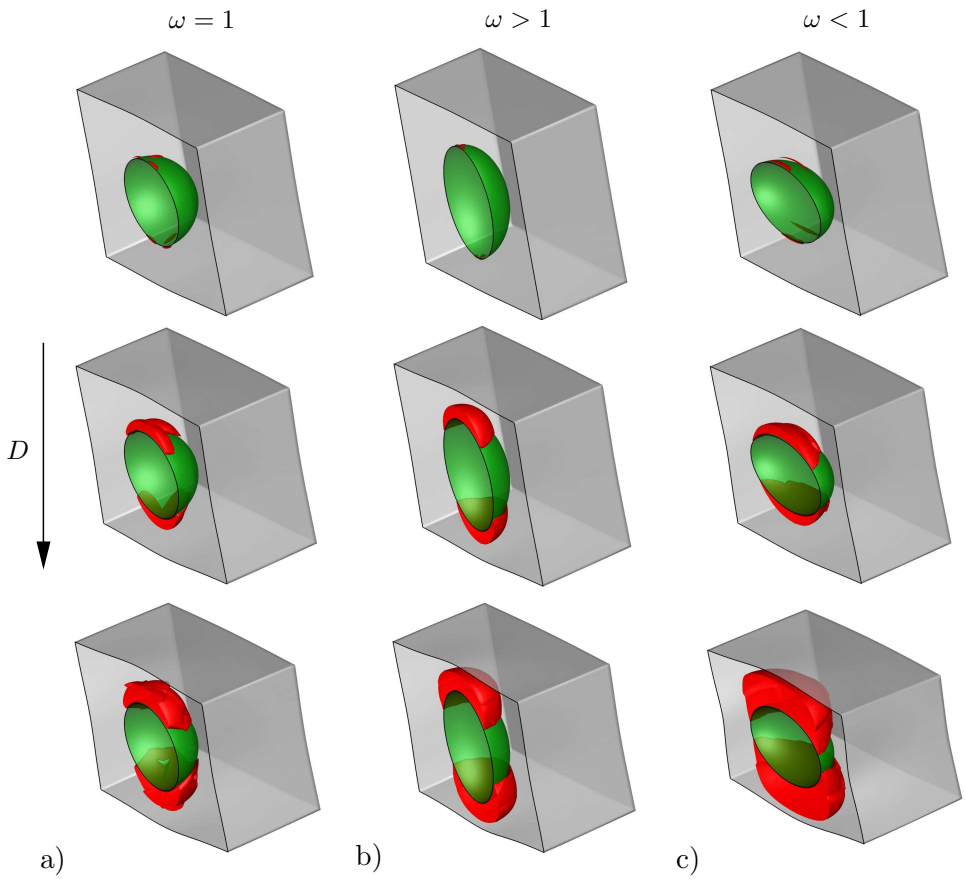

Figure 7.9: *Evolution of material limit-point instabilities.* For inhomogeneous materials with a) spherical, b) parallel ellipsoidal and c) perpendicular ellipsoidal inclusions of $\mathfrak{v} = 5\%$ volume fraction, the evolution of unstable zones are highlighted in red. As a local check, the eigenvalues of the respective tangent moduli at Gauss level are investigated. A negative eigenvalue coincides with the loss of positive semi-definiteness of the tangent. The instabilities first evolve on the top and bottom surface of the inclusion.

bottom of the sphere. From there, they develop in the direction of the adjacent surfaces of the body. This behavior is by no means arbitrary, but follows the critical electric field level. Figure 7.10a displays in a contour plot the electric field $\mathbb{E}_3'$ and reveals critical electric field levels $\mathbb{E}_0'$ first on top and bottom of the spherical inclusion. As the inclusion itself is a nearly perfect conductor, the electric field inside the inclusion tends to zero as the electric counterfield inside the inclusion negates the induced electric field. Therefore, the largest electric potential difference appears at the bounding surface between the matrix and inclusion material, due to the jump of the electric susceptibility, in applied field direction.

In comparison, the spherical void is considered in Figure 7.12a. Material stability is first lost around the void with a tendency to the corners of the cubic body, see Figure 7.12a. Here, the electric field within the void has a certain value, resulting in the highest potential difference between the sides of the inclusion and the matrix. Again, the unstable zones follow the regions of high electric field, Figure 7.13a, while the critical electric field overall tends to be lower.

Composites with ellipsoidal inclusions or voids. Next, as an inhomogeneity, either a stiff ellipsoidal inclusion with high relative permittivity or an ellipsoidal void, with

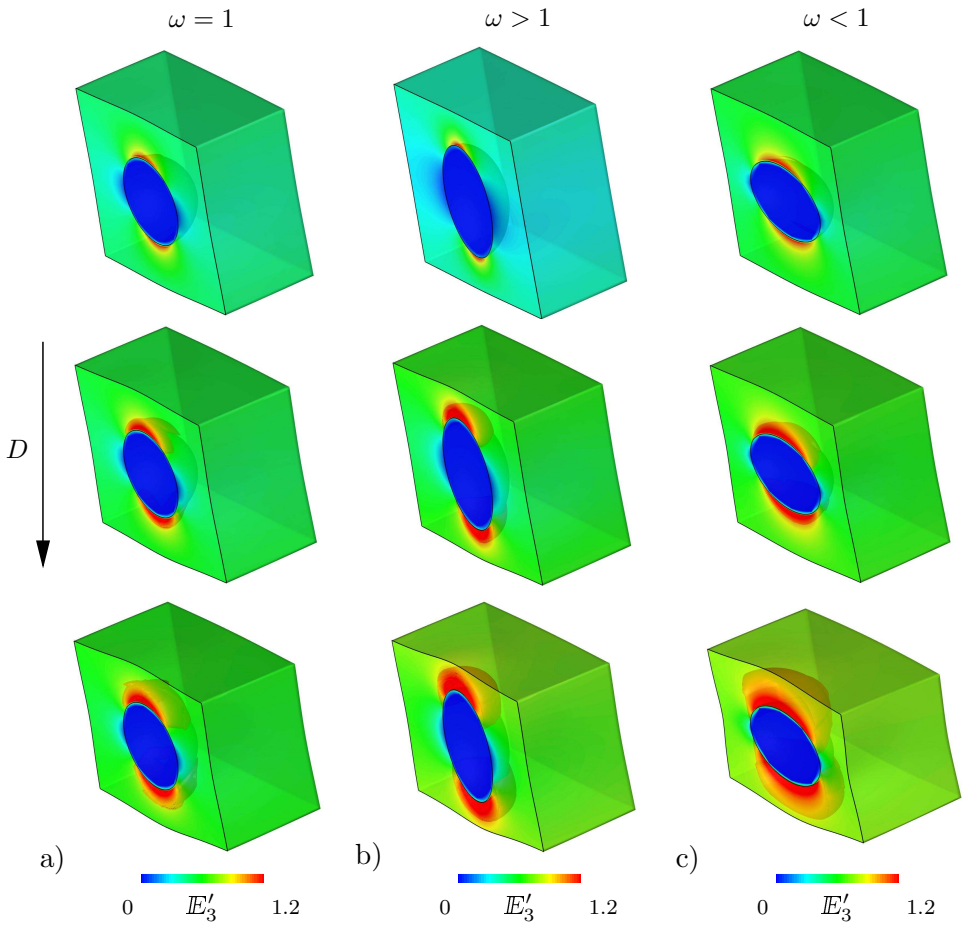

Figure 7.10: *Local limit-point stability analysis of inhomogeneous materials.* The contour plots in a), b), and c) show the resulting electric field $\mathbb{E}'_3$ for spherical, parallel ellipsoidal, and perpendicular ellipsoidal stiff inclusions, respectively. Inside the material, the developed unstable zones are highlighted in red. For increasing loading D, the electric field is highest on top and bottom interface between the inclusion and the matrix material. The evolving instabilities follow the critical field $\mathbb{E}'_0$.

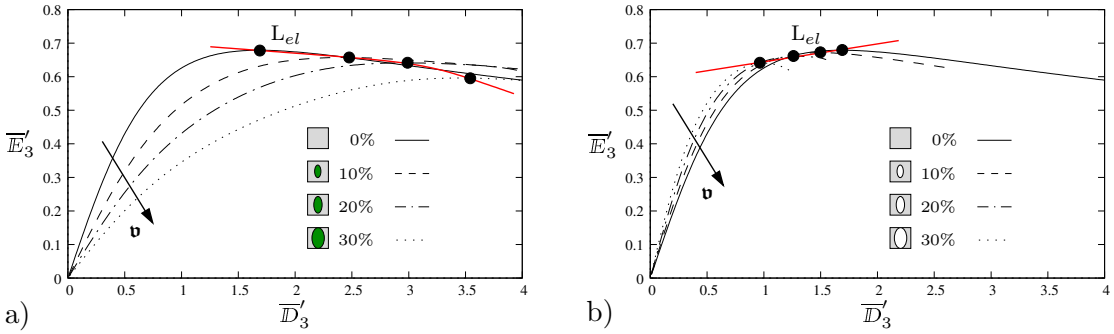

Figure 7.11: *Structural electro-mechanical instabilities of inhomogeneous materials.* Averaged electro-mechanical response of *ellipsoidal* a) inclusions and b) voids of different volume fractions, with the major axis *parallel to the loading direction* is displayed. The onset of structural electro-mechanical instability L_{el} is highlighted. For increasing volume fractions $\mathfrak{v}$ the instability occurs at lower electric field levels.

varying volume fractions of $\mathfrak{v} = \{\, 10, 20, 30 \,\}$ [%] is used to perturb the fields in an electro-active-polymer composite. Not only the shape of the inclusion, but also its orientation in the body, aligned ($\omega > 1$) or perpendicular ($\omega < 1$) to the resulting electric field direction,

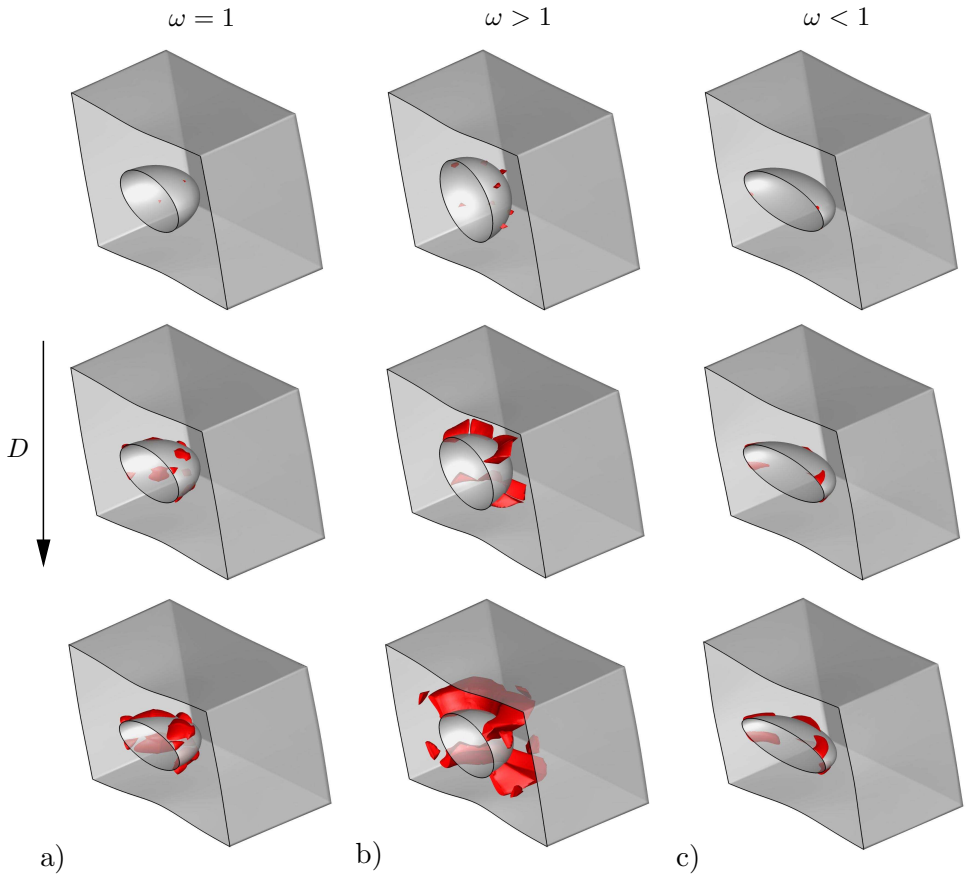

Figure 7.12: *Evolution of material limit-point instabilities.* For inhomogeneous materials with a) spherical, b) parallel ellipsoidal, and c) perpendicular ellipsoidal voids of $\mathfrak{v} = 5\%$ volume fraction, the evolution of unstable zones are highlighted in red. As a local check, the eigenvalues of the respective tangent moduli at Gauss level are investigated. A negative eigenvalue coincides with the loss of positive semi-definiteness of the tangent. The instabilities first evolve around the sides of the void.

is under investigation. Note that the ratio ω remains the same for either volume fraction.

For an ellipsoidal inclusion and void with the major axis parallel to the resulting electric field $\mathbb{E}'_3$ the global structural instability is investigated first. Again, the limit-point in the electro-mechanical equilibrium path characterized by the averaged fields $\overline{\mathbb{E}}'_3$-$\overline{\mathbb{D}}'_3$ diagram, Figure 7.11, reflects the onset of structural electro-mechanical instability. The structural stability criterion as summarized in Box 7.2, i.e. the positive semi-definiteness of the diagonal structural stability matrix $\underline{\mathbf{K}}^*_{stab}$ is lost at the global limit-point of the equilibrium curve, as marked in Figure 7.11a,b in the case of the inclusion and void, respectively. While for a void the critical electric field $\mathbb{E}'_0$ just decreases slightly for increasing volume fractions, in case of the stiff ellipsoidal inclusion the criterion is met for even lower electric field levels.

Investigating the evolution of material electro-mechanical instabilities within the inhomogeneous body by a local limit-point analysis, Figure 7.9b reveals, similar to the spherical inclusions, unstable zones first around the top and bottom in terms of the stiff inclusion of $\omega > 1$. The development of the electric field $\mathbb{E}'_3$ within the composite shows in Figure 7.10b the correlation between the local critical electric field $\mathbb{E}'_0$ and the evolving material instabilities.

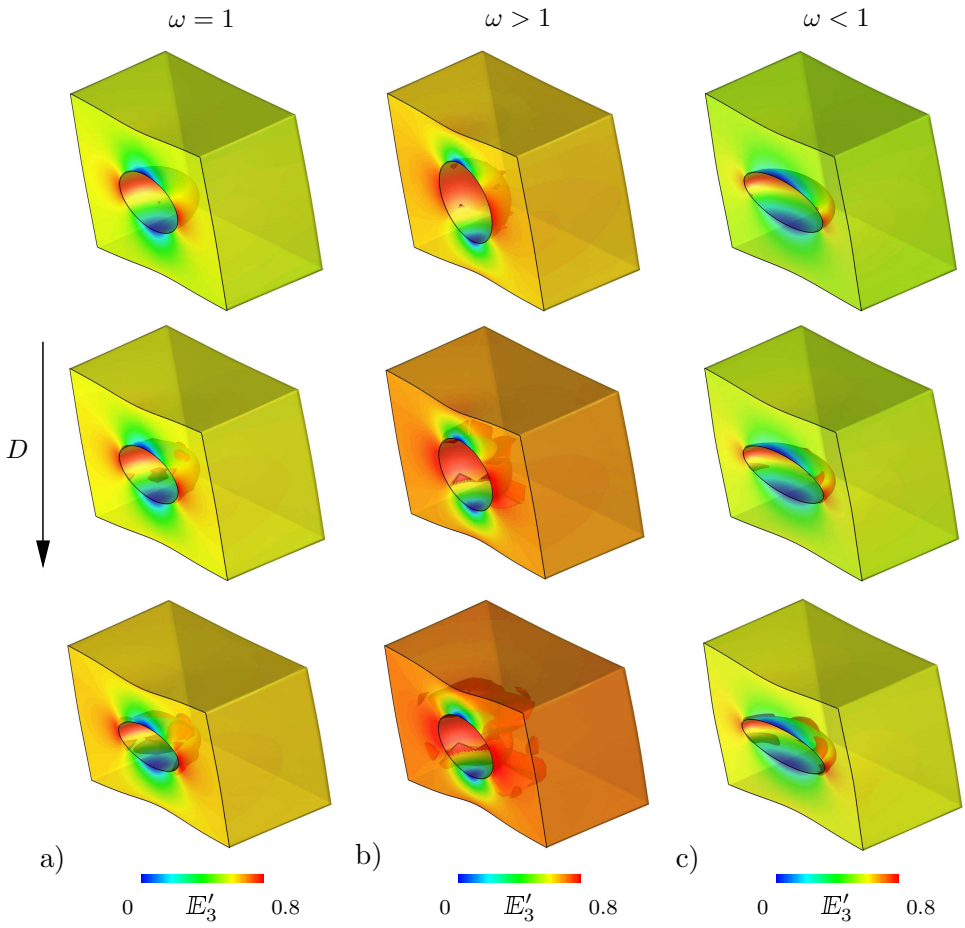

Figure 7.13: *Local limit-point stability analysis of inhomogeneous materials.* The contour plots in a), b), and c) show the resulting electric field $\mathbb{E}'_3$ for spherical, parallel ellipsoidal, and perpendicular ellipsoidal voids, respectively. Inside the material, the developed unstable zones are highlighted in red. For increasing loading D, the electric field is highest on the side interface between inclusion and matrix material. The evolving instabilities follow the critical field $\mathbb{E}'_0$.

In comparison, by assuming an ellipsoidal void within the dielectric elastomer of volume fraction $\mathfrak{v} = \{ 10, 20, 30 \}$ [%], the unstable zones develop in a circular shape around the deforming void with a tendency to the diagonals, Figure 7.12b. Note that the material limit-point criterion is met for lower local critical electric field values in case of the void, i.e. more element tangent moduli lost positive semi-definiteness in comparison to the stiff inclusions. This result, however, partly depends on the increased overall stiffness of the composite material with stiff inclusion. The electric field results in large compression, especially in the center of the material, due to the voids.

Last, ellipsoidal inclusions and voids with the major axis perpendicular to the electric field $\mathbb{E}'_3$ direction are in focus. Again, structural instability, highlighted in the global electro-mechanical response for different volume fractions are found, Figure 7.14a,b for an inclusion and void, respectively. In both cases an increasing volume fraction leads to lower critical electrical field limits $\mathbb{E}'_0$.

Material instabilities for the stiff inclusion follow the characteristic behavior of pronounced loss of positive semi-definiteness of the diagonal matrix on the top and bottom of the inclusion, see Figure 7.9c and 7.10c. For the void with $\omega < 1$ however, far less pronounced material instabilities are found. This is due to the large possible compressions due to the perpendicular alignment of the inclusions, as displayed in Figure 7.12c. Likewise, the

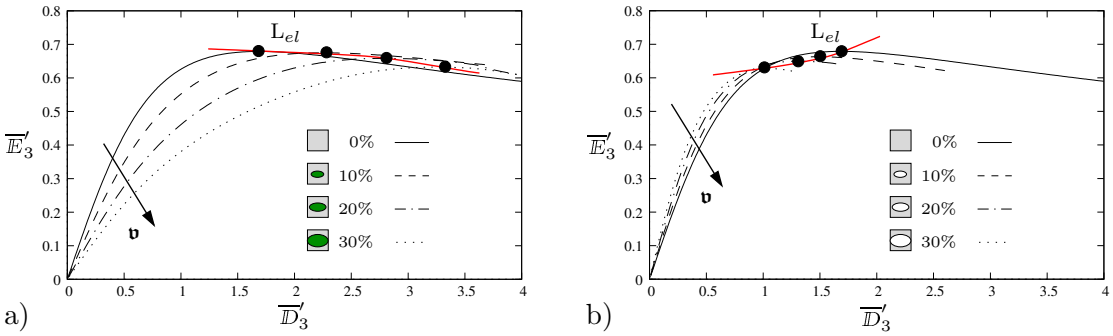

Figure 7.14: *Structural electro-mechanical instabilities of inhomogeneous materials.* Averaged electro-mechanical response of *ellipsoidal* a) inclusions and b) voids of different volume fractions, with the major axis *perpendicular to the loading direction* is displayed. The onset of structural electro-mechanical instability L_{el} is highlighted. For increasing volume fractions $\boldsymbol{\upsilon}$ the instability occurs at lower electric field levels.

electric fields are lower in general for perpendicular voids, Figure 7.13c.

Summary of observations. Accompanying stability checks of the enthalpy formulation summarized in Box 7.2 were applied on simple inhomogeneous boundary value problems of a polymeric matrix enclosing either a stiff inclusion of high electric permittivity or a void. The *structural stability criterion* $\det[\underline{\mathbf{K}}^*_{stab}] \geq 0$ reveals limit-points in the global electric response and shows that for increasing volume fractions structural instability arises for lower critical electric field values in both cases. Especially for stiff inclusions with high permittivity the critical electric field level reduces decisively.

For investigations on material instabilities, by applying the *local limit-point analysis* $\det[\mathbf{C}^*_{stab}] \geq 0$, the inhomogeneity induced by the inclusion localizes the development of unstable zones around the top and bottom inclusion-matrix interface, where the resulting electric fields are the highest. The spherical inclusion yields the most stable result, followed by the perpendicular inclusion, and concluded by the parallel inclusion. In terms of a void, the unstable zones evolve around the void as the potential difference is the highest at the sides. Note, that the critical electric fields are distinctively smaller, i.e. the instability criterion is met earlier. Again, the spherical void yields, together with the perpendicular ellipsoidal void, the most robust response while the vertically aligned inclusion is the least favorable.

7.8.2. Problem 2: multiscale stability analysis of magneto-active composites

The multiscale stability analysis of magnetorheological elastomers is in focus. These two-phase composite materials are especially useful due to their relatively low magnetic actuation fields and their various forms of industrial applications. Likewise to their electric counterpart, they consist of a soft matrix material and magnetically highly susceptible filler particles, such as iron. In the following, the influence of magnetic susceptibility on the overall macroscopic response as well as the famous magnetic stiffening effect is under investigation. In both cases a focus is set on the evolution of macro- and microscopic material instabilities following the criteria as summarized in the Boxes 7.2 and 7.1.

Convenient enthalpy principle of magneto-elasto-statics. The material modeling refers to the convenient enthalpy formulation which provides a two-field saddle-point variational principle as introduced in Chapter 6 for the electro-mechanical case. The primary field variables for phenomenological finite deformations magneto-mechanics are the deformation $\boldsymbol{\varphi}$ and the magnetic scalar potential ϕ^m in the body, such that

$$\boldsymbol{\varphi}\colon \begin{cases} \mathcal{B}\times\mathcal{T}\to\mathcal{R}^3 \\ (\boldsymbol{X},t)\mapsto\boldsymbol{\varphi}(\boldsymbol{X},t)=\boldsymbol{x} \end{cases} \quad\text{and}\quad \phi^m\colon \begin{cases} \mathcal{B}\times\mathcal{T}\to\mathcal{R} \\ (\boldsymbol{X},t)\mapsto\phi^m(\boldsymbol{X},t)\ . \end{cases} \tag{7.148}$$

The gradients of these two fields are denoted as the deformation gradient and the Lagrangian magnetic field

$$\boldsymbol{F}=\nabla\boldsymbol{\varphi}(\boldsymbol{X},t) \quad\text{and}\quad \mathbb{H}=-\nabla\phi^m(\boldsymbol{X},t)\ , \tag{7.149}$$

respectively. This ansatz automatically fulfills the mechanical compatibility condition $\operatorname{Curl}\boldsymbol{F}=\boldsymbol{0}$ and Ampère's law of magnetostatics $\operatorname{Curl}\mathbb{H}=\boldsymbol{0}$. In the most general case, Chapter 5 provided the variational principle for grade-one dissipative materials and generalized Euler-Lagrange equations were derived. Here, we reduce the given functions to cover finite magneto-elastic response, by eliminating the dependency on a general order parameter. Note that elastic response allows a time independent treatment. The reduced set of objective state variables then reads $\mathfrak{c}:=\{\boldsymbol{C},\mathbb{H}\}$, obtained by a two-field saddle-point variational principle

$$\{\boldsymbol{\varphi},\phi^m\}=\arg\Big\{\inf_{\boldsymbol{\varphi}\in\mathcal{W}_{\boldsymbol{\varphi}}}\sup_{\phi^m\in\mathcal{W}_{\phi^m}}\Pi(\boldsymbol{\varphi},\phi^m)\Big\} \tag{7.150}$$

subjected to the admissible spaces $\mathcal{W}_{\boldsymbol{\varphi}}:=\{\boldsymbol{\varphi}\,|\,\boldsymbol{\varphi}=\overline{\boldsymbol{\varphi}}\text{ on }\partial\mathcal{B}_{\boldsymbol{\varphi}}\}$ and $\mathcal{W}_{\phi^m}:=\{\phi^m\,|\,\phi^m=\overline{\phi}^m\text{ on }\partial\mathcal{B}_{\phi^m}\}$. The potential consists of the energy storage, i.e. a mixed energy-enthalpy function and the external loading contribution Π_{ext}

$$\Pi(\boldsymbol{\varphi},\phi^m):=\int_{\mathcal{B}}\psi^*(\mathfrak{c})\,dV-\Pi_{ext}\,, \tag{7.151}$$

as suggested in Chapter 6. The necessary equilibrium condition is obtained by the first variation, yielding the Euler-Lagrange equations recalled here for completeness

$$\begin{array}{llrll} 1. & \textit{Balance of linear momentum} & \operatorname{Div}[\partial_{\boldsymbol{F}}\psi^*]+\overline{\boldsymbol{\gamma}}^m &= \boldsymbol{0} & \text{in } \mathcal{B} \\ 2. & \textit{Prescribed tractions} & \partial_{\boldsymbol{F}}\psi^*\cdot\boldsymbol{N} &= \boldsymbol{T} & \text{on } \partial\mathcal{B}_{\boldsymbol{T}} \\ 3. & \textit{Gauss-Ampère law} & \operatorname{Div}[-\partial_{\mathbb{H}}\psi^*] &= 0 & \text{in } \mathcal{B} \\ 4. & \textit{Magnetic surface flux} & \partial_{\mathbb{H}}\psi^*\cdot\boldsymbol{N} &= \overline{B} & \text{on } \partial\mathcal{B} \end{array} \tag{7.152}$$

The constitutive dual variables, namely the nominal stress tensors $\boldsymbol{P}:=\partial_{\boldsymbol{F}}\psi^*$ and the magnetic induction vector $\mathbb{B}:=-\partial_{\mathbb{H}}\psi^*$ are identified.

Definition of the model problem. Magnetorheological elastomers are characterized by a non-magnetic elastomer matrix material and stiff inclusions with high magnetic susceptibility such as iron. The magnetic mixed energy-enthalpy function is additively decomposed into a mechanical and a magnetic part

$$\psi^*(\boldsymbol{C},\mathbb{H})=\psi^*_{mech}(\boldsymbol{C})+\psi^*_{mag}(\boldsymbol{C},\mathbb{H})\,. \tag{7.153}$$

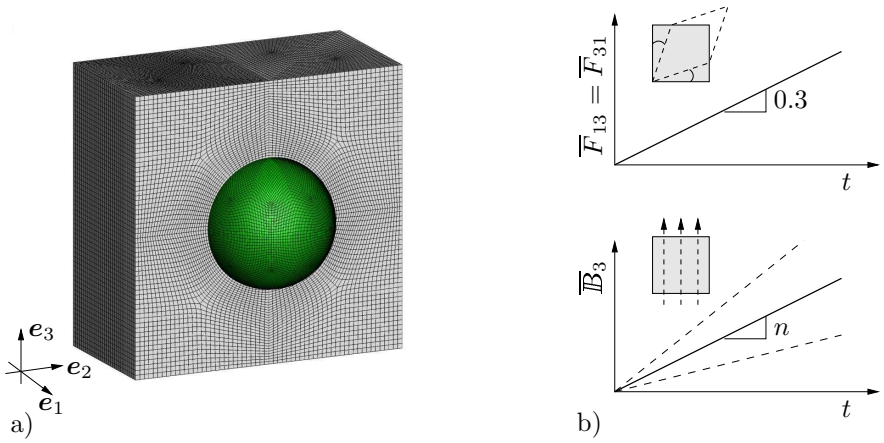

Figure 7.15: *Boundary-value-problem for a magnetic two-phase composite.* a) Representative volume element of size $30\,\mu\text{m} \times 30\,\mu\text{m} \times 30\,\mu\text{m}$ with spherical magnetic iron particle inclusion of radius $r = 6.37\,\mu\text{m}$ resulting in a volume fraction of 4%. The center of the inclusion and the cubic matrix coincide. b) Mechanical pure shear deformation $\overline{F}_{13} = \overline{F}_{31} = 0.3 \cdot t$ and applied magnetic induction $\overline{\mathbb{B}}_3 = n \cdot t$ characterized by the slope n.

Scanning electron microscope (SEM) images of typical magnetorheological elastomers with different volume fractions are given in Varga et al. [259], Danas et al. [49], and Saxena et al. [211]. The mechanical part of the two-phase composite is described by a neo-Hookean model for hyperelastic material response, which is given in (7.143). The magnetic energy-enthalpy is formulated such that it reflects the relation $\mathbb{b} = \mu_0^{mag}(\mathbb{h} + \mathbb{m})$ for the magnetic induction in the current configuration. For a linear, isotropic material the magnetization is assumed to be proportional to the magnetic field such that

$$\mathbb{b} = \mu_0^{mag}(\mathbb{h} + \mathbb{m}) = \mu_0^{mag}(1 + \tilde{\chi}^m)\mathbb{h} = \mu^{mag}\mathbb{h} \quad \text{with} \quad \tilde{\chi}^m = \frac{\varrho\chi^m}{\varrho_0} = \frac{\chi^m}{J} \tag{7.154}$$

due to the density dependent magnetic permeability $\mu^{mag} := \mu_0^{mag}(1 + \tilde{\chi}^m)$. This permeability is formulated in terms of the deformation dependent term $\tilde{\chi}^m = \chi^m/J$ with constant magnetic susceptibility χ^m, see McMeeking & Landis [152] for the corresponding electric case. Hence, we get

$$\psi^*_{mag}(\boldsymbol{C}, \mathbb{h}) = -\int_{\boldsymbol{0}}^{\mathbb{h}} \mathbb{b} \cdot d\mathbb{h} = -\frac{\mu_0^{mag}}{2}(1 + \frac{\chi^m}{J})\mathbb{h} \cdot \mathbb{h} \tag{7.155}$$

for the free energy-enthalpy per unit current volume formulated in terms of the deformation gradient and the Eulerian magnetic field. A formulation of the magnetic enthalpy in terms of the reference magnetic field $\mathbb{H} = \boldsymbol{F}^T\mathbb{h}$ results in

$$\psi^*_{mag}(\boldsymbol{C}, \mathbb{H}) = -\frac{\mu_0^{mag}}{2}(1 + \frac{\chi^m}{J})J\boldsymbol{C}^{-1} : (\mathbb{H} \otimes \mathbb{H}) \tag{7.156}$$

per unit reference volume. The magnetic permeability of free space is $\mu_0^{mag} = 4\pi \cdot 10^{-1}\,[\text{N/kA}^2]$, a physical measure of the amount of resistance encountered when forming a magnetic field in a vacuum. Note that in this first simple example, the saturation of the magnetic field is not incorporated, as the instability behavior of the composite under different loading cases is in focus. A more realistic modeling of magnetic materials can be found in later stages of this work in Chapter 9.

For a stable numerical treatment, dimensionless quantities are used. The energy-enthalpy

Table 7.3: Material parameters for elastomer matrix and iron particle inclusion.

no.	par.	name	elastomer	iron particle	unit
1.	μ	shear modulus	$3.45 \cdot 10^{-6}$	$81.78 \cdot 10^{-3}$	N/μm^2
2.	ν	Poisson ratio	0.45	0.29	–
3.	χ^m	magnetic susceptibility	0.0	5000	–

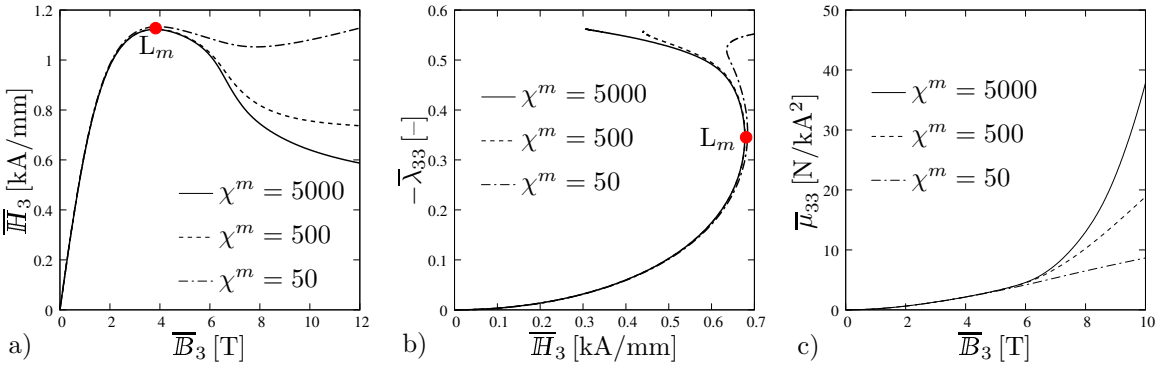

Figure 7.16: *Influence of magnetic susceptibility on macroscopic material instability.* a) Magnetic response by comparing the magnetic induction $\overline{\mathbb{B}}_3$ versus the magnetic field $\overline{\mathbb{H}}_3$ is shown for three different susceptibilities $\chi^m = \{50, 500, 5000\}$. Note that the response only differs in the post-critical regime. b) Magneto-mechanical material response of the composite causing a shrinking in the direction of the magnetic induction. Pre-critical actuation only differs slightly. c) Macroscopic magnetic permeability defined by $\overline{\mu}_{33}$ versus the applied loading. Increasing susceptibility leads to higher coupling.

function $\psi^*(\boldsymbol{F}, \mathbb{H})$ is normalized by the shear modulus μ and the magnetic permittivity μ_0^{mag}. This defines the dimensionless first Piola-Kirchhoff stress, the magnetic field, and the magnetic induction by

$$\boldsymbol{P}' := \frac{\boldsymbol{P}}{\mu} = \partial_{\boldsymbol{F}} \psi^{*\prime} \,, \quad \mathbb{H}' := \frac{\mathbb{H}}{\sqrt{\mu/\mu_0^{mag}}} \,, \quad \mathbb{B}' := \frac{\mathbb{B}}{\sqrt{\mu \mu_0^{mag}}} = -\partial_{\mathbb{H}'} \psi^{*\prime} \,. \tag{7.157}$$

The material parameters of carbonyl iron particles (CIP-SQ BASF) dispersed in an elastomer matrix (Elastosil LR 3000/03) of the magnetic two phase composite are given in Table 7.3, see also Javili et al. [103].

The periodic representative volume element of size $30\,\mu\text{m} \times 30\,\mu\text{m} \times 30\,\mu\text{m}$ has a spherical magnetic iron particle inclusion of radius $r = 6.37\,\mu$m embedded in a polymer matrix, resulting in a volume fraction of 4%, see Figure 7.15a. The combined macroscopic loading schemes for the two-phase composite, consisting of a linear increasing pure shear deformation and a magnetic induction, is given in Figure 7.15b.

Macroscopic material instability: influence of magnetic susceptibility. The current study investigates the influence of different magnetic susceptibilities of the inclusion on the overall response of the composite and on the onset of macroscopic material instabilities. The susceptibility is chosen as $\chi^m = \{50, 500, 5000\}$ for this study. The representative volume element with a 4% iron particle inclusion is driven by a linear increasing macroscopic magnetic induction $\overline{\mathbb{B}}_3$. Figure 7.16a compares the magnetic response by the magnetic induction versus magnetic field curve. Up to the limit-point (L$_m$) at $\overline{\mathbb{B}}_3 \approx 4\,$T

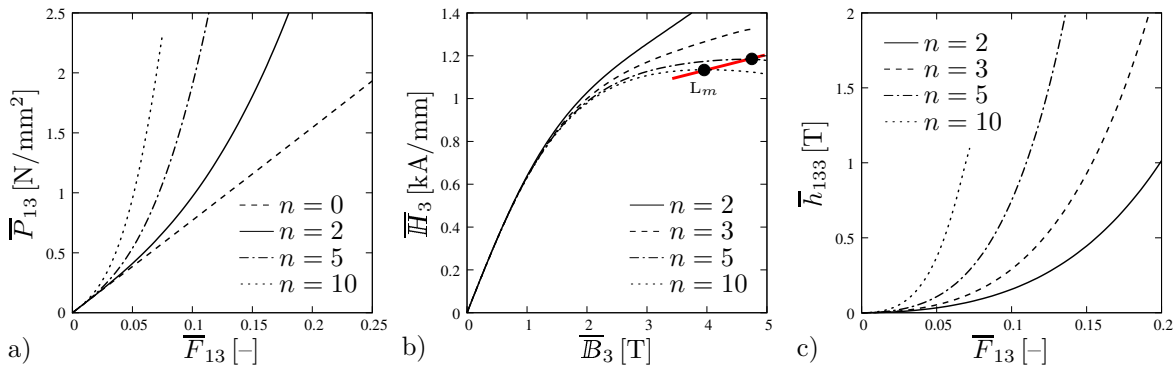

Figure 7.17: *Stiffening for an applied magnetic induction.* a) Mechanical response of macroscopic stress $\overline{P}_{13}$ versus applied shear deformation $\overline{F}_{13}$ for $n = \{0, 2, 5, 10\}$ characterizing the magnetic load. b) Influence of varying magnetic loads on the magnetic material response comparing macroscopic magnetic field $\overline{H}_3$ and applied induction $\overline{B}_3$. Depending on the magnitude of magnetic loading macroscopic magnetic limit-points (L_m) are reached earlier. c) Magnetomechanical coupling coefficient $\overline{h}_{133}$ versus shear deformation $\overline{F}_{13}$.

the material behavior slightly differs for the varying susceptibilities. In the post-critical regime where an increasing magnetic induction causes decreasing magnetic fields the influence of the susceptibility of the particle is more pronounced. Interestingly, For a small susceptibility ($\chi^m = 50$) the material becomes stable again with positive curvature after reaching the limit-point.
Furthermore, the magneto-mechanical material response of the composite is depicted in Figure 7.16b. The perfectly ordered iron particles of the periodic representative volume element cause the material to shrink in the direction of the macroscopically applied magnetic induction, see Danas et al. [49] for a sketch of the deformation mechanism. With respect to the onset of macroscopic material instability, the susceptibility of the filler particle seems to have no influence.
In Figure 7.16c, however, the average macroscopic magnetic permeability defined by $\overline{\mu}_{33} := -\partial\overline{B}_3/\partial\overline{H}_3$ versus the applied loading is shown. The curves are shifted to the origin of the coordinate system in order to ensure comparability. Here, for an increase in the susceptibility χ^m the permeability of the two phase composite increases. Hence, the high permeability inclusion should be preferred for industrial applications. For the subsequent simulations we choose $\chi^m = 5000$ representing an iron (99.8% pure) particle inclusion.

Macroscopic material instability: magnetic reinforcement. This study investigates the magnetic reinforcement effect of combined loading schemes for a two-phase composite with iron particles, compare with Figure 7.15b. A linear increasing pure shear deformation $\overline{F}_{13} = \overline{F}_{31} = 0.3 \cdot t$ is combined with a varying magnetic induction $\overline{B}_3 = n \cdot t$ in vertical $\boldsymbol{e}_3$-direction. Here, t is the proportionality factor for the loading in the FE-context and the integer n characterizes the slope of the magnetic load. The results on the magneto-mechanical response are summarized in Figure 7.17. The mechanical response of the first Piola-Kirchhoff stress $\overline{P}_{13}$ over the shear deformation $\overline{F}_{13}$ is depicted in Figure 7.17a. When combining the mechanical shear load with a magnetic induction, the *overall mechanical stiffness* of the composite *increases* due to the interaction of iron particles, see for instance Yalcintas & Dai [268], Kankanala & Triantafyllidis [110], and Varga et al. [259]. For comparison the curve for pure shear deformation

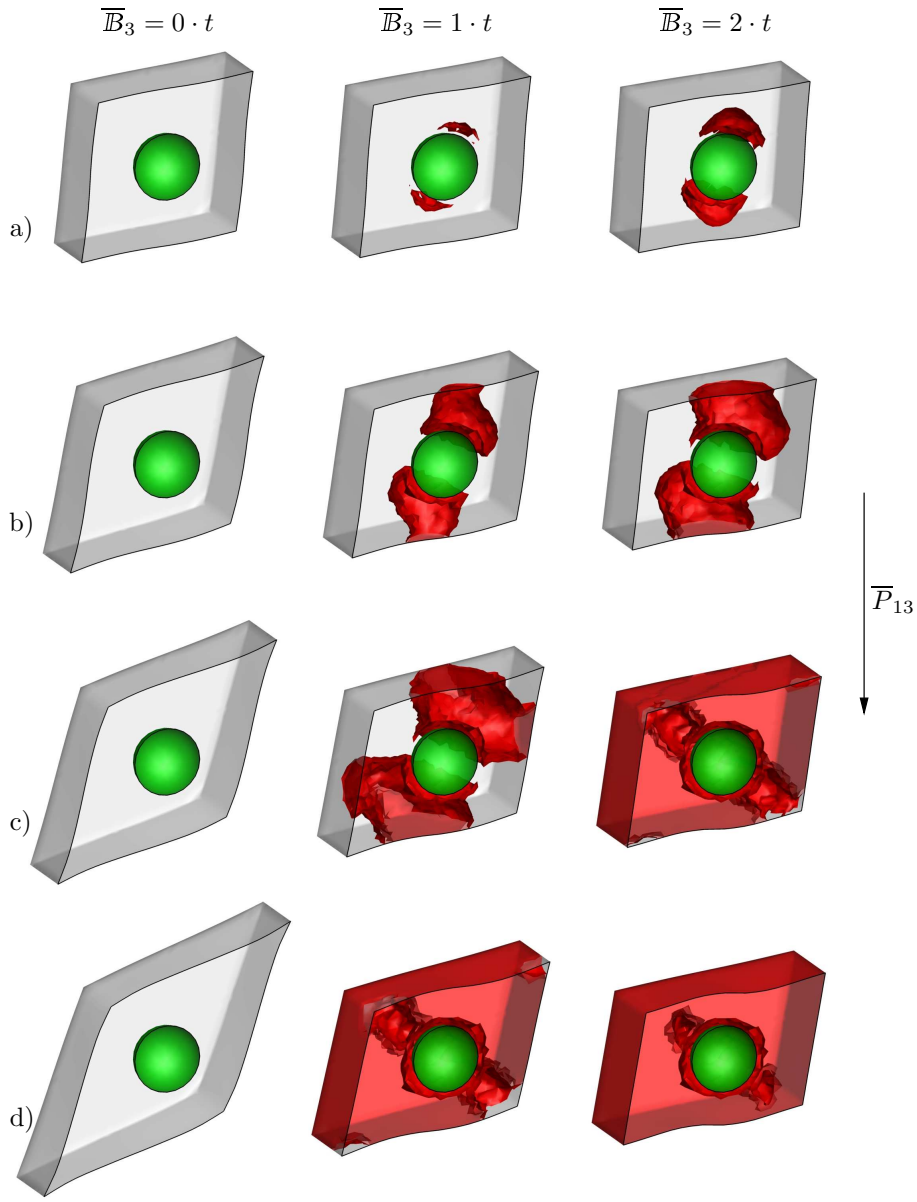

Figure 7.18: *Local limit-point stability analysis of magneto-mechanics.* The deformation states and reaching of local material limit-points are compared at different macroscopic stress states $\overline{P}_{13} = \{0.5, 1.0, 1.5, 2.0\}$ [N/mm^2] from a)-d), and applied magnetic induction $\overline{\mathbb{B}}_3 = n \cdot t$ with $n = \{0, 1, 2\}$ (column 1-3). Post-critical elements are marked red. While (increasing) magnetic loading stiffens the material it comes with the drawback of (earlier) magnetic instability.

without magnetic loading is depicted ($n = 0$). The second plot, Figure 7.17b, shows the purely magnetic response as the macroscopic magnetic field $\overline{\mathbb{H}}_3$ versus magnetic induction $\overline{\mathbb{B}}_3$ is plotted. The combined loading suppresses the formation of a macroscopic limit-point instability for small magnetic load. An increasing magnetic induction results in the post-critical drop of the magnetic behavior. Figure 7.17c shows the magneto-mechanical coupling coefficient $\overline{h}_{133} := \partial \overline{P}_{13} / \partial \overline{\mathbb{H}}_3$ over the prescribed shear deformation $\overline{F}_{13}$. The curves are shifted to the origin of the coordinate system to ensure comparability. Again, we observe that the increasing magnetic load stiffens the material response and raises the amount of coupling.

Microscopic material instability: limit-point analysis. For the combined loading of a shear deformation and magnetic induction the local stability analysis is performed. Post-critical magneto-mechanical zones, where the eigenvalue criterion outlined in Box 7.2 for the magnetic case is met, are shown in Figure 7.18. The figure depicts different macroscopic stress states $\overline{P}_{13} = \{0.5, 1.0, 1.5, 2.0\}\,[\mathrm{N/mm^2}]$ a)-d) for $n = \{0, 1, 2\}$ (left to right) defining the magnetic induction $\overline{\mathcal{B}}_3 := n \cdot t$. For a pure mechanical loading (first column in Figure 7.18) the shear deformation is clearly visible and no local stability issues occur in the hyperelastic case. As soon as a combination with magnetic loading is performed (second and third column), the shear deformation decreases due to the accompanied compression of the micro-structure by the magnetic influence and due to the stiffening of the composite discussed in the previous section. The sequence of pictures clearly outlines that the onset of local magneto-mechanical instability is linked to the amount of applied magnetic load, see e.g. the three snapshots corresponding to a stress state of $\overline{P}_{13} = 0.5\,[\mathrm{N/mm^2}]$ Figure 7.18a.

7.8.3. Problem 3: multiscale stability analysis of magneto-electro-mechanics

Three-phase magneto-electro-elastic composite materials are a possibility to enhance the magneto-electric coupling of single- or two-phase materials. Stresses induced by a magnetic (electric) field get transduced to the electric (magnetic) filler particle, resulting in an induced electric (magnetic) field due to the piezoelectric (magnetostrictive) property of the materials. The goal of this model problem is to determine the magneto-electric coupling coefficient on a computational basis, while also investigating to improve this coupling effects by tuning the three-phase material. A material stability analysis of the micro-structure accompanies the numerical computations.

Definition of the model problem. Outlined is a simple phenomenological model structure governing all relevant effects of three-phase magneto-electro-elastic composites. They are characterized by an elastic polymer matrix material (e.g. epoxy or polyurethane) and magnetostrictive as well as piezoelectric filler particles. The basic energy-enthalpy functions for the individual constituents are presented in the following, and normalization conditions are developed to ensure numerical stability. The energy-enthalpy function of the three-phase composite is additively decomposed in mechanical, electric, and magnetic parts, i.e.

$$\psi^*(\boldsymbol{C}, \mathbb{E}, \mathbb{H}) = \psi^*_{mech}(\boldsymbol{C}) + \psi^*_{elec}(\boldsymbol{C}, \mathbb{E}) + \psi^*_{piezo}(\boldsymbol{C}, \mathbb{E}; \boldsymbol{A}) + \psi^*_{mag}(\boldsymbol{C}, \mathbb{H})\,. \tag{7.158}$$

Note that both the electric and magnetic parts are coupled to the mechanical deformation. The polymer matrix material transfers the elastic deformation to the piezoelectric (magnetostrictive) particles producing an electric (magnetic) field due to the direct piezoelectric (magnetostrictive) effect. The mechanic ψ^*_{mech} and magnetic energies ψ^*_{mag} were already discussed previously in Problem 2. In addition to the isotropic electric part ψ^*_{elec}, specified in the above numerical examples, representing the interaction of matter and free space, an anisotropic piezoelectric contribution induced by the polarization is introduced. Piezoelectricity is a non-dissipative behavior and is characterized by a constant polarization director $\boldsymbol{A} := \mathbb{P}/\|\mathbb{P}\|$ in the Lagrangian configuration. This director serves as a structural tensor describing the anisotropy induced by the polarization. The author refers

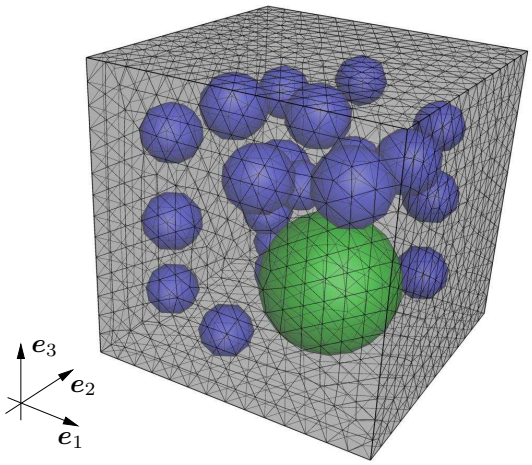

Figure 7.19: *Magneto-electric three-phase composite.* Representative volume element of size $30\,\mu\text{m} \times 30\,\mu\text{m} \times 30\,\mu\text{m}$ with magnetostrictive cobalt ferrite particle (green) and randomly distributed piezoelectric barium titanate particles (blue). The piezoelectric particles are poled in positive e_3-direction with structural vector $\boldsymbol{A} := [0, 0, 1]^T$. The sample is discretized by 32603 four node tetrahedron finite elements.

to the essential electro-mechanical coupling phenomena introduced in Miehe & Rosato [165]. The piezoelectric material response is described by an objective energy-enthalpy function given in terms of the Green-Lagrange strain $\boldsymbol{E}$ as the transversely isotropic function

$$\psi^*_{piezo} = -\alpha_0 \operatorname{tr}[\boldsymbol{E}(\boldsymbol{A} \otimes \boldsymbol{A})] \operatorname{tr}[\mathbb{E} \otimes \boldsymbol{A}] - \alpha_\perp \operatorname{tr}[\boldsymbol{E}] \operatorname{tr}[\mathbb{E} \otimes \boldsymbol{A}] - \alpha_= \operatorname{tr}[\boldsymbol{E}(\mathbb{E} \otimes \boldsymbol{A})] \,. \quad (7.159)$$

The three additional material parameters are the axial piezoelectric expansion α_0, the lateral piezoelectric expansion $\alpha_\perp$, and the piezoelectric shearing $\alpha_=$. They are related to the piezoelectric material parameters found in literature via the relations

$$\alpha_0 = 2\mu(d_{33} - d_{31} - d_{15}) \,, \quad \alpha_\perp = 2\mu d_{31} + \lambda(d_{33} + 2d_{31}) \,, \quad \alpha_= = 2\mu d_{15} \,, \quad (7.160)$$

where λ is the first and μ the second Lamé parameter, see Miehe & Rosato [165].
For numerical stability dimensionless quantities are introduced. The total energy-enthalpy function is normalized by the shear modulus μ. This defines the dimensionless first Piola-Kirchhoff stress, the electric and magnetic fields, and the electric displacements and magnetic induction in terms of the permittivity of free space ϵ_0 and permeability of free space μ_0^{mag}. Note that these two physical constants are related by the speed of light in vacuum via $c_0 = 1/\sqrt{\epsilon_0 \mu_0^{mag}}$. For the anisotropic piezoelectric energy-enthalpy function the normalization results in normalized material parameters

$$\alpha'_0 = \frac{\alpha_0}{\sqrt{\mu\epsilon_0}} \,, \quad \alpha'_\perp = \frac{\alpha_\perp}{\sqrt{\mu\epsilon_0}} \,, \quad \alpha'_= = \frac{\alpha_=}{\sqrt{\mu\epsilon_0}} \,. \quad (7.161)$$

For the numerical determination of the magneto-electric effect the complex micro-structure shown in Figure 7.19 is used as a representative example. A single magnetostrictive cobalt ferrite particle (green) and several randomly distributed piezoelectric barium titanate particles (blue) are embedded in a soft polymer matrix. The piezoelectric particles are pre-poled in positive $\boldsymbol{e}_3$-direction via the structural vector $\boldsymbol{A} := [0, 0, 1]^T$. The influence of the matrix material on the magneto-electric coupling coefficient is investigated by considering two different epoxy polymers as the binder material. Macroscopic mechanically

free $\overline{\boldsymbol{P}} = \boldsymbol{0}$ and open circuit measurement conditions $\overline{\mathbb{D}} = \boldsymbol{0}$ are applied. The magnetic induction in $\boldsymbol{e}_3$-direction is prescribed as an external loading condition $\overline{\mathbb{B}} = [0, 0, \overline{\mathbb{B}}_3]^T$. The macroscopic loading is transferred to the micro-structure by periodic boundary conditions for the primary fields, that are the displacement, the electric scalar potential and the magnetic scalar potential. The material parameters used in the subsequent numerical simulations are outlined in Table 7.4.

Magneto-electric coupling coefficient. The macroscopic magneto-electric (ME) coupling observed in the three-phase composite is achieved due to the indirect coupling by the matrix material. It transfers the strains, produced by the magnetic loading, to the electric particles which creates an electric field due to the piezoelectric effect. The magnetic loading causes a macroscopic magneto-electric coefficient in the overall tangent moduli. Formally, the ME coupling tensor and its normalization can be defined by

$$\overline{\boldsymbol{\alpha}} = -\frac{\partial \overline{\mathbb{D}}}{\partial \overline{\mathbb{H}}} = -\left(\frac{\partial \overline{\mathbb{B}}}{\partial \overline{\mathbb{E}}}\right)^T \quad \text{and} \quad \overline{\boldsymbol{\alpha}}' = \frac{\overline{\boldsymbol{\alpha}}}{\sqrt{\epsilon_0 \mu_0^{mag}}}\,, \tag{7.162}$$

see for instance Labusch et al. [126]. The latter is evaluated using partitions of the homogenized tangent moduli $\overline{\mathbf{C}}^*$.

In a first step, the influence of the electric susceptibility χ^e of the matrix material on the magneto-electric effect is in focus, followed by the study of varying shear moduli μ on the overall response. For the cobalt ferrite and barium titanate particles the material parameters outlined in Table 7.4 are used. The magneto-electric coupling coefficient $\overline{\alpha}_{33}$ is determined for varying susceptibilities $\chi^e = \{5, 10, 15\}$ of the matrix material of the representative volume element. The result is shown in Figure 7.20a showing an increasing magneto-electric effect for an increasing susceptibility of the epoxy matrix. The highest susceptibility investigated causes more than a doubling of the ME effect in the three-phase composite. However, the peak of all three curves can be found for almost identical magnetic loading fields $\overline{\mathbb{B}}_3$. Hence, the necessary magnetic load slightly changes, but the resultant ME coupling increases drastically. Similar conclusions related to the investigation of different conductivities of the matrix material are drawn in Tsang et al. [256], and Chau et al. [42]. In a second step, the *stiffness of the matrix material* is studied. Figure 7.20b depicts four different shear moduli in descending order $\mu_i = \{128.00, 70.40, 12.80, 1.28\} \cdot 10^{-5}$ for constant electric susceptibility $\chi^e = 10$ of the epoxy matrix. For a soft matrix material, the maximum magneto-electric effect appears at much lower magnetic loads, but on the other hand the maximum value decreases accordingly. Solely for $\mu_2 = 70.40 \cdot 10^{-5}$ an aberration is observed. Here, the necessary field

Table 7.4: Material parameters for three-phase magneto-electro-elastic composites.

no.	par.	name	epoxy	$BaTiO_3$	$CoFe_2O_4$	unit
1.	μ	shear modulus	$1.28 \cdot 10^{-3}$	$4.30 \cdot 10^{-2}$	$4.53 \cdot 10^{-2}$	$\mathrm{N}/\mu\mathrm{m}^2$
2.	ν	Poisson ratio	0.35	0.32	0.40	–
3.	χ^e	electric susceptibility	10.0	1250.0	10.0	–
4.	χ^m	magnetic susceptibility	0.0	5.0	125.0	–
5.	α_0	axial piezoel. expansion	0.0	18.6	0.0	$\mathrm{N}/\mathrm{MV}\mu\mathrm{m}$
6.	$\alpha_\perp$	lateral piezoel. expansion	0.0	-4.4	0.0	$\mathrm{N}/\mathrm{MV}\mu\mathrm{m}$
7.	$\alpha_=$	piezoel. shearing	0.0	11.6	0.0	$\mathrm{N}/\mathrm{MV}\mu\mathrm{m}$

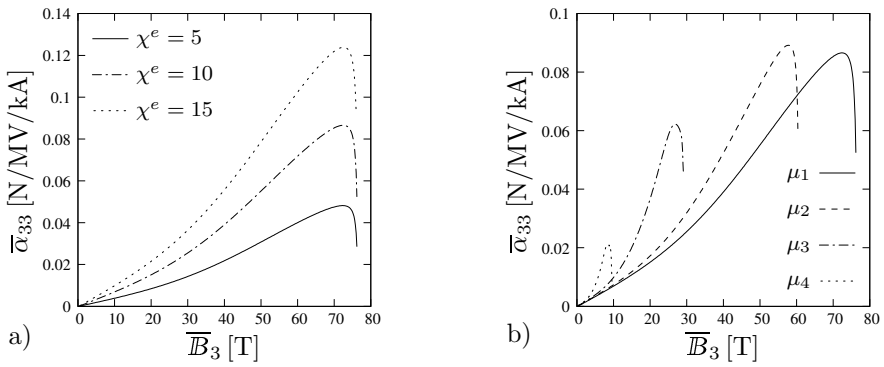

Figure 7.20: *Magneto-electric coupling coefficient.* Magneto-electric coupling in loading direction for a) varying electric susceptibility χ^e of the matrix material with fixed matrix stiffness $\mu_1 = 1.28{\cdot}10^{-3}$ and b) varying matrix stiffness $\mu_1 = 1.28{\cdot}10^{-3}$, $\mu_2 = 7.04{\cdot}10^{-4}$, $\mu_3 = 1.28{\cdot}10^{-4}$, $\mu_4 = 1.28 \cdot 10^{-5}$ for a fixed value of electric susceptibility $\chi^e = 10$.

still decreases, but the amount of magneto-electric coupling obtained from the three-phase composite increases. For industrial applications high coupling for low magnetic/electric fields are mandatory. As matrix material a polymer with high electric susceptibility and low shear modulus are beneficial. However, as the stiffness of the three phases are highly different, the safe compound of the materials need to be the primary goal.

Microscopic material instability: limit-point analysis. Following the criteria presented in Box (7.2), the local electro-magneto-mechanical instability is investigated by checking for negative eigenvalues of the block diagonal stiffness matrix in the convenient enthalpy formulation. Elements in which negative eigenvalues occur are highlighted red. Prescribing the magnetic induction yields a growing magnetic field inside the material, especially localized on top and bottom of the magnetic inclusion. Following the critical magnetic field level, the material limit-point criterion is first met on the top and bottom of the magnetic inclusion as the stiffness of the matrix material weakens most in these areas. As the piezoelectric particles have a higher susceptibility than the matrix material the critical field level is met on top and bottom as well as in between adjacent particles, in conjunction with the loading and polarization direction.

Summary of observations

The various soft composite materials investigated show different types of instability phenomena, which even might be exploited for future enhancement of their performance. This covers micro-structural instabilities, such as buckling of micro-fibers or particles, as well as material instabilities in the form of limit-points in the local constitutive response. Here, the homogenization-based scale-bridging links long wavelength micro-structural instabilities to material instabilities at the macroscale. For the accompanying multiscale stability analysis, a convenient enthalpy formulation, based on an energy, is employed which leads to a simple decoupled diagonal structure of the local and global tangent moduli. Positive semi-definiteness of said tangent is checked by an eigenvalue analysis, where the change of sign of the lowest eigenvalue defines the onset of instability. For phenomenological coupled electro-, magneto- and magneto-electro-elasticity the characteristic features were presented and analyzed with respect to the onset of macroscopic

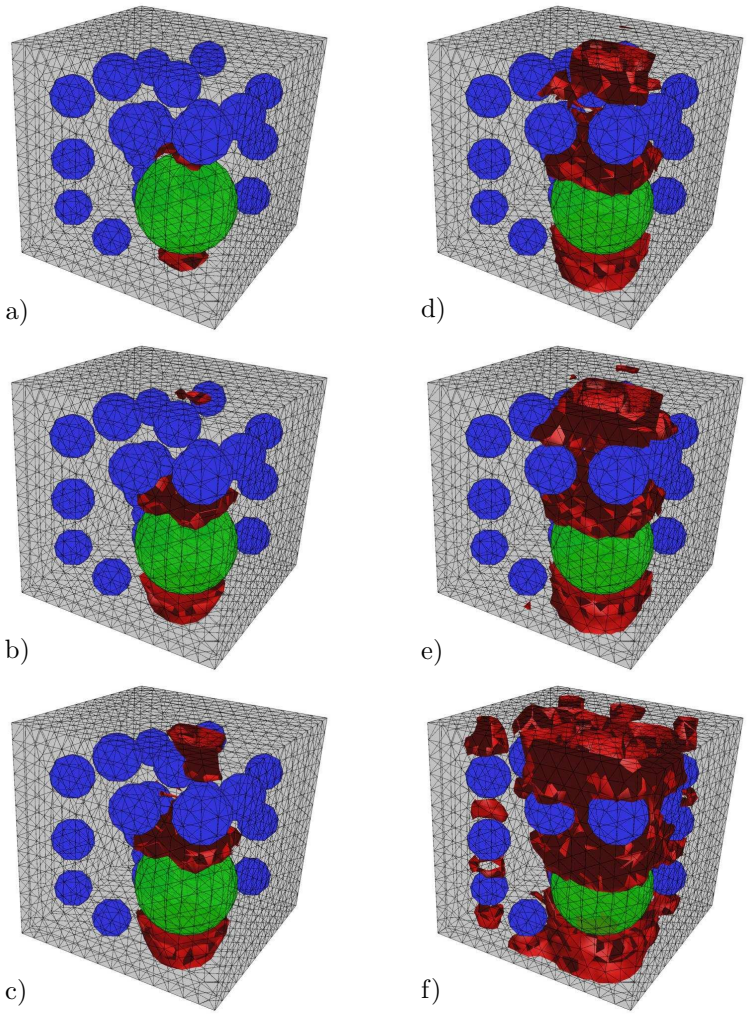

Figure 7.21: *Local limit-point analysis of the micro-structure.* Representative volume element with magnetostrictive (green) and piezoelectric inclusions (blue) under prescribed magnetic induction loading. The red zones indicate elements with negative eigenvalues of the block diagonal stiffness matrix. For increasing magnetic induction loading the post-critical zones first evolve on top and bottom of the magnetic inclusion a) and then spread aligned with the field direction in between adjacent particles b)-f).

and microscopic material instability. It was found that on the interface of the two- and three-phase materials the resulting electric and magnetic fields are the highest due to the jump in the permittivity of either material. This leads to the evolution of unstable zones which ultimately may lead to material failure. It was shown that while increasing volume fractions of the highly susceptible filler particle enhances the actuation of the composite, it also comes with earlier instabilities. This yields an optimization problem that might determine problem specific optimized micro-structures.

— Part IV —

Computational Homogenization in Micro-Magneto-Electro-Mechanics

Chapter 8

Phase-field modeling of finite deformation micro-electro-mechanics

Particle-particle interactions on the microscale of EAP and MRE composite materials add to the respective coupling properties. To cover these effects and thereby improving the predictive qualities of macroscopic models, the dissipative micro-structure, i.e. evolution of electric and magnetic domains within the particles, is incorporated via a phase-field approach into a two-scale computation. While this topic is already covered in literature for small strain scenarios and single-phase materials, Zäh & Miehe [273], Sridhar et al. [235], the author proposes a large strain formulation that is capable to predict effective macroscopic responses based on interactions on the microscale of two-phase composite materials, see also Vallicotti et al. [257].

Investigations on the evolution and motion of electric and magnetic domain walls on the microscale are based on the *domain theory of magnetization* initiated by the seminal work of Landau & Lifshitz [129], and further investigations by Brown [32, 33, 34]. The application of a phase-field theory to describe the evolution and motion of electric domain walls can be found in the works of Zhang & Bhattacharya [277, 278], Su & Landis [239], Schrade et al. [212], and Zäh & Miehe [272, 273].

In the following, a variational homogenization framework is provided, that covers the dissipative micro-structure and relates the microscopic potential to the macro-structure by appropriate averaging theorems based on a generalized Hill-Mandel homogeneity condition. Then, the influence of particle-particle and particle-matrix interactions on the effective material response is investigated. The effective characteristic dielectric and butterfly hysteresis curves are obtained for different particle shapes and volume fractions, and the resulting macroscopic deformation is displayed.

8.1. Two-scale finite deformation micro-electro-mechanics

8.1.1. Macroscopic variables and gradient fields

In the following, the convenient enthalpy formulation as introduced in Chapter 6 is employed on both the macro- and microscale. For the macroscopic boundary-value-problem of coupled electro-mechanics at finite deformations, the deformation map $\overline{\boldsymbol{\varphi}}$ and the scalar electric potential $\overline{\phi^e}$ are recalled as

$$\overline{\boldsymbol{\varphi}} : \begin{cases} \overline{\mathcal{V}} \times \overline{\mathcal{T}} \to \overline{\mathcal{S}} = \overline{\boldsymbol{\varphi}}_t(\overline{\mathcal{V}}) \\ (\overline{\boldsymbol{X}}, t) \mapsto \overline{\boldsymbol{x}} = \overline{\boldsymbol{\varphi}}(\overline{\boldsymbol{X}}, t) \end{cases} \quad \text{and} \quad \overline{\phi^e} : \begin{cases} \overline{\mathcal{V}} \times \overline{\mathcal{T}} \to \mathcal{R} \\ (\overline{\boldsymbol{X}}, t) \mapsto \overline{\phi^e}(\overline{\boldsymbol{X}}, t) \end{cases} , \tag{8.1}$$

see Figure 5.1 in the generalized formulation. The related gradient fields

$$\overline{\boldsymbol{F}} = \overline{\nabla} \overline{\boldsymbol{\varphi}}(\overline{\boldsymbol{X}}, t) \quad \text{and} \quad \overline{\mathbb{E}} = -\overline{\nabla}\, \overline{\phi^e}(\overline{\boldsymbol{X}}, t) , \tag{8.2}$$

are the macroscopic deformation gradient and the macroscopic electric field, respectively. This specific ansatz satisfies directly the mechanical compatibility condition $\overline{\mathrm{Curl}}[\overline{\boldsymbol{F}}] = \boldsymbol{0}$ of the deforming solid as well as Faraday's law of electrostatics $\overline{\mathrm{Curl}}[\overline{\mathbb{E}}] = \boldsymbol{0}$ in $\overline{\mathcal{V}}$. Note that the motion $\overline{\boldsymbol{\varphi}}$ is constrained by the condition $\det[\overline{\boldsymbol{F}}] > 0$ to rule out material penetration.

8.1.2. Macroscopic rate-type variational principle

We postulate the evolution of the macroscopic deformation and electric potential to depend on a rate-type saddle-point variational principle at a given state $\{\, \overline{\boldsymbol{\varphi}}, \overline{\phi^e} \,\}$

$$\{\, \dot{\overline{\boldsymbol{\varphi}}}, \dot{\overline{\phi^e}} \,\} = \arg \Big\{ \inf_{\dot{\overline{\boldsymbol{\varphi}}} \in \overline{\mathcal{W}}_{\overline{\boldsymbol{\varphi}}}} \sup_{\dot{\overline{\phi^e}} \in \overline{\mathcal{W}}_{\overline{\phi^e}}} \int_{\overline{\mathcal{V}}} \overline{\pi^*}(\overline{\boldsymbol{F}}, \overline{\mathbb{E}}, \dot{\overline{\boldsymbol{F}}}, \dot{\overline{\mathbb{E}}})\, dV - \overline{\Pi}_{ext}(\dot{\overline{\boldsymbol{\varphi}}}) \Big\} \tag{8.3}$$

based on the macroscopic potential density $\overline{\pi^*}$, for admissible deformations and electric potentials restricted to the Dirichlet conditions

$$\overline{\mathcal{W}}_{\dot{\overline{\boldsymbol{\varphi}}}} := \{ \dot{\overline{\boldsymbol{\varphi}}} \mid \dot{\overline{\boldsymbol{\varphi}}} = \dot{\overline{\boldsymbol{\varphi}}}_D \text{ on } \partial\overline{\mathcal{B}}_{\overline{\boldsymbol{\varphi}}} \cup \partial\overline{\mathcal{V}} \} \quad \text{and} \quad \overline{\mathcal{W}}_{\dot{\overline{\phi^e}}} := \{ \dot{\overline{\phi^e}} \mid \dot{\overline{\phi^e}} = \dot{\overline{\phi^e}}_D \text{ on } \partial\overline{\mathcal{V}} \} . \tag{8.4}$$

The external mechanical loading is given for completeness, in terms of the macroscopic mechanical body force per unit volume $\overline{\boldsymbol{\gamma}^m}$ and the prescribed tractions $\overline{\boldsymbol{T}}$

$$\overline{\Pi}_{ext}(\dot{\overline{\boldsymbol{\varphi}}}) = \int_{\overline{\mathcal{B}}} \overline{\boldsymbol{\gamma}^m} \cdot \dot{\overline{\boldsymbol{\varphi}}}\, dV + \int_{\partial\overline{\mathcal{B}}_{\overline{\boldsymbol{T}}}} \overline{\boldsymbol{T}} \cdot \dot{\overline{\boldsymbol{\varphi}}}\, dA . \tag{8.5}$$

Note that no external electric loading contributions are considered in this framework. The first variation of (8.3) then yields the necessary equilibrium condition

$$\begin{aligned} 0 = \; & -\int_{\overline{\mathcal{V}}} (\overline{\mathrm{Div}}[\partial_{\dot{\overline{\boldsymbol{F}}}} \overline{\pi^*}] + \overline{\boldsymbol{\gamma}^m}) \cdot \delta\dot{\overline{\boldsymbol{\varphi}}}\, dV + \int_{\partial\overline{\mathcal{B}}_{\overline{\boldsymbol{T}}}} ([\![\partial_{\dot{\overline{\boldsymbol{F}}}} \overline{\pi^*}]\!] \cdot \overline{\boldsymbol{N}} - \overline{\boldsymbol{T}}) \cdot \delta\dot{\overline{\boldsymbol{\varphi}}}\, dA \\ & + \int_{\overline{\mathcal{V}}} (-\overline{\mathrm{Div}}[-\partial_{\dot{\overline{\mathbb{E}}}} \overline{\pi^*}])\, \delta\dot{\overline{\phi^e}}\, dV , \end{aligned} \tag{8.6}$$

with the referential outward normal $\overline{\boldsymbol{N}}$. The related macroscopic Euler-Lagrange equations and respective Neumann boundary condition read

$$\overline{\mathrm{Div}}[\partial_{\dot{\overline{\boldsymbol{F}}}}\overline{\pi^*}] + \overline{\boldsymbol{\gamma}^m} = \boldsymbol{0} \text{ in } \overline{\mathcal{V}} \quad \text{and} \quad \overline{\mathrm{Div}}[-\partial_{\dot{\overline{\mathbb{E}}}}\overline{\pi^*}] = 0 \text{ in } \overline{\mathcal{V}} \tag{8.7}$$

with the jump $[\![\partial_{\dot{\overline{\boldsymbol{F}}}}\overline{\pi^*}]\!] \cdot \overline{\boldsymbol{N}} = \overline{\boldsymbol{T}}$ on $\partial\overline{\mathcal{B}}_{\overline{\boldsymbol{T}}}$. We identify the dual variables, namely the Piola stress $\overline{\boldsymbol{P}} := \partial_{\dot{\overline{\boldsymbol{F}}}}\overline{\pi^*}$ and the electric displacement $\overline{\mathbb{D}} := -\partial_{\dot{\overline{\mathbb{E}}}}\overline{\pi^*}$ as partial derivatives of the macroscopic potential density.

8.1.3. Macroscopic incremental variational principle

For a numerical treatment of the macroscopic boundary-value-problem, a time discretization of the introduced rate-type principle is considered in a typical time step $\tau = t_{n+1} - t_n$. From now on, all macroscopic variables without a subscript are evaluated at current time t_{n+1}. The time-discrete incremental dual to the variational principle (8.3) then reads

$$\{\overline{\boldsymbol{\varphi}}, \overline{\phi^e}\} = \arg\Big\{ \inf_{\overline{\boldsymbol{\varphi}} \in \overline{\mathcal{W}}_{\overline{\boldsymbol{\varphi}}}} \sup_{\overline{\phi^e} \in \overline{\mathcal{W}}_{\overline{\phi^e}}} \int_{\overline{\mathcal{B}}} \overline{\pi^*}^{\tau}(\overline{\boldsymbol{F}}, \overline{\mathbb{E}})\, dV - \overline{\Pi}_{ext}(\overline{\boldsymbol{\varphi}} - \overline{\boldsymbol{\varphi}}_n) \Big\} \tag{8.8}$$

in terms of the incremental macroscopic potential density $\overline{\pi^*}^{\tau}$ obtained by applying a time integration algorithm on the continuous potential $\overline{\pi^*}$, i.e.

$$\overline{\pi^*}^{\tau}(\overline{\boldsymbol{F}}, \overline{\mathbb{E}}) := ALGO\Big\{ \int_{t_n}^{t} \overline{\pi^*}(\dot{\overline{\boldsymbol{F}}}, \dot{\overline{\mathbb{E}}})\, d\tau \Big\}. \tag{8.9}$$

For the mechanical external loading, a backward-Euler time integration algorithm is used to discretize the rate $\dot{\overline{\boldsymbol{\varphi}}}^{\tau} = (\overline{\boldsymbol{\varphi}} - \overline{\boldsymbol{\varphi}}_n)/\tau$. Considering the admissible fields for the stationary point $\overline{\mathcal{W}}_{\overline{\boldsymbol{\varphi}}} := \{\overline{\boldsymbol{\varphi}} \mid \overline{\boldsymbol{\varphi}} = \overline{\boldsymbol{\varphi}}_D \text{ on } \partial\overline{\mathcal{B}}_{\overline{\boldsymbol{\varphi}}} \cup \partial\overline{\mathcal{V}}\}$ and $\overline{\mathcal{W}}_{\overline{\phi^e}} := \{\overline{\phi^e} \mid \overline{\phi^e} = \overline{\phi^e}_D \text{ on } \partial\overline{\mathcal{V}}\}$ the Euler-Lagrange equations read in their time-discrete form

$$\overline{\mathrm{Div}}[\partial_{\dot{\overline{\boldsymbol{F}}}}\overline{\pi^*}^{\tau}] + \overline{\boldsymbol{\gamma}^m} = \boldsymbol{0} \text{ in } \overline{\mathcal{V}} \quad \text{and} \quad \overline{\mathrm{Div}}[-\partial_{\dot{\overline{\mathbb{E}}}}\overline{\pi^*}^{\tau}] = 0 \text{ in } \overline{\mathcal{V}} \tag{8.10}$$

with the jump condition $[\![\partial_{\dot{\overline{\boldsymbol{F}}}}\overline{\pi^*}^{\tau}]\!] \cdot \overline{\boldsymbol{N}} = \overline{\boldsymbol{T}}$ on $\partial\overline{\mathcal{B}}_{\overline{\boldsymbol{T}}}$. The macroscopic dual fields at the discrete time t_{n+1} are obtained as the derivatives of the incremental potential $\overline{\pi^*}^{\tau}$ and read $\overline{\boldsymbol{P}} := \partial_{\dot{\overline{\boldsymbol{F}}}}\overline{\pi^*}^{\tau}$ and $\overline{\mathbb{D}} := -\partial_{\dot{\overline{\mathbb{E}}}}\overline{\pi^*}^{\tau}$ for the Piola stress and the electric displacements, respectively.

8.1.4. Microscopic variables and gradient fields

The micro-structural primary and dual fields are introduced in a Lagrangian geometric setting referring to the undeformed body $\mathcal{B} \subset \mathcal{R}^3$. Following the standard approach of micro-electro-mechanics we introduce the three microscopic primary fields

$$\boldsymbol{\varphi} : \begin{cases} \mathcal{B} \times \mathcal{T} \to \mathcal{S} = \boldsymbol{\varphi}_t(\mathcal{B}) \\ (\boldsymbol{X}, t) \mapsto \boldsymbol{x} = \boldsymbol{\varphi}(\boldsymbol{X}, t) \end{cases}, \quad \phi^e : \begin{cases} \mathcal{B} \times \mathcal{T} \to \mathcal{R} \\ (\boldsymbol{X}, t) \mapsto \phi^e(\boldsymbol{X}, t) \end{cases}, \boldsymbol{\mathcal{P}} : \begin{cases} \mathcal{B} \times \mathcal{T} \to \mathcal{R}^3 \\ (\boldsymbol{X}, t) \mapsto \boldsymbol{\mathcal{P}}(\boldsymbol{X}, t) \end{cases}, \tag{8.11}$$

see Figure 5.2. The referential electric polarization vector $\boldsymbol{\mathcal{P}}$ describes at time $t \in \mathcal{T}$ the electric state of the ferroelectric body at $\boldsymbol{X} \in \mathcal{B}$ and is obtained by a pull-back operation

of the current polarization $\mathfrak{p} = \boldsymbol{F}^{-1}\boldsymbol{\mathcal{P}}$ at $\boldsymbol{x} \in \mathcal{S}$. Here, a crucial difference to the theory of micro-magnetics occurs, as the polarization vector is not restricted by the tedious unity constraint of the magnetization. Also note, that the order parameter is assumed to only be defined within the ferroelectric body $\mathcal{B}_{\mathfrak{f}} \subset \mathcal{B} \subset \mathcal{R}^3$ such that

$$\boldsymbol{\mathcal{P}}(\boldsymbol{X}) := \begin{cases} \boldsymbol{\mathcal{P}} & \text{for } \boldsymbol{X} \in \mathcal{B}_{\mathfrak{f}} \\ \boldsymbol{0} & \text{otherwise} \end{cases} . \tag{8.12}$$

The gradient fields

$$\boldsymbol{F} = \nabla\boldsymbol{\varphi}(\boldsymbol{X}, t) , \quad \mathbb{E} = -\nabla\phi^e(\boldsymbol{X}, t) , \quad \nabla\boldsymbol{\mathcal{P}} = \nabla\boldsymbol{\mathcal{P}}(\boldsymbol{X}, t) , \tag{8.13}$$

are the deformation gradient, the electric field and the gradient of the polarization, respectively. This ansatz directly satisfies the mechanical compatibility condition $\operatorname{Curl}[\boldsymbol{F}] = \boldsymbol{0}$ of the deforming solid as well as Faraday's law of electrostatics $\operatorname{Curl}[\mathbb{E}] = \boldsymbol{0}$. Note, that the motion $\boldsymbol{\varphi}$ is constrained by the condition $\det[\boldsymbol{F}] > 0$ to rule out material penetration.

8.1.5. Microscopic rate-type variational principle

Due to the dissipative nature of the polarization in the context of ferroelectrics, the rates of the microscopic deformation, electric potential and polarization are governed by a rate-type potential at a given state $\{\, \boldsymbol{\varphi}, \phi^e, \boldsymbol{\mathcal{P}} \,\}$ as

$$\{\dot{\boldsymbol{\varphi}}, \dot{\phi}^e, \dot{\boldsymbol{\mathcal{P}}}\} = \arg\Big\{ \inf_{\dot{\boldsymbol{\varphi}} \in \mathcal{W}_{\dot{\boldsymbol{\varphi}}}} \sup_{\dot{\phi}^e \in \mathcal{W}_{\dot{\phi}^e}} \inf_{\dot{\boldsymbol{\mathcal{P}}} \in \mathcal{W}_{\dot{\boldsymbol{\mathcal{P}}}}} \int_{\mathcal{B}} \pi^*(\dot{\boldsymbol{C}}, \dot{\mathbb{E}}, \dot{\boldsymbol{\mathcal{P}}}, \nabla\dot{\boldsymbol{\mathcal{P}}})\, dV \Big\} , \tag{8.14}$$

in terms of the admissible states of the deformation and potential on the micro-structure

$$\mathcal{W}_{\dot{\boldsymbol{\varphi}}} := \{\dot{\boldsymbol{\varphi}} \,|\, [\![\dot{\boldsymbol{\varphi}}]\!] = \dot{\overline{\boldsymbol{F}}} \cdot [\![\boldsymbol{X}]\!] \text{ on } \partial\mathcal{B}\} \quad \text{and} \quad \mathcal{W}_{\dot{\phi}^e} := \{\dot{\phi}^e \,|\, [\![\dot{\phi}^e]\!] = -\dot{\overline{\mathbb{E}}} \cdot [\![\boldsymbol{X}]\!] \text{ on } \partial\mathcal{B}\} . \tag{8.15}$$

The polarization is treated as a internal variable that doesn't have a macroscopic external counterpart. The admissible space for periodic micro-structures is given as

$$\mathcal{W}_{\dot{\boldsymbol{\mathcal{P}}}} := \{\dot{\boldsymbol{\mathcal{P}}} \,|\, [\![\dot{\boldsymbol{\mathcal{P}}}]\!] = \boldsymbol{0} \text{ on } \partial\mathcal{B}\} . \tag{8.16}$$

Here, $[\![\cdot]\!] := (\cdot)^+ - (\cdot)^-$ denotes the jump of a quantity $(\cdot)$ with respect to opposite faces of the periodic micro-structure. We define at a given state the microscopic potential density (8.14) in terms of the rate of the mixed energy-enthalpy function ψ^* and the dissipation function Φ as

$$\pi^*(\dot{\boldsymbol{C}}, \dot{\mathbb{E}}, \dot{\boldsymbol{\mathcal{P}}}, \nabla\dot{\boldsymbol{\mathcal{P}}}) := \frac{d}{dt}\psi^*(\boldsymbol{C}, \mathbb{E}, \boldsymbol{\mathcal{P}}, \nabla\boldsymbol{\mathcal{P}}; \boldsymbol{\mathcal{A}}) + \Phi(\dot{\boldsymbol{\mathcal{P}}}; \boldsymbol{C}) . \tag{8.17}$$

The necessary or equilibrium condition of the variational principle (8.14) is obtained by the first variation

$$\begin{aligned} 0 := \frac{1}{|\mathcal{B}|}\Big\{ \int_{\mathcal{B}} & -\operatorname{Div}[\partial_{\boldsymbol{F}}\psi^*] \cdot \delta\dot{\boldsymbol{\varphi}} - \operatorname{Div}[\partial_{\mathbb{E}}\psi^*]\delta\dot{\phi}^e + (\partial_{\boldsymbol{\mathcal{P}}}\psi^* + \partial_{\boldsymbol{\mathcal{P}}}\Phi - \operatorname{Div}[\partial_{\nabla\boldsymbol{\mathcal{P}}}\psi^*]) \cdot \delta\dot{\boldsymbol{\mathcal{P}}}\, dV \\ & + \int_{\partial\mathcal{B}} (\partial_{\boldsymbol{F}}\psi^* \cdot \boldsymbol{N}) \cdot \delta\dot{\boldsymbol{\varphi}} + (\partial_{\mathbb{E}}\psi^* \cdot \boldsymbol{N})\delta\dot{\phi}^e + (\partial_{\nabla\boldsymbol{\mathcal{P}}}\psi^* \cdot \boldsymbol{N}) \cdot \delta\dot{\boldsymbol{\mathcal{P}}}\, dA \Big\} . \end{aligned} \tag{8.18}$$

Hence the Euler-Lagrange equations for the variational principle (8.14) read

$$\boxed{\begin{array}{lll} 1. \quad \textit{Balance of linear momentum} & \mathrm{Div}[\partial_{\boldsymbol{F}}\psi^*] = \boldsymbol{0} & \text{in} \quad \mathcal{B}\,, \\ 2. \quad \textit{Gauss's law} & \mathrm{Div}[-\partial_{\mathbb{E}}\psi^*] = 0 & \text{in} \quad \mathcal{B}\,, \\ 3. \quad \textit{Polarization evolution} & \mathrm{Div}[\partial_{\nabla\boldsymbol{\mathcal{P}}}\psi^*] - \partial_{\boldsymbol{\mathcal{P}}}\psi^* - \partial_{\boldsymbol{\mathcal{P}}}\Phi = \boldsymbol{0} & \text{in} \quad \mathcal{B}\,, \end{array}} \tag{8.19}$$

and are a specification of the general balance equations introduced in (5.23).

8.1.6. Microscopic incremental variational principle

For the numerical setting, we consider an incremental variational principle which governs the micro-electro-mechanical problem at discrete time t_{n+1} for finite time increments $\tau = t_{n+1} - t_n$. This definition is conceptually in line with formulations for non-linear mechanical problems in Miehe [158], as well as Sridhar et al. [235] for micro-magnetics. The incremental potential density $\pi^{*\tau}$ is related to the rate-type potential density π^* by the algorithm

$$\pi^{*\tau}(\boldsymbol{C}, \mathbb{E}, \boldsymbol{\mathcal{P}}, \nabla\boldsymbol{\mathcal{P}}) := ALGO\Big\{ \int_{t_n}^{t} \pi^*(\dot{\boldsymbol{C}}, \dot{\mathbb{E}}, \dot{\boldsymbol{\mathcal{P}}}, \nabla\dot{\boldsymbol{\mathcal{P}}})\, d\tau \Big\}\,. \tag{8.20}$$

Application of an implicit backward-Euler time-integration scheme yields the discrete counterpart to (8.17) that reads

$$\pi^{*\tau}(\boldsymbol{C}, \mathbb{E}, \boldsymbol{\mathcal{P}}, \nabla\boldsymbol{\mathcal{P}}) := \psi^*(\boldsymbol{C}, \mathbb{E}, \boldsymbol{\mathcal{P}}, \nabla\boldsymbol{\mathcal{P}}; \boldsymbol{\mathcal{A}}) - \psi^*_n + \tau\Phi([\boldsymbol{\mathcal{P}} - \boldsymbol{\mathcal{P}}_n/\tau])\,. \tag{8.21}$$

and gives, related to (8.19), the time-discrete Euler-Lagrange equations in algorithmic form

$$\boxed{\begin{array}{lll} 1. \quad \textit{Balance of linear momentum} & \mathrm{Div}[\partial_{\boldsymbol{F}}\psi^*] = \boldsymbol{0} & \text{in} \quad \mathcal{B}\,, \\ 2. \quad \textit{Gauss's law} & \mathrm{Div}[-\partial_{\mathbb{E}}\psi^*] = 0 & \text{in} \quad \mathcal{B}\,, \\ 3. \quad \textit{Polarization evolution} & \mathrm{Div}[\partial_{\nabla\boldsymbol{\mathcal{P}}}\psi^*] - \partial_{\boldsymbol{\mathcal{P}}}\psi^* - \tau\partial_{\boldsymbol{\mathcal{P}}}\Phi = \boldsymbol{0} & \text{in} \quad \mathcal{B}\,. \end{array}} \tag{8.22}$$

Note that all quantities without a subscript are evaluated at time t_{n+1}.

8.1.7. Microscopic variational principle of homogenization

The macroscopic incremental potential density $\overline{\pi^*}^{\tau}$ is assumed to be defined by the incremental variational principle of homogenization

$$\overline{\pi^*}^{\tau}(\overline{\boldsymbol{F}}, \overline{\mathbb{E}}) = \inf_{\boldsymbol{\varphi}\in\mathcal{W}_{\boldsymbol{\varphi}}} \sup_{\phi^e\in\mathcal{W}_{\phi^e}} \inf_{\boldsymbol{\mathcal{P}}\in\mathcal{W}_{\boldsymbol{\mathcal{P}}}} \frac{1}{|\mathcal{B}|} \int_{\mathcal{B}} \pi^{*\tau}(\boldsymbol{C}, \mathbb{E}, \boldsymbol{\mathcal{P}}, \nabla\boldsymbol{\mathcal{P}})\, dV\,, \tag{8.23}$$

optimizing the volume average of the microscopic algorithmic potential density (8.20). The respective admissible spaces are given by

$$\begin{aligned} \mathcal{W}_{\boldsymbol{\varphi}} &:= \{\boldsymbol{\varphi} \,|\, [\![\boldsymbol{\varphi}]\!] = \overline{\boldsymbol{F}} \cdot [\![\boldsymbol{X}]\!] \text{ on } \partial\mathcal{B}\}\,, \\ \mathcal{W}_{\phi^e} &:= \{\phi^e \,|\, [\![\phi^e]\!] = -\overline{\mathbb{E}} \cdot [\![\boldsymbol{X}]\!] \text{ on } \partial\mathcal{B}\}\,, \\ \mathcal{W}_{\mathcal{P}} &:= \{\boldsymbol{\mathcal{P}} \,|\, [\![\boldsymbol{\mathcal{P}}]\!] = \boldsymbol{0} \text{ on } \partial\mathcal{B}\}\,, \end{aligned} \tag{8.24}$$

related to (8.15) and (8.16).
Appropriate boundary conditions imposed on the micro-structure are obtained by a generalized Hill-Mandel macro-homogeneity condition, Hill [91], such as proposed in Schröder & Keip [216], Zäh & Miehe [272], Keip et al. [115] and Sridhar et al. [235] for coupled electro- and magneto-mechanical multiscale problems. Section 3.2 deals with the micro-to-macro transition of magneto-electro-mechanical two-scale problems. In the following, we restrict ourselves to periodic boundary conditions.

8.2. Finite element implementation of homogenization

While the variational framework of an FE^2 method was presented and can be applied for solving two-scale boundary value problems, the author chose a macroscopic driving routine that reduces the approach such that the heterogeneous micro-structure is solved by a full finite element scheme, while the (usually homogeneous) macro-structure is idealized by a one Gauss-point problem as introduced in Section 5.3. The discretization and update algorithm of the micro-structure are described in the following.

8.2.1. Generalized arrays and microscopic equilibrium

The primary variables of the micro-structure

$$\boldsymbol{\varphi} = \overline{\boldsymbol{F}} \cdot \boldsymbol{X} + \widetilde{\boldsymbol{\varphi}} \quad \text{and} \quad -\phi^e = \overline{\mathbb{E}} \cdot \boldsymbol{X} - \widetilde{\phi}^e, \tag{8.25}$$

are decomposed into macroscopic linear parts associated with the macroscopic Dirichlet-type driving, and superimposed microscopic fluctuations. Note that the order parameter $\boldsymbol{\mathcal{P}}$ is not decomposed, as no direct macroscopic driving is considered. For a compact notation of the following finite element implementation, generalized arrays are introduced

$$\overline{\mathsf{F}^*} := [\,\overline{\boldsymbol{F}}, \overline{\mathbb{E}}, \boldsymbol{0}, \boldsymbol{0}\,]^T \quad \text{and} \quad \mathsf{F}^* := [\,\boldsymbol{F}, \mathbb{E}, \boldsymbol{\mathcal{P}}, \nabla\boldsymbol{\mathcal{P}}\,]^T\,, \tag{8.26}$$

for the macro- and microscopic primary fields, respectively. The fluctuation fields and polarization vector as the microscopic degrees of freedom are discretized by a finite element method such that

$$\widetilde{\mathsf{F}^*} := [\,\nabla\widetilde{\boldsymbol{\varphi}}, -\nabla\widetilde{\phi}^e, \boldsymbol{\mathcal{P}}, \nabla\boldsymbol{\mathcal{P}}\,]^T = \underline{\mathbf{B}}(\boldsymbol{X})\underline{\mathbf{d}}(t) \tag{8.27}$$

in terms of the interpolation matrix $\underline{\mathbf{B}}$ and a global vector of discrete fluctuations

$$\underline{\mathbf{d}} = \mathop{\mathsf{A}}_{I=1}^{N^h} [\,\widetilde{\boldsymbol{\varphi}}, \widetilde{\phi}^e, \boldsymbol{\mathcal{P}}\,]_I^T \in \mathcal{R}^{(d+1)N^h} \tag{8.28}$$

at the nodes of the discretized geometry. With this ansatz at hand, the finite-step-size discrete stationary principle reads

$$\overline{\pi^*}^{\tau}(\overline{\mathbf{F}^*};\underline{\mathbf{d}}) = \frac{1}{|\mathcal{B}|}\int_{\mathcal{B}} \pi^{*\tau}(\overline{\mathbf{F}^*} + \underline{\mathbf{B}}\,\underline{\mathbf{d}})\,dV\ . \tag{8.29}$$

The first and second derivatives of this functional provide all necessary information for the finite element solution of the equilibrium state of the micro-structure and the overall homogenized quantities. In particular, the first and second derivatives by the fluctuation field $\underline{\mathbf{d}}$ give the finite element arrays

$$\begin{aligned}
\underline{\mathbf{R}}^* &:= \overline{\pi^*}^{\tau}_{,\underline{\mathbf{d}}} = \frac{1}{|\mathcal{B}|}\int_{\mathcal{B}} \underline{\mathbf{B}}^T \partial_{\mathbf{F}^*}\pi^{*\tau}\,dV = \frac{1}{|\mathcal{B}|}\int_{\mathcal{B}} \left\{\underline{\mathbf{B}}^T[\partial_{\mathbf{F}^*}\psi^*] + \tau\underline{\mathbf{G}}^T[\partial_{\mathcal{P}}\Phi]\right\} dV,\\
\underline{\mathbf{K}}^* &:= \overline{\pi^*}^{\tau}_{,\underline{\mathbf{d}}\,\underline{\mathbf{d}}} = \frac{1}{|\mathcal{B}|}\int_{\mathcal{B}} \underline{\mathbf{B}}^T \partial^2_{\mathbf{F}^*\mathbf{F}^*}\pi^{*\tau}\underline{\mathbf{B}}\,dV = \frac{1}{|\mathcal{B}|}\int_{\mathcal{B}} \left\{\underline{\mathbf{B}}^T[\partial^2_{\mathbf{F}^*\mathbf{F}^*}\psi^*]\underline{\mathbf{B}} + \tau\underline{\mathbf{G}}^T[\partial^2_{\mathcal{P}\mathcal{P}}\Phi]\underline{\mathbf{G}}\right\} dV,
\end{aligned} \tag{8.30}$$

providing the basis for the computation of the equilibrium state of the micro-structure. Here, $\mathcal{P} = \underline{\mathbf{G}}(\boldsymbol{X})\underline{\mathbf{d}}$ is inserted as an extraction of (8.27). A typical Newton-Raphson update

$$\underline{\mathbf{d}} \Leftarrow \underline{\mathbf{d}} - \underline{\mathbf{K}}^{*-1}\underline{\mathbf{R}}^* \quad \text{until} \quad \|\underline{\mathbf{R}}^*\| < tol_{micro} \tag{8.31}$$

for the nodal fluctuations based on the finite element tangent matrix $\underline{\mathbf{K}}^*$, provides an equilibrium state for a vanishing finite element residual $\underline{\mathbf{R}}^* = \boldsymbol{0}$.

8.2.2. Homogenized macroscopic stress and moduli

With the solution of the micro-structure at hand, the overall macroscopic stresses and moduli are computed at current time t_{n+1}. The averaging routine is based on the works Miehe [158] for pure mechanics and follows the approach of Zäh [274] and Miehe et al. [174] for coupled problems. The homogenized generalized stress array reads

$$\overline{\mathbf{S}^*} = [\,\overline{\boldsymbol{P}}, -\overline{\mathbb{D}}\,]^T := \partial_{\overline{\mathbf{F}^*}}\overline{\pi^*}^{\tau} = \overline{\pi^*}^{\tau}_{,\overline{\mathbf{F}^*}} + [\,\overline{\pi^*}^{\tau}_{,\underline{\mathbf{d}}}]\,[\underline{\mathbf{d}}_{,\overline{\mathbf{F}^*}}] = \frac{1}{|\mathcal{B}|}\int_{\mathcal{B}} \partial_{\mathbf{F}^*}\pi^{*\tau}\,dV, \tag{8.32}$$

where the necessary condition $\overline{\pi^*}^{\tau}_{,\underline{\mathbf{d}}} = \boldsymbol{0}$ is considered. The second derivative yields the moduli of the macro-structure

$$\overline{\mathbf{C}^*} := \overline{\pi^*}^{\tau}_{,\overline{\mathbf{F}^*}\,\overline{\mathbf{F}^*}} + [\,\overline{\pi^*}^{\tau}_{,\overline{\mathbf{F}^*}\,\underline{\mathbf{d}}}]\,[\underline{\mathbf{d}}_{,\overline{\mathbf{F}^*}}] = \overline{\pi^*}^{\tau}_{,\overline{\mathbf{F}^*}\,\overline{\mathbf{F}^*}} - [\,\overline{\pi^*}^{\tau}_{,\overline{\mathbf{F}^*}\,\underline{\mathbf{d}}}]\,[\,\overline{\pi^*}^{\tau}_{,\underline{\mathbf{d}}\underline{\mathbf{d}}}]^{-1}\,[\,\overline{\pi^*}^{\tau}_{,\underline{\mathbf{d}}\overline{\mathbf{F}^*}}] = \mathbf{C}^* - \underline{\mathbf{L}}^{*T}\underline{\mathbf{K}}^{*-1}\underline{\mathbf{L}}^* \tag{8.33}$$

with the average of the micro-moduli $\mathbf{C}^* = \overline{\pi^*}^{\tau}_{,\overline{\mathbf{F}^*}\,\overline{\mathbf{F}^*}}$ and a softening part accounting for the flexibility of the micro-structure, based on the additional finite element arrays $\underline{\mathbf{L}}^* = \overline{\pi^*}^{\tau}_{,\underline{\mathbf{d}}\overline{\mathbf{F}^*}}$ and $\underline{\mathbf{L}}^{*T} = \overline{\pi^*}^{\tau}_{,\overline{\mathbf{F}^*}\,\underline{\mathbf{d}}}$. Note that the derivative of the fluctuations with respect to the macroscopic primary fields is obtained by the linearization of the microscopic equilibrium condition such that

$$[\,\overline{\pi^*}^{\tau}_{,\underline{\mathbf{d}}\overline{\mathbf{F}^*}}] + [\,\overline{\pi^*}^{\tau}_{,\underline{\mathbf{d}}\underline{\mathbf{d}}}]\underline{\mathbf{d}}_{,\overline{\mathbf{F}^*}} = \boldsymbol{0} \quad \longrightarrow \quad \underline{\mathbf{d}}_{,\overline{\mathbf{F}^*}} = -[\,\overline{\pi^*}^{\tau}_{,\underline{\mathbf{d}}\underline{\mathbf{d}}}]^{-1}\,[\,\overline{\pi^*}^{\tau}_{,\underline{\mathbf{d}}\overline{\mathbf{F}^*}}]\,. \tag{8.34}$$

The necessary arrays for the homogenized macroscopic quantities in a finite element context read

$$\begin{aligned}
\overline{\mathsf{S}^*} &:= \overline{\pi^{*\tau}}_{,\overline{\mathsf{F}^*}} &&= \frac{1}{|\mathcal{B}|} \mathop{\mathsf{A}}_{\#=1}^{E} \int_{\mathcal{B}_\#} \partial_{\mathsf{F}} \pi^{*\tau}\, dV, \\
\mathsf{C}^* &:= \overline{\pi^{*\tau}}_{,\overline{\mathsf{F}^*}\,\overline{\mathsf{F}^*}} &&= \frac{1}{|\mathcal{B}|} \mathop{\mathsf{A}}_{\#=1}^{E} \int_{\mathcal{B}_\#} \partial^2_{\mathsf{F}^*\mathsf{F}^*} \pi^{*\tau}\, dV, \\
\underline{\mathsf{L}}^* &:= \overline{\pi^{*\tau}}_{,\underline{\mathbf{d}}\overline{\mathsf{F}^*}} &&= \frac{1}{|\mathcal{B}|} \mathop{\mathsf{A}}_{\#=1}^{E} \int_{\mathcal{B}_\#} \underline{\mathbf{B}}^T \partial^2_{\mathsf{F}^*\mathsf{F}^*} \pi^{*\tau}\, dV.
\end{aligned} \tag{8.35}$$

These arrays are of importance for the equilibrium condition of the macroscopic driving routine as described in Section 5.3.

8.3. Energy storage and dissipation potential

To describe the energy storage in terms of the objective state variables, a mixed energy-enthalpy density function ψ^* and the dissipation function Φ for the evolution and motion of the electric domain walls are introduced. For the energy storage one needs to describe two contributions to the energy density: a contribution $\psi^*_{\mathfrak{v}}(\boldsymbol{C}, \mathbb{E})$ due to the presence of an electric field in the full surrounding material $\mathcal{B}$, and an additional elastic contribution $\psi^*_{\mathfrak{e}}(\boldsymbol{C})$ in the domain $\mathcal{B} \setminus \mathcal{B}_{\mathfrak{f}}$ or $\psi^*_{\mathfrak{f}}(\boldsymbol{C}, \boldsymbol{\mathcal{P}}, \nabla\boldsymbol{\mathcal{P}})$ in the ferroelectric domain $\mathcal{B}_{\mathfrak{f}}$. Here $\psi_{\mathfrak{f}}$ additionally accounts for the electric behavior of the ferroelectric material. Hence, the free-energy density can be written as,

$$\psi^*(\boldsymbol{C}, \mathbb{E}, \boldsymbol{\mathcal{P}}, \nabla\boldsymbol{\mathcal{P}}; \boldsymbol{\mathcal{A}}) := \begin{cases} \psi^*_{\mathfrak{f}}(\boldsymbol{C}, \boldsymbol{\mathcal{P}}, \nabla\boldsymbol{\mathcal{P}}; \boldsymbol{\mathcal{A}}) + \psi^*_{\mathfrak{v}}(\boldsymbol{C}, \mathbb{E}) & \text{for} \quad \boldsymbol{X} \in \mathcal{B}_{\mathfrak{f}} \\ \psi^*_{\mathfrak{e}}(\boldsymbol{C}) + \psi^*_{\mathfrak{v}}(\boldsymbol{C}, \mathbb{E}) & \text{for} \quad \boldsymbol{X} \in \mathcal{B} \setminus \mathcal{B}_{\mathfrak{f}} \end{cases} \tag{8.36}$$

in terms of the objective right Cauchy-Green tensor $\boldsymbol{C} = \boldsymbol{F}^T\boldsymbol{F}$ and the anisotropy axes $\boldsymbol{\mathcal{A}}$.

The energy contribution of the ferroelectric body $\psi^*_{\mathfrak{f}}$ depends on the deformation $\boldsymbol{C}$, the polarization $\boldsymbol{\mathcal{P}}$ and the gradient of the polarization $\nabla\boldsymbol{\mathcal{P}}$. It is assumed to consist of three contributions,

$$\psi^*_{\mathfrak{f}}(\boldsymbol{C}, \boldsymbol{\mathcal{P}}, \nabla\boldsymbol{\mathcal{P}}; \boldsymbol{\mathcal{A}}) = \psi^*_e(\boldsymbol{C}) + \psi^*_{an}(\boldsymbol{C}, \boldsymbol{\mathcal{P}}, \boldsymbol{A}_1, \boldsymbol{A}_2) + \psi^*_{ex}(\nabla\boldsymbol{\mathcal{P}}) \tag{8.37}$$

where ψ^*_e is the elastic energy, ψ^*_{an} is the Landau energy, and ψ^*_{ex} is the gradient energy. $\boldsymbol{A}_1$ and $\boldsymbol{A}_2$ are the referential anisotropy axes of the crystalline ferroelectric material in a two dimensional setting. The elastic energy density defines the energy storage due to the mechanical deformation in the representative volume element. This is given as

$$\psi^*_e(\boldsymbol{C}) = \frac{\mu}{2}(\mathrm{tr}[\boldsymbol{C}] - 3) + \frac{\mu}{\beta}(J^{-\beta} - 1)\,, \tag{8.38}$$

where μ is the shear modulus and $\beta = \frac{\lambda}{\nu} = \frac{2\nu}{1-2\nu}$ formulated in terms of Poisson's ratio ν.

In a ferroelectric material with an inherent crystalline structure, the polarization energy depends on the direction of polarization relative to the structural axes of the material.

In two dimensions it is modeled by the even anisotropy energy density

$$\begin{aligned}\psi^*_{an}(\boldsymbol{C},\boldsymbol{\mathcal{P}};\boldsymbol{A}_1,\boldsymbol{A}_2) &= \frac{K_1}{2}[(\boldsymbol{C}:(\boldsymbol{\mathcal{P}}\otimes\boldsymbol{A}_1))^2+(\boldsymbol{C}:(\boldsymbol{\mathcal{P}}\otimes\boldsymbol{A}_2))^2]\\ &+\frac{K_2}{4}[(\boldsymbol{C}:(\boldsymbol{\mathcal{P}}\otimes\boldsymbol{A}_1))^4+(\boldsymbol{C}:(\boldsymbol{\mathcal{P}}\otimes\boldsymbol{A}_2))^4]+\frac{K_3}{6}[(\boldsymbol{C}:(\boldsymbol{\mathcal{P}}\otimes\boldsymbol{A}_1))^6+(\boldsymbol{C}:(\boldsymbol{\mathcal{P}}\otimes\boldsymbol{A}_2))^6]\\ &+\frac{K_4}{2}[(\boldsymbol{C}:(\boldsymbol{\mathcal{P}}\otimes\boldsymbol{A}_1)^2)(\boldsymbol{C}:(\boldsymbol{\mathcal{P}}\otimes\boldsymbol{A}_2))^2]+\frac{K_5}{4}[(\boldsymbol{C}:(\boldsymbol{\mathcal{P}}\otimes\boldsymbol{A}_1))^4(\boldsymbol{C}:(\boldsymbol{\mathcal{P}}\otimes\boldsymbol{A}_2))^4]\,,\end{aligned} \tag{8.39}$$

with the anisotropy coefficients $[K_i]_{i=1,5}$, see also Zäh & Miehe [272] for the small strain representation. Note that a Lagrangian representation is chosen related to a pull-back operation on the polarization.

The separation energy ψ^*_{ex} models the tendency of neighboring polarization states to align. Restricted to an isotropic response we formulate the simple form of the energy as

$$\psi^*_{ex}(\nabla\boldsymbol{\mathcal{P}}) = \frac{L}{2}[\nabla\boldsymbol{\mathcal{P}}:\nabla\boldsymbol{\mathcal{P}}]\,, \tag{8.40}$$

with the exchange coefficient $L>0$ acting as a penalty parameter.

The vacuum energy-enthalpy $\psi^*_{\mathfrak{v}}(\boldsymbol{C},\mathbb{E},\boldsymbol{\mathcal{P}})$ defines the energy storage due to the presence of an electric field in the free space and reads, after a Legendre transformation from the energy density $\psi_{\mathfrak{v}}(\boldsymbol{C},\mathbb{D},\boldsymbol{\mathcal{P}})$,

$$\psi^*_{\mathfrak{v}}(\boldsymbol{C},\mathbb{E},\boldsymbol{\mathcal{P}},) = -\frac{\epsilon_0 J}{2}\boldsymbol{C}^{-1}:(\widetilde{\mathbb{E}}\otimes\widetilde{\mathbb{E}})-\epsilon_0\boldsymbol{\mathcal{P}}\cdot\mathbb{E}\,, \tag{8.41}$$

with the Jacobian $J=\det[\boldsymbol{F}]$ and the permittivity of free space ϵ_0. At this point it is important to note, that only the electric self-field $\widetilde{\mathbb{E}}$ is assumed to contribute to the electrical stresses. The macroscopic electric field and macroscopic electric self-field are considered to be homogeneous across the full space of the macro-scale and thus do not enter in the microscopic electric stresses. Likewise, the coupled contribution of the macroscopic field with the microscopic self-field vanishes as the average of the microscopic self-field needs to be zero. For further explanation of the individual free energies we refer to the works Zäh & Miehe [272] for small strain micro-electro-mechanics, Keip & Sridhar [114] for micro-magneto-mechanics and Keip & Rambausek [111, 112] for more elaborated assumption on the macroscopic field contribution.

To complete the variational framework we define the dissipation potential functional

$$\Phi(\dot{\boldsymbol{\mathcal{P}}};\boldsymbol{C}) = \frac{\eta}{2}\boldsymbol{C}:(\dot{\boldsymbol{\mathcal{P}}}\otimes\dot{\boldsymbol{\mathcal{P}}})\,. \tag{8.42}$$

where the scalar parameter η is an inverse mobility coefficient, which governs the kinetics of the domain-wall evolution.

8.4. Representative numerical examples

Numerical examples demonstrate the presented theory of computational homogenization. We focus on capturing physical characteristic behavior of electro-active polymers with

embedded ferroelectric inclusion of different shapes and provide insight on the influence of the micro-structure on the overall response. Furthermore, the characteristic dielectric and butterfly hysteresis curves of the homogenized material is of interest. The chosen representative volume elements are of rather academic nature, however reflect the desired interactions.

Due to the large differences in the magnitudes of material parameters we use normalized quantities to achieve better numerical stability. The normalization is based on four physical parameters, namely the shear modulus of the matrix material μ_m [N/m^2], the spontaneous polarization p_s [C/m^2], the electric exchange coefficient L [Nm^4/C^2] and the inverse mobility parameter η [Nm^{2}s/C^2], see also Zhang & Bhattacharya [277, 278] and Zäh & Miehe [273]. The normalized primary fields $(\cdot)'$ in terms of their counterparts $(\cdot)$ are related via

$$\boldsymbol{\varphi}' = \boldsymbol{\varphi}\sqrt{\mu_m/L}/p_s\,, \quad \boldsymbol{\mathcal{P}}' = \boldsymbol{\mathcal{P}}/p_s\,, \quad -\phi^{e\prime} = -\phi^e/\sqrt{\mu_m L}\,, \quad t' = t\mu_m/(\eta p_s^2)\,. \tag{8.43}$$

A polyurethane matrix material and barium titanate piezoceramic inclusions are employed. All the material parameters in their normalized form are provided in Table 8.1.

Table 8.1: Material parameters for polyurethane matrix and $BaTiO_3$ ceramic inclusion.

no.	par.	name	polyurethane	$BaTiO_3$
1.	ν	Poisson's ratio	0.45	0.3
2.	μ'	shear modulus	37.0	3700.0
3.	K_1'	anisotropy coefficient	0.0	−0.007
4.	K_2'	anisotropy coefficient	0.0	−0.009
5.	K_3'	anisotropy coefficient	0.0	0.018
6.	K_4'	anisotropy coefficient	0.0	0.0261
7.	K_5'	anisotropy coefficient	0.0	5.0
8.	ϵ_0	free space permittivity	0.131	0.131

8.4.1. Problem 1: polycrystalline micro-structure

As first boundary value problem a single-phase micro-structure consisting of an idealized polycrystal with nine grains is investigated, inspired by Zäh & Miehe [272]. The easy axes of each grain are rotated such that the polarization gap between neighboring grains is maximized. All material parameters in each grain are equal. A schematic drawing of the $\mathcal{RVE}$ is depicted in Figure 8.1a.

To obtain an appropriate starting point for the subsequent simulation, a random polarization distribution is initialized in each grain. With no applied electric field, i.e. $\overline{\mathbb{E}}_1 = \overline{\mathbb{E}}_2 = 0$, and an assumed macroscopic mechanically stress free state $\overline{\boldsymbol{P}} = \boldsymbol{0}$, an equilibrium state is found as shown in Figure 8.1b. White arrows indicate the average polarization direction of each grain. Note that the macroscopic boundary conditions already imposes a strong condition onto the micro-structure. It is interesting to see that the polarization directions in each grain don't necessarily completely coincide with the

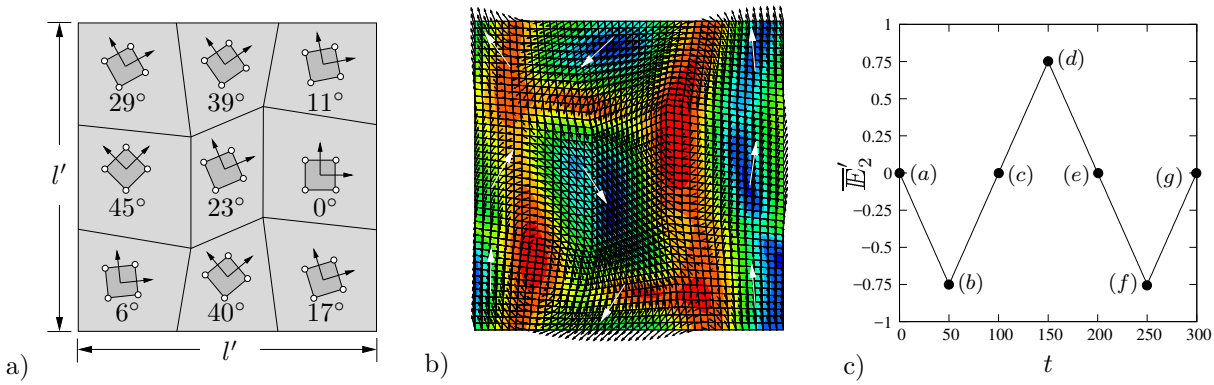

Figure 8.1: *Polycrystal micro-structure.* a) The polycrystalline micro-structure of dimension $l' \times l'$ consists of nine grains with different electric anisotropy directions. Starting from a random polarization distribution, an equilibrium state is formed in b). White arrows indicate the averaged direction of the order parameter in each grain. The contour plot of $||\nabla \mathcal{P}||$ displays the steep gradients of the polarization evolving at electric domain walls. This initial state serves as a starting point for further computations. c) Saw-tooth type macroscopic electric loading of the micro-structure. Points of interest in the loading curve are highlighted by (a)-(g).

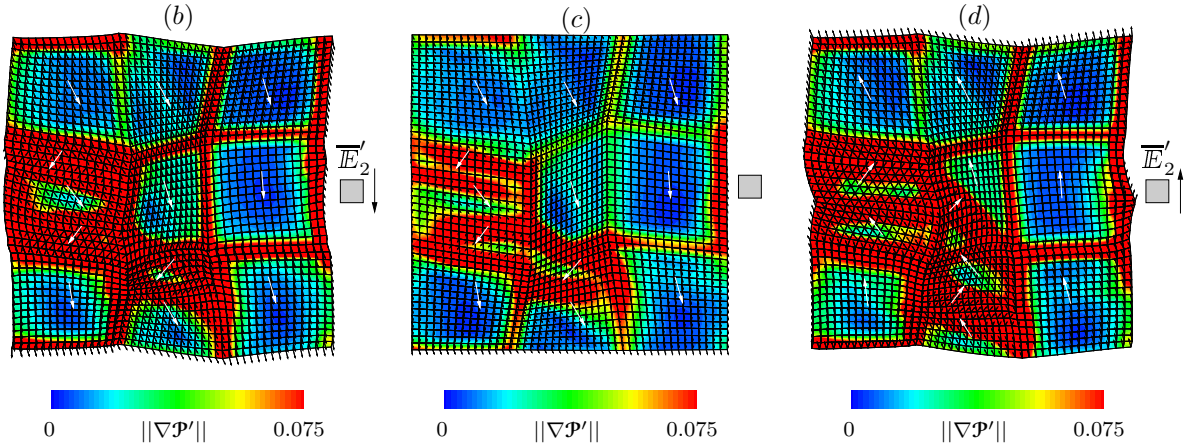

Figure 8.2: *Deformation and polarization states of the micro-structure.* Related to the sawtooth-type electric loading in Figure 8.3b, the particular polarization and deformation states (b)-(d) are displayed. The polarization within the grains try to align in field direction, however are restricted by their easy axes. Reversing the loading yields a remanent polarization for no applied field (c). The contour plot indicates the evolving domain walls within the micro-structure.

preferred direction. The contour plot shows the respective gradients of the polarization, visualizing the evolved domain walls.

Starting from the obtained equilibrium state, a macroscopic electric sawtooth-type loading to a maximum of $\overline{\mathbb{E}}_2^{\prime max} = 0.75$ is applied to the specimen, see Figure 8.1c. Such type of loading causes microscopic domain wall motions in the polycrystalline micro-structure. For different loading stages of applied electric field, the related polarization is displayed in Figure 8.2. It is observable that the polarizations within the grains tries to align in applied field direction, leading to 90° and 180° switching of the electric domains. The anisotropy direction within each grain however delay the full alignment in field direction, which would only be possible for higher field levels. For a maximum applied field $\overline{\mathbb{E}}_2^{\prime max}$, at loading point (b), Figure 8.2(b) displays the deformed state of the polycrystal

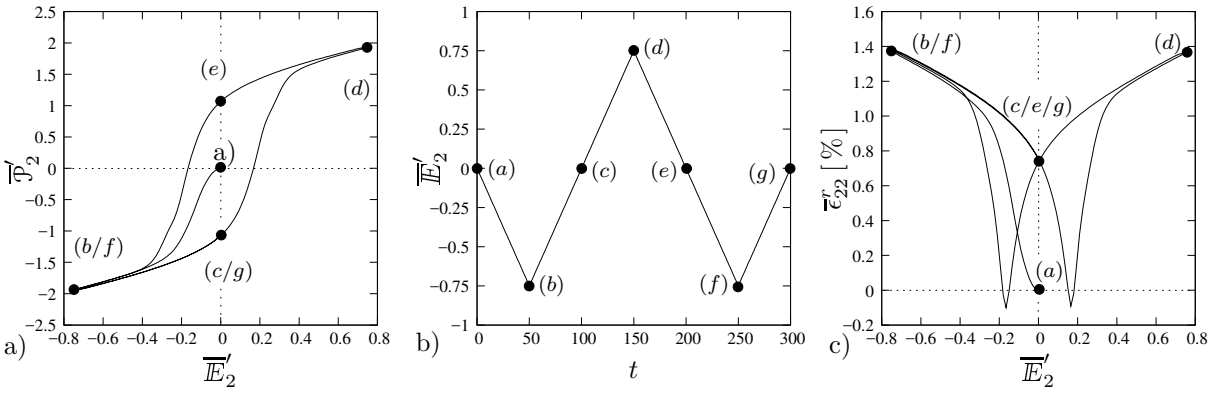

Figure 8.3: *Dielectric and butterfly hysteresis of polycrystalline micro-structure.* a) The homogenized polarization is plotted over the applied electric field up to $\overline{\mathbb{E}}_2^{\prime max} = 0.75$. Different states of the related sawtooth-loading, as displayed in b), are highlighted. c) The typical butterfly hysteresis shows the remanent strain $\overline{\epsilon}_{22}^{r}$ plotted over the applied field.

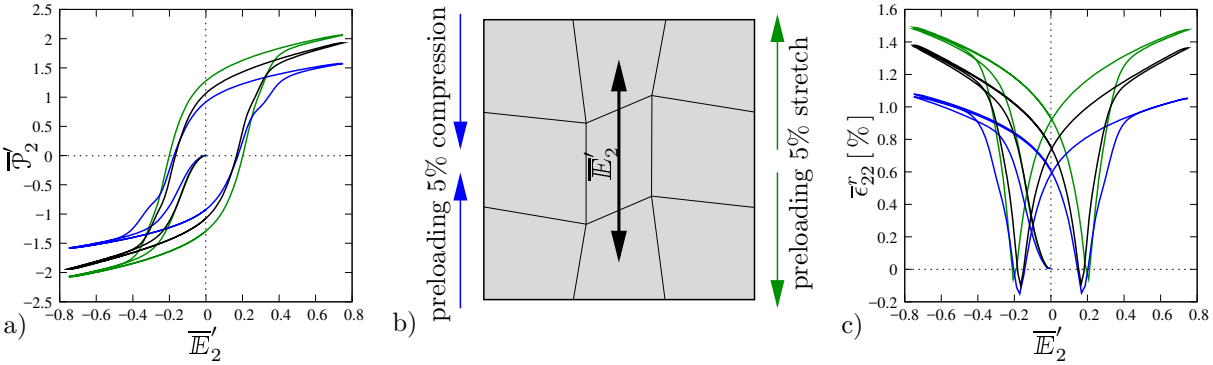

Figure 8.4: *Influence of mechanical pre-loading on hystereses.* Prior to electrical loading, a mechanical pre-compression or pre-stretch of up to 5% is applied onto the specimen. The effect of subsequent electrical loading is in focus. a/c) Pre-stretch/pre-compression leads to increased/decreased dielectric and butterfly hysteresis.

with the contour plot highlighting the domain walls indicated by high gradients of the polarization. Unloading $\overline{\mathbb{E}}_2^{\prime} \to 0$ results in changes of the magnitude of polarization, while not influencing its direction, see Figure 8.2(c). Reversing the loading direction, the polarization switches, which ultimately leads to the inverse state, Figure 8.2(d).
The homogenized material response, i.e. the typical dielectric and butterfly hysteresis curves are now in focus. Figure 8.3 displays, for the respective loading states (a)-(g), the dissipative character and time dependency of the poling process on the micro scale. In Figure 8.3a the homogenized polarization is plotted over the applied electrical field. Here, starting from a zero net polarization equilibrium state, the steep ascend to a nearly saturated state in $(b)/(f)$ and (d) is followed by a linear electric behavior for increasing loads $\overline{\mathbb{E}}_2^{\prime} > \overline{\mathbb{E}}_2^{\prime max}$. In Figure 8.3c the butterfly hysteresis of the averaged remanent strain is shown. It is evident that after unloading, for a state $\overline{\mathbb{E}}_2^{\prime} = 0$ remanent strains of 0.8% are still present.

In a second step, the influence of mechanical pre-stress on the dielectric and butterfly hystereses curves is investigated. A macroscopic pre-loading of up to 5% compression (blue) or tension (green) is followed by a sawtooth-type loading. In Figure 8.4a,c the homogenized response is compared with the solely electric loading case (black). A pre-extension induces a poling in tension direction, which coincides with the subsequent

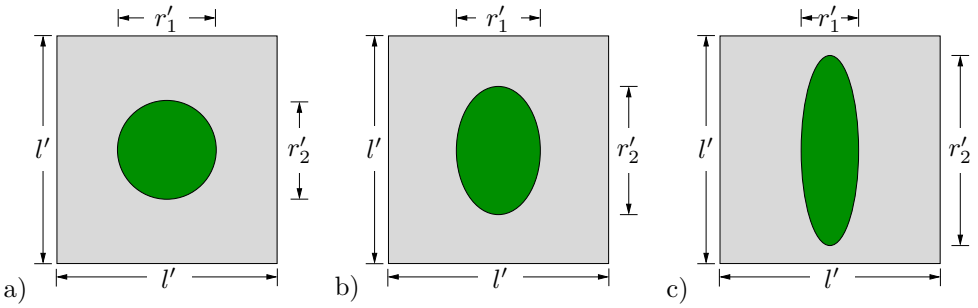

Figure 8.5: *Two-phase boundary value problem with different aspect ratios of the filler particle of 12.5% volume fraction.* The micro-structure consists of a matrix material (gray) of normalized dimension $l' \times l'$ with $l' = 1$ and a piezoceramic filler particle (green) of different aspect ratio. a) Circular particle of normalized dimension $r_1' = r_2' = 0.2$, b) elliptic particle with $r_1' = 0.16$, $r_2' = 0.25$ and c) 'needle'-shaped elliptic particle of dimension $r_1' = 0.1$, $r_2' = 0.4$.

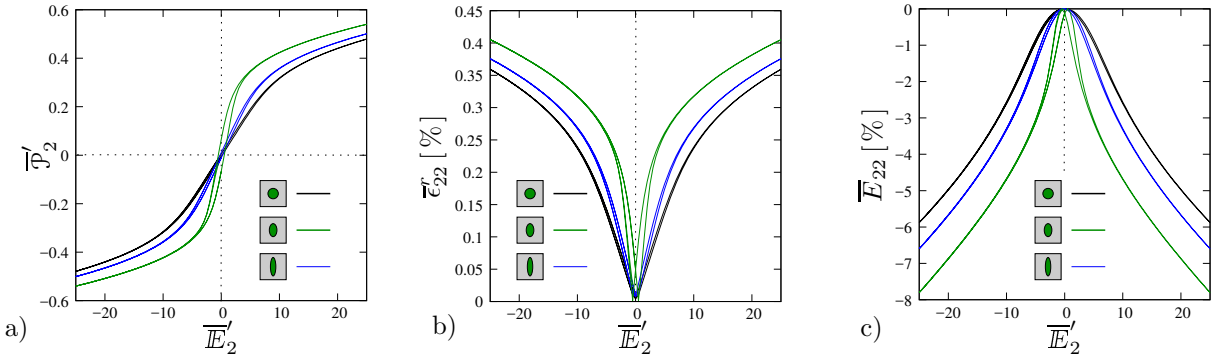

Figure 8.6: *Homogenized response of a two-phase micro-structure.* For different aspect ratios of the piezoceramic filler particle the homogenized dielectric and butterfly hysteresis curves are shown in a) and b), respectively. In both cases the anisotropic geometric shape effect is evident, as pronounced elliptic inclusions aligned in applied field direction lead to higher hysteresis. b) The particle attraction on the microscale results in positive remanent strain of the inclusions up to 0.4%. c) Overall macroscopic response is a compression of up to 8% due to the particle interaction. The shape effect results in higher deformation for aligned elliptic particles, especially for "needle"-shaped geometries.

electric loading direction. This results in stronger hysteresis in both the dielectric and butterfly hystereses curves. In contrast, pre-compression results in a polarization perpendicular to the applied field direction which leads to less pronounced hystereses, as the poling in field direction is harder to achieve.

8.4.2. Problem 2: influence of inclusion shape in two-phase composites

A two-phasic composite micro-structure consisting of an elastomeric matrix material (gray) and a piezoceramic filler particle (green) of 12.5% volume fraction is considered. While the volume fraction is not particularly high, in this example the focus is set on the shape of the filler particle. It varies from circular $r_1' = r_2' = 0.2$ to needle shaped elliptic $r_1' = 0.16$, $r_2' = 0.25$ and $r_1' = 0.1$, $r_2' = 0.4$, see Figure 8.5a–c. Note that the micro-structure is of normalized dimension $l' = 1$. Again, an electric loading $\overline{\mathbb{E}}_2'$ is applied for a mechanical stress-free macroscopic state.
The resulting homogenized dielectric and butterfly hysteresis is displayed for the different inclusion shapes in Figure 8.6a,b. Here, the anisotropic shape-effect of the filler particle

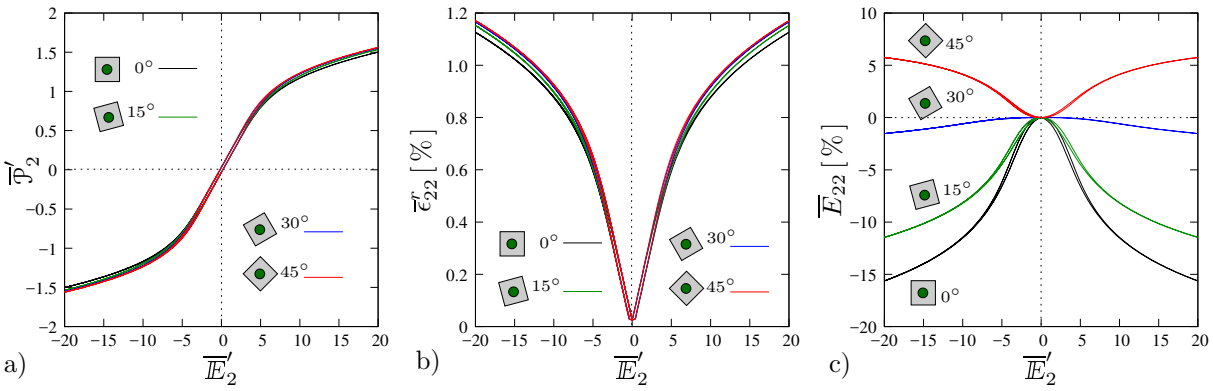

Figure 8.7: *Influence of micro-structure orientation on homogenized response.* For a circular ferroelectric inclusion of 30% volume fraction, the micro-structure is reoriented by an angle $\Theta_c = \{\, 0°, 15°, 30°, 45° \,\}$. a)-b) The homogenized dielectric and butterfly hysteresis curves are identical for all orientations due to the shape isotropy of the inclusion. c) The overall deformation however severely depends on the angle Θ_c. For $\Theta_c = \{\, 0°, 15°, 30° \,\}$ compression is observed, while $\Theta_c = 45°$ shows stretch in applied field direction.

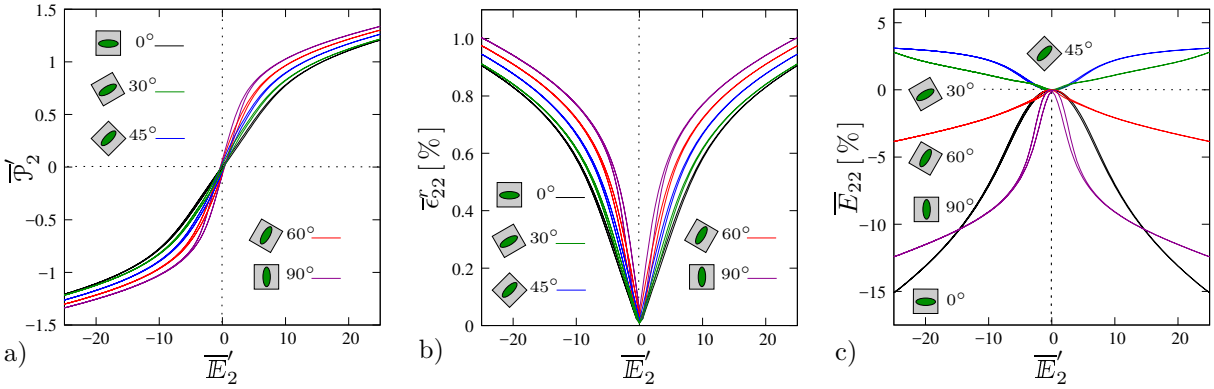

Figure 8.8: *Influence of micro-structure orientation on homogenized response.* For an elliptic ferroelectric inclusion of 30% volume fraction, the micro-structure is reoriented by an angle $\Theta_e = \{\, 0°, 30°, 45°, 60°, 90° \,\}$. a)-b) The homogenized dielectric and butterfly hysteresis curves differ for the various orientations due to the shape aniisotropy of the elliptic inclusion. c) The overall deformation severely depends on the angle Θ_e. For $\Theta_e = \{\, 0°, 60°, 90° \,\}$ compression is observed, while $\Theta_e = \{\, 30°, 45° \,\}$ shows stretch in applied field direction.

is evident, i.e. for pronounced "needle-shaped" ellipses in applied field direction higher dielectric and butterfly hysteresis is observed. The piezoceramic filler particles elongate in field direction, see Figure 8.6b.
Of high interest, especially for industrial applications, is the overall deformation due to the particle interaction. Figure 8.6c shows compression for all three cases up to 8%. Again, the geometric anisotropy effect is evident as elliptic particles aligned in applied field direction result in higher deformations.

8.4.3. Problem 3: influence of micro-structure orientation

The distribution of filler particles within the micro-structure is known to have high effects on the overall macroscopic response. In the following, for circular and elliptic inclusion of 30% volume fraction, micro-structures of different orientations are compared. A reorientation angle of $\Theta_c = \{\, 0°, 15°, 30°, 45° \,\}$ for circular and $\Theta_e = \{\, 0°, 30°, 45°, 60°, 90° \,\}$ for

elliptic particles are investigated. This results in particle orientation perpendicular to the applied field direction for $\Theta_e = 0°$ or fully aligned for $\Theta_e = 90°$ of the elliptic inclusion. Starting with the circular inclusion, the hysteresis curves as well as the overall macroscopic deformation response due to the particle interaction is investigated for the different orientation angles Θ_c. First, due to the shape isotropy of the circular filler particle, the hysteresis curves coincide for either setting, see Figure 8.7a,b. The macroscopic deformation however shows severe differences. Orientation angles Θ_c up to 30° result in compression. Here, the magnitude of compressive stretch decreases with increasing angle from up to 17% for $\Theta_c = 0°$ down to 2% for $\Theta_c = 30°$. In the case of $\Theta_c = 45°$ the deformation changes to a stretch up to 5% for higher electric field levels, Figure 8.7c. These different results are due to the particle-particle interactions and their relative placement to the applied field direction. While for $\Theta_c = 0°$ a perfectly aligned chain structure of the particles is inherent, a distortion of this state leads to a reorientation of the particles under applied fields. They try to align with the field which can ultimately lead to completely different overall deformation behavior.

As observed in Problem 2, the shape anisotropy of the inclusions plays a crucial role for the overall response. In the following an elliptic inclusion of 30% volume fraction, defined by $r_1' = 0.4$, $r_2' = 0.25$, is considered. For the different orientation angles $\Theta_e = \{\, 0°, 30°, 45°, 60°, 90° \,\}$ the dielectric and butterfly hysteresis curves as well as the effective macroscopic response are compared in Figure 8.8. In comparison to the circular inclusion, the ellipse experiences a different dissipative response depending on the orientation of the micro-structure. For increasing angle Θ_e both the dielectric and butterfly hysteresis increases, Figure 8.8a,b. This is due to the easier polarization of the ellipse in major axis direction. If this anisotropy axis is aligned with the applied field direction a more pronounced hysteresis is observed. The overall deformation varies from compression up to 15% for an ellipse oriented perpendicular to the applied electric field direction to stretch of approximately 3% under $\Theta_e = 45°$. It is interesting to see that the perpendicularly aligned inclusions result in higher compression when comparing with the perfectly aligned ellipse under $\Theta_e = 90°$. However this is only true for higher ranges of applied fields. For lower fields the vertically aligned ellipse is still favorable, see Figure 8.8c.

Chapter 9

Phase-field modeling of finite deformation micro-magneto-mechanics

In the following, the variational structure for the two-scale solution of dissipative materials as proposed in the former chapter is extended to account for the additional difficulty of the physical unity constraint in micro-magneto-mechanics. This requires a modification in the algorithmic solution scheme associated with the macroscopic driving routine. A possibility based on a staggered solution scheme with a magnetic predictor and magneto-mechanic corrector step, as suggested in Sridhar et al. [235], is displayed and reviewed shortly. Then, the magneto-mechanical coupling effects are investigated based on particle-particle and particle-matrix interactions on the microscale. The overall deformation related to macroscopic stress-free boundary conditions for different micro-structures, and the magneto-mechanical stiffening effect is obtained via appropriate scale-bridging.

9.1. Two-scale finite deformation micro-magneto-mechanics

9.1.1. Macroscopic variables and gradient fields

For the macroscopic problem of finite magneto-elasticity the generalized form of Chapter 5 is followed, where for the objective set of state variables $\overline{\mathfrak{c}}^* := \{ \overline{\boldsymbol{F}}, \overline{\mathbb{H}} \}$ the deformation gradient and magnetic field are chosen. These gradient fields are obtained by the mixed energy-enthalpy approach based on the mechanical deformation map and the magnetic scalar potential

$$\overline{\boldsymbol{\varphi}} : \begin{cases} \overline{\mathcal{V}} \times \overline{\mathcal{T}} \to \overline{\mathcal{S}} = \overline{\boldsymbol{\varphi}}_t(\overline{\mathcal{V}}) \\ (\overline{\boldsymbol{X}}, t) \mapsto \overline{\boldsymbol{x}} = \overline{\boldsymbol{\varphi}}(\overline{\boldsymbol{X}}, t) \end{cases} \quad \text{and} \quad \overline{\phi^m} : \begin{cases} \overline{\mathcal{V}} \times \overline{\mathcal{T}} \to \mathcal{R} \\ (\overline{\boldsymbol{X}}, t) \mapsto \overline{\phi^m}(\overline{\boldsymbol{X}}, t) \,. \end{cases} \tag{9.1}$$

The deformation map or motion $\overline{\boldsymbol{\varphi}}$ maps at time $t \in \overline{\mathcal{T}}$ points $\overline{\boldsymbol{X}} \in \overline{\mathcal{V}}$ of the reference configuration $\overline{\mathcal{V}} \subset \mathcal{R}^3$ onto points $\overline{\boldsymbol{x}} = \overline{\boldsymbol{\varphi}}_t(\overline{\boldsymbol{X}}) \in \overline{\mathcal{S}}$ of the current or Eulerian configuration $\overline{\mathcal{S}} = \overline{\boldsymbol{\varphi}}_t(\overline{\mathcal{V}}) \subset \mathcal{R}^3$. The ansatz of a scalar magnetic potential $\overline{\phi^m}$ is used to govern the macroscopic magnetic field. Note that the particular ansatz for the deformation gradient and the magnetic field $\overline{\boldsymbol{F}} = \overline{\nabla} \overline{\boldsymbol{\varphi}}$ and $\overline{\mathbb{H}} = -\overline{\nabla}\, \overline{\phi^m}$ automatically satisfies the mechanical

compatibility condition to avoid material penetration $\det[\overline{\boldsymbol{F}}] > 0$, as well as Ampère's law $\overline{\mathrm{Curl}[\mathbb{H}]} = \boldsymbol{0}$. The variational structure as introduced in Chapter 5 and Chapter 8 can strictly be followed for a full macroscopic variational framework.

9.1.2. Microscopic variables and gradient fields

The micro-structural primary and dual fields are introduced in a Lagrangian geometric setting referring to the undeformed body $\mathcal{B} \subset \mathcal{R}^3$. Following a micro-magneto-mechanical approach, we introduce the three microscopic primary fields

$$\boldsymbol{\varphi}\colon \begin{cases} \mathcal{B}\times\mathcal{T}\to\mathcal{S}=\boldsymbol{\varphi}_t(\mathcal{B}) \\ (\boldsymbol{X},t)\mapsto \boldsymbol{x}=\boldsymbol{\varphi}(\boldsymbol{X},t) \end{cases}, \phi^m\colon \begin{cases} \mathcal{B}\times\mathcal{T}\to\mathcal{R} \\ (\boldsymbol{X},t)\mapsto \phi^m(\boldsymbol{X},t) \end{cases}, \boldsymbol{\mathfrak{M}}\colon \begin{cases} \mathcal{B}\times\mathcal{T}\to\mathcal{S}^{d-1} \\ (\boldsymbol{X},t)\mapsto \boldsymbol{\mathfrak{M}}(\boldsymbol{X},t) \end{cases}. \tag{9.2}$$

The deformation map or motion $\boldsymbol{\varphi}$ maps at time $t \in \mathcal{T}$ points $\boldsymbol{X} \in \mathcal{B}$ of the reference configuration $\mathcal{B} \subset \mathcal{R}^3$ onto points $\boldsymbol{x} = \boldsymbol{\varphi}_t(\boldsymbol{X}) \in \mathcal{S}$ of the current or Eulerian configuration $\mathcal{S} = \boldsymbol{\varphi}_t(\mathcal{B}) \subset \mathcal{R}^3$. The referential magnetization director $\boldsymbol{\mathfrak{M}}$ describes at time $t \in \mathcal{T}$ the magnetic state of the ferromagnetic body at $\boldsymbol{X} \in \mathcal{B}$ and is obtained by a pull-back operation of the current magnetization director $\boldsymbol{\mathfrak{m}} = \boldsymbol{F}^{-1}\boldsymbol{\mathfrak{M}}$ at $\boldsymbol{x} \in \mathcal{S}$. The referential magnetization is considered here as the inclusions are assumed to be rigid, i.e. do not deform under applied fields. It can then be computed as $\boldsymbol{M} = m_s\boldsymbol{\mathfrak{M}}$ based on the magnetization director $\boldsymbol{\mathfrak{M}} \in \mathcal{S}^{d-1}$ under the physical constraint $\|\boldsymbol{\mathfrak{M}}\| = 1$ and the saturation magnetization m_s of the respective material. Note that the magnetization is per definition only defined within the ferromagnetic body $\mathcal{B}_{\mathfrak{f}} \subset \mathcal{B} \subset \mathcal{R}^3$ such that

$$\boldsymbol{M}(\boldsymbol{X}) := \begin{cases} m_s\boldsymbol{\mathfrak{M}} & \text{for } \boldsymbol{X} \in \mathcal{B}_{\mathfrak{f}} \\ \boldsymbol{0} & \text{otherwise} \end{cases}. \tag{9.3}$$

The ansatz of a scalar magnetic potential ϕ^m is used to govern the magnetic field within the body. The gradient fields

$$\boldsymbol{F} = \nabla\boldsymbol{\varphi}(\boldsymbol{X},t)\,, \quad \mathbb{H} = -\nabla\phi^m(\boldsymbol{X},t)\,, \quad \nabla\boldsymbol{\mathfrak{M}} = \nabla\boldsymbol{\mathfrak{M}}(\boldsymbol{X},t), \tag{9.4}$$

are the deformation gradient, the gradient of the order parameter and the magnetic field, respectively. This ansatz directly satisfies the mechanical compatibility condition $\mathrm{Curl}[\boldsymbol{F}] = \boldsymbol{0}$ of the deforming solid as well as Ampère's law $\mathrm{Curl}[\mathbb{H}] = \boldsymbol{0}$. Note, that the motion $\boldsymbol{\varphi}$ is constrained by the condition $\det[\boldsymbol{F}] > 0$ to avoid material penetration.

9.1.3. Microscopic rate-type variational principle

Based on the rate of the objective state variables $\dot{\mathfrak{c}}^* := \{\dot{\boldsymbol{C}}, \dot{\mathbb{H}}, \dot{\boldsymbol{\mathfrak{M}}}, \nabla\dot{\boldsymbol{\mathfrak{M}}}\}$ a rate-type potential is introduced that governs the primary fields by a variational principle at a given state $\{\boldsymbol{\varphi}, \phi^m, \boldsymbol{\mathfrak{M}}\}$ such that

$$\{\dot{\boldsymbol{\varphi}}, \dot{\phi}^m, \dot{\boldsymbol{\mathfrak{M}}}\} = \arg\Big\{ \inf_{\dot{\boldsymbol{\varphi}}\in\mathcal{W}_{\dot{\boldsymbol{\varphi}}}} \sup_{\dot{\phi}^m\in\mathcal{W}_{\dot{\phi}^m}} \inf_{\dot{\boldsymbol{\mathfrak{M}}}\in\mathcal{W}_{\dot{\boldsymbol{\mathfrak{M}}}}} \int_{\mathcal{B}} \pi^*(\dot{\mathfrak{c}}^*)\, dV \Big\}, \tag{9.5}$$

in terms of the admissible states of the deformation and potential on the micro-structure

$$\mathcal{W}_{\dot{\boldsymbol{\varphi}}} := \{\dot{\boldsymbol{\varphi}} \,|\, [\![\dot{\boldsymbol{\varphi}}]\!] = \dot{\overline{\boldsymbol{F}}} \cdot [\![\boldsymbol{X}]\!] \text{ on } \partial\mathcal{B}\} \quad \text{and} \quad \mathcal{W}_{\dot{\phi}} := \{\dot{\phi^m} \,|\, [\![\dot{\phi^m}]\!] = -\dot{\overline{\mathbb{H}}} \cdot [\![\boldsymbol{X}]\!] \text{ on } \partial\mathcal{B}\}\,. \tag{9.6}$$

The magnetization is treated as a generalized internal variable that does not have a macroscopic external counterpart. The admissible space for periodic micro-structures is given as

$$\mathcal{W}_{\dot{\mathfrak{M}}} := \{\dot{\mathfrak{M}} \in T\mathcal{S}^{d-1} |\ [\![\dot{\mathfrak{M}}]\!] = \boldsymbol{0} \text{ on } \partial\mathcal{B}\}\,, \tag{9.7}$$

where $T\mathcal{S}^{d-1}$ is the tangent-bundle of the unit sphere $\mathcal{S}^{d-1}$. Here, $[\![\cdot]\!] := (\cdot)^+ - (\cdot)^-$ denotes the jump of a quantity $(\cdot)$ with respect to opposite faces of the periodic micro-structure. Note carefully, that the variational principle (9.5) must account for the geometric structure of the magnetization $\mathfrak{M}$ with $\|\mathfrak{M}\| = 1$, see Sridhar et al. [235] for a detailed discussion. The microscopic potential density is defined in terms of the mixed energy-enthalpy and dissipation function such that

$$\pi^*(\dot{\boldsymbol{C}}, \dot{\mathbb{H}}, \dot{\mathfrak{M}}, \nabla\dot{\mathfrak{M}}) := \frac{d}{dt}\psi^*(\boldsymbol{C}, \mathbb{H}, \mathfrak{M}, \nabla\mathfrak{M}; \boldsymbol{\mathcal{A}}) + \Phi(\dot{\mathfrak{M}}; \boldsymbol{C}). \tag{9.8}$$

The necessary or equilibrium condition of the variational principle (9.5) is obtained by the first variation with the introduced exact update of the magnetization (9.10) and in terms of the mixed free energy-enthalpy density

$$\begin{aligned} 0 := \frac{1}{|\mathcal{B}|}\Bigg\{ \int_{\mathcal{B}} &- \mathrm{Div}[\partial_{\boldsymbol{F}}\psi^*] \cdot \delta\dot{\boldsymbol{\varphi}} - \mathrm{Div}[\partial_{\mathbb{H}}\psi^*]\delta\dot{\phi^m} - \big[\mathfrak{M} \times (\mathbb{H}_{eff} - \eta\boldsymbol{C}\cdot\dot{\mathfrak{M}})\big] \cdot \delta\dot{\boldsymbol{\Theta}}\, dV \\ &+ \int_{\partial\mathcal{B}} [\mathfrak{M} \times (\partial_{\nabla\mathfrak{M}}\psi^* \cdot \boldsymbol{N})] \cdot \delta\dot{\boldsymbol{\Theta}} + \partial_{\mathbb{H}}\psi^* \cdot \boldsymbol{N}\delta\dot{\phi^m} + [\partial_{\boldsymbol{F}}\psi^* \cdot \boldsymbol{N}] \cdot \delta\dot{\boldsymbol{\varphi}}\, dA \Bigg\}. \end{aligned} \tag{9.9}$$

Here, the variation of the rate of magnetization is rewritten

$$\delta\dot{\mathfrak{M}} = \delta\dot{\boldsymbol{\Theta}} \times \mathfrak{M}\,, \tag{9.10}$$

in terms of the spin of the magnetization $\dot{\boldsymbol{\Theta}}$. The resulting Euler-Lagrange equations of the micro-structure then read

1.	*Balance of linear momentum*	$\mathrm{Div}[\partial_{\boldsymbol{F}}\psi^*] = \boldsymbol{0}$	in	$\mathcal{B}$,
2.	*Gauss's law*	$\mathrm{Div}[-\partial_{\mathbb{H}}\psi^*] = 0$	in	$\mathcal{B}$,
3.	*Evolution equation*	$\mathfrak{M} \times (-\mathbb{H}_{eff} + \eta\boldsymbol{C}\cdot\dot{\mathfrak{M}}) = \boldsymbol{0}$	in	$\mathcal{B}_{\mathfrak{f}} \subset \mathcal{B}$.

(9.11)

Here, the *effective magnetic field* $\mathbb{H}_{eff}$ is introduced as $\mathbb{H}_{eff} := \mathrm{Div}[\mathfrak{M}] - \mathbb{M}$ with $\mathfrak{M} := \partial_{\nabla\mathfrak{M}}\psi^*$ and $\mathbb{M} := \partial_{\mathfrak{M}}\psi^*$, and one can identify that, for vanishing rate of magnetization $\dot{\mathfrak{M}} = \boldsymbol{0}$, $(9.11)_3$ yields the equilibrium condition given by the the first equation of Brown [33]

$$\mathfrak{M} \times \mathbb{H}_{eff} = \boldsymbol{0} \quad \text{in} \quad \mathcal{B}_{\mathfrak{f}}\ . \tag{9.12}$$

It shows that the torque exerted on the magnetization by the effective field $\mathbb{H}_{eff}$ vanishes at equilibrium. Note that $\mathbb{M}$ is the influence of the self-field onto the overall magnetic field. The evolution equation for the magnetization director of the form,

$$\boldsymbol{C}\cdot\dot{\mathfrak{M}} = -\frac{1}{\eta}\mathfrak{M} \times \mathfrak{M} \times \mathbb{H}_{eff}\ . \tag{9.13}$$

is obtained by reformulating $(9.11)_3$. This evolution equation of the magnetization is consistent with the *Landau-Lifshitz equation*.

9.1.4. Microscopic incremental variational principle

For the numerical setting, an incremental variational principle which governs the micro-magneto-mechanical problem at discrete time t_{n+1} for finite time increments $\tau = t_{n+1} - t_n$ is considered. This definition is conceptually in line with formulations for non-linear mechanical problems in Miehe [158] and Ponte Castañeda & Suquet [199] as well as Sridhar et al. [235] and Keip & Sridhar [114]. The incremental potential density $\pi^{*\tau}$ is related to the rate-type potential π^* by the algorithm

$$\pi^{*\tau}(\boldsymbol{C}, \mathbb{H}, \mathfrak{M}, \nabla\mathfrak{M}) := ALGO\Big\{ \int_{t_n}^{t_{n+1}} \pi^*(\dot{\boldsymbol{C}}, \dot{\mathbb{H}}, \dot{\mathfrak{M}}, \nabla\dot{\mathfrak{M}}) d\tau \Big\} . \tag{9.14}$$

The related admissible spaces for the deformation, scalar potential and the magnetic director read

$$\begin{aligned} \mathcal{W}_{\boldsymbol{\varphi}} &:= \{ \boldsymbol{\varphi} \,|\, [\![\boldsymbol{\varphi}]\!] = \overline{\boldsymbol{F}} \cdot [\![\boldsymbol{X}]\!] \text{ on } \partial\mathcal{B} \} , \\ \mathcal{W}_{\phi^m} &:= \{ \phi^m \,|\, [\![\phi^m]\!] = -\overline{\mathbb{H}} \cdot [\![\boldsymbol{X}]\!] \text{ on } \partial\mathcal{B} \} , \\ \mathcal{W}_{\mathfrak{M}} &:= \{ \mathfrak{M} \in T\mathcal{S}^{d-1} \,|\, [\![\mathfrak{M}]\!] = \boldsymbol{0} \text{ on } \partial\mathcal{B} \} , \end{aligned} \tag{9.15}$$

where the macroscopic deformation gradient and magnetic field serve as driving variables.

Macroscopic variational principle of homogenization. Assume now that the macroscopic potential density $\overline{\pi}^*$ is governed by the displacement and the magnetic potential for a steady state of the magnetic director on the microscale. Then the saddle-point variational principle of homogenization is given by

$$\overline{\pi^{*\tau}}(\overline{\boldsymbol{\varphi}}, \overline{\phi^m}) = \inf_{\boldsymbol{\varphi} \in \mathcal{W}_{\boldsymbol{\varphi}}} \sup_{\phi^m \in \mathcal{W}_{\phi^m}} \frac{1}{|\mathcal{B}|} \int_{\mathcal{B}} \pi^{*\tau}(\boldsymbol{C}, \mathbb{H}, \hat{\mathfrak{M}}, \nabla\hat{\mathfrak{M}}) \, dV . \tag{9.16}$$

Note that the microscopic potential is assumed to be in a quasi-static state $\hat{\pi}^{*\tau}(\boldsymbol{C}, \mathbb{H}) = \pi^{*\tau}(\boldsymbol{C}, \mathbb{H}, \hat{\mathfrak{M}}, \nabla\hat{\mathfrak{M}})$ and $\hat{\mathfrak{M}}$ is defined such that $\|\hat{\mathfrak{M}} - \mathfrak{M}_n\| \leq \epsilon$, where $\epsilon \ll 1$ is a small real number. Exact algorithmic treatment of this condition is discussed in the following.

9.2. Finite element implementation of homogenization

The numerical implementation of the constrained magnetization on the micro-level is a challenging task and active field of research. We employ and refer to the ansatz of Sridhar et al. [235] that proposes an operator split method with accompanying renormalization routine for the magnetization director. In the following their solution method is revisited shortly. Additionally, the algorithmic scale-bridging based on volume averaging and specifications on the macroscopic driving routine are presented.

9.2.1. Generalized arrays

The primary variables of the micro-structure

$$\boldsymbol{\varphi} = \overline{\boldsymbol{F}} \cdot \boldsymbol{X} + \widetilde{\boldsymbol{\varphi}} \quad \text{and} \quad -\phi^m = \overline{\mathbb{H}} \cdot \boldsymbol{X} - \widetilde{\phi}^m , \tag{9.17}$$

are decomposed into macroscopic linear parts associated with the Dirichlet-type driving and microscopic fluctuations. Note that the magnetization director $\boldsymbol{\mathcal{M}}$ as the third primary field is not decomposed, as no direct macroscopic driving is considered. For a compact notation of the following finite element implementation we introduce generalized arrays

$$\overline{\mathsf{F}^*} := [\,\overline{\boldsymbol{F}}, \overline{\mathbb{H}}, \boldsymbol{0}, \boldsymbol{0}\,]^T \quad \text{and} \quad \mathsf{F}^* := [\,\boldsymbol{F}, \mathbb{H}, \boldsymbol{\mathcal{M}}, \nabla\boldsymbol{\mathcal{M}}\,]^T , \tag{9.18}$$

for the macro- and microscopic primary fields, respectively. The fluctuation fields and magnetization director as the microscopic degrees of freedom are discretized by a finite element method such that

$$\tilde{\mathsf{F}}^* := [\,\nabla\widetilde{\boldsymbol{\varphi}}, \nabla\widetilde{\phi}^m, \boldsymbol{\mathcal{M}}, \nabla\boldsymbol{\mathcal{M}}\,]^T = \underline{\mathbf{B}}(\boldsymbol{X})\underline{\mathbf{d}}(t) \tag{9.19}$$

in terms of the interpolation matrix $\underline{\mathbf{B}}$ and a global vector of discrete fluctuations

$$\underline{\mathbf{d}} = \mathop{\mathbf{A}}_{I=1}^{N^h} \big[\,\widetilde{\boldsymbol{\varphi}}, \widetilde{\phi}^m, \boldsymbol{\mathcal{M}}\,\big]_I^T \in \mathcal{R}^{(d+1)N^h} \tag{9.20}$$

at the nodes of the discretized geometry. For the following staggered solution scheme, the required quantities are picked from these generalized arrays.

9.2.2. Microscopic staggered solution scheme

The microscopic time-discrete finite element solution is based on an operator split with renormalization routine, achieved by a staggered solution algorithm of the form

$$ALGO = ALGO_{\boldsymbol{\varphi}\phi^m} \circ ALGO_{\boldsymbol{\mathcal{M}}} \,. \tag{9.21}$$

The update of the magnetization director in $ALGO_{\boldsymbol{\mathcal{M}}}$ is a predictor step, followed by the corrector step $ALGO_{\boldsymbol{\varphi}\phi^m}$ determining the deformation and magnetic potential. As already stated, the solution of the magnetization director consists of two parts, namely

$$ALGO_{\boldsymbol{\mathcal{M}}} = ALGO^2_{\boldsymbol{\mathcal{M}}} \circ ALGO^1_{\boldsymbol{\mathcal{M}}} \,, \tag{9.22}$$

where $ALGO^1_{\boldsymbol{\mathcal{M}}}$ is the unconstrained update and $ALGO^2_{\boldsymbol{\mathcal{M}}}$ enforces the physical unity constraint by a renormalization.

Magnetic predictor step. For the solution of the magnetic director $\boldsymbol{\mathcal{M}}$ the other microscopic fields are frozen, such that they are not considered in this solution step. We end up with the finite-step sized stationary principle

$$\underline{\mathbf{d}}_{\boldsymbol{\mathcal{M}}} = \arg\Big\{ \inf_{\underline{\mathbf{d}}_{\boldsymbol{\mathcal{M}}}} \frac{1}{|\mathcal{B}_\mathfrak{f}|} \int_{\mathcal{B}_\mathfrak{f}} \pi^{*\tau}_{\boldsymbol{\mathcal{M}}}(\underline{\mathbf{B}}_{\boldsymbol{\mathcal{M}}}\underline{\mathbf{d}}_{\boldsymbol{\mathcal{M}}})\, dV \Big\} \tag{9.23}$$

based on the respective entries of the generalized arrays. This determines the unconstrained values for the nodal magnetization directors at current time t_{n+1} by a standard Newton-Raphson method. The necessary residual and tangent arrays for the update are obtained by

$$\underline{\mathbf{R}}^*_{\boldsymbol{\mathcal{M}}} := \frac{1}{|\mathcal{B}_\mathfrak{f}|} \int_{\mathcal{B}_\mathfrak{f}} \underline{\mathbf{B}}^T_{\boldsymbol{\mathcal{M}}} \partial_{\underline{\mathbf{F}}^*_{\boldsymbol{\mathcal{M}}}} \pi^{*\tau}_{\boldsymbol{\mathcal{M}}}\, dV \quad \text{and} \quad \underline{\mathbf{K}}^*_{\boldsymbol{\mathcal{M}}} := \frac{1}{|\mathcal{B}_\mathfrak{f}|} \int_{\mathcal{B}_\mathfrak{f}} \underline{\mathbf{B}}^T_{\boldsymbol{\mathcal{M}}} \partial^2_{\underline{\mathbf{F}}^*_{\boldsymbol{\mathcal{M}}}\underline{\mathbf{F}}^*_{\boldsymbol{\mathcal{M}}}} \pi^{*\tau}_{\boldsymbol{\mathcal{M}}} \underline{\mathbf{B}}_{\boldsymbol{\mathcal{M}}}\, dV \,. \tag{9.24}$$

The subsequent renormalization routine $ALGO^2_{\mathfrak{M}}$ of the magnetization director performs the following operation

$$\underline{\mathbf{d}}_{\mathfrak{M}} = \mathop{\mathbf{A}}_{I=1}^{N^h} \left[\mathfrak{M}/|\mathfrak{M}|\right]_I^T \tag{9.25}$$

at the nodal points of the discretized geometry.

Magneto-mechanical corrector step. For the solution of the magneto-mechanical corrector the renormalized magnetic director is frozen. We end up with the finite-step sized stationary principle

$$\underline{\mathbf{d}}_{\boldsymbol{\varphi}\phi^m} = \arg\Big\{ \inf_{\underline{\mathbf{d}}_{\boldsymbol{\varphi}}} \sup_{\underline{\mathbf{d}}_{\phi^m}} \frac{1}{|\mathcal{B}|} \int_{\mathcal{B}} \pi^{*\tau}_{\boldsymbol{\varphi}\phi^m}(\underline{\mathbf{B}}_{\boldsymbol{\varphi}\phi^m}\underline{\mathbf{d}}_{\boldsymbol{\varphi}\phi^m})\, dV \Big\} \tag{9.26}$$

based on the respective entries of the generalized arrays. The necessary residual and tangent arrays for the Newton-Raphson updates are obtained by

$$\begin{aligned} \underline{\mathbf{R}}^*_{\boldsymbol{\varphi}\phi^m} &:= \frac{1}{|\mathcal{B}|}\int_{\mathcal{B}} \underline{\mathbf{B}}^T_{\boldsymbol{\varphi}\phi^m}\partial_{\underline{\mathbf{F}}^*_{\boldsymbol{\varphi}\phi^m}}\pi^{*\tau}_{\boldsymbol{\varphi}\phi^m}\, dV\,, \\ \underline{\mathbf{K}}^*_{\boldsymbol{\varphi}\phi^m} &:= \frac{1}{|\mathcal{B}|}\int_{\mathcal{B}} \underline{\mathbf{B}}^T_{\boldsymbol{\varphi}\phi^m}\partial^2_{\underline{\mathbf{F}}^*_{\boldsymbol{\varphi}\phi^m}\underline{\mathbf{F}}^*_{\boldsymbol{\varphi}\phi^m}}\pi^{*\tau}_{\boldsymbol{\varphi}\phi^m}\underline{\mathbf{B}}_{\boldsymbol{\varphi}\phi^m}\, dV\,. \end{aligned} \tag{9.27}$$

Generalized macro-stress and moduli. With the solution of the micro-structure at hand, the overall macroscopic stresses and moduli are computed. The averaging routine is based on the works Miehe [158] for pure mechanics and follows the approach of Zäh [274] and Miehe et al. [174] for coupled problems. The homogenized generalized stress array reads

$$\overline{\mathbf{S}^*} = [\,\overline{\boldsymbol{P}}, -\overline{\mathbb{B}}\,]^T := \partial_{\overline{\mathbf{F}^*}}\overline{\pi^{*\tau}} = \overline{\pi^{*\tau}}_{,\overline{\mathbf{F}^*}} + [\overline{\pi^{*\tau}}_{,\underline{\mathbf{d}}}]\,[\underline{\mathbf{d}}_{,\overline{\mathbf{F}^*}}] = \frac{1}{|\mathcal{B}|}\int_{\mathcal{B}} \partial_{\mathbf{F}^*}\pi^{*\tau}\, dV, \tag{9.28}$$

where the necessary condition $\overline{\pi^{*\tau}}_{,\underline{\mathbf{d}}} = \boldsymbol{0}$ is considered. The second derivative yields the moduli of the macro-structure

$$\overline{\mathbf{C}^*} := \overline{\pi^{*\tau}}_{,\overline{\mathbf{F}^*}\,\overline{\mathbf{F}^*}} + [\,\overline{\pi^{*\tau}}_{,\overline{\mathbf{F}^*}\,\underline{\mathbf{d}}}\,]\,[\,\underline{\mathbf{d}}_{,\overline{\mathbf{F}^*}}] = \overline{\pi^{*\tau}}_{,\overline{\mathbf{F}^*}\,\overline{\mathbf{F}^*}} - [\,\overline{\pi^{*\tau}}_{,\overline{\mathbf{F}^*}\,\underline{\mathbf{d}}}\,]\,[\,\overline{\pi^{*\tau}}_{,\underline{\mathbf{d}}\underline{\mathbf{d}}}]^{-1}\,[\overline{\pi^{*\tau}}_{,\underline{\mathbf{d}}\overline{\mathbf{F}^*}}] = \mathbf{C}^* - \underline{\mathbf{L}}^{*T}\underline{\mathbf{K}}^{*-1}\underline{\mathbf{L}}^* \tag{9.29}$$

with the average of the micro-moduli $\mathbf{C}^* = \overline{\pi^{*\tau}}_{,\overline{\mathbf{F}^*}\,\overline{\mathbf{F}^*}}$ and a softening part accounting for the flexibility of the micro-structure, based on the additional finite element arrays $\underline{\mathbf{L}}^* = \overline{\pi^{*\tau}}_{,\underline{\mathbf{d}}\overline{\mathbf{F}^*}}$ and $\underline{\mathbf{L}}^{*T} = \overline{\pi^{*\tau}}_{,\overline{\mathbf{F}^*}\,\underline{\mathbf{d}}}$. Note that the derivative of the fluctuations with respect to the macroscopic primary fields is obtained by the linearization of the microscopic equilibrium condition such that

$$[\,\overline{\pi^{*\tau}}_{,\underline{\mathbf{d}}\overline{\mathbf{F}^*}}\,] + [\,\overline{\pi^{*\tau}}_{,\underline{\mathbf{d}}\underline{\mathbf{d}}}\,]\underline{\mathbf{d}}_{,\overline{\mathbf{F}^*}} = \boldsymbol{0} \quad\longrightarrow\quad \underline{\mathbf{d}}_{,\overline{\mathbf{F}^*}} = -[\,\overline{\pi^{*\tau}}_{,\underline{\mathbf{d}}\underline{\mathbf{d}}}\,]^{-1}\,[\,\overline{\pi^{*\tau}}_{,\underline{\mathbf{d}}\overline{\mathbf{F}^*}}\,]\,. \tag{9.30}$$

The necessary arrays for the homogenized macroscopic quantities in a finite element context read

$$\begin{aligned}
\overline{\mathbf{S}^*} &:= \overline{\pi^{*\tau}}_{,\overline{\mathbf{F}^*}} &&= \frac{1}{|\mathcal{B}|} \overset{E}{\underset{\#=1}{\mathbf{A}}} \int_{\mathcal{B}_\#} \partial_{\mathbf{F}} \pi^{*\tau} \, dV, \\
\mathbf{C}^* &:= \overline{\pi^{*\tau}}_{,\overline{\mathbf{F}^*}\,\overline{\mathbf{F}^*}} &&= \frac{1}{|\mathcal{B}|} \overset{E}{\underset{\#=1}{\mathbf{A}}} \int_{\mathcal{B}_\#} \partial^2_{\mathbf{F}^*\mathbf{F}^*} \pi^{*\tau} \, dV, \\
\underline{\mathbf{L}}^* &:= \overline{\pi^{*\tau}}_{,\underline{\mathbf{d}\mathbf{F}^*}} &&= \frac{1}{|\mathcal{B}|} \overset{E}{\underset{\#=1}{\mathbf{A}}} \int_{\mathcal{B}_\#} \underline{\mathbf{B}}^T \partial^2_{\mathbf{F}^*\mathbf{F}^*} \pi^{*\tau} \, dV.
\end{aligned} \tag{9.31}$$

9.2.3. Algorithmic two-scale solution scheme

The realization of the presented two-scale solution scheme containing a finite element solution on the micro- and a driver routine on the macroscale is in focus now. Based on an algorithmic flow-chart the solving procedure for a typical finite strain micro-magneto-mechanical boundary-value-problem is explained in detail, see Figure 9.1. The solution is build up on two blocks that are treated separately, the finite element solution on the micro-structure and the Newton-Raphson update of the macro-structure. As described in Chapter 5 the first step is to define the vector of macroscopic unknowns $\overline{\boldsymbol{\mathcal{U}}}$ as well as the equilibrium stresses $\overline{\mathbf{S}}_{eq}$ based on the desired macroscopic boundary and loading conditions. The provided flow-chart in Figure 9.1 proposes a classical energy-enthalpy loading of the primary field variables $\overline{\mathbf{F}^*} = \{\overline{\boldsymbol{F}}, \overline{\mathbb{H}}\}$, however a full energetic driving based on the dual variables is also possible. As macroscopic loading condition standard linear ramping or more advanced saw-tooth loading is controlled by the loading factor λ which also serves as a macroscopic pseudo-timescale. It is incremented after every converged macroscopic step. The linear macroscopic generalized primary fields $\overline{\mathbf{F}^*}$ are then prescribed onto the micro-structure. On the microscale the balance of linear momentum, Gauss's law and the Landau-Lifshitz-Gilbert equation for the magnetization need to be solved. However in two dimensions it is sufficient to solve the Landau-Lifshitz equation (LLE) as the additional precession damping term is only valid in three dimensions, see Keip & Sridhar [114]. The numerical implementation of the LLE with consistent update of the magnetization has been an active field of research for some time. Different approaches were developed Miehe & Ethiraj [163], Krishnaprasad & Tan [125], Wang et al. [265], and Yi & Xu [271], however a detailed analysis is beyond the scope of this work. Here, a staggered solution scheme is employed solving first for the magnetization director $\mathfrak{M}$ of arbitrary length accompanied by a normalization routine to ensure the physical unity constraint $\|\mathfrak{M}\| = 1$, see (9.23)-(9.25). With this updated solution the other fluctuation degrees of freedom $\widetilde{\boldsymbol{\varphi}}$ and $\widetilde{\phi}^m$ are computed. Note that the viscous nature of the magnetization requires a time-evolution on the microscale to ensure the proper rotation and alignment of the magnetization under the respective macroscopic loading and evolving self-field. To ensure a stationary state of the micro-structure, which is necessary for macroscopic convergence, we evaluate a residuum based on the time discrete rate of change of the magnetization director $\|\dot{\mathfrak{M}}\|$ with $\dot{\mathfrak{M}} = (\mathfrak{M}_{n+1} - \mathfrak{M}_n)/\tau$ and the timestep-size τ. For $\|\dot{\mathfrak{M}}\| \neq 0$ the magnetization director is updated and the microscopic time evolves $t_n \to t_{n+1}$. For a stationary microscopic state volume averages of the generalized stresses and moduli are computed and returned to the macro-structure. Here, the macroscopic moduli $\overline{\mathbf{C}^*}$ are computed, as described in (9.29) by subtracting

the softening terms, and the macroscopic residuum $\overline{\mathfrak{R}^*}$ (5.31) is formed. By following the steps (5.32)–(5.36) the update of the macroscopic unknowns $\overline{\mathfrak{U}}$ is computed. Based on the evaluation of the macroscopic residuum $\|\overline{\mathfrak{R}^*}\|$ we either prescribe the (possibly) updated primary fields as linear parts onto the micro-structure again for $\|\overline{\mathfrak{R}^*}\| > \text{tol}_{macro}$ or increase the macroscopic loading factor $\lambda = \lambda + 1$ and proceed with the next computation step if $\|\overline{\mathfrak{R}^*}\| < \text{tol}_{macro}$.

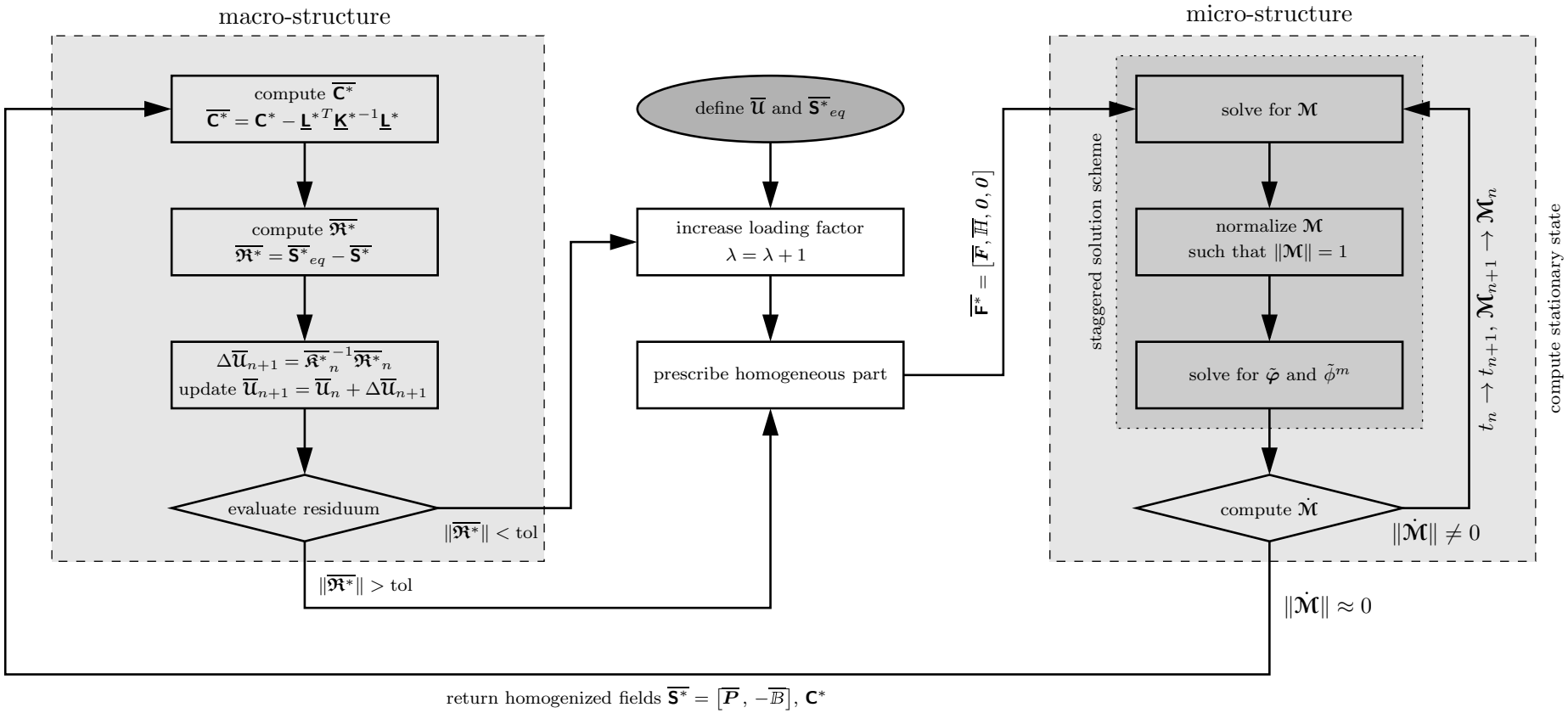

Figure 9.1: *Algorithmic two-scale solution scheme.* The two-scale solution scheme is based on a macroscopic driving routine prescribing the linear macroscopic fields onto the micro-structure which is then solved by the finite element method. A staggered solution scheme on the micro-structure allows for a post-processing routine to satisfy the physical unity constraint on the magnetization by a normalization routine. Microscopic iterations are performed till the rate of change of the magnetization director is below a given tolerance, i.e. a steady state is reached, to ensure macroscopic convergence. Homogenized stresses and moduli are then returned to the macro-structure. Update of the macroscopic unknows $\overline{\mathfrak{U}}$ is based on a Newton-Raphson scheme. If macroscopic convergence is achieved the macroscopic loading factor λ is increased, initiating the next loading step.

9.3. Representative numerical model problems

Numerical examples demonstrate the presented theory of computational homogenization based on a macroscopic driving routine. We focus on capturing physical characteristic behavior of MREs and ferromagnetic particles and provide insights on the influence of the micro-structure on the overall response. We restrict ourselves to 2D simulations. The chosen representative volume elements are of rather academical nature, however reflect the desired interactions. We investigate composite materials based on stiff ferromagnetic particles embedded in non-magnetizable, soft elastomer matrix materials.

The mixed energy-enthalpy density ψ^* as well as the dissipation function Φ need to be based on objective state variables, see also Keip & Sridhar [114]. For that the objective Cauchy-Green tensor $\boldsymbol{C} := \boldsymbol{F}^T\boldsymbol{F}$ is employed. For the energy storage two contributions to the energy density are necessary: a contribution $\psi^*_{\mathfrak{v}}(\boldsymbol{C}, \mathbb{H})$ due to the presence of a magnetic field in the full free space $\mathcal{B}$, and an additional elastic contribution $\psi^*_{\mathfrak{e}}(\boldsymbol{C})$ in the domain $\mathcal{B} \setminus \mathcal{B}_{\mathfrak{f}}$ and $\psi^*_{\mathfrak{f}}(\boldsymbol{C}, \mathfrak{M}, \nabla\mathfrak{M})$ in the domain of the ferromagnetic material $\mathcal{B}_{\mathfrak{f}}$. Hence, the free-energy density can be written as,

$$\psi^*(\boldsymbol{C}, \mathbb{H}, \mathfrak{M}, \nabla\mathfrak{M}; \boldsymbol{\mathcal{A}}) := \begin{cases} \psi^*_{\mathfrak{f}}(\boldsymbol{C}, \mathfrak{M}, \nabla\mathfrak{M}; \boldsymbol{\mathcal{A}}) + \psi^*_{\mathfrak{v}}(\boldsymbol{C}, \mathbb{H}) & \text{for} \quad \boldsymbol{X} \in \mathcal{B}_{\mathfrak{f}} \\ \psi^*_{\mathfrak{e}}(\boldsymbol{C}) + \psi^*_{\mathfrak{v}}(\boldsymbol{C}, \mathbb{H}) & \text{for} \quad \boldsymbol{X} \in \mathcal{B} \setminus \mathcal{B}_{\mathfrak{f}} \,. \end{cases} \tag{9.32}$$

A major advantage of the chosen phase-field formulation for the magnetization is that realistic material parameters and dimensions can be employed. However, due to the large differences in the magnitude of some parameters normalized quantities are used to help achieve numerical stability. The normalization is based on four physical parameters, namely mechanical stiffness μ [N/m^2], the saturation magnetization $\hat{m} = \rho m_s$ [A/m], magnetic exchange constant L [N] and magnetic viscosity η [Ns^2/m^2]. The normalized primary fields $(\cdot)'$ in terms of their counterparts $(\cdot)$ are related via

$$\boldsymbol{\varphi}' = \boldsymbol{\varphi}\sqrt{\mu/L}\,, \quad -\phi^{m\prime} = -\phi^m\sqrt{\mu/L\hat{m}^2}\,, \quad \mathfrak{M}' = \mathfrak{M}\,, \quad t' = t\sqrt{\mu/\eta}\,. \tag{9.33}$$

In the following the normalized energies are introduced. The material part of the free energy function of the ferromagnet depends on the deformation $\boldsymbol{C}$, the magnetization director $\mathfrak{M}$ and the gradient operator of the magnetization $\nabla\mathfrak{M}$. It is assumed to consist of three contributions,

$$\psi^{*\prime}_{\mathfrak{f}}(\boldsymbol{C}, \mathfrak{M}', \nabla\mathfrak{M}'; \boldsymbol{\mathcal{A}}) = \psi^{*\prime}{}_{mech}(\boldsymbol{C}) + \psi^{*\prime}{}_{an}(\boldsymbol{C}, \mathfrak{M}'; \boldsymbol{A}) + \psi^{*\prime}{}_{ex}(\nabla\mathfrak{M}') \tag{9.34}$$

where $\psi^{*\prime}{}_{mech}$ is the elastic energy, $\psi^{*\prime}{}_{an}$ is the magnetic-anisotropy energy, and $\psi^{*\prime}{}_{ex}$ is the exchange energy. $\boldsymbol{A}$ is the referential *magnetic easy axis* that characterizes the *magneto-crystalline anisotropy* of the ferromagnetic material. The elastic energy density defines the energy storage due to the mechanical deformation in the representative volume-element, this is given as

$$\psi^{*\prime}{}_{mech}(\boldsymbol{C}) = \frac{1}{2}(\mathrm{tr}[\boldsymbol{C}] - 3) + \frac{1}{\beta}(J^{-\beta} - 1)\,, \tag{9.35}$$

where $\beta = \frac{\lambda}{\nu} = \frac{2\nu}{1-2\nu}$ is given in terms of the Poisson ratio ν. In a ferromagnetic material with an inherent crystalline structure, the magnetization energy depends on the direction

of magnetization relative to the structural axes of the material. It is modeled by the even anisotropy energy density $\psi^{*\prime}_{an} : \mathcal{S}^{d-1} \mapsto [-\infty, +\infty]$

$$\psi^{*\prime}_{an}(\boldsymbol{C}, \boldsymbol{\mathcal{M}}'; \boldsymbol{A}) = \frac{K'}{2}[1 - \{\boldsymbol{C} : (\boldsymbol{\mathcal{M}}' \otimes \boldsymbol{A})^2\}] \,. \tag{9.36}$$

with the anisotropy coefficient K. The gradient energy $\psi^{*\prime}_{ex} : Lin(d) \mapsto [0, +\infty]$ models the tendency of neighboring magnetizations to align. Focusing on an isotropic response we formulate the simple form of the energy as

$$\psi^{*\prime}_{ex}(\nabla\boldsymbol{\mathcal{M}}') = \frac{1}{2}[\nabla\boldsymbol{\mathcal{M}}' : \nabla\boldsymbol{\mathcal{M}}'] \,. \tag{9.37}$$

The vacuum energy $\psi^{*\prime}_{\mathfrak{v}} : \mathcal{R}^d \times \mathcal{R}^d \to [0, \infty]$, defines the energy storage due to the presence of a magnetic field in the free space and reads

$$\psi^{*\prime}_{\mathfrak{v}}(\boldsymbol{C}, \widetilde{\mathbb{H}}', \boldsymbol{\mathcal{M}}') = -\frac{\mu'_0 J}{2}\boldsymbol{C}^{-1} : (\widetilde{\mathbb{H}}' \otimes \widetilde{\mathbb{H}}') - \rho\mu'_0 m'_s \boldsymbol{\mathcal{M}}' \cdot \widetilde{\mathbb{H}}' \,. \tag{9.38}$$

Furthermore, the vacuum contribution is reformulated to only depend on the *self-field* $\widetilde{\mathbb{H}}$, following the arguments presented in Section 8.3. For further explanation of the individual free energies the interested reader is referred to the work Keip & Sridhar [114] where all energy terms with their respective physical motivation are covered in detail. Finally the dissipation potential reads

$$\Phi(\dot{\boldsymbol{\mathcal{M}}}'; \boldsymbol{C}) = \frac{\eta'}{2}\boldsymbol{C} : (\dot{\boldsymbol{\mathcal{M}}}' \otimes \dot{\boldsymbol{\mathcal{M}}}') \,. \tag{9.39}$$

A polyurethane matrix material and permalloy magnetic inclusions are chosen for the boundary value problems in focus. Permalloy is an alloy consisting of 20% Nickel (Ni) and 80% Iron (Fe) and is widely used in magnetic applications. The material parameters for permalloy are taken from Hubert & Schäfer [98]. All the material parameters in their normalized form are provided in Table 9.1.

9.3.1. Problem 1: evolution and motion of magnetic domain walls

A preliminary example shows the ability of the microscopic material model to evolve magnetic domains, that align in the direction of a magnetic field, and delivers the starting point for further investigations on circular inclusions. The initial state is a random magnetization within the ferromagnetic particle for a $\mathcal{RVE}$ as described in Figure 9.2a. Note

Table 9.1: Material parameters for polyurethane matrix and permalloy inclusion.

no.	par.	name	polyurethane	permalloy
1.	β'	1^{st} mechanical parameter	$1.0 \cdot 10^{1}$	1.5
2.	μ'	2^{nd} mechanical parameter	$1.6 \cdot 10^{-5}$	$2.6 \cdot 10^{-1}$
3.	K'	anisotropy coefficient	0.0	$5.0 \cdot 10^{-6}$
4.	L'	exchange coefficient	0.0	1.0
5.	m'_s	saturation magnetization	0.0	1.0
6.	η'	magnetic viscosity	0.0	$3.0 \cdot 10^{-3}$
7.	μ'_0	free space permeability	$8.32 \cdot 10^{-3}$	$8.32 \cdot 10^{-3}$

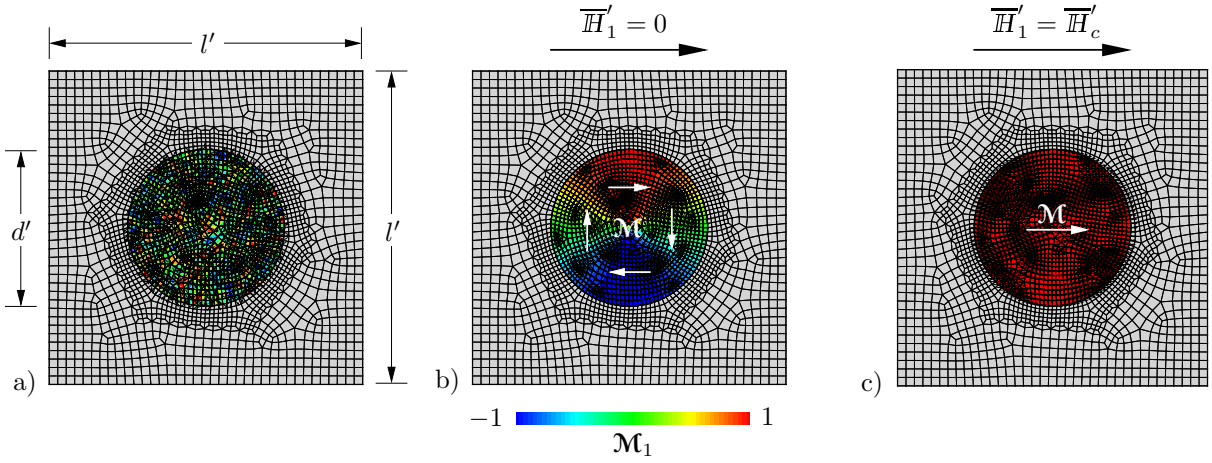

Figure 9.2: *Evolution and motion of magnetic domain walls.* a) Magnetization director is initialized randomly. Dimensions of the $\mathcal{RVE}$ for different volume fractions and aspect ratios can be found in Table 9.2. b) Without an applied external magnetic field the magnetization reorients to a stable, energetically favorable, vortex state with zero net magnetization. c) Application of a magnetic field $\overline{\mathbb{H}}_1'$ results in reorientation of the magnetization in field direction. This state is a starting point for further investigations.

Table 9.2: Dimensions of the $\mathcal{RVE}$ for different volume fractions of a circular inclusion.

%	diameter d'	length l'	#elements
20	500	1000	2766
25	500	880	3375
30	500	810	3764

that the dimensions of the micro-structure and diameters of the magnetic inclusion are summarized in Table 9.2. The geometry is discretized by Q1 quadrilateral finite elements, with a finer mesh for the inclusion in order to properly resolve the phase field. With evolving time on the micro-scale and without a macroscopic magnetic loading condition the system wants to minimize its self-energy by forming a state of zero net magnetization, see Figure 9.2b. This vortex-type arrangement of the magnetization also depends on the size of the particle as well as the characteristic domain wall width of the material. In a final step, application of a magnetic field $\overline{\mathbb{H}}_1'$ reorients the magnetization in field direction, resulting in a monodomain as depicted in Figure 9.2c. For the field $\overline{\mathbb{H}}_1' = \overline{\mathbb{H}}_c'$ the magnetization is saturated and fully poled in field direction which is also the anisotropy direction. $\mathbb{H}_c'$ denotes the respective coercive field. Periodicity of the micro-structure gives rise to particle-particle forces, in this case attractive forces between horizontally aligned inclusions. The overall macroscopic deformation, even though not plotted here, is a compression in field direction and stretch perpendicular to it. This state of the MRE serves as a initial state and all further analysis is done *relative to this configuration*.

9.3.2. Problem 2: influence of different volume fractions

The most natural way to influence the macroscopic response is to increase the amount of ferromagnetic particle volume fraction of the composite material. However, as the evolution and motion of magnetic domains within the particle is highly dependent on the size of the particle, we rather modify the dimension of the surrounding matrix material

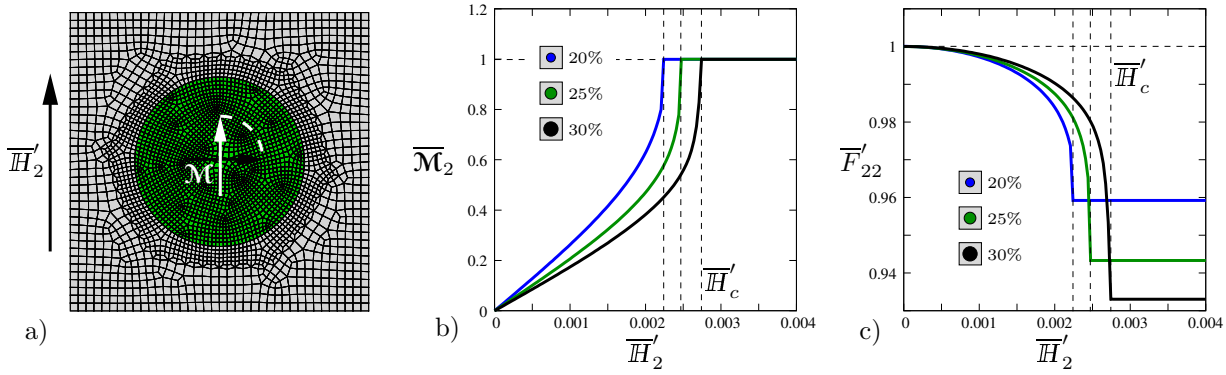

Figure 9.3: *Analysis of different volume fractions for circular inclusions.* a) To achieve maximum deformation the initial magnetization state (small black arrow) is chosen perpendicularly to the applied field direction $\bar{H}_2'$. b) The magnetization director for each volume fraction saturates towards 1, satisfying the physical unity constraint on the magnetization. c) Increasing volume fraction results in higher compression of up to 6.5%. The deformation saturates with the magnetization and is plotted in relation to its initial state, to ensure comparability.

to change the relative particle fraction within the $\mathcal{RVE}$, while keeping the particle size constant. The boundary-value-problem is displayed in Figure 9.3a. As a high magneto-mechanical coupling is required for reasonable deformations we restrict the range of ferromagnetic inclusions to 20, 25 and 30%. Based on the previous example, the initial magnetization direction is perpendicular (small black arrow) to the applied field direction $\overline{H}_2'$, parallel to the chosen magnetic anisotropy direction. This results in an attraction of horizontally aligned particles and therefore to a pre-deformation, i.e. a tension in vertical direction. Application of a linearly increasing magnetic field up to $\overline{H}_2' = 0.004$ [–] leads to a rotation of the magnetization in field direction (white arrow). Note, that the averaged magnetization director $\overline{\mathfrak{M}}_2$, obtained by averaging only over the ferromagnetic domain, saturates to 1 when reaching the coercive fields $\overline{H}_c' = \{\, 0.00223, 0.00248, 0.00275 \,\}$ [–] for 20, 25 and 30% volume fraction respectively, and thereby satisfies the physical unity constraint on the magnetization, see Figure 9.3b. The homogenized macroscopic deformation is compared in Figure 9.3c. For the chosen micro-structure and loading condition we obtain compression of up to 6.5%. Note, that the deformation is initialized to ensure comparability and is measured relative to the pre-stretched condition. Naturally, an increased volume fraction of the ferromagnetic particle increases the deformation due to a higher magneto-mechanical coupling. It is important to note though that the deformation mirrors the behavior of the magnetization and saturates with the applied field. This effect is explained by the particle-particle interaction on the micro-scale. The attractive forces in between the neighboring particles depend on the magnetization of either particle and therefore a maximum attractive force is achieved for fully saturated magnetization.

9.3.3. Problem 3: influence of micro-structure orientation

To identify the influence of the chosen micro-structure on the overall response, different micro-structures, based on a rotation angle $\Theta = \{\, 0°, 15°, 30°, 45° \,\}$, are investigated for circular inclusion of 30% volume fraction, see Figure 9.4a. Due to this rotation, the particle-particle forces are not aligned with the major coordinate axes anymore, i.e. attractive or repulsive forces between adjacent particles (particles with the smallest distance

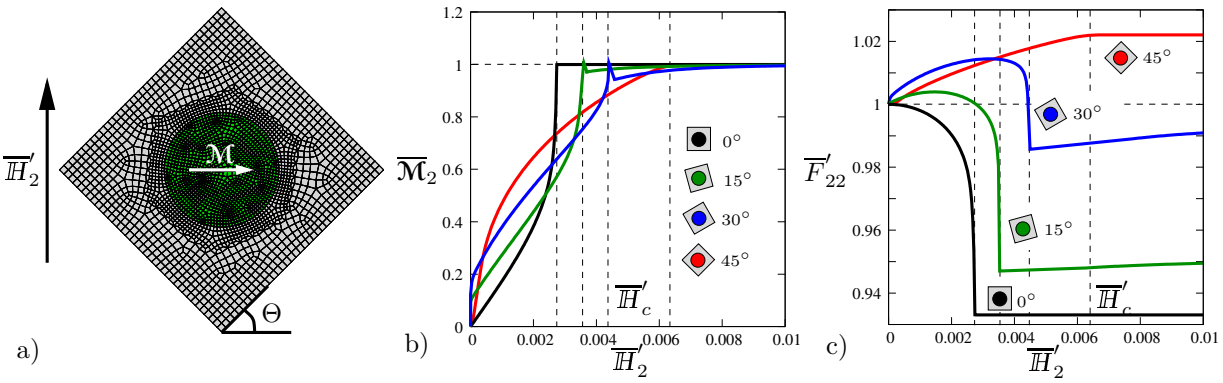

Figure 9.4: *Analysis of different micro-structures for circular inclusions.* a) The micro-structure depends on angle $\Theta = \{\,0°, 15°, 30°, 45°\,\}$, i.e. different micro-structures are investigated for an magnetic inclusion of 30% volume fraction. b) The magnetization director saturates to 1 for the respective coercive fields $\overline{\mathbb{H}}_c'$. The influence of the micro-structure is evident, as the magnetization director approaches its saturation value in completely different ways due to particle interactions. c) Depending on the angle the overall macroscopic deformation is either a compression or stretch in field direction and is plotted relative to its initial state to ensure comparability.

with respect to each other) are now also rotated by Θ. The initial magnetization direction still coincides with the easy axes, and is such, that a monodomain is formed pointing in horizontal direction (white arrow Figure 9.4a). The particle interaction pushes the magnetization to rotate towards the imposed angle Θ leading to further attraction of the particles and ultimately to extension in vertical direction as the particles try to move and form a chain structure. This effect, however, is opposed and ultimately suppressed by the applied magnetic field $\overline{\mathbb{H}}_2'$ which forces the magnetization to align in field direction. For increasing fields $\overline{\mathbb{H}}_2' \to \overline{\mathbb{H}}_c'$ the rotation of the magnetization in applied field direction surpasses the particle effects which leads to overall compression in case of $\Theta = \{\,0°, 15°, 30°\,\}$, however for $\Theta = 45°$ stretch in field direction remains. A closer analysis of the particle interactions on the magnetization is done in Figure 9.5. These are the corresponding magnetic induction $\mathbb{B}_1'$ contour plots for $\Theta = \{\,0°, 15°, 30°, 45°\,\}$. In Figure 9.5a the initial magnetization gradually aligns in applied field direction $\overline{\mathbb{H}}_2'$ for increasing macroscopic loading factor λ. Note though that in the beginning for low loading the rotation is slower, as the magnetic anisotropy as well as the magnetic self field of the particles try to keep the magnetization aligned in horizontal direction. This effect can also be seen in the slope of the magnetization in Figure 9.4b for $\Theta = 0°$. At some point the magnetic moment due to the applied field overcomes the anisotropy and self-energy and the magnetization rapidly aligns with the field direction. In contrast, the magnetization of the rotated micro-structures switches rather fast from its initial configuration into direction of the neighboring particle due to the evolving self-field, see Figure 9.5b/c/d. Afterwards, the process slows down as the applied field opposes the anisotropy- as well as self-energy. For increasing loading factor $\lambda = 115$ the magnetization overcomes the vertical alignment for $\Theta = \{\,15°, 30°\,\}$, as the attraction of the closest particle is more dominant. This effect is not observed for $\Theta = 45°$ in Figure 9.5d due to the symmetry of the micro-structure. From these states the magnetization slowly saturates for increasing applied fields and ultimately aligns in vertical direction for $\overline{\mathbb{H}}_2' \to \overline{\mathbb{H}}_c'$ with $\lambda = 300$ for all the analyzed micro-structures.

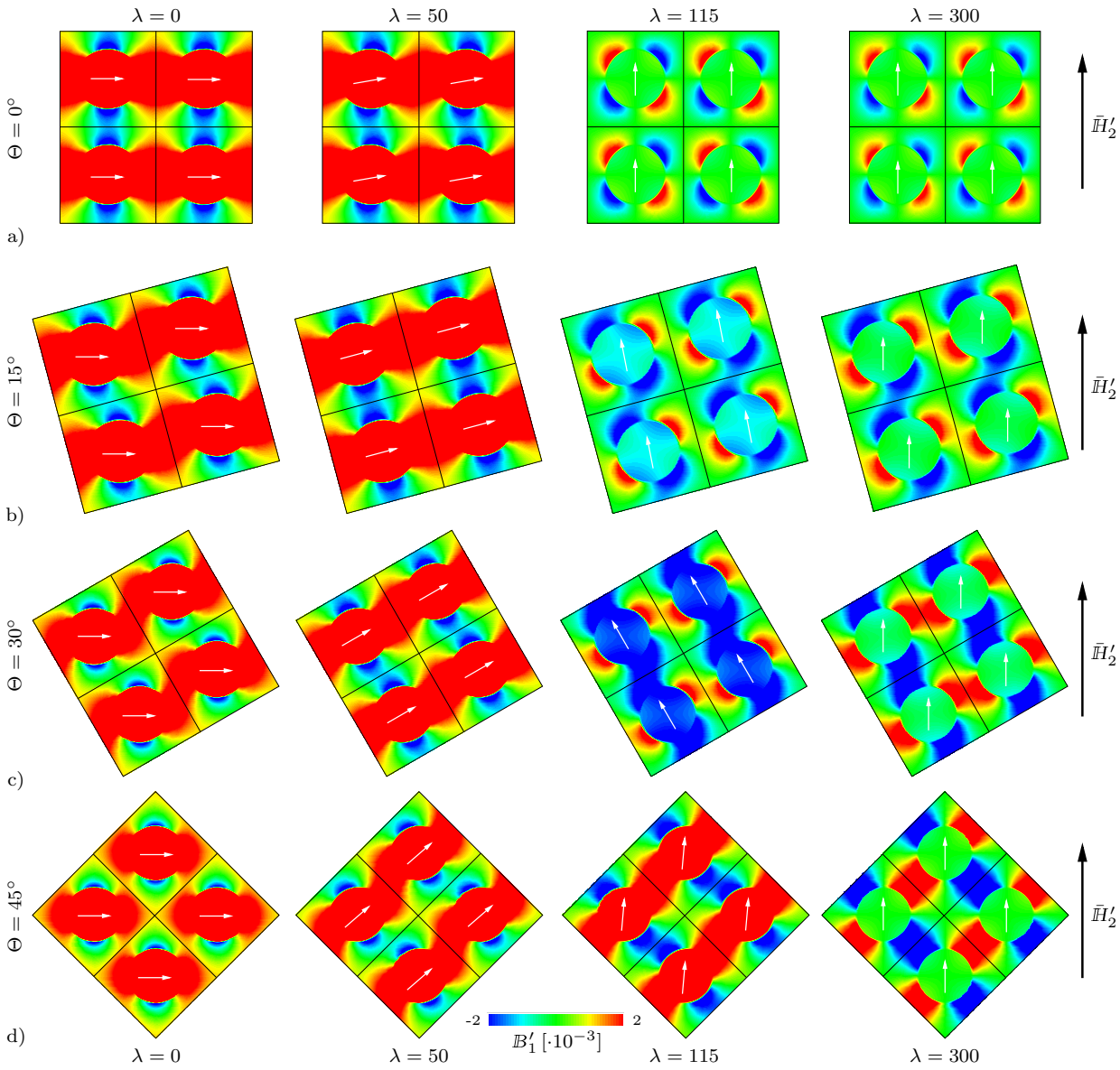

Figure 9.5: *Analysis of different micro-structures for circular inclusions.* The contour plots show the evolving magnetic induction $I\!B'_1$ for different macroscopic loading steps λ of micro-structures characterized by $\Theta = \{\, 0°, 15°, 30°, 45° \,\}$. The magnetization direction of the mon-odomains is summarized by white arrows and the magnetic loading is given by $\overline{I\!H}'_2$.

9.3.4. Problem 4: the magnetic stiffening-effect

One major case of industrial application of MREs is as damping units with tuneable stiffness. The idea is to modify the materials mechanical response by magnetic pre-loading. Experimental results on the magnetic stiffening effect were published in Jolly et al. [105], and numerically based on a phenomenological material model by Han et al. [84], Javili et al. [103], Miehe et al. [174], and Keip & Rambausek [111]. We investigate a circular magnetic particle of 20 and 30% volume fraction and linearly apply a mechanic shear loading up to $\overline{F}'_{12} = 0.2$ [–], as described in the legend of Figure 9.6a. Here, the dotted lines denote the homogenized material stress-strain response for 20 (blue) and 30% (green) volume fraction, under pure mechanical shear loading. The difference of the two lines is due to the increased overall stiffness for a higher volume fraction of the relatively

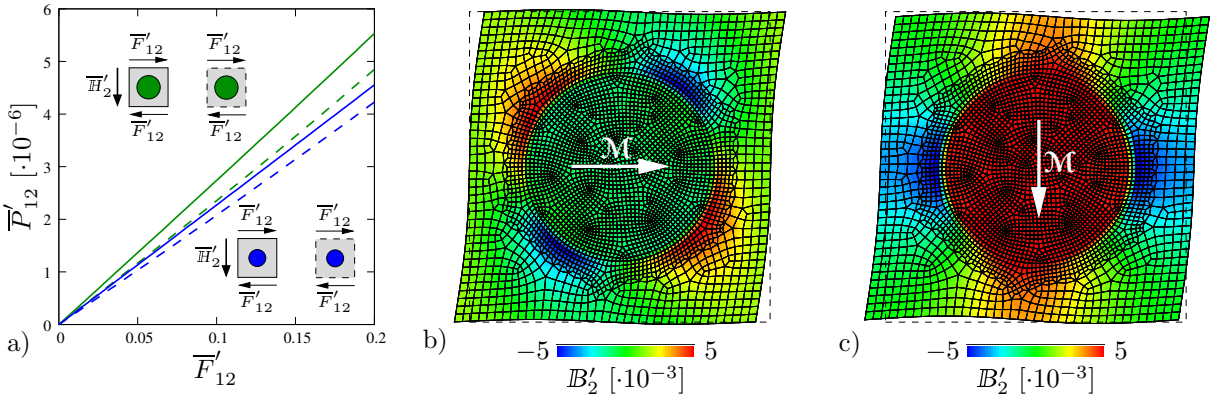

Figure 9.6: *Magnetic stiffening effect for different volume fractions.* a) For 20% (blue) and 30% (green) volume fraction of a circular magnetic inclusion the stress-strain response is compared for shear loading $\overline{F}'_{12}$ (dotted lines) and pre-applied magnetic loading $\overline{\mathbb{H}}'_2$ followed by shear loading (full lines). Increased mechanical stiffness results from particle-particle forces and magnetically induced pre-compression. b) Under shear loading the magnetization direction stays aligned with the easy axis in the inital horizontal direction. c) Pre-applied magnetic loading rotates the magnetization and induces compression. Deformed state of the micro-structure for b) mechanical and c) combined magnetic and mechanical loading is displayed.

stiff magnetic particle. In comparison, we analyze the homogenized response after a pre-applied magnetic loading of up to $\overline{\mathbb{H}}'_2 = \overline{\mathbb{H}}'_c = \{\, 0.00223, 0.00275 \,\}$ [–] for 20 and 30% volume fraction, respectively. Under that field strength, magnetic saturation is achieved, and no further deformation for higher fields is expected, as shown in Figure 9.3c. Note that the magnetic field is kept constant during the subsequent shear loading. The full green and blue lines in Figure 9.6a reveal the stiffer homogenized response with a pre-applied magnetic field, while a higher volume fraction naturally leads to a more pronounced stiffening effect due to higher magneto-mechanical interactions. The tuning of damping devices by an applied magnetic field works based on the particle-particle forces under an applied magnetic field. The attractive force impede a mechanical shear deformation while also compressing the material and thereby yielding a stiffer response. Figure 9.6b shows the magnetic induction $\mathbb{B}'_2$, that is close to zero, as the initial magnetizations, aligned with the easy axis, is pointing in horizontal direction. The deformed state of the $\mathcal{RVE}$ is displayed. Note, that $\mathbb{B}'_1$ is more developed due to the magnetic self field of the particle however not plotted here. In contrast, the magnetic induction after magnetic loading in Figure 9.6c displays the maximum field evolving in between vertically adjacent particles and within the particle due to the now rotated magnetization. Again, the deformed state is displayed, where a slight compressive mode can be seen relative to the deformed state of Figure 9.6b. The dotted lines indicate the undeformed micro-structure in both cases.

Chapter 10

Conclusion

In this work, magneto-electro-mechanical coupling phenomena were investigated, with a focus on the variational treatment of both, energetic minimizers and mixed energy-enthalpy saddle-point structures. The material modelling is based on a phenomenological ansatz, as well as on a micro-magneto-electro-mechanical motivated approach, that captures the evolution and motion of magnetic and electric domains on the microscale with a phase-field model. For that, the work is divided into four main parts. Part I recapitulates the foundations of multiscale variational magneto-electro-mechanics and stability analysis. In Part II the minimization and mixed principles are compared and difficulties in either formulation are pointed out. Part III provides energetic criteria for an accompanying multiscale stability analysis. In Part IV the effective material response is related to particle interactions on the microscale, where the respective electric and magnetic properties come from the domain structure.

Starting from the canonical minimization problem with magnetic and electric vector potentials, the difficulties of the non-uniqueness of the potentials with respect to added gradient fields was shown. Two different solution methods, a Coulomb gauging and a Hu-Washizu finite element formulation were presented. Both approaches are able to improve the formulation. The Coulomb gauge (CG) method however is subjected to a tedious fitting of the related penalty parameter and has additional drawbacks in terms of solution accuracy at interfaces of two different materials. A reduced integration of the added Coulomb gauge penalty energy term was proposed and showed to improve the performance of the CG method. While the Hu-Washizu (HW) formulation gives good results, the numerical implementation is non-standard. It was shown, that the reduced integrated CD method coincides with the HW formulation and therefore appears to be the ansatz of choice when dealing with vector potential formulations.

On the basis of a local convexity condition, as well as the notion of quasi- and rank-one convexity, suitable instability checks for structural and material instabilities on the macro- and micro-structure were developed for coupled finite magneto-electro-mechanics. The criteria demand positive definiteness of the assembled stiffness matrix or the local tangent, respectively. A reformulation of the checks to a mixed energy-enthalpy formulation, achieved by a Legendre-Fenchel transformation in the magnetic and electric slots,

show a remarkable result. Due to the elimination equation of the Legendre transformation, a diagonal structure of the stiffness matrices appears. This simplifies the analysis of instability points in terms of numerical costs and convenience. The capabilities of the formulated multiscale stability criteria were displayed in analytical and numerical two-scale examples.

To relate the effective material response on the evolution and motion of magnetic and electric domains on the microscale, the powerful phase-field model was employed. Here, the magnetization director and polarization vector are the respective order parameters. To ensure the physical unity constraint on the magnetization, a staggered solution algorithm for the finite element computation is used on the micro-structure. A magnetic predictor step computes the new direction of the magnetization, while keeping all other degrees of freedom fixed. A proceeding normalization routine scales that direction to unit length in a magnetic corrector step. With this updated solution, the other degrees of freedoms are computed. Homogenized stresses and moduli are computed by averaging theorems stemming from a generalized Hill-Mandel homogeneity condition and enable a macroscopic equilibrium condition. The two-scale algorithmic solution scheme provides the basis for the investigations of the influence of particular micro-structures on the overall material response. In especially, the shape and volume fraction of electric and magnetic inclusions, as well as the general orientation of the particles within the composite material are of interest. It was shown, that depending on the geometry and arrangement of the particles, different macroscopic deformations can be obtained. This enables the optimization of the underlying micro-structure for specific macroscopic response.

Up to now, the proposed homogenization techniques and material modelling are of rather academical nature. A comparison to experiments in the field of magneto-electro-mechanics would be of great benefit in the validation process of the tendencies obtained in the numerical simulations. As possible extensions to the presented work, further multiscale stability analyses based on the Bloch-Floquet wave theory can be considered. A first step in this direction for electro-mechanical composites can be found in the recent work Polukhov et al. [196]. Furthermore, the possible exploitation of instabilities for increased coupling behavior in magneto-electro-mechanics is a promising field. The proposed techniques and stability criteria for the FE^2 setting can be helpful tools for this endeavor. An extension of the phase-field approach of micro-electro- and magneto-mechanics to combined magneto-electro-elastic three-field composites where both, the evolution of electric and magnetic domains are covered, is a logical expansion of the presented two-scale variational formulation.

Bibliography

[1] Abbundi, R.; Clark, A. [1977]: *Anomalous thermal expansion and magnetostriction of single crystal $tb_{27}dy_{73}fe_2$.* IEEE Transactions on Magnetics, 13(5): 1519–1520.

[2] Abeyaratne, R.; Triantafyllidis, N. [1984]: *An investigation of localization in a porous elastic material using homogenization theory.* Journal of Applied Mechanics, 51: 481–486.

[3] Anthoine, A. [1995]: *Derivation of the in-plane elastic characteristics of masonry thorugh homogenization theory.* International Journal of Solids and Structures, 32: 137–163.

[4] Antman, S. S. [1983]: *Regular and singular problems for large elastic deformations of tubes, wedges, and cylinders.* Archive for Rational Mechanics and Analysis, 83(1): 1–52.

[5] Başar, Y.; Weichert, D. [2000]: *Nonlinear Continuum Mechanics of Solids.* Springer.

[6] Baesu, E. [2003]: *On electroacoustic energy flux.* Zeitschrift für angewandte Mathematik und Physik, 54(6): 1001–1009.

[7] Baesu, E.; Fortune, D.; Soós, E. [2003]: *Incremental behaviour of hyperelastic dielectrics and piezoelectric crystals.* Zeitschrift für angewandte Mathematik und Physik, 54(1): 160–178.

[8] Ball, J. M. [1977]: *Constitutive inequalities and existence theorems in nonlinear elastostatics.* In Knops, R. J. (Editor), *Nonlinear Analysis and Mechanics: Heriot-Watt Symposium.* Pitman Publishing Ltd.

[9] Ball, J. M. [1977]: *Convexity conditions and existence theorems in nonlinear elasticity.* Archive of Rational Mechanics and Analysis, 63: 337–403.

[10] Bar-Cohen, Y. [2002]: *Electro-active polymers: Current capabilities and challenges.* Proceedings of the SPIE Smart Structures and Materials Symposium, 4695-02: 1–6.

[11] Bar-Cohen, Y.; Zhang, Q. [2008]: *Electro-active polymer actuators and sensors.* MRS Bulletin, 33: 173–181.

[12] Bassiouny, E.; Maugin, G. A. [1989]: *Thermodynamical formulation for coupled electromechanical hysteresis effects—III. Parameter identification.* International Journal of Engineering Science, 27(8): 975–987.

[13] Bassiouny, E.; Maugin, G. A. [1989]: *Thermodynamical formulation for coupled electromechanical hysteresis effects—IV. Combined electromechanical loading.* International Journal of Engineering Science, 27(8): 989–1000.

[14] Bassiouny, E.; Ghaleb, A. F.; Maugin, G. A. [1988]: *Thermodynamical*

formulation for coupled electromechanical hysteresis effects—I. Basic equations. International Journal of Engineering Science, 26(12): 1279–1295.

[15] Bassiouny, E.; Ghaleb, A. F.; Maugin, G. A. [1988]: *Thermodynamical formulation for coupled electromechanical hysteresis effects—II. Poling of ceramics.* International Journal of Engineering Science, 26(12): 1297–1306.

[16] Bednarek, S. [1999]: *The giant magnetostriction in ferromagnetic composites within an elastomer matrix.* Applied Physics A, 68(1): 63–67.

[17] Bellan, C.; Bossis, G. [2002]: *Field dependence of viscoelastic properties of MR elastomers.* International Journal of Modern Physics B, 16(17–18): 2447–2453.

[18] Bertoldi, K.; Boyce, M. [2008]: *Wave propagation and instabilities in monolithic and periodically structured elastomeric materials undergoing large deformations.* Physical Review B, 78.

[19] Bertoldi, K.; Gei, M. [2011]: *Instabilities in multilayered soft dielectrics.* Journal of the Mechanics and Physics of Solids, 59: 18–42.

[20] Bertoldi, K.; Boyce, M.; Deschanel, S.; Prange, S.; Mullin, T. [2008]: *Mechanics of deformation-triggered pattern transformations and superelastic behavior in periodic elastomeric structures.* Journal of the Mechanics and Physics of Solids, 56: 2642–2668.

[21] Bertram, H. [1994]: *Theory of magnetic recording.* Cambridge University Press.

[22] Biot, M. [1965]: *Mechanics of Incremental Deformations.* John Wiley & Sons, Inc., New York.

[23] Biro, O.; Preis, K. [1989]: *On the use of the magnetic vector potential in the finite element analysis of three-dimensional eddy currents.* IEEE Transactions on Magnetics, 25(4): 3145–3159.

[24] Biro, O.; Preis, K.; Richter, K. R. [1996]: *On the use of the magnetic vector potential in the nodal and edge finite element analysis of 3d magnetostatic problems.* IEEE Transactions on Magnetics, 32(3): 651–654.

[25] Biro, O.; Paul, C.; Preis, K.; Russenschuck, S. [1999]: *A/sub r/ formulation using edge elements, for the calculation of 3-d fields in superconducting magnets.* IEEE Transactions on Magnetics, 35(3): 1391–1393.

[26] Boczkowska, A.; Awietjan, S. [2012]: *Microstructure and properties of magnetorheological elastomers.* In *Advanced Elastomers - Technology, Properties and Applications.* InTech.

[27] Böse, H.; Rabindranath, R.; Ehrlich, J. [2012]: *Soft magnetorheological elastomers as new actuators for valves.* Journal of Intellegent Material Systems and Structures, 14: 743–765.

[28] Brassart, L.; Stainier, L.; Doghri, I.; Delannay, L. [2011]: *A variational formulation for the incremental homogenization of elasto-plastic composites.* Journal of the Mechanics and Physics of Solids, 59(12): 2455–2475.

[29] Brigadnov, A. L.; Dorfmann, A. [2003]: *Mathematical modeling of magneto-sensitive elastomers.* International Journal of Solids and Structures, 40: 4659–4674.

[30] Brown, Jr., W. F. [1951]: *Electric and magnetic forces: A direct calculation. i.* American Journal of Physics, 19: 290–304.

[31] Brown, Jr., W. F. [1951]: *Electric and magnetic forces: A direct calculation. ii.* American Journal of Physics, 19: 333–350.

[32] Brown, Jr., W. F. [1962]: *Magnetoelastic Principles in Ferromagnetism*, Vol. 1. North-Holland Publishing Company.

[33] Brown, Jr., W. F. [1963]: *Micromagnetics*. Interscience Publishers.
[34] Brown, Jr., W. F. [1966]: *Magnetoelastic Interactions*, Vol. 9 of *Tracts in Natural Philosophy*. Springer-Verlag.
[35] Buryachenko, V. A. [2007]: *Micromechanics of Heterogeneous Materials*. Springer-Verlag.
[36] Bustamante, R.; Dorfmann, A.; Ogden, R. W. [2007]: *On variational formulations in nonlinear magnetoelastostatics*. Mathematics and Mechanics of Solids, 13(8): 725–745.
[37] Bustamante, R.; Dorfmann, A.; Ogden, R. W. [2009]: *Nonlinear electroelastostatics: a variational framework*. Zeitschrift für angewandte Mathematik und Physik, 60: 154–177.
[38] Cao, C.; Zhao, X. [2013]: *Tunable stiffness of electrorheological elastomers by designing mesostructures*. Applied Physics Letters, 103(4): 041901.
[39] Capriz, G. [1989]: *Continua with Microstructure*. Springer.
[40] Capriz, G.; Podio-Guidugli, P.; Williams, W. [1982]: *On balance equations of materials with affine structure*. Meccanica, 17: 80–84.
[41] Chatzigeorgiou, G.; Javili, A.; Steinmann, P. [2014]: *Unified magnetomechanical homogenization framework with application to magnetorheological elastomers*. Mathematics and Mechanics of Solids, 19: 193–211.
[42] Chau, K. H.; Wong, Y. W.; Shin, F. G. [2009]: *Magnetoelectric effect of polymer electrolyte composites with terfenol-d and lead zirconate titanate inclusions*. Applied Physics Letters, 94(202902): 1–3.
[43] Ciarlet, P. [1988]: *Mathematical Elasticity*. Elsevier Science Publishers B.V., Amsterdam.
[44] Claeyssen, F.; Lhermet, N.; Le Letty, R.; Bouchilloux, P. [1997]: *Actuators, transducers and motors based on giant magnetostrictive materials*. Journal of alloys and compounds, 258(1-2): 61–73.
[45] Clark, A.; Restorff, J.; Wun-Fogle, M.; Hathaway, K.; Lograsso, T.; Huang, M.; Summers, E. [2007]: *Magnetostriction of ternary fe–ga–x (x= c, v, cr, mn, co, rh) alloys*. Journal of applied physics, 101(9): 09C507.
[46] Coleman, B. D.; Noll, W. [1959]: *On the thermostatics of continuous media*. Archive of Rational Mechanics and Analysis, 4: 97–128.
[47] Dacorogna, B. [1989]: *Direct methods in the calculus of variations*. Springer.
[48] Danas, K. [2017]: *Effective response of classical, auxetic and chiral magnetoelastic materials by use of a new variational principle*. Journal of Mechanics and Physics of Solids, 105: 25–53.
[49] Danas, K.; Kankanala, S. V.; Triantafyllidis, N. [2012]: *Experiments and modeling of iron-particle-filled magnetorheological elastomers*. Journal of the Mechanics and Physics of Solids, 60: 120–138.
[50] Davis, L. C. [1999]: *Model of magnetorheological elastomers*. Journal of Applied Physics, 85(6): 3348–3351.
[51] deBotton, G.; Tevet-Deree, L.; Socolsky, E. [2007]: *Electroactive heterogeneous polymers: analysis and applications to laminated composites*. Mechanics of Advanced Materials and Structures, 14: 13–22.
[52] Demerdash, N.; Wang, R. [1990]: *Theoretical and numerical difficulties in 3-d vector potential methods in finite element magnetostatic computations*. IEEE Transactions on Magnetics, 26(5): 1656–1658.

[53] DeSimone, A.; James, R. D. [2002]: *A constrained theory of magnetoelasticity.* Journal of the Mechanics and Physics of Solids, 50: 283–320.

[54] Destrade, M.; Ogden, R. [2011]: *On magneto-acoustic waves in finitely deformed elastic solids.* Mathematics and Mechanics of Solids, 16(6): 594–604.

[55] Dorfmann, A.; Ogden, R. [2010]: *Nonlinear electroelastostatics: Incremental equations and stability.* International Journal of Engineering Science, 48: 1–14.

[56] Dorfmann, A.; Ogden, R. W. [2003]: *Magnetoelastic modelling of elastomers.* European Journal of Mechanics A/Solids, 22: 497–507.

[57] Dorfmann, A.; Ogden, R. W. [2004]: *Nonlinear magnetoelastic deformations of elastomers.* Acta Mechanica, 167(1–2): 13–28.

[58] Dorfmann, A.; Ogden, R. W. [2004]: *Nonlinear magnetoelastic deformations.* The Quaterly Journal of Mechanics and Applied Mathematics, 57(4): 599–622.

[59] Dorfmann, A.; Ogden, R. W. [2005]: *Nonlinear electroelasticity.* Acta Mechanica, 174: 167–183.

[60] Dorfmann, A.; Ogden, R. W.; Saccomandi, G. [2005]: *The effect of rotation on the nonlinear magnetoelastic response of a circular cylindrical tubee.* International Journal of Solids and Structures, 42: 3700–3715.

[61] Dyke, S.; Spencer Jr, B.; Sain, M.; Carlson, J. [1996]: *Seismic response reduction using magnetorheological dampers.* IFAC Proceedings Volumes, 29(1): 5530–5535.

[62] Eerenstein, W.; Mathur, N. D.; Scott, J. F. [2006]: *Multiferroic and magnetoelectric materials.* Nature, 442: 759–765.

[63] Eringen, A. C. [1963]: *On the foundations of electroelastostatics.* International Journal of Engineering Science, 1(1): 127–153.

[64] Eringen, A. C.; Maugin, G. A. [1990]: *Electrodynamics of Continua I: Foundations and Solid Media.* Springer-Verlag.

[65] Eringen, A. C.; Maugin, G. A. [1990]: *Electrodynamics of Continua II: Fluid and Complex Media.* Springer-Verlag.

[66] Ethiraj, G. [2014]: *Computational Modeling of Ferromagnetics and Magnetorheological Elastomers.* Report No. I-33, Institute of Applied Mechanics (CE) Chair I, University of Stuttgart.

[67] Etier, M.; Shvartsman, V.; Gao, Y.; Landers, J.; Wende, H.; Lupascu, D. [2012]: *Magnetoelectric effect in (0-3) $cofe_2o_4$-$batio_3$(20/80) composite ceramics prepared by the organosol route.* Ferroelectrics, 448: 77–85.

[68] Fernandes, P.; Perugia, I. [2001]: *Vector potential formulation for magnetostatics and modeling of permanent magnets.* IMA Journal of Applied Mathematics, 66: 293–318.

[69] Feyel, F.; Chaboche, J.-L. [2000]: *FE^2 multiscale approach for modelling the elastoviscoplastic behaviour of long fibre SiC/Ti composite materials.* Computer Methods in Applied Mechanics and Engineering, 183: 309–330.

[70] Frémond, M. [2002]: *Non-Smooth Thermomechanics.* Springer.

[71] Galipeau, E.; Ponte Castañeda, P. [2012]: *The effect of particle shape and distribution on the macroscopic behavior of magnetoelastic composites.* International Journal of Solids and Structures, 49: 1–17.

[72] Galipeau, E.; Ponte Castañeda, P. [2013]: *Giant field-induced strains in magnetoactive elastomer composites.* Proceedings of the Royal Society of London A, 469.

[73] Geers, M. G. D.; Kouznetsova, V. G.; Brekelmans, W. A. M. [2010]: *Multi-scale computational homogenization: Trends and challenges.* Journal of Computational and Applied Mathematics, 234: 2175–2182.

[74] Geymonat, G.; Müller, S.; Triantafyllidis, N. [1993]: *Homogenization of nonlinearly elastic materials, microscopic bifurcation and macroscopic loss of rank-one convexity.* Archive of Rational Mechanics and Analysis, 122: 231–290.

[75] Gilbert, T. L. [2004]: *A phenomenological theory of damping in ferromagnetic materials.* IEEE Trans. Magn., 40: 3443–3449.

[76] Ginder, J. M.; Clark, S. M.; Schlotter, W. F.; Nichols, M. E. [2002]: *Magnetostrictive phenomena in magnetorheological elastomers.* International Journal of Modern Physics B, 16: 2412–2418.

[77] Goll, D.; Kronmüller, H. [2000]: *High-performance permanent magnets.* Naturwissenschaften, 87(10): 423–438.

[78] Greaves, S. [2008]: *Micromagnetic simulations of magnetic recording media.* In *High Performance Computing on Vector Systems 2007*, pp. 229–244. Springer.

[79] Griffiths, D. J. [2012]: *Introduction to Electrodynamics.* Addison-Wesley, 4th Edition.

[80] Gurtin, M. E. [1981]: *An Introduction to Continuum Mechanics*, Vol. 158 of *Mathematics in Science and Engineering.* Academic Press.

[81] Gurtin, M. E.; Fried, E.; Anand, L. [2010]: *The Mechanics and Thermodynamics of Continua.* Cambridge University Press.

[82] Hadamard, J. [1903]: *Leçons sur la propagation des ondes et les équations de l'hydrodynamique.* Hermann, Paris.

[83] Halphen, B.; Nguyen, Q. S. [1975]: *Sur les matéraux standards généralisés.* Journal de Mécanique, 40: 39–63.

[84] Han, Y.; Hong, W.; L.E., F. [2013]: *Field-stiffening effect of magneto-rheological elastomers.* International Journal of Solids and Structures, 50: 2281–2288.

[85] Hashin, Z. [1983]: *Analysis of composite materials – A survey.* ASME Journal of Applied Mechanics, 50: 481–505.

[86] Hashin, Z.; Shtrikman, S. [1963]: *A variational approach to the theory of the elastic behaviour of multiphase materials.* Journal of the Mechanics and Physics of Solids, 11: 127–140.

[87] Haupt, P. [2002]: *Continuum Mechanics and Theory of Materials.* Springer.

[88] Hill, R. [1950]: *The Mathematical Theory of Plasticity.* Oxford University Press.

[89] Hill, R. [1957]: *On uniqueness and stability in the theory of finite elastic strains.* Journal of the Mechanics and Physics of Solids, 5: 229–241.

[90] Hill, R. [1962]: *Acceleration waves in solids.* Journal of the Mechanics and Physics of Solids, 10: 1–16.

[91] Hill, R. [1963]: *Elastic properties of reinforced solids: Some theoretical principles.* Journal of the Mechanics and Physics of Solids, 11: 357–372.

[92] Hill, R. [1965]: *A self-consistent mechanics of composite materials.* Journal of the Mechanics and Physics of Solids, 13: 213–222.

[93] Hill, R. [1972]: *On constitutive macro-variables for heterogeneous solids at finite strain.* Proceedings of the Royal Society of London (Series A), 326: 131–147.

[94] Hill, R. [1984]: *On macroscopic effects of heterogeneity in elastoplastic media at finite strain.* Mathematical Proceedings of the Cambridge Philosophical Society, 95(3): 481–494.

[95] Holzapfel, G. A. [2000]: *Nonlinear solid mechanics*. John Wiley & Sons.
[96] Hu, R.; Soh, A.-K.; Zheng, G.-P.; Ni, Y. [2006]: *Micromagnetic modeling studies on the effects of stress on magnetization reversal and dynamic hysteresis*. Journal of Magnetism and Magnetic Materials, 301(2): 458–468.
[97] Huber, J. E.; Fleck, N. A. [2001]: *Multi-axial electrical switching of a ferroelectric: Theory versus experiment*. Journal of Mechanics and Physics of Solids, 49: 785–811.
[98] Hubert, A.; Schäfer, R. [2001]: *Magnetic Domains*. Springer-Verlag, New York.
[99] Hutter, K.; Ven, A. A. F. van de ; Ursescu, A. [2006]: *Electromagnetic Field Matter Interactions in Thermoelastic Solids and Viscous Fluids*, Vol. 710 of *Lecture Notes in Physics*. Springer-Verlag, Berlin, Heidelberg.
[100] Irodov, I. E. [1986]: *Basic laws of electromagnetism*. CBS Publishers & Distributors.
[101] Jackson, J. D. [1999]: *Classical Electrodynamics*. John Wiley & Sons, 3rd Edition.
[102] Jaffe, B.; Cook, W. R.; Jaffe, H. [1971]: *Piezoelectric Ceramics*. Academic Press.
[103] Javili, A.; Chatzigeorgiou, G.; Steinmann, P. [2013]: *Computational homogenization in magnetomechanics*. International Journal of Solids and Structures, 50: 4197–4216.
[104] Jiménez, S. M. A.; McMeeeking, R. M. [2013]: *Deformation dependent dielectric permittivity and its effect on actuator performance and stability*. International Journal of Non-Linear Mechanics, 57: 183–191.
[105] Jolly, M. R.; Carlson, D.; Muñoz, B. C.; Bullions, T. A. [1996]: *The magnetoviscoelastic response of elastomer composites consisting of ferrous particles embedded in a polymer matrix*. Journal of Intelligent Material Systems and Structures, 7: 613–612.
[106] Kalina, K.; Metsch, P.; Kästner, M. [2016]: *Microscale modeling and simulation of magnetorheological elastomers at finite strains: A study on the influence of mechanical preloads*. International Journal of Solids and Structures, 102: 286–296.
[107] Kallio, M. [2005]: *The Elastic and Damping Properties of Magnetorheological Elastomers*. Ph.D. Thesis, Tampere University of Technology.
[108] Kaltenbacher, M.; Reitzinger, S. [2002]: *Appropriate finite-element formulations for 3-d electromagnetic-field problems*. IEEE Transactions on Magnetics, 38(2): 513–516.
[109] Kamlah, M. [2001]: *Ferroelectric and ferroelastic piezoceramics – Modelling of electromechanical hysteresis phenomena*. Continuum Mechanics and Thermodynamics, 13: 219–268.
[110] Kankanala, S. V.; Triantafyllidis, N. [2004]: *On finitely strained magnetorheological elatomers*. Journal of the Mechanics and Physics of Solids, 52: 2869–2908.
[111] Keip, M.-A.; Rambausek, M. [2016]: *A multiscale approach to the computational characterization of magnetorheological elastomers*. International Journal for Numerical Methods in Engineering, 107(4): 338–360.
[112] Keip, M.-A.; Rambausek, M. [2017]: *Computational and analytical investigations of shape effects in the experimental characterization of magnetorheological elastomers*. International Journal of Solids and Structures, 121: 1–20.
[113] Keip, M.-A.; Schröder, J. [2018]: *Multiscale modeling of electroactive polymer*

composites. In *Ferroic Functional Materials*, pp. 263–285. Springer.

[114] Keip, M.-A.; Sridhar, A. [2019]: *A variationally consistent phase-field approach for micro-magneto domain evolution at finite deformations*. Journal of the Mechanics and Physics of Solids, 125: 805–824.

[115] Keip, M.-A.; Steinmann, P.; Schröder, J. [2014]: *Two-scale computational homogenization of electro-elasticity at finite strains*. Computer Methods in Applied Mechanics and Engineering, 278: 62–79.

[116] Keip, M.-A.; Schrade, D.; Thai, H.; Schröder, J.; Svendsen, B.; Müller, R.; Gross, D. [2015]: *Coordinate-invariant phase field modeling of ferroelectrics, part ii: Application to composites and poly-crystals*. GAMM-Mitteilungen, 38(1): 115–131.

[117] Keplinger, C.; T., L.; Baumgartner, R.; Suo, Z.; Bauer, S. [2012]: *Harnessing snap-through instability in soft dielectrics to achieve giant voltage-triggered deformation*. Soft Matter, 8(285).

[118] Klassen, M.; Xu, B. X.; Klinkel, S.; Müller, R. [2012]: *Material modeling and microstructural optimization of dielectric elastomer actuators*. Technische Mechanik, 32(1): 38–52.

[119] Klinkel, S. [2006]: *A phenomenological constitutive model for ferroelastic and ferroelectric hysteresis effects in ferroelectric ceramics*. International Journal of Solids and Structures, 43: 7197–7222.

[120] Kornbluh, R.; Pelrine, R.; Joseph, J. [1995]: *Elastomeric dielectric artificial muscle actuators for small robots*. Proceedings of the Materials Research Society.

[121] Kornbluh, R.; Pelrine, R.; Joseph, J.; Heydt, R.; Pei, Q.; Chiba, S. [1999]: *High-field electrostriction of elastomeric polymer dielectrics for actuation*. Proceedings of the SPIE: Smart Structures and Materials, 3669: 149–161.

[122] Kouznetsova, V.; Geers, M. G. D.; Brekelmans, W. A. M. [2002]: *Multi-scale constitutive modelling of heterogeneous materials with a gradient-enhanced computational homogenization scheme*. International Journal for Numerical Methods in Engineering, 54: 1235–1260.

[123] Kovetz, A. [2000]: *Electromagnetic Theory*. Oxford University Press.

[124] Krawietz, A. [1975]: *A comprehensive constitutive inequality in finite elastic strain*. Archive for Rational Mechanics and Analysis, 58(2): 127–149.

[125] Krishnaprasad, P. S.; Tan, X. [2001]: *Cayley transforms in micromagnetics*. Physica B: Condensed Matter, 306(1-4): 195– 99.

[126] Labusch, M.; Etier, M.; Lupascu, D. C.; Schröder, J.; Keip, M.-A. [2014]: *Product properties of a two-phase magneto-electric composite: Synthesis and numerical modeling*. Computational Mechanics.

[127] Lahellec, N.; Suquet, P. [2007]: *On the effective behavior of nonlinear inelastic composites: I. Incremental variational principles*. Journal of the Mechanics and Physics of Solids, 55(9): 1932–1963.

[128] Lanczos, C. [1986]: *The Variational Principles of Mechanics*. Dover Publications Inc., New York.

[129] Landau, L. D.; Lifshitz, E. M. [1935]: *On the theory of the dispersion of magnetic permeability in ferromagnetic bodies*. Physikalische Zeitschrift der Sowjetunion, 8: 153–169.

[130] Landau, L. D.; Lifshitz, E. M. [1960]: *Electrodynamics of Continuous Media*. Pergamon Press.

[131] Landis, C. M. [2002]: *Fully coupled, multi-axial, symmetric constitutive laws for polycrystalline ferroelectric ceramics*. Journal of Mechanics and Physics of Solids, 50: 127–152.

[132] Landis, C. M. [2002]: *A new finite-element formulation for electromechanical boundary value problems*. International Journal for Numerical Methods in Engineering, 55: 613–628.

[133] Landis, C. M. [2008]: *A continuum thermodynamics formulation for micromagnetomechanics with applications to ferromagnetic shape memory alloys*. Journal of the Mechanics and Physics of Solids, 56: 3059–3076.

[134] Lefèvre, V.; Lopez-Pamies, O. [2017]: *Nonlinear electroelastic deformations of dielectric elastomer composites: Ii-non-gaussian elastic dielectrics*. Journal of the Mechanics and Physics of Solids, 99: 438–470.

[135] Li, T.; Keplinger, C.; Baumgartner, R.; Bauer, S.; Yang, W.; Suo, Z. [2013]: *Giant voltage-induced deformation in dielectric elastomers near the verge of snap-through instability*. Journal of the Mechanics and Physics of Solids, 61: 611–628.

[136] Liang, C.-Y.; Keller, S.; Sepulveda, A.; Bur, A.; Sun, W.-Y.; Wetzlar, K.; Carman, G. [2014]: *Modeling of magnetoelastic nanostructures with a fully coupled mechanical-micromagnetic model*. Nanotechnology, 25(43): 435701.

[137] Lines, M. E.; Glass, A. M. [1977]: *Principles and Applications of Ferroelectrics and Related Materials*. Clarendon Press.

[138] Linnemann, K.; Klinkel, S.; Wagner, W. [2009]: *A constitutive model for magnetostrictive and piezoelectric materials*. International Journal of Solids and Structures, 46: 1149–1166.

[139] Mandel, J. [1972]: *Plasticité clasique et viscoplasticité*. In *CISM Courses and Lectures, No. 97*. Springer.

[140] Marauska, S.; Jahns, R.; Kirchhof, C.; Claus, M.; Quandt, E.; Knöchel, R.; Wagner, B.: *Packaged mems magnetic field sensor based on magnetoelectric composites*.

[141] Marcellini, P. [1978]: *Periodic solutions and homogenization of nonlinear variational problems*. Annali Mat. Pura Appl., 117: 139–152.

[142] Marsden, J. E.; Hughes, T. J. R. [1983]: *Mathematical foundations of elasticity*. Prentice-Hall, Englewood Cliffs, New Jersey.

[143] Martin, J. B. [1975]: *Plasticity. Fundamentals and General Results*. MIT Press, Cambridge.

[144] Martins, P.; Lanceros-Méndez, S. [2013]: *Polymer-based magnetoelectric materials*. Advanced Functional Materials, 23: 3371–3385.

[145] Maugin, G. A. [1988]: *Continuum Mechanics of Electromagnetic Solids*. Elsevier.

[146] Maugin, G. A. [1990]: *Internal variables and dissipative structures*. Journal of Non-Equilibrium Thermodynamics, 15: 173–192.

[147] Maugin, G. A.; Epstein, M. [1991]: *The electroelastic energy-momentum tensor*. Proceedings of the Royal Society A, 433: 299–312.

[148] Maugin, G. A.; Eringen, A. C. [1971]: *Deformable magnetically saturated media. i. field equations*. Journal of Mathematical Physics, 13: 143 – 155.

[149] Maugin, G. A.; Muschik, W. [1994]: *Thermodynamics with internal variables part i. general concepts*. Journal of Non-Equilibrium Thermodynamics, 19: 217–249.

[150] Maugin, G. A.; Muschik, W. [1994]: *Thermodynamics with internal variables*

part ii. applications. Journal of Non-Equilibrium Thermodynamics, 19: 250–289.

[151] McMeeking, R. M.; Landis, C. M. [2002]: *A phenomenological multi-axial constitutive law for switching in polycrystaline ferroelectric ceramics.* International Journal of Engineering Science, 40: 1553–1577.

[152] McMeeking, R. M.; Landis, C. M. [2005]: *Electrostatic forces and stored energy for deformable dielectric materials.* Journal of Applied Physics, 72: 581–590.

[153] Metsch, P.; Kalina, K.; Spieler, C.; Kästner, M. [2016]: *A numerical study on magnetostrictive phenomena in magnetorheological elastomers.* Computational Materials Science, 124: 364–374.

[154] Meyberg, K.; Vachenauer, P. [2006]: *Höhere Mathematik 2: Differentialgleichungen, Funktionentheorie, Fourier-Analysis, Variationsrechnung.* Springer-Verlag.

[155] Michel, J. C.; Moulinec, H.; Suquet, P. [1999]: *Effective properties of composite materials with periodic microstructure: A computational approach.* Computer Methods in Applied Mechanics and Engineering, 172: 109–143.

[156] Michel, J. C.; Lopez-Pamies, O.; Ponte Castañeda, P.; Triantafyllidis, N. [2007]: *Microscopic and macroscopic instabilities in finitely strained porous elastomers.* Journal of the Mechanics and Physics of Solids, 55: 900–938.

[157] Michel, J. C.; Lopez-Pamies, O.; Ponte Castañeda, P.; Triantafyllidis, N. [2010]: *Microscopic and macroscopic instabilities in finitely strained fiber-reinforced elastomers.* Journal of the Mechanics and Physics of Solids, 58: 1776–1803.

[158] Miehe, C. [2002]: *Strain-driven homogenization of inelastic microstructures and composites based on an incremental variational formulation.* International Journal for Numerical Methods in Engineering, 55: 1285–1322.

[159] Miehe, C. [2011]: *A multi-field incremental variational framework for gradinet-type standard dissipative solids.* Journal of Mechanics and Physics of Solids, 59(4): 898–923.

[160] Miehe, C. [2013]: *Geometrical methods of nonlinear continuum mechanics and continuum thermodynamics.* Lecture Notes.

[161] Miehe, C. [2014]: *Variational gradient plasticity at finite strains. Part I: Mixed potentials for the evolution and update problems of gradient-extended dissipative solids.* Computer Methods in Applied Mechanics and Engineering, 268: 677–703.

[162] Miehe, C. [2014]: *Theoretical and computer-oriented material theory.* Lecture Notes.

[163] Miehe, C.; Ethiraj, G. [2012]: *A geometrically consistent incremental variational formulation for phase field models in micromagnetics.* Computer Methods in Applied Mechanics and Engineering, 245: 331–347.

[164] Miehe, C.; Lambrecht, M. [2003]: *Analysis of micro-structure development in shearbands by energy relaxation of incremental stress potentials: Large-strain theory for standard dissipative materials.* International Journal for Numerical Methods in Engineering, 58: 1–41.

[165] Miehe, C.; Rosato, D. [2011]: *A rate-dependent incremental variational formulation of ferroelectricity.* International Journal of Engineering Science, 49: 466–496.

[166] Miehe, C.; Schröder, J. [1994]: *Post-critical discontinuous localization analysis of small-strain softening elastoplastic solids.* Archive of Applied Mechanic, 64: 267–285.

[167] Miehe, C.; Schotte, J.; Schröder, J. [1999]: *Computational micro-macro transitions and overall moduli in the analysis of polycrystals at large strains.* Computational Materials Science, 16: 372–382.

[168] Miehe, C.; Schröder, J.; Schotte, J. [1999]: *Computational homogenization analysis in finite plasticity. Simulation of texture development in polycrystalline materials.* Computer Methods in Applied Mechanics and Engineering, 171(3–4): 387–418.

[169] Miehe, C.; Schröder, J.; Becker, M. [2002]: *Computational homogenization analysis in finite elasticity: material instabilities on the micro- and macro-scales of periodic composites and their interaction.* Computer Methods in Applied Mechanics and Engineering, 191: 4971–5005.

[170] Miehe, C.; Kiefer, B.; Rosato, D. [2011]: *An incremental variational formulation of dissipative magnetostriction at the macroscopic continuum level.* International Journal of Solids and Structures, 48: 1846–1866.

[171] Miehe, C.; Rosato, D.; Kiefer, B. [2011]: *Variational principles in dissipative electro-magneto-mechanics: A framework for the macro-modeling of functional materials.* International Journal for Numerical Methods in Engineering, 86: 1225–1276.

[172] Miehe, C.; Zäh, D.; Rosato, D. [2012]: *Variational-based modeling of micro-electro-elasticity with electric field- and stress-driven domain evolution.* International Journal for Numerical Methods in Engineering, 91(2): 115–141.

[173] Miehe, C.; Vallicotti, D.; Zäh, D. [2015]: *Computational structural and material stability analysis in finite electro-elasto-statics of electro-active materials.* International Journal for Numerical Methods in Engineering, 102(10): 1605–1637.

[174] Miehe, C.; Vallicotti, D.; Teichtmeister, S. [2016]: *Homogenization and multiscale stability analysis in finite magneto-electro-elasticity. application to soft matter ee, me and mee composites.* Computer Methods in Applied Mechanics and Engineering, 300: 294–346.

[175] Morrey, C. B. [1952]: *Quasi-convexity and the lower semicontinuity of multiple integrals.* Pacific Journal of Mathematics, 2(1): 25–53.

[176] Moulson, A. J.; Herbert, J. M. [2003]: *Electroceramics: Materials, Properties, Applications.* John Wiley & Sons, 2nd Edition.

[177] Müller, R.; Xu, B.; Gross, D.; Lyschik, M. Schrade, D.; Klinkel, S. [2010]: *Deformable dielectrics - optimization of heterogeneities.* International Journal of Engineering Science, 48: 647–657.

[178] Müller, S. [1987]: *Homogenization of nonconvex integral functionals and cellular elastic materials.* Archive of Rational Mechanics and Analysis, 99: 189–212.

[179] Nan, C.-W.; Cai, N.; Liu, L.; Zhai, J.; Ye, Y.; Lin, Y. [2003]: *Coupled magnetic-electric properties and critical behavior in multiferroic particulate composites.* Journal of Applied Physics, 94(9): 5930–5936.

[180] Nan, C.-W.; Bichurin, M. I.; Dong, S.; Viehland, D.; Srinivasan, G. [2008]: *Multiferroic magnetoelectric composites: Historical perspective, status, and future directions.* Journal of Applied Physics, 103: 031101.

[181] Nédélec, J. C. [1980]: *Mixed finite elements in* $\mathcal{R}^3$. Numerische Mathematik, 35: 315–341.

[182] Nédélec, J. C. [1986]: *A new family of mixed finite elements in* $\mathcal{R}^3$. Numerische Mathematik, 50: 57–81.

[183] Nemat-Nasser, S.; Hori, M. [1999]: *Micromechanics: Overall properties of*

heterogeneous materials, Vol. 36 of *North-Holland series in Applied Mathematics and Mechanics*. Elsevier Science Publisher B. V., 2nd Edition.

[184] Nguyen, Q. [2000]: *Stability and Nonlinear Solid Mechanics*. John Wiley & Sons, LTD, Chichester.

[185] Ogden, R. W. [1984]: *Nonlinear Elastic Deformations*. John Wiley & Sons.

[186] Olabi, A.-G.; Grunwald, A. [2008]: *Design and application of magnetostrictive materials*. Materials & Design, 29(2): 469–483.

[187] Ortiz, M.; Stainier, L. [1999]: *The variational formulation of viscoplastic constitutive updates*. Computer Methods in Applied Mechanics and Engineering, 171: 419–444.

[188] Ortiz, M.; Leroy, Y.; Needleman, A. [1987]: *A finite element method for localized failure analysis*. Computer Methods in Applied Mechanics and Engineering, 61(2): 189–214.

[189] Pak, Y. E.; Herrmann, G. [1986]: *Conservation laws and the material momentum tensor for the elastic dielectric*. International Journal of Engineering Science, 24: 1365–1374.

[190] Pao, Y.-H. [1978]: *Electromagnetic forces in deformable continua*. In Nemat-Nasser, S. (Editor), *Mechanics today*, Vol. 4, chapter 4, pp. 209–305. Pergamon Press, New York.

[191] Pao, Y.-H.; Hutter, K. [1975]: *Electrodynamics for moving elastic solids and viscous fluids*. Proceedings of the IEEE, 63: 1011–1021.

[192] Pelrine, R.; Kornbluh, R. D.; Joseph, J. [1998]: *Electrostriction of polymer dielectrics with compliant electrodes as a means of actuation*. Sensors and Actuators A: Physical, 64: 77–85.

[193] Pelrine, R.; Kornbluh, R.; Joseph, J.; Heydt, R.; Pei, Q.; Chiba, S. [2000]: *High-field deformation of elastomeric dielectrics for actuators*. Materials Science and Engineering: C, 11(2): 89–100.

[194] Penfield, P.; Haus, H. A. [1967]: *Electrodynamics of Moving Media*. M.I.T. Press.

[195] Plante, J.-S.; Dubowsky, S. [2006]: *Large-scale failure modes of dielectric elastomer actuators*. International Journal of Solids and Structures, 43: 7727–7751.

[196] Polukhov, E.; Vallicotti, D.; Keip, M.-A. [2018]: *Computational stability analysis of periodic electroactive polymer composites across scales*. Computer Methods in Applied Mechanics and Engineering, 337: 165–197.

[197] Ponte Castañeda, P.; Galipeau, E. [2011]: *Homogenization-based constitutive models for magnetorheological elastomers at finite strain*. Journal of the Mechanics and Physics of Solids, 59: 194–215.

[198] Ponte Castañeda, P.; Siboni, M. H. [2012]: *A finite-strain constitutive theory for electro-active polymer composites via homogenization*. International Journal of Non-Linear Mechanics, 47: 293–306.

[199] Ponte Castañeda, P.; Suquet, P. [1997]: *Nonlinear composites*. Academic Press.

[200] Ponte Castañeda, P.; Suquet, P. [1997]: *Nonlinear composites*. Vol. 34 of *Advances in Applied Mechanics*, pp. 171–302. Elsevier.

[201] Reuss, A. [1929]: *Berechnung der Fließgrenze von Mischkristallen aufgrund der Plastizitätsbedingung für Einkristalle*. Zeitschrift für angewandte Mathematik und Mechanik, 9: 49–58.

[202] Rosato, D. [2010]: *On the Formulation and Numerical Implementation of Dissipative Electro-Mechanics at Large Strains.* Ph.D. Thesis, Institute of Applied Mechanics (CE), Chair I, University of Stuttgart.

[203] Rosato, D.; Miehe, C. [2014]: *Dissipative ferroelectricity at finite strains. variational principles, constitutive assumptions and algorithms.* International Journal of Engineering Science, 74: 163–189.

[204] Rudykh, S.; Bertoldi, K. [2013]: *Stability of anisotropic magnetorheological elastomers in finite deformations: A micromechanical approach.* Journal of the Mechanics and Physics of Solids, 61(4): 949–967.

[205] Rudykh, S.; deBotton, G. [2011]: *Stability of anisotropic electroactive polymers with application to layered media.* Zeitschrift f'ur angewandte Mathematik und Physik, 62(6): 1131–1142.

[206] Rudykh, S.; Bhattacharya, K.; deBotton, G. [2012]: *Snap-through actuation of thick-wall electroactive balloons.* International Journal of Non-Linear Mechanics, 47(2): 206–209.

[207] Rudykh, S.; Lewinstein, A.; Uner, G.; deBotton, G. [2013]: *Analysis of microstructural induced enhancement of electromechanical coupling in soft dielectrics.* Applied Physics Letters, 102: 151905.

[208] Rudykh, S.; Bhattacharya, K.; deBotton, G. [2014]: *Multiscale instabilities in soft heterogeneous dielectric elastomers.* Proceedings of the Royal Society A: Mathematical, Physical and Engineering Science, 470: 20130618.

[209] Sandlund, L.; Fahlander, M.; Cedell, T.; Clark, A.; Restorff, J.; Wun-Fogle, M. [1994]: *Magnetostriction, elastic moduli, and coupling factors of composite terfenol-d.* Journal of Applied Physics, 75(10): 5656–5658.

[210] Saxena, P.; Hossain, M.; Steinmann, P. [2013]: *A theory of finite deformation magneto-viscoelasticity.* International Journal of Solids and Structures, 50: 3886–3897.

[211] Saxena, P.; Hossain, M.; Steinmann, P. [2014]: *Nonlinear magneto-viscoelasticity of transversally isotropic magneto-active polymers.* Proceedings of the Royal Society A, 470: 1–23.

[212] Schrade, D.; Müller, R.; Xu, B. X.; Gross, D. [2007]: *Domain evolution in ferroelectric materials: A continuum phase field model and finite element implementation.* Computer Methods in Applied Mechanics and Engineering, 196: 4365–4374.

[213] Schrefl, T.; Fidler, J.; Kronmüller, H. [1994]: *Remanence and coercivity in isotropic nanocrystalline permanent magnets.* Physical Review B, 49(9): 6100.

[214] Schröder, J. [2000]: *Homogenisierungsmethoden der nichtlinearen Kontinuumsmechanik unter Beachtung von Stabilitätsproblemen.* Habilitationsschrift, Institut für Mechanik (Bauwesen), Lehrstuhl, I, Universität Stuttgart. Bericht Nr. I-7.

[215] Schröder, J. [2009]: *Derivation of the localization and homogenization conditions for electro-mechanically coupled problems.* Computational Materials Science, 46: 595–599.

[216] Schröder, J.; Keip, M.-A. [2012]: *Two-scale homogenization of electromechanically coupled boundary value problems.* Computational Mechanics, 50(2): 229–244.

[217] Schröder, J.; Labusch, M. [2018]: *A 3d magnetostrictive preisach model for the simulation of magneto-electric composites on multiple scales.* In *Multiscale Modeling of Heterogeneous Structures*, pp. 303–327. Springer.

[218] Schröder, J.; Romanowski, H. [2005]: *A thermodynamically consistent mesoscopic model for transversely isotropic ferroelectric ceramics in a coordinate-invariant setting.* Archive of Applied Mechanics, 74: 863–877.

[219] Schröder, J.; Labusch, M.; Keip, M.-A. [2016]: *Algorithmic two-scale transition for magneto-electro-mechanically coupled problems: Fe2-scheme: localization and homogenization.* Computer Methods in Applied Mechanics and Engineering, 302: 253–280.

[220] Schröder, J.; Labusch, M.; Keip, M.-A. [2016]: *Algorithmic two-scale transition for magneto-electro-mechanically coupled problems: Fe2-scheme: localization and homogenization.* Computer Methods in Applied Mechanics and Engineering, 302: 253–280.

[221] Segurado, J.; Llorca, J. [2002]: *A numerical approximation to the elastic properties of sphere-reinforced composites.* Journal of the Mechanics and Physics of Solids, 50(10): 2107–2121.

[222] Semenov, A. S.; Kessler, H.; Liskowsky, A.; Balke, H. [2006]: *On a vector potential formulation for 3d electromechanical finite element analysis.* Communication in Numerical Methods in Engineering, 22: 357–375.

[223] Semenov, A. S.; Liskowsky, A.; Balke, H. [2007]: *Vector potential formulation for the three-dimensional finite element analysis of nonlinear electromechanical problems.* In Dapino, M. J. (Editor), *Behavior and Mechanics of Multifunctional and Composite Materials 2007.* Proceeding of SPIE Vol. 6526.

[224] Seth, B. R. [1964]: *Generalized strain measure with application to physical problems.* In Reiner, M., A. D. (Editor), *Second-Order Effects in Elasticity, Plasticity and Fluid Dynamics*, pp. 162–172. Pergamon Press, Oxford.

[225] Shi, Z.; Nan, C.-W.; Liu, J. M.; Filippov, D. A.; Bichurin, M. I. [2004]: *Influence of mechanical boundary conditions and microstructural features on magnetoelectric behavior in a three-phase multiferroic particulate composite.* Physical Review B, 70: 134417.

[226] Shu, Y. C.; Lin, M. P.; C., W. K. [2004]: *Micromagnetic modeling of magnetostrictive materials under intrinsic stress.* Mechanics of Materials, 36(10): 975–997. Active Materials.

[227] Shvartsman, V.; Alawneh, F.; Borisov, P.; Kozodaev, D.; Lupascu, D. C. [2011]: *Converse magnetoelectric effect in $cofe_2o_4$-$batio_3$ composites with a core-shell structure.* Smart Materials and Structures, 20: 075006(6pp).

[228] Siboni, M. H.; Ponte Castañeda, P. [2014]: *Fiber-constrained, dielectric-elastomer composites: Finite-strain response and stability analysis.* Journal of the Mechanics and Physics of Solids, 68: 211–238.

[229] Siboni, M. H.; Avazmohammadi, R.; Ponte Castañeda, P. [2014]: *Electromechanical instabilities in fiber-constrained, dielectric-elastomer composites subjected to all-around dead loading.*

[230] Silhavý, M. [1997]: *The Mechanics and Thermodynamics of Continuous Media.* Springer–Verlag, Berlin.

[231] Simó, J. C.; Honein, T. [1990]: *Variational formulation, discrete conservation laws, and path–domain independent integrals for elasto–viscoplasticity.* Journal of Applied Mechanics, 57: 488–497.

[232] Smit, R. J. M.; Brekelmans, W. A. M.; Meijer, H. E. H. [1998]: *Prediction of the mechanical behavior of nonlinear heterogeneous systems by multi-level element*

modeling. Computer Methods in Applied Mechanics and Engineering, 155: 181–192.

[233] Smith, R. [2005]: *Smart Material Systems: Model Development*. SIAM, Society for Industrial and Applied Mathematics.

[234] Smith, R. C.; Dapino, M. J.; Seelecke, S. [2003]: *Free energy model for hysteresis in magnetostrictive transducers*. Journal of Applied Physics, 93(1): 458–466.

[235] Sridhar, A.; Keip, M.-A.; Miehe, C. [2016]: *Homogenization in micro-magneto-mechanics*. Computational Mechanics, 58(1): 151–169.

[236] Steigmann, D. J. [2004]: *Equilibrium theory for magnetic elastomers and magnetoelastic membranes*. International Journal of Non-Linear Mechanics, 39: 1193–1216.

[237] Steinmann, P. [2015]: *Geometrical Foundations of Continuum Mechanics*. Springer.

[238] Steinmann, P.; Vu, D. K. [2012]: *Computational challenges in the simulation of nonlinear electroelasticity*. Computer Assisted Methods in Engineering and Science, 19: 199–212.

[239] Su, Y.; Landis, C. M. [2007]: *Continuum thermodynamics of ferroelectric domain evolution: Theory, finite element implementation, and application to domain wall pinning*. Journal of the Mechanics and Physics of Solids, 55: 280–305.

[240] Suo, Z. [2010]: *Theory of dielectric elastomers*. Acta Mechanica Solida Sinica, 23(6): 549–578.

[241] Suo, Z.; Zhao, X.; Greene, W. H. [2008]: *A nonlinear field theory of deformable dielectrics*. Journal of the Mechanics and Physics of Solids, 56: 467–486.

[242] Suquet, P. M. [1987]: *Elements of homogenization for inelastic solid mechanics*. In Sanchez-Palenzia, E.; Zaoui, A. (Editors), *Lecture Notes in Physics: Homogenization Techniques for Composite Materials*, pp. 193–278. Springer-Verlag.

[243] Szambolics, H.; Buda-Prejbeanu, L.; Toussaint, J.-C.; Fruchart, O. [2008]: *A constrained finite element formulation for the landau–lifshitz–gilbert equations*. Computational Materials Science, 44(2): 253–258.

[244] Tanaka, K.; Mori, T. [1972]: *Note on volume integrals of the elastic field around an ellipsoidal inclusion*. Journal of Elasticity, 2: 199–200.

[245] Terada, K.; Kikuchi, T. [2001]: *A class of general algorithms for multi-scale analyses of heterogeneous media*. Computer Methods in Applied Mechanics and Engineering, 190: 5427–5464.

[246] Terada, K.; Hori, M.; Kyoya, T.; Kikuchi, N. [2000]: *Simulation of the multi-scale convergence in computational homogenization approaches*. International Journal of Solids and Structures, 37(16): 2285–2311.

[247] Thylander, S.; Menzel, A.; Ristinmaa, M. [2012]: *An electromechanically coupled micro-sphere framework: application to the finite element analysis of electrostrictive polymers*. Smart Materials and Structures, 21.

[248] Tian, L.; Tevet-Deree, L.; deBotton, G.; Bhattacharya, K. [2012]: *Dielectric elastomer composites*. Journal of the Mechanics and Physics of Solids, 60(1): 181–198.

[249] Tiersten, H. F. [1965]: *Variational principle for saturated magnetoelastic insulators*. Journal of Mathematical Physics, 6 (5): 779–787.

[250] Tiersten, H. F. [1971]: *On the nonlinear equations of thermo-electroelasticity*. International Journal of Engineering Science, 9(7): 587–604.

[251] Toupin, R. [1960]: *Stress tensors in elastic dielectrics.* Archive for Rational Mechanics and Analysis, 5: 440–452.

[252] Toupin, R. A. [1956]: *The elastic dielectric.* Journal of Rational Mechanics and Analysis, 5(6): 849–915.

[253] Triantafyllidis, T.; Maker, B. [1985]: *On the comparison between microscopic and macroscopic instability mechanisms in a class of fiber-reinforced composites.* Journal of Applied Mechanics, 52: 794–800.

[254] Truesdell, C.; Noll, W. [1965]: *The nonlinear field theories of mechanics.* In Fluegge, S. (Editor), *Handbuch der Physik Bd. III/3*. Springer-Verlag.

[255] Truesdell, C.; Toupin, R. [1960]: *The classical field theories.* In Flügge, S. (Editor), *Principles of Classical Mechanics and Field Theory*, Vol. III/1 of *Encyclopedia of Physics*, pp. 226–795. Springer-Verlag, Berlin.

[256] Tsang, C. H.; Chau, K. H.; Wong, C.; Wong, Y. W.; Shin, F. G. [2008]: *Modeling of the magnetoelectric effect of three-phase multiferroic particulate composites.* Integrated Ferroelectrics, 100: 177–197.

[257] Vallicotti, D.; Sridhar, A.; Keip, M.-A. [2018]: *Variationally consistent computational homogenization of micro-electro-mechanics at finite deformations.* International Journal for Multiscale Computational Engineering, 16: 377–395.

[258] Varga, Z.; Filipcsei, G.; Zrínyi [2005]: *Smart composites with controlled anisotropy.* Polymer, 46: 7779–7787.

[259] Varga, Z.; Filipcsei, G.; Zrínyi [2006]: *Magnetic field sensitive functional elastomers with tunable elastic modulus.* Polymer, 47: 227–233.

[260] Vogel, F.; Bustamante, R.; Steinmann, P. [2013]: *On some mixed variational principles in magneto-elastostatics.* International Journal of Non-Linear Mechanics, 51: 157–169.

[261] Voigt, W. [1887]: *Über die Beziehung zwischen den beiden Elastizitätskonstanten isotroper Körper.* Annalen der Physik, 38: 573–587.

[262] Vu, D. K.; Steinmann, P. [2007]: *Nonlinear electro- and magneto-elastostatics: Material and spatial settings.* Technical report, Chair of Applied Mechanics, University of Kaiserslautern.

[263] Vu, D. K.; Steinmann, P. [2010]: *A 2-d coupled bem-fem simulation of electroelastostatics at large strain.* Computer Methods in Applied Mechanics and Engineering, 199: 1124–1133.

[264] Vu, D. K.; Steinmann, P.; Possart, G. [2007]: *Numerical modelling of nonlinear electroelasticity.* International Journal for Numerical Methods in Engineering, 70: 685–704.

[265] Wang, X.-P.; Garcia-Cervera, C.; Weinan, E. [2001]: *A gauss–seidel projection method for micromagnetics simulations.* Journal of Computational Physics, 171(1): 357–372.

[266] Willis, J. R. [1977]: *Bounds and self-consistent estimates for the overall properties of anisotropic composites.* Journal of the Mechanics and Physics of Solids, 25: 185–202.

[267] Willis, J. R. [1981]: *Variational and related methods for the overall properties of composites.* Advances in Applied Mechanics, 21: 1–78.

[268] Yalcintas, M.; Dai, H. [2004]: *Vibration suppression capabilities of magnetorheological materials based adaptive structures.* Smart Materials and Structures, 13: 1–11.

[269] Yang, J. [2005]: *An introduction to the theory of piezoelectricity*. In Gao, D. Y.; Ogden, R. W. (Editors), *Advances in Mechanics and Mathematics*, Vol. 9. Springer Science + Business Media, Inc.

[270] Yang, J. S.; Batra, R. C. [1995]: *Mixed variational principles in non-linear electroelasticity*. International Journal of Non-Linear Mechanics, 30: 719–725.

[271] Yi, M.; Xu, B.-X. [2014]: *A constraint-free phase field model for ferromagnetic domain evolution*. Proceedings of the Royal Society of London A: Mathematical, Physical and Engineering Sciences, 470.

[272] Zäh, D.; Miehe, C. [2013]: *Computational homogenization in dissipative electromechanics of functional materials*. Computer Methods in Applied Mechanics and Engineering, 267: 487–510.

[273] Zäh, D.; Miehe, C. [2015]: *Multiplicative electro-elasticity of electroactive polymers accounting for micromechanically-based network models*. Submitted to Computer Methods in Applied Mechanics and Engineering.

[274] Zäh, D. [2014]: *Variational Homogenization in Electro-Mechanics: From Micro-Electro-Elasticity to Electroactive Polymers*. Report No. I-32, Institute of Applied Mechanics (CE) Chair I, University of Stuttgart.

[275] Zhang, J. X.; Chen, L. Q. [2005]: *Phase-field microelasticity theory and micromagnetic simulations of domain structures in giant magnetostrictive materials*. Acta Materialia, 53: 2845–2855.

[276] Zhang, J. X.; Chen, L. Q. [2005]: *Phase-field model for ferromagnetic shape-memory alloys*. Philosophical Magazine Letters, 85: 533–541.

[277] Zhang, W.; Bhattacharya, K. [2005]: *A computational model of ferroelectric domains. Part I: Model formulation and domain switching*. Acta Materialia, 53: 185–198.

[278] Zhang, W.; Bhattacharya, K. [2005]: *A computational model of ferroelectric domains. Part II: Grain boundaries and defect pinning*. Acta Materialia, 53: 199–209.

[279] Zhao, X.; Suo, Z. [2007]: *Method to analyze electromechanical stability of dielectric elastomers*. Applied Physics Letters, 91: 061921.

[280] Zhao, X.; Wang, Q. [2014]: *Harnessing large deformation and instabilities of soft dielectrics: Theory, experiment, and application*. Applied Physics Reviews, 1: 021304.

[281] Zhao, X.; Hong, W.; Suo, Z. [2007]: *Electromechanical hysteresis and coexistent states in dielectric elastomers*. Physical Review B, 76: 134113.

[282] Zohdi, T. I.; Wriggers, P. [2005]: *An introduction to computational micromechanics*. In Pfeiffer, F.; Wriggers, P. (Editors), *Lecture Notes in Applied and Computational Mechanics*, Vol. 20. Springer-Verlag.

[283] Zohdi, T. [2010]: *Simulation of coupled microscale multiphysical-fields in particulate-doped dielectrics with staggered adaptive fdtd*. Computer Methods in Applied Mechanics and Engineering, 199(49-52): 3250–3269.

[284] Zohdi, T. [2012]: *Electromagnetic properties of multiphase dielectrics: a primer on modeling, theory and computation*, Vol. 64. Springer Science & Business Media.

In dieser Schriftenreihe bisher erschienene Berichte

IAM 1 (2018) *Numerically efficient computational homogenization: Fourier-accelerated nodal solvers and reduced basis model order reduction*, M. Leuschner, Dissertation, 2018.

IAM 2 (2019) *Magneto-Electro-Mechanical Coupling Phenomena Across Multiple Length-Scales: Variational Framework and Stability Analysis*, D. Vallicotti, Dissertation, 2019.

Institute of Applied Mechanics (IAM)
Chair of Materials Theory

With the rapid advances in micro-electronics and data-processing, multiscale material models can be incorporated in the development process of innovative functional materials. In this work, the broad field of magneto-electro-mechanically coupled devices is in focus. Here, the interactions of electric, magnetic and mechanical fields give rise to smart materials that are used as sensors and actuators in industrial applications. This work provides the basis for multiscale investigations of magneto-electro-mechanics both in a phenomenological and micro-mechanically motivated setting.

Starting from a canonical variational principle, a numerically convenient mixed formulation of finite magneto-electro-mechanics is developed. It serves as a basis for multiscale structural and material stability analyses in a phenomenological material modeling framework. In a next step, phase-field models are employed to focus on the evolution and motion of electric and magnetic domains in the micro-structure. The related interactions of particles and their influence on the overall macroscopic deformation states are investigated.

ISBN 978-3-937859-23-1